



Universidade de Aveiro  
2021

**SORAIA PATRÍCIA  
SILVA FERNANDES**

**REDES ORGÂNICAS COVALENTES PARA A  
CAPTURA DE COMPOSTOS PERIGOSOS DA ÁGUA**

**COVALENT ORGANIC FRAMEWORKS TO CAPTURE  
HAZARDOUS COMPOUNDS FROM WATER**





Universidade de Aveiro  
2021

**SORAIA PATRÍCIA  
SILVA FERNANDES**

**REDES ORGÂNICAS COVALENTES PARA A  
CAPTURA DE COMPOSTOS PERIGOSOS DA ÁGUA**

**COVALENT ORGANIC FRAMEWORKS TO CAPTURE  
HAZARDOUS COMPOUNDS FROM WATER**

Tese apresentada à Universidade de Aveiro para cumprimento dos requisitos necessários à obtenção do grau de Doutor em Química, realizada sob a orientação científica do Doutor Artur Manuel Soares da Silva, Professor Catedrático do Departamento de Química da Universidade de Aveiro, da Doutora Laura Salonen e da Doutora Begoña Espiña, ambas Investigadoras do Laboratório Ibérico de Nanotecnologia, Braga.

Trabalho desenvolvido com o apoio financeiro da FCT através da bolsa de doutoramento com a referência SFRH/BD/131791/2017.

**FCT** Fundação  
para a Ciência  
e a Tecnologia



Dedico este trabalho aos meus pais, irmão e, de forma muito especial ao meu noivo Ricardo pelo incansável apoio durante estes últimos 4 anos.  
E de uma forma ainda mais especial ao meu príncipe Afonso que me acompanhou durante este último ano.

I dedicate this work to my parents, brother and, in a very special way, to my fiancé Ricardo for his tireless support during these last 4 years.  
And in an even more special way to my baby Afonso, who accompanied me during this last year.



## o júri

Presidente:

Prof. Doutor Delfim Fernando Marado Torres

Professor Catedrático, Universidade de Aveiro

Vogais:

Prof. Doutor Carlos Alberto Mateus Afonso

Professor Catedrático, Universidade de Lisboa

Prof. Doutor Tito da Silva Trindade

Professor Catedrático, Universidade de Aveiro

Prof.<sup>a</sup> Doutora Maria Magdalena Cid Fernández

Professora Catedrática, Universidade de Vigo

Prof.<sup>a</sup> Doutora Maria Carmen Louzao Ojeda

Professora Titular, Universidade de Santiago de Compostela

Doutora Laura Salonen

Investigadora, International Iberian Nanotechnology Laboratory (INL)





## **Acknowledgment**

This thesis represents the conclusion of a 4-year stage, full of new teaching, personal and professional growth.

I would like to express my sincere appreciation to my supervisors, Professor Dr. Artur Silva, Dr. Laura Salonen and Dr. Begoña Espiña for their support, dedication and availability to guide me in this self-learning process.

I would like to thank Dr. Elisa Pinto for her help in carrying out the NMR analysis, as well as Dr. Rosário Soares with the XRD analysis.

I would like to thank the collaborators, Dr. Milan Pšenička, Dr. Petr Kovár, and Dr. Dana Medina for their support in computational modelling and X-ray computational studies. To Dr. Vanessa Fonseca and Dr. Patrick Reis-Santos from Marine and Environmental Sciences Centre (MARE) for their opportunity to work with natural water samples and expand the scope of my thesis project.

I would like to thank to Sara Pinela and Dr. Vanesa Romero for their support and shared knowledge during our time working together in the laboratory.

I would like to thank all the members of the Nanochemistry and Water Quality groups of INL for all the time we spend together working and sharing good moments that will remain in my memory.

Special thanks to my family (father, mother and brother) for their patience, support in all moments, and motivation to never give up on my goals.

Ricardo and Afonso, the most special thank you of all...! There are no words to describe everything you both did for me as a Family!

To all of you, Thank you so much!



## palavras-chave

Redes Orgânicas Covalentes (COFs); COFs baseados em Tp; COFs baseados em duplas ligações (C=C); Adsorção; Biotoxinas (Ácido ocaidaico e Microcistinas); Poluentes Farmacêuticos; Amostras ambientais de água.

## resumo

O crescente aumento da presença de compostos perigosos na água é um grande problema em todo o mundo, levantando preocupações sobre os seus potenciais efeitos negativos nos ecossistemas aquáticos, bem como na saúde humana. Assim, tornou-se urgente o desenvolvimento de metodologias mais eficientes para a sua monitorização e captura. Devido à sua simplicidade e robustez, a adsorção surge como uma técnica adequada, promissora e económica para a monitorização e purificação da água. As redes orgânicas covalentes (COFs) são materiais nanoporosos e cristalinos obtidos através da condensação de unidades monoméricas orgânicas que se organizam numa estrutura em camadas, com elevada integridade estrutural. Além disto, devido à sua elevada área superficial e, ajustável superfície de poros, os COFs surgem como materiais interessantes para aplicações de adsorção. Nesta tese, COFs baseados em Tp, cristalinos e estáveis em água foram sintetizados com sucesso e usados como eficientes adsorventes para contaminantes presentes na água, com aplicabilidade demonstrada até no meio ambiente. Além disso, a capacidade dos COFs para serem estruturalmente adaptados para a captura preferencial de compostos perigosos também foi demonstrada. Biotoxinas, como o ácido ocaidaico (OA) em água do mar e, microcistinas (MCs) em água doce, detectadas em todo o mundo e altamente tóxicas, foram adsorvidas pelos COFs selecionados com elevada eficiência. As MCs, devido à sua grande variedade de análogos, demonstraram ser uma excelente classe de compostos alvo para adquirir uma compreensão mais profunda das interações estabelecidas entre COF e molécula-alvo, essenciais para o desenvolvimento de materiais COF mais eficientes e selectivos. COFs à base de Tp também foram utilizados para capturar com eficiência poluentes farmacêuticos emergentes, como o ibuprofeno, a partir de amostras de água natural, mesmo em competição com outros produtos farmacêuticos. A capacidade de reutilização dos COFs também foi demonstrada para todos os compostos perigosos testados, mantendo intacta a integridade estrutural e as propriedades dos COFs selecionados. Por fim, com o objetivo de explorar a síntese de novos COFs cristalinos e estáveis em água, um novo COF baseado em ligações duplas foi preparado. Este COF apresenta propriedades óticas interessantes para ser utilizado como fotocatalisador na degradação de poluentes orgânicos da água. Em resumo, COFs com elevada capacidade de adsorção foram preparados, conduzindo ao desenvolvimento de novas ferramentas para monitorizar e remover compostos perigosos presentes na água.



**keywords**

Covalent Organic Frameworks (COFs); Tp-based COFs; sp<sup>2</sup>-based COFs; Adsorption; Biotoxins (Okadaic acid and Microcystins); Pharmaceutical pollutants; Environmental water samples.

**abstract**

Increasing occurrence of hazardous compounds in water is a major worldwide problem raising concerns about their potential negative effects on aquatic ecosystems, as well as in human health. Therefore, the development of more efficient methodologies for their monitoring and capturing are urgently needed. Owing to its simplicity and robustness, adsorption appears as a fit-for-purpose/adequate/promising and economical technique for water monitoring and depuration. Crystalline nanoporous covalent organic frameworks (COFs), formed by the self-assembly of purely organic building blocks into a layered structure, are versatile materials with high structural regularity and tunability, and due to their high surface areas and tunable pore surfaces, they are interesting materials for adsorption applications.

In this thesis, water stable crystalline Tp-based COFs were successfully synthesized and used as efficient adsorbents for water contaminants, with demonstrated usability even in the environmental field. Beyond that the capacity of COFs to be tuned for the preferential capture of the selected hazardous compounds was also demonstrated. Biotoxins, such as okadaic acid (OA) in seawater and microcystins (MCs) in freshwater, detected worldwide and highly toxic, were adsorbed by Tp-based COFs with high efficiency. MCs owing to its broad range of derivatives has been shown to be an excellent family model of target compounds to provide in-depth understanding of COF-adsorbate interactions, and essential for the development of more efficient and selective adsorbent COF materials. Tp-based COFs were also used to efficiently capture pharmaceutical pollutants of emerging concern, such as ibuprofen from natural water samples, even in competition with other pharmaceuticals. COFs reusability was also demonstrated for all tested highly adsorbed hazardous compounds with the structural integrity and properties of the COF remaining intact. Finally, aiming to explore the synthesis of novel crystalline and highly water-stable COFs, a novel sp<sup>2</sup>-based COF was prepared. This COF presents interesting optical properties to be used as photocatalyst for the degradation of organic pollutants from water. In summary, COFs with proven high adsorption capabilities can lead to the development of new tools for monitoring and removing waterborne hazardous compounds.



## Table of Contents

List of schemes .....	i
List of figures .....	iii
List of tables .....	xi
List of abbreviations .....	xiii
<b>Chapter 1 – Introduction</b> .....	<b>1</b>
1.1. Porous materials .....	1
1.2. Covalent organic frameworks.....	1
1.2.1. Design and synthetic principles .....	2
1.2.2. Water stability of COFs .....	5
1.2.3. Supramolecular interactions as driving force for COF synthesis.....	9
1.2.4. Functionalization of COFs .....	11
1.2.5. Structural analysis of COFs .....	16
1.3. Water quality.....	18
1.3.1. Biotoxins.....	20
1.3.2. Pharmaceutical pollutants .....	22
1.3.3. Water monitoring and treatment.....	23
1.3.4. State-of-the-art adsorbents for biotoxins and pharmaceuticals.....	27
1.3.5. COFs for adsorption applications.....	30
1.4. Objectives.....	32
<b>Chapter 2 – Tailoring COFs for the adsorption of hazardous compounds</b> .....	<b>33</b>
2.1. COFs for the adsorption of biotoxins.....	33
2.1.1. Okadaic acid <sup>[246]</sup> .....	33
2.1.2. Microcystin (MC) <sup>[249]</sup> .....	42
2.2. COFs for the adsorption of pharmaceutical pollutants.....	65
2.2.1. Pharmaceutical pollutants <sup>[61]</sup> .....	65
2.2.2. Ibuprofen adsorption from natural waters samples <sup>[248]</sup> .....	74
2.2.3. Screening of pharmaceutical pollutants in Tagus estuary using COF as adsorbent – an environmental case study <sup>[250]</sup> .....	84
<b>Chapter 3 – Expanding chemical synthesis of sp<sup>2</sup>-based COFs</b> .....	<b>93</b>
3.1. Selection of building block units – model system preparation .....	94
3.2. Synthesis of sp <sup>2</sup> -based COFs – preliminary tests .....	100
3.3. Photocatalytic degradation of dyes by TFB-Phen COF – preliminary tests .....	106

<b>Chapter 4 – Conclusions and outlook</b> .....	109
<b>Chapter 5 – Experimental</b> .....	113
5.1. Materials and methods .....	113
5.1.1. Reagents and chemicals .....	113
5.1.2. Characterization techniques.....	114
5.1.3. Theoretical calculations.....	115
5.1.3.1. MC computational studies.....	115
5.1.3.2. Ibuprofen computational studies in natural water samples .....	119
5.1.4. Stability tests .....	120
5.2. Synthetic procedures .....	120
5.3. Adsorption procedures.....	124
5.3.1. Okadaic acid adsorption procedure.....	124
5.3.2. Microcystin adsorption procedure .....	127
5.3.3. Ibuprofen, acetaminophen, and ampicillin adsorption procedure .....	132
5.3.4. Ibuprofen adsorption in natural water samples .....	139
5.3.5. Pharmaceutical pollutants adsorption in Tagus estuary .....	147
5.4. Characterization Data.....	151
5.4.1. NMR spectra.....	151
5.4.2. N <sub>2</sub> Physisorption .....	152
5.4.3. FT-IR data .....	156
5.4.4. TGA data.....	159
5.4.5. Water contact angle measurements .....	163
5.4.6. SEM data .....	164
5.4.7. Computational models .....	165
5.4.8. Point of zero charge (pzc) of TpBD-(CF <sub>3</sub> ) <sub>2</sub> .....	165
<b>References</b> .....	167



## List of schemes

<b>Scheme 1.</b> Schematic representation of some of irreversible reactions used to lock and increase stability of imine bond in COFs via chemical conversion to amide (A), <sup>[97]</sup> azole derivatives (B), <sup>[98,100]</sup> and quinoline (C) <sup>[99]</sup> linkages.....	7
<b>Scheme 2.</b> Schematic representation of reversible-irreversible reaction sequence for the formation of water stable $\beta$ -ketoenamine linkage. ....	8
<b>Scheme 3.</b> Synthesis of TpBD-(CH <sub>3</sub> ) <sub>2</sub> through reaction of Tp and <i>o</i> -tolidine (BD-(CH <sub>3</sub> ) <sub>2</sub> ). ..	34
<b>Scheme 4.</b> Synthesis of TpBD-(CF <sub>3</sub> ) <sub>2</sub> from Tp and 3,3'-bis(trifluoromethyl)benzidine (BD-(CF <sub>3</sub> ) <sub>2</sub> ).....	45
<b>Scheme 5.</b> Synthesis of TpBD-(NO <sub>2</sub> ) <sub>2</sub> from Tp and 3,3'-dinitrobenzidine (BD-(NO <sub>2</sub> ) <sub>2</sub> ), followed by a PSM reduction reaction to afford TpBD-(NH <sub>2</sub> ) <sub>2</sub> .....	49
<b>Scheme 6.</b> Representation of synthetic strategies reported for the synthesis of sp <sup>2</sup> -based COFs.....	93
<b>Scheme 7.</b> Synthesis of COF-1 and COF-2 <sup>[333]</sup> via aldol condensation of trimethyltriazine with reactive aldehyde derivatives terephthalaldehyde and naphthalene-2,6-dicarbaldehyde, respectively, under basic conditions. ....	95
<b>Scheme 8.</b> Synthesis of model compound <b>2</b> in 40% yield from reaction of Phen with benzaldehyde ( <b>1</b> ).....	97
<b>Scheme 9.</b> Synthesis of model compound <b>3</b> in 50% yield from reaction of Tda with benzaldehyde ( <b>1</b> ).....	98
<b>Scheme 10.</b> Synthesis of model compound <b>4</b> from reaction of Tz with benzaldehyde ( <b>1</b> ).99	
<b>Scheme 11.</b> Synthesis of model compound <b>5</b> from reaction of Tf with benzaldehyde ( <b>1</b> ). 99	
<b>Scheme 12.</b> Synthesis of sp <sup>2</sup> -based TFB-Phen COF from TFB and Phen. ....	101



## List of figures

<b>Figure 1.</b> Schematic representation of a 2D <sup>[25]</sup> (A) and 3D <sup>[26]</sup> (B) COF structure. Adapted with permission. Copyright 2016 and 2013, American Chemical Society. ....	2
<b>Figure 2.</b> Representation of possible combination of building blocks with different geometries to yield 2D COFs. ....	3
<b>Figure 3.</b> Representation of most common covalent bonds used to make 2D COFs. ....	5
<b>Figure 4.</b> Representation of two main functionalization approaches in 2D COFs: bottom-up and PSM approach.....	12
<b>Figure 5.</b> Classification of physisorption isotherms by IUPAC. <sup>[149]</sup> Adapted with permission. Copyright, IUPAC & De Gruyter, 2015. ....	18
<b>Figure 6.</b> Most commonly detected contaminants in water resources (PCBs: polychlorinated biphenyls; PFCs: perfluorinated compounds; VOCs: volatile organic compounds).....	19
<b>Figure 7.</b> Chemical structures of okadaic acid (OA) and microcystins (MC). ....	21
<b>Figure 8.</b> Chemical structure of OA. Molecular weight and LD <sub>50</sub> values.....	33
<b>Figure 9.</b> (A) SAXS pattern of TpBD-(CH <sub>3</sub> ) <sub>2</sub> prepared in mg (red curve) and gram scale (orange curve). (B) N <sub>2</sub> adsorption (filled spheres) and desorption (hollow spheres) isotherm profiles measured at 77 K of the TpBD-(CH <sub>3</sub> ) <sub>2</sub> prepared in mg (red curve) and gram scale (orange curve). ....	35
<b>Figure 10.</b> SAXS pattern comparison of pristine TpBD-(CH <sub>3</sub> ) <sub>2</sub> (red curve), and after soaking for 7 days in ultrapure water (light grey curve) and synthetic seawater (dark grey curve). ....	37
<b>Figure 11.</b> SEM images of TpBD-(CH <sub>3</sub> ) <sub>2</sub> as synthesized (A), and after soaking for 7 days in ultrapure water (B) and in synthetic seawater (C). ....	37
<b>Figure 12.</b> Adsorption kinetic curves of TpBD-(CH <sub>3</sub> ) <sub>2</sub> expressed as quantity adsorbed, $q_t$ (mg g <sup>-1</sup> ), for initial OA concentrations of 10, 15, 50, and 100 μmol L <sup>-1</sup> , at 19 °C in synthetic seawater. ....	38
<b>Figure 13.</b> (A) Amount of OA adsorbed in equilibrium, $q_e$ (mg g <sup>-1</sup> ), as a function of OA concentration in equilibrium, $C_e$ (mg L <sup>-1</sup> ); (B) linear regression of the Freundlich isotherm for the experimental adsorption of OA by TpBD-(CH <sub>3</sub> ) <sub>2</sub> .....	39
<b>Figure 14.</b> Desorption kinetic of OA from TpBD-(CH <sub>3</sub> ) <sub>2</sub> , expressed in %, as an average of two independent experiments, performed in duplicates, in ethanol 70% at 4 °C. Error bars correspond to the standard deviation of the mean.....	40

<b>Figure 15.</b> Reusability of TpBD-(CH <sub>3</sub> ) <sub>2</sub> for OA, expressed as quantity adsorbed, $q_t$ (mg g <sup>-1</sup> ), in three consecutive cycles of adsorption/desorption, with an initial OA concentration of 10 μmol L <sup>-1</sup> in each of the adsorption cycles (seawater at 19 °C). Desorption was carried out using ethanol 70%. Results are expressed as the mean of duplicates. Error bars correspond to the standard deviation of the mean.....	41
<b>Figure 16.</b> Chemical structures of MC-LA, -LR, -RR, -YR at neutral pH. Molecular weight and LD <sub>50</sub> <sup>[184,185]</sup> values. *Molecular weight of MCs at zero net charge.....	43
<b>Figure 17.</b> The structure of TpBD-(CF <sub>3</sub> ) <sub>2</sub> , TpBD-(NO <sub>2</sub> ) <sub>2</sub> and TpBD-(NH <sub>2</sub> ) <sub>2</sub> .....	44
<b>Figure 18.</b> (A) PXRD pattern of TpBD-(CF <sub>3</sub> ) <sub>2</sub> . (B) N <sub>2</sub> adsorption (filled spheres) and desorption (hollow spheres) isotherm profiles measured at 77 K of TpBD-(CF <sub>3</sub> ) <sub>2</sub> . ....	45
<b>Figure 19.</b> Simulation of the crystal unit cell calculated in an eclipsed AA arrangement in the P6 space group. Top: view on ab-plane; bottom: view along b-axis. ....	46
<b>Figure 20.</b> The experimentally obtained PXRD pattern of TpBD-(CF <sub>3</sub> ) <sub>2</sub> (black), Pawley refinement (red), and the simulated PXRD pattern obtained by the Reflex module in Materials Studio based on an eclipsed AA arrangement. ....	46
<b>Figure 21.</b> SEM images of TpBD-(CF <sub>3</sub> ) <sub>2</sub> prepared in mg scale (A) and TpBD-(CF <sub>3</sub> ) <sub>2</sub> prepared in gram scale (B). ....	47
<b>Figure 22.</b> (A) SAXS pattern of TpBD-(CF <sub>3</sub> ) <sub>2</sub> synthesized on a gram scale. (B) N <sub>2</sub> adsorption (filled spheres) and desorption (hollow spheres) isotherm profiles measured at 77 K.....	48
<b>Figure 23.</b> (A) SAXS pattern of TpBD-(NO <sub>2</sub> ) <sub>2</sub> (purple curve) and TpBD-(NH <sub>2</sub> ) <sub>2</sub> (green curve). (B) N <sub>2</sub> adsorption (filled spheres) and desorption (hollow spheres) isotherm profiles measured at 77 K of TpBD-(NO <sub>2</sub> ) <sub>2</sub> (purple curve) and TpBD-(NH <sub>2</sub> ) <sub>2</sub> (green curve). ....	51
<b>Figure 24.</b> Quantification of the MC-LA, MC-LR, MC-RR, and MC-YR adsorption (A) and desorption (B) efficiencies (%) onto TpBD-(CF <sub>3</sub> ) <sub>2</sub> , TpBD-(NO <sub>2</sub> ) <sub>2</sub> , and TpBD-(NH <sub>2</sub> ) <sub>2</sub> , as an average of three independent experiments, performed in duplicates, in ultrapure water at 19 °C and pH 6–7 and propan-2-ol at 4 °C, respectively. Error bars correspond to the standard deviation of the mean. ....	53
<b>Figure 25.</b> A top view along z axis of the atomistic model of MC-LA with TpBD-(NH <sub>2</sub> ) <sub>2</sub> . Reprinted with permission from Ref. [249]. Copyright 2021, American Chemical Society.. ....	54
<b>Figure 26.</b> A top view along z axis (A) and side view along x axis (B) of the atomistic model of MC-RR with TpBD-(NO <sub>2</sub> ) <sub>2</sub> , located on the surface of COF. Reprinted with permission from Ref. [249]. Copyright 2021, American Chemical Society.....	57
<b>Figure 27.</b> Adsorption kinetics of: (A) MC-LR onto TpBD-(CF <sub>3</sub> ) <sub>2</sub> ; (B) MC-LA onto TpBD-(NH <sub>2</sub> ) <sub>2</sub> ; and (C) MC-RR onto TpBD-(NO <sub>2</sub> ) <sub>2</sub> expressed as quantity adsorbed, $q_t$ (mg g <sup>-1</sup> ), for initial MCs	

concentrations of 1, 5, 10, and 15  $\mu\text{mol L}^{-1}$ , at 19 °C in ultrapure water at pH 6–7. Results are expressed as the mean of three independent experiments with measurements performed in duplicates. Error bars correspond to the standard deviation of the mean. . 58

**Figure 28.** Reusability of TpBD-(CF<sub>3</sub>)<sub>2</sub> for MC-LR and MC-YR, TpBD-(NO<sub>2</sub>)<sub>2</sub> for MC-RR, and TpBD-(NH<sub>2</sub>)<sub>2</sub> for MC-LA, in three consecutive cycles of adsorption-desorption, with an initial MC concentration of 10  $\mu\text{mol L}^{-1}$  in each of the adsorption cycles (ultrapure water at 19 °C and pH 6–7). Desorption was carried out using methanol/ammonium hydroxide mixture at pH 9.7 for MC-LR, MC-YR, and MC-RR, and methanol/formic acid mixture at pH 2.7 for MC-LA. Results are expressed as the mean of duplicates. Error bars correspond to the standard deviation of the mean. .... 64

**Figure 29.** Ibuprofen adsorption kinetics expressed as quantity adsorbed,  $q_t$  ( $\text{mg g}^{-1}$ ), by TpBD-(CF<sub>3</sub>)<sub>2</sub> (black) and TpBD-(CH<sub>3</sub>)<sub>2</sub> (orange) at 21 °C in ultrapure water at pH 6–7. Results are expressed as the mean of two separate experiments with measurements performed in duplicate. Error bars correspond to the standard deviation of the mean. .... 67

**Figure 30.** (A) SAXS pattern and (B) N<sub>2</sub> adsorption (filled spheres) and desorption (hollow spheres) isotherm profiles measured at 77 K of TpBD-(CF<sub>3</sub>)<sub>2</sub> as-synthesized (black), after adsorption of ibuprofen (cyan), and after desorption (grey)..... 69

**Figure 31.** FT-IR spectra (A) and TGA data (B) of ibuprofen (red) and of TpBD-(CF<sub>3</sub>)<sub>2</sub> as-synthesized (black), after adsorption of ibuprofen (cyan), and after desorption of ibuprofen (grey)..... 70

**Figure 32.** (A) The adsorbed quantities of the ibuprofen, acetaminophen, and ampicillin by TpBD-(CF<sub>3</sub>)<sub>2</sub> as a function of pH (pH 6 denotes ultrapure water,  $C_0(\text{pharmaceutical}) = 20 \text{ mg L}^{-1}$ ,  $C_0(\text{TpBD}-(\text{CF}_3)_2) = 100 \text{ mg L}^{-1}$ ,  $t = 120 \text{ min}$ ). (B) The adsorbed quantities of ibuprofen by TpBD-(CF<sub>3</sub>)<sub>2</sub> as a function of solvent polarity (water and ethanol as selected solvents,  $C_0(\text{pharmaceutical}) = 20 \text{ mg L}^{-1}$ ,  $C_0(\text{TpBD}-(\text{CF}_3)_2) = 100 \text{ mg L}^{-1}$ ,  $t = 120 \text{ min}$ ). Results are expressed as the mean of two separate experiments with measurements performed in duplicate. Error bars correspond to the standard deviation of the mean. .... 71

**Figure 33.** Electrostatic potential (ESP) surfaces of the studied pharmaceuticals generated at the HF/STO-3G level of theory using an isovalue of 0.02 with scale from –0.2 red to 0.2 blue. The geometry of the molecules resembles those of the X-ray crystal structures, obtained from the Cambridge Structural Database (CSD) with the following codes: diclofenac: CCDC-1102110, ibuprofen: CCDC-1041382, acetaminophen: CCDC-150969, ampicillin: CCDC-298547. The charges are expressed as found at pH 6. .... 72

**Figure 34.** ESP surfaces of truncated model system TpBD-(CF<sub>3</sub>)<sub>2</sub> (left) and TpBD-(CH<sub>3</sub>)<sub>2</sub> (right), where the more electronegative character of the CF<sub>3</sub> moiety is evident..... 72

<b>Figure 35.</b> (A) SAXS pattern of TpBD-(CH <sub>3</sub> ) <sub>2</sub> as synthesized (orange), after adsorption of ibuprofen (cyan), and after desorption (grey). (B) The adsorbed quantity of the ibuprofen by TpBD-(CH <sub>3</sub> ) <sub>2</sub> as a function of pH (pH 6 denotes ultrapure water, C <sub>0</sub> (ibuprofen) = 20 mg L <sup>-1</sup> , C <sub>0</sub> (TpBD-(CH <sub>3</sub> ) <sub>2</sub> ) = 100 mg L <sup>-1</sup> , t = 120 min).....	74
<b>Figure 36.</b> Adsorption efficiency (%) of ibuprofen by TpBD-(CF <sub>3</sub> ) <sub>2</sub> in natural water samples collected from lake, river, and estuary (C <sub>0</sub> (TpBD-(CF <sub>3</sub> ) <sub>2</sub> ) = 330 mg L <sup>-1</sup> , C <sub>0</sub> (ibuprofen) = 10.31 and 20.63 mg L <sup>-1</sup> , t = 120 min). .....	78
<b>Figure 37.</b> (A) A view along the TpBD-(CF <sub>3</sub> ) <sub>2</sub> pore axis showing the orientations of six deprotonated ibuprofen molecules. (B) A view perpendicular to the TpBD-(CF <sub>3</sub> ) <sub>2</sub> pore axis showing the protonated ibuprofen in tilted and parallel orientation with respect to the TpBD-(CF <sub>3</sub> ) <sub>2</sub> pore axis.....	78
<b>Figure 38.</b> A view along the COF pore axis showing the orientations of protonated (A) and deprotonated (B) ibuprofen in water environment. ....	79
<b>Figure 39.</b> Adsorption efficiency (%) of ibuprofen (red) at concentrations of 50 and 100 μM, and acetaminophen (green) and phenobarbital (blue) at concentrations of 50, 100, and 150 μM by TpBD-(CF <sub>3</sub> ) <sub>2</sub> in lake water. The experiment was performed in duplicate. (C <sub>0</sub> (TpBD-(CF <sub>3</sub> ) <sub>2</sub> ) = 330 mg L <sup>-1</sup> , t = 120 min). .....	82
<b>Figure 40.</b> Adsorption efficiency (%) of binary mixtures of ibuprofen and acetaminophen or phenobarbital, at concentration ratios of 50/150 and 100/100 μM, by TpBD-(CF <sub>3</sub> ) <sub>2</sub> (C <sub>0</sub> = 330 mg L <sup>-1</sup> ) in lake water samples. (C <sub>0</sub> (TpBD-(CF <sub>3</sub> ) <sub>2</sub> ) = 330 mg L <sup>-1</sup> , t = 120 min). .....	84
<b>Figure 41.</b> Overview of the studied methods.....	87
<b>Figure 42.</b> Detection and adsorption efficiencies (%) obtained for all identified pharmaceuticals with Method 2 in Tagus estuary. Results are the average of 5 samples collected in the same site.....	88
<b>Figure 43.</b> The structures of the pharmaceuticals at pH 8. The pK <sub>a</sub> values of the relevant functional groups are presented in the figures in red and blue. ....	91
<b>Figure 44.</b> Electron-deficient building blocks selected to be tested for the synthesis of sp <sup>2</sup> -based COFs. ....	96
<b>Figure 45.</b> (A) PXRD patterns of selected experimental conditions tested for the synthesis of sp <sup>2</sup> -based TFB-Phen COF. (B) PXRD pattern of TFB-Phen prepared following the optimal conditions. ....	101
<b>Figure 46.</b> (A) N <sub>2</sub> adsorption (filled spheres) and desorption (hollow spheres) isotherm profiles measured at 77 K of TFB-Phen COF. (B) Multi-point BET plot and linear fit of TFB-Phen COF. (C) Pore size distribution (hollow spheres) and cumulative pore volume (filled spheres) profile of TFB-Phen COF. ....	103

<b>Figure 47.</b> FT-IR spectra of model compound <b>2</b> (black), 1,3,5-triformylbenzene (blue), 3,8-dimethyl-4,7-phenanthroline (green), and TFB-Phen COF (red). .....	104
<b>Figure 48.</b> TGA data of TFB-Phen COF (red) and 3,8-dimethyl-4,7-phenanthroline (green). .....	104
<b>Figure 49.</b> (A) UV/vis diffuse reflectance spectra (DRS) of TFB-Phen COF, and (B) band gap determined from the Kubelka–Munk-transformed reflectance spectra.....	105
<b>Figure 50.</b> Chemical structure of MO and MB at neutral pH. ....	106
<b>Figure 51.</b> (A) Photocatalytic degradation of 10 ppm MO (green) and MB (black) over TFB-Phen. (B) Kinetic linear simulation curve of MO photodegradation over TFB-Phen. The data fitted well to the pseudo-second-order kinetics model. ....	107
<b>Figure 52.</b> OA calibration curve in synthetic seawater (A) and ethanol 70% (B). ....	125
<b>Figure 53.</b> MC-LR calibration curve in ultrapure water (A) and propan-2-ol (B). ....	128
<b>Figure 54.</b> MC-LA calibration curve in ultrapure water (A) and propan-2-ol (B). ....	128
<b>Figure 55.</b> MC-RR calibration curve in ultrapure water (A) and propan-2-ol (B). ....	129
<b>Figure 56.</b> MC-YR calibration curve in ultrapure water (A) and propan-2-ol (B). ....	129
<b>Figure 57.</b> Adsorption kinetics at 10 $\mu\text{mol L}^{-1}$ of: (A) MC-LA; (B) MC-RR; and (C) MC-YR in TpBD-(CF <sub>3</sub> ) <sub>2</sub> , expressed as quantity adsorbed, $q_t$ (mg g <sup>-1</sup> ) in function of time, 0.5, 5, 10, 30, 60, 100, 120, and 240 min, at 19 °C in ultrapure water at pH 6–7. Results are expressed as the mean of three independent experiments with measurements performed in duplicates. Error bars correspond to the standard deviation of the mean. ....	130
<b>Figure 58.</b> Linear regression of the Langmuir isotherm for the experimental adsorption of (A) MC-LR by TpBD-(CF <sub>3</sub> ) <sub>2</sub> ; (B) MC-LA by TpBD-(NH <sub>2</sub> ) <sub>2</sub> ; and MC-RR by TpBD-(NO <sub>2</sub> ) <sub>2</sub> . ....	131
<b>Figure 59.</b> Linear regression of the Freundlich isotherm for the experimental adsorption of (A) MC-LR by TpBD-(CF <sub>3</sub> ) <sub>2</sub> ; (B) MC-LA by TpBD-(NH <sub>2</sub> ) <sub>2</sub> ; and MC-RR by TpBD-(NO <sub>2</sub> ) <sub>2</sub> . ....	132
<b>Figure 60.</b> (A) Pseudo-first-order adsorption kinetics, and (B) pseudo-second-order adsorption kinetics of ibuprofen onto TpBD-(CF <sub>3</sub> ) <sub>2</sub> . ....	133
<b>Figure 61.</b> Calibration curve of ibuprofen in ultrapure water (A), propan-2-ol (B), buffer at pH 2 (C), buffer at pH 10 (D), and ethanol (E) as measured by UV-Vis spectroscopy at 220 nm. ....	136
<b>Figure 62.</b> Calibration curve of acetaminophen in ultrapure water (A), buffer at pH 2 (B), and buffer at pH 10 (C) as measured by UV-Vis spectroscopy at 243 nm. ....	137
<b>Figure 63.</b> Calibration curve of ampicillin in ultrapure water (A), buffer at pH 2 (B), and buffer at pH 10 (C) as measured by UV-Vis spectroscopy at 210 nm. ....	138

<b>Figure 64.</b> Calibration curve of diclofenac in ultrapure water as measured by UV-Vis spectroscopy at 273 nm. ....	139
<b>Figure 65.</b> Calibration curve of (A) ibuprofen in ultrapure water measured at $\lambda = 220$ nm (B) acetaminophen in ultrapure water measured at $\lambda = 243$ nm, and (C) phenobarbital in ultrapure water measured at $\lambda = 210$ nm by HPLC-DAD spectrophotometer.....	142
<b>Figure 66.</b> HPLC-DAD chromatogram for lake natural water sample ( $\lambda = 220$ nm)....	143
<b>Figure 67.</b> HPLC-DAD chromatogram for river natural water sample ( $\lambda = 220$ nm) ...	143
<b>Figure 68.</b> HPLC-DAD chromatogram for estuary natural water sample ( $\lambda = 220$ nm). ....	143
<b>Figure 69.</b> HPLC-DAD chromatogram for lake natural water sample ( $\lambda = 243$ nm)....	143
<b>Figure 70.</b> HPLC-DAD chromatogram for lake natural water sample ( $\lambda = 210$ nm)....	143
<b>Figure 71.</b> HPLC-DAD chromatogram for lake natural water sample ( $\lambda = 220$ nm, $C_0$ (ibuprofen) = 20.63 mg L <sup>-1</sup> , $C_f$ (ibuprofen) = 23.5 mg L <sup>-1</sup> ).....	144
<b>Figure 72.</b> HPLC-DAD chromatogram for river natural water sample ( $\lambda = 220$ nm, $C_0$ (ibuprofen) = 20.63 mg L <sup>-1</sup> , $C_f$ (ibuprofen) = 22.1 mg L <sup>-1</sup> ).....	144
<b>Figure 73.</b> HPLC-DAD chromatogram for estuary natural water sample ( $\lambda = 220$ nm, $C_0$ (ibuprofen) = 20.63 mg L <sup>-1</sup> , $C_f$ (ibuprofen) = 26.9 mg L <sup>-1</sup> ).....	144
<b>Figure 74.</b> HPLC-DAD chromatogram for lake natural water sample ( $\lambda = 243$ nm, $C_0$ (acetaminophen) = 15.12 mg L <sup>-1</sup> , $C_f$ (acetaminophen) = 10.5 mg L <sup>-1</sup> ). ....	145
<b>Figure 75.</b> HPLC-DAD chromatogram for lake natural water sample ( $\lambda = 210$ nm, $C_0$ (phenobarbital) = 34.84 mg L <sup>-1</sup> , $C_f$ (phenobarbital) = 35.7 mg L <sup>-1</sup> ). ....	145
<b>Figure 76.</b> HPLC-DAD chromatogram for lake natural water sample ( $\lambda = 220$ nm, $C_0$ (ibuprofen) = 0.10 mmol L <sup>-1</sup> ). ....	145
<b>Figure 77.</b> HPLC-DAD chromatogram for river natural water sample ( $\lambda = 220$ nm, $C_0$ (ibuprofen) = 0.10 mmol L <sup>-1</sup> ). ....	146
<b>Figure 78.</b> HPLC-DAD chromatogram for estuary natural water sample ( $\lambda = 220$ nm, $C_0$ (ibuprofen) = 0.10 mmol L <sup>-1</sup> ). ....	146
<b>Figure 79.</b> HPLC-DAD chromatogram for lake natural water sample ( $\lambda = 243$ nm, $C_0$ (acetaminophen) = 0.15 mmol L <sup>-1</sup> ). ....	146
<b>Figure 80.</b> HPLC-DAD chromatogram for lake natural water sample ( $\lambda = 210$ nm, $C_0$ (phenobarbital) = 0.15 mmol L <sup>-1</sup> ).....	146
<b>Figure 81.</b> <sup>1</sup> H NMR spectrum of Tp measured at 400 MHz, in CDCl <sub>3</sub> . ....	151



<b>Figure 82.</b> $^1\text{H}$ NMR spectrum of model compound 2 at 400 MHz, in $\text{DMSO-d}_6$ .....	151
<b>Figure 83.</b> $^1\text{H}$ NMR spectrum of model compound 3 at 400 MHz, in $\text{DMSO-d}_6$ .....	152
<b>Figure 84.</b> Multi-point BET plot and linear fit (A), and pore size distribution (hollow spheres) and cumulative pore volume (filled spheres) profile (B).....	152
<b>Figure 85.</b> Multi-point BET plot and linear fit (A), and pore size distribution (hollow spheres) and cumulative pore volume (filled spheres) profile (B).....	153
<b>Figure 86.</b> Multi-point BET plot and linear fit (A), and pore size distribution (hollow spheres) and cumulative pore volume (filled spheres) profile (B).....	153
<b>Figure 87.</b> Multi-point BET plot and linear fit (A), and pore size distribution (hollow spheres) and cumulative pore volume (filled spheres) profile (B).....	154
<b>Figure 88.</b> Multi-point BET plot and linear fit (A), and pore size distribution (hollow spheres) and cumulative pore volume (filled spheres) profile (B).....	154
<b>Figure 89.</b> Multi-point BET plot and linear fit (A), and pore size distribution (hollow spheres) and cumulative pore volume (filled spheres) profile (B).....	155
<b>Figure 90.</b> Multi-point BET plot and linear fit (A) and pore size distribution (hollow spheres) and cumulative pore volume (filled spheres) profile (B) of $\text{TpBD}-(\text{CF}_3)_2$ after adsorption of ibuprofen. ....	155
<b>Figure 91.</b> Multi-point BET plot and linear fit (A) and pore size distribution (hollow spheres) and cumulative pore volume (filled spheres) profile (B) of $\text{TpBD}-(\text{CF}_3)_2$ after desorption of ibuprofen. ....	156
<b>Figure 92.</b> FT-IR spectrum of $\text{TpBD}-(\text{CH}_3)_2$ prepared in mg scale (red) and in gram scale (orange). ....	156
<b>Figure 93.</b> FT-IR spectrum of $\text{TpBD}-(\text{NO}_2)_2$ and $\text{TpBD}-(\text{NH}_2)_2$ . ....	157
<b>Figure 94.</b> FT-IR spectrum of $\text{TpBD}-(\text{CF}_3)_2$ prepared in mg scale (black) and in gram scale (blue).....	157
<b>Figure 95.</b> FT-IR spectrum of model compound 2.....	158
<b>Figure 96.</b> FT-IR spectrum of model compound 3.....	158
<b>Figure 97.</b> TGA data of $\text{TpBD}-(\text{CH}_3)_2$ prepared in mg scale (A), and 1 <sup>st</sup> derivative of the TGA data (B). ....	159
<b>Figure 98.</b> TGA data of $\text{TpBD}-(\text{CH}_3)_2$ prepared in gram scale (A), and 1 <sup>st</sup> derivative of the TGA data (B). ....	159
<b>Figure 99.</b> TGA data of $\text{TpBD}-(\text{NO}_2)_2$ (A), and 1 <sup>st</sup> derivative of the TGA data (B). ....	160
<b>Figure 100.</b> TGA data of $\text{TpBD}-(\text{NH}_2)_2$ (A), and 1 <sup>st</sup> derivative of the TGA data (B). ....	160

<b>Figure 101.</b> TGA data of TpBD-(CF <sub>3</sub> ) <sub>2</sub> prepared in mg scale (A), and 1 <sup>st</sup> derivative of the TGA data (B). .....	161
<b>Figure 102.</b> TGA data of TpBD-(CF <sub>3</sub> ) <sub>2</sub> prepared in gram scale (A), and 1 <sup>st</sup> derivative of the TGA data (B).....	161
<b>Figure 103.</b> 1 <sup>st</sup> derivative of the TGA data of TpBD-(CF <sub>3</sub> ) <sub>2</sub> after adsorption of ibuprofen (A) and after desorption of ibuprofen (B). .....	162
<b>Figure 104.</b> 1 <sup>st</sup> derivative of the TGA data of ibuprofen. ....	162
<b>Figure 105.</b> Contact angles of 18° for TpBD-(CH <sub>3</sub> ) <sub>2</sub> . ....	163
<b>Figure 106.</b> Contact angles of 15° for TpBD-(NO <sub>2</sub> ) <sub>2</sub> (A) and 6.3° for TpBD-(NH <sub>2</sub> ) <sub>2</sub> (B).....	163
<b>Figure 107.</b> Contact angles of 133° for TpBD-(CF <sub>3</sub> ) <sub>2</sub> prepared in mg scale (A), and 126° for TpBD-(CF <sub>3</sub> ) <sub>2</sub> prepared in gram scale (B).....	164
<b>Figure 108.</b> SEM images of TpBD-(NO <sub>2</sub> ) <sub>2</sub> (A) and TpBD-(NH <sub>2</sub> ) <sub>2</sub> (B).....	164
<b>Figure 109.</b> SEM image of TpBD-(CF <sub>3</sub> ) <sub>2</sub> after desorption of ibuprofen. ....	164
<b>Figure 110.</b> A top view along z axis (A) and side view along x axis (B) of the atomistic model of MC-LA in TpBD-(NH <sub>2</sub> ) <sub>2</sub> , located on the surface of COF. ....	165
<b>Figure 111.</b> A top view along z axis of the atomistic model of MC-RR in TpBD-(NO <sub>2</sub> ) <sub>2</sub> . ...	165
<b>Figure 112.</b> pH <sub>pzc</sub> value of TpBD-(CF <sub>3</sub> ) <sub>2</sub> . ....	166

## List of tables

<b>Table 1.</b> Some of the reported COF-based composites used for adsorption of pollutants from water.....	31
<b>Table 2.</b> Freundlich isotherm equation constant and correlation coefficient derived from the graph in Figure 13B. ....	40
<b>Table 3.</b> Amount of MC-LA, MC-LR, MC-RR, and MC-YR adsorbed and desorbed in equilibrium, $q_e$ ( $\text{mg g}^{-1}$ ), by TpBD-(CF <sub>3</sub> ) <sub>2</sub> , TpBD-(NO <sub>2</sub> ) <sub>2</sub> , and TpBD-(NH <sub>2</sub> ) <sub>2</sub> COF.....	52
<b>Table 4.</b> Adsorption energy values ( $\text{kcal mol}^{-1}$ ) of the MC-LA and MC-RR models with TpBD-(CF <sub>3</sub> ) <sub>2</sub> , TpBD-(NO <sub>2</sub> ) <sub>2</sub> , and TpBD-(NH <sub>2</sub> ) <sub>2</sub> . <sup>a</sup> .....	54
<b>Table 5.</b> Rate of adsorption of MC-LA, MC-LR, MC-RR, and MC-YR in COF derivatives until reaching the equilibrium of adsorption.....	57
<b>Table 6.</b> Freundlich and Langmuir isotherm equation constants and correlation coefficient obtained for MC-LR in TpBD-(CF <sub>3</sub> ) <sub>2</sub> , for MC-LA in TpBD-(NH <sub>2</sub> ) <sub>2</sub> , and for MC-RR in TpBD-(NO <sub>2</sub> ) <sub>2</sub> . ....	60
<b>Table 7.</b> Reported performance of most commonly used MCs adsorbents. $q_m$ as the maximum adsorption capacity, in $\text{mg g}^{-1}$ , and $t_{\text{eq}}$ as the time needed to reach the equilibrium, in minutes. ....	61
<b>Table 8.</b> The properties of the studied pharmaceuticals. <sup>a</sup> pH 7.4. Dimensions of pharmaceuticals were obtained by measuring the furthest distances of C, N, or O atoms from the X-ray crystal structures obtained from the Cambridge Structural Database (CSD) with the following codes: <sup>b</sup> CCDC-1102110, <sup>c</sup> CCDC-1041382, <sup>d</sup> CCDC-150969, <sup>e</sup> CCDC-298547. ....	66
<b>Table 9.</b> The rate constants, amount of adsorbed pharmaceutical in equilibrium, and the coefficient of determination obtained using the kinetic models.....	68
<b>Table 10.</b> Physical-chemical parameters of river, lake and estuary water collected. GH = Total hardness; KH = carbonate hardness; LOD = Limit of detection; n/a = not applicable. ....	75
<b>Table 11.</b> Adsorption capacity, $q_t$ ( $\text{mg g}^{-1}$ ), of ibuprofen by TpBD-(CF <sub>3</sub> ) <sub>2</sub> at 21 °C in lake, river, and estuary water. ( $C_0(\text{TpBD}-(\text{CF}_3)_2) = 330 \text{ mg L}^{-1}$ , $C_0(\text{ibuprofen}) = 10.31$ and $20.63 \text{ mg L}^{-1}$ , $t = 120 \text{ min}$ ).....	76
<b>Table 12.</b> The properties of the studied pharmaceuticals. Dimensions of pharmaceuticals were obtained by measuring the furthest distances of C, N, or O atoms from the X-ray crystal structures obtained from the Cambridge Structural Database (CSD) with the following codes: <sup>b</sup> CCDC-1041382, <sup>c</sup> CCDC-150969, <sup>d</sup> CCDC-1149948. <sup>a</sup> for more informations check also Table 8.....	81

<b>Table 13.</b> Adsorption capacity, $q_t$ ( $\text{mg g}^{-1}$ ), of TpBD-(CF <sub>3</sub> ) <sub>2</sub> in binary mixtures of ibuprofen and acetaminophen or phenobarbital (concentration ratios of pharmaceuticals 50/150 and 100/100 $\mu\text{M}$ , $C(\text{TpBD}-(\text{CF}_3)_2) = 330 \text{ mg L}^{-1}$ , $t = 120 \text{ min}$ ).....	82
<b>Table 14.</b> Pharmaceutical occurrence found in waters collected in the Tagus river estuary. LOQ: limit of quantification; nd: not detected. The pharmaceuticals detected with an efficiency >50% of the SPE are marked with *; results outperforming standard SPE are indicated in boldface. Concentrations and % are expressed as average values of the 5 samples $\pm$ standard deviation. In brackets: the detected interval in the 5 samples. ....	92
<b>Table 15.</b> Experimental conditions tested for the synthesis of model compound 2. ....	97
<b>Table 16.</b> Experimental conditions tested for the synthesis of model compounds 4 and 5. ....	99
<b>Table 17.</b> Experimental conditions tested for the synthesis of sp <sup>2</sup> -based TFB-Phen COF at 150 °C.....	101
<b>Table 18.</b> Band gap value of some of the reported sp <sup>2</sup> -based COFs.....	105
<b>Table 19.</b> Reported performance of COF materials as photocatalysts for degradation of organic pollutants.....	107
<b>Table 20.</b> The values for limit of detection (LOD) and limit of quantification (LOQ) as well as recovery for the pharmaceuticals detected in this study and precision as standard deviation.....	149

## List of abbreviations

<b>AC</b>	Activated carbon
<b>AcOH</b>	Acetic acid
<b>AIBN</b>	Azobis(isobutyronitrile)
<b>AOPs</b>	Advanced oxidation processes
<b>aq.</b>	Aqueous
<b>BD-(CF<sub>3</sub>)<sub>2</sub></b>	3,3'-bis(trifluoromethyl)benzidine
<b>BD-(CH<sub>3</sub>)<sub>2</sub></b>	<i>o</i> -tolidine
<b>BD-(NO<sub>2</sub>)<sub>2</sub></b>	3,3'-dinitrobenzidine
<b>BET</b>	Brunauer-Emmett-Taller
<b>COFs</b>	Covalent-organic frameworks
<b>CSD</b>	Cambridge structural database
<b>CTFs</b>	Covalent triazine frameworks
<b>DBU</b>	1,8-diazabicyclo[5.4.0]undec-7-ene
<b>DES</b>	Deep eutectic solvent
<b>DRS</b>	Diffusive reflectance spectra
<b><i>o</i>-DCB</b>	<i>o</i> -dichlorobenzene
<b>DFT</b>	Density functional theory
<b>DMA</b>	<i>N,N</i> -Dimethylacetamide
<b>DSP</b>	Diarrheic shellfish poisoning
<b>ECs</b>	Emerging contaminants
<b>ESP</b>	Electrostatic potential surface
<b>GenX</b>	Ammonium perfluoro-2-propoxypropionate
<b>GH</b>	Total Hardness
<b>HABs</b>	Harmful algal blooms
<b>KH</b>	Carbonate hardness
<b>KOtBu</b>	Potassium <i>tert</i> -butoxide
<b>LD<sub>50</sub></b>	Lethal dose
<b>LDPE</b>	Low density polyethylene
<b>LOD</b>	Limit of detection
<b>LOQ</b>	Limit of quantification
<b>MB</b>	Methylene blue
<b>MCs</b>	Microcystins
<b>MC-LA</b>	Microcystin-LA
<b>MC-LR</b>	Microcystin-LR
<b>MC-RR</b>	Microcystin-RR
<b>MC-YR</b>	Microcystin-YR
<b>MIPs</b>	Molecularly imprinted polymers
<b>MMMs</b>	Mixed matrix membranes

<b>MO</b>	Methyl orange
<b>MOFs</b>	Metal-organic frameworks
<b>MPTs</b>	Microporous polyethylene tubes
<b>NOM</b>	Natural organic matter
<b>OA</b>	Okadaic acid
<b>PCBs</b>	Perchlorinated biphenyls
<b>PFA</b> s	Per- and polyfluorinated alkyl substances
<b>Phen</b>	3,8-dimethyl-4,7-phenanthroline
<b>POCIS</b> s	Polar organic chemical integrative samplers
<b>PP</b>	Protein phosphatase enzyme
<b>ppb</b>	parts per billion
<b>ppm</b>	parts per million
<b>PSM</b>	Post-synthetic modification
<b>PXRD</b>	Powder X-ray diffraction
<b>QSDFT</b>	Quenched-solid density functional theory
<b>rpm</b>	Revolutions per minute
<b>SAXS</b>	Small-angle X-ray scattering
<b>SEM</b>	Scanning electron microscopy
<b>SPATT</b>	solid-phase adsorption toxin tracking
<b>SPE</b>	Solid-phase extraction
<b>SPME</b>	Solid-phase microextraction
<b>t</b>	time
<b>Tda</b>	2,5-dimethyl-1,3,4-thiadiazole
<b>TEM</b>	Transmission electron microscopy
<b>TFA</b>	Trifluoroacetic acid
<b>TFB</b>	1,3,5-triformylbenzene
<b>Tf</b>	2,3,5,6-tetrafluoro- <i>p</i> -xylene
<b>THF</b>	Tetrahydrofuran
<b>Tp</b>	1,3,5-triformylphloroglucinol
<b>Tz</b>	3,6-dimethyl-1,2,4,5-tetrazine
<b>UHPLC-TOF-MS</b>	Ultra-High-Performance Liquid Chromatography combined with Time-of-Flight Mass Spectrometry
<b>VOCs</b>	Volatile organic chemicals
<b>WHO</b>	World Health Organization
<b>WWTPs</b>	Wastewater treatment plants

## Chapter 1 – Introduction

### 1.1. Porous materials

Over the past decades, the field of porous materials has been widely explored, catching the attention of researchers interested in improving their structural and functional properties.<sup>[1,2]</sup> Porous materials encompass a wide variety of inorganic and organic materials (e.g. zeolites, silica, and activated carbon), inorganic–organic hybrid materials metal-organic frameworks (MOFs), as well as crystalline covalent organic frameworks (COFs).<sup>[3,4]</sup> In general pore size, geometry, and shape, as well as surface area and stability are very important factors that influence the performance of porous material.<sup>[1,5]</sup> COFs, first reported by Yaghi and co-workers<sup>[6]</sup> in 2005, are a generation of crystalline porous materials incorporating an extended periodic and porous network, widely used in adsorption<sup>[7,8]</sup> and catalysis<sup>[9–11]</sup> applications, among others.<sup>[3,12]</sup>

### 1.2. Covalent organic frameworks

COFs endowed with good crystallinity, as well as porosity, are formed by self-assembly of purely organic building blocks through strong covalent bonds, using the design principles of reticular chemistry.<sup>[13–17]</sup> So far, the reticular chemistry concept has allowed to explore the design and synthesis of COFs through careful selection of well-defined building blocks linked to create an extended crystalline framework.<sup>[18,19]</sup> The geometry and size of the building blocks guide not only the development of well-defined and predictable two- (2D) or three-dimensional (3D) extended frameworks (Figure 1), but also their topology and pore diameter.<sup>[17,20–23]</sup> Additionally, the functional groups on the building blocks determine the pore surface characteristics. Therefore, by careful molecular design and selection of building units, the COF structure can be tuned, which allows the formation of versatile structures with long-range order and permanent porosity.<sup>[17]</sup> Moreover, COFs feature high surface areas and low density due to the presence of light elements, such as C, B, O, Si, and N, connected by strong covalent bonds.<sup>[14,24]</sup>

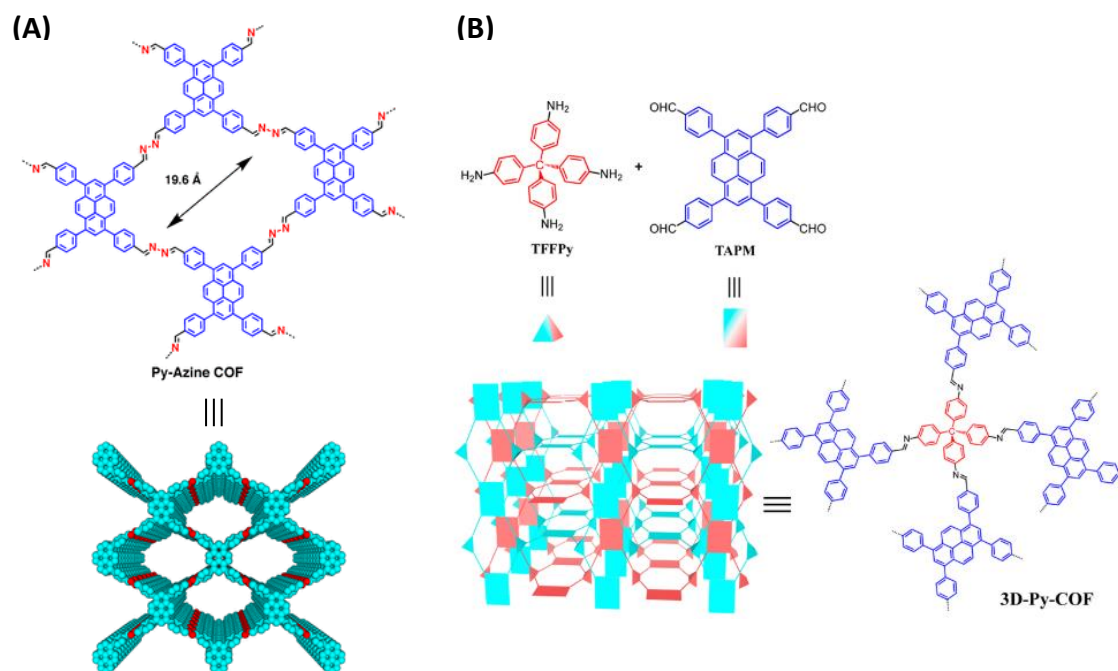


**Figure 1.** Schematic representation of a 2D<sup>[25]</sup> (A) and 3D<sup>[26]</sup> (B) COF structure. Adapted with permission. Copyright 2016 and 2013, American Chemical Society.

Due to their structural versatility and tunability, COFs have been explored for a wide range of applications,<sup>[14,24]</sup> such as gas storage<sup>[27–30]</sup> and separation<sup>[30,31]</sup> catalysis,<sup>[9–11]</sup> optoelectronics,<sup>[32–34]</sup> and sensing.<sup>[35–38]</sup> These materials have also shown potential as adsorbents for organic dyes,<sup>[38–42]</sup> heavy metals (i.e.  $\text{Hg}^{2+}$ ,<sup>[43–46]</sup>  $\text{Pb}^{2+}$ ,<sup>[47,48]</sup>  $\text{Cu}^{2+}$ <sup>[49,50]</sup>) and radionuclides,<sup>[51–54]</sup> as carriers for drug delivery,<sup>[55–57]</sup> and for isolation of industrially relevant compounds.<sup>[58–64]</sup>

### 1.2.1. Design and synthetic principles

The topology of COFs is mainly determined by the geometry and connectivity of the building units, offering an advantage to achieve fascinating tailor-made porous structures. As represented in Figure 2, 2D COFs can acquire different types of geometries from hexagonal, trigonal, tetragonal, and kagome to rhombic structures.<sup>[22,24]</sup>



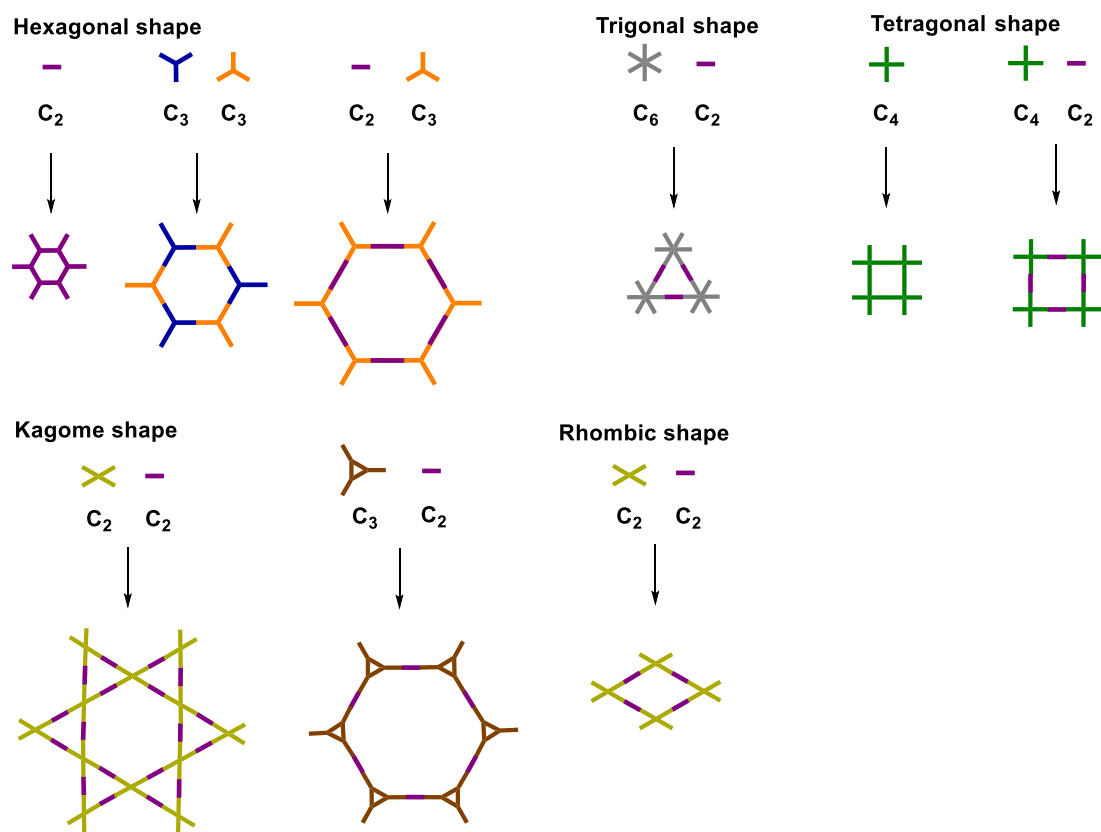


**Figure 2.** Representation of possible combination of building blocks with different geometries to yield 2D COFs.

The nature of the chemical bond formed within the framework between the reactive sites of building blocks is crucial for the crystallinity and stability of the formed COF material.<sup>[15,17,22,24]</sup> These properties can be compromised by COF delamination, in which through mechanical (i.e. grinding<sup>[65]</sup> and sonication<sup>[66]</sup>) or chemical<sup>[67,68]</sup> methods a perturbation of the stacking of COF sheets lead to the formation of layered structures without long-range order.

COF synthesis is controlled by reversible covalent bond forming reactions that allow the formation of an extended, thermodynamically stable framework. The reversibility of the reactions allows for self-healing during the synthesis, which reduces the incidence of structural defects, and it is of utmost importance to find the appropriate conditions to promote the reversibility of covalent bond formation reaction to allow for the formation of a crystalline COF structure.<sup>[15,17,24]</sup>

A wide variety of methods have been explored to obtain thermodynamically stable crystalline COFs.<sup>[17,22,24]</sup> To date, solvothermal synthesis is the most widely used method for COF formation. It is highly dependent on the solubility and reactivity of building units, which, allied to long reaction times, high temperatures, specific solvent conditions, and catalyst concentration, influence the reversibility of the reaction. A balance between solvent combinations and ratio is extremely important to obtain a crystalline and ordered COF structure.<sup>[17,22]</sup>

Microwave-assisted method has been used as an effective approach to reduce the long time needed in solvothermal methods, reducing the time required from days to hours and even minutes, opening the access for industrial production.<sup>[17,22]</sup> Ionothermal synthesis have been developed mainly for the synthesis of CTFs (covalent triazine frameworks), involving the use of very harsh conditions (e.g.  $\text{ZnCl}_2$  at 400 °C), which limits the selection of building blocks that can be used, as well as the formation of crystalline and ordered materials.<sup>[17,22]</sup> Recently, ionic liquids have been explored as an environmentally friendly reaction media to synthesize 2D COFs with enhanced crystallinity under mild conditions.<sup>[69,70]</sup> More importantly, the use of deep eutectic solvents (DES) as another type of green solvents for the synthesis of highly crystalline 2D<sup>[71,72]</sup> and 3D COFs<sup>[71]</sup> under ambient conditions have been shown to be a quick, simple, and low price strategy.

Mechanochemical methods performed at room temperature in grinding solvent-free conditions offer a simple and an economic approach, overcoming some of the limitations of solvothermal method.<sup>[17,22,24]</sup> Another alternative to the solvothermal synthesis is the sonochemical method, which requires the use of ultrasounds in the reaction system to accelerate the crystallization process reducing the required time from days to hours.<sup>[73]</sup>

For the synthesis of crystalline COFs the use of reversible covalent bonds (Figure 3), such as boronate ester,<sup>[6,74,75]</sup> imine,<sup>[24,76,77]</sup> azine,<sup>[25,78,79]</sup> hydrazone<sup>[49,80,81]</sup> and  $\beta$ -ketoenamine,<sup>[61,65,82,83]</sup> have been described. In addition, more recently the use of irreversible nucleophilic aromatic substitution reactions (Figure 3), resulting in phenazine,<sup>[84,85]</sup> dioxin,<sup>[86,87]</sup> as well as olefin,<sup>[52,88,89]</sup> linkages have been used with success in COF synthesis, expanding the synthetic toolbox for these materials.

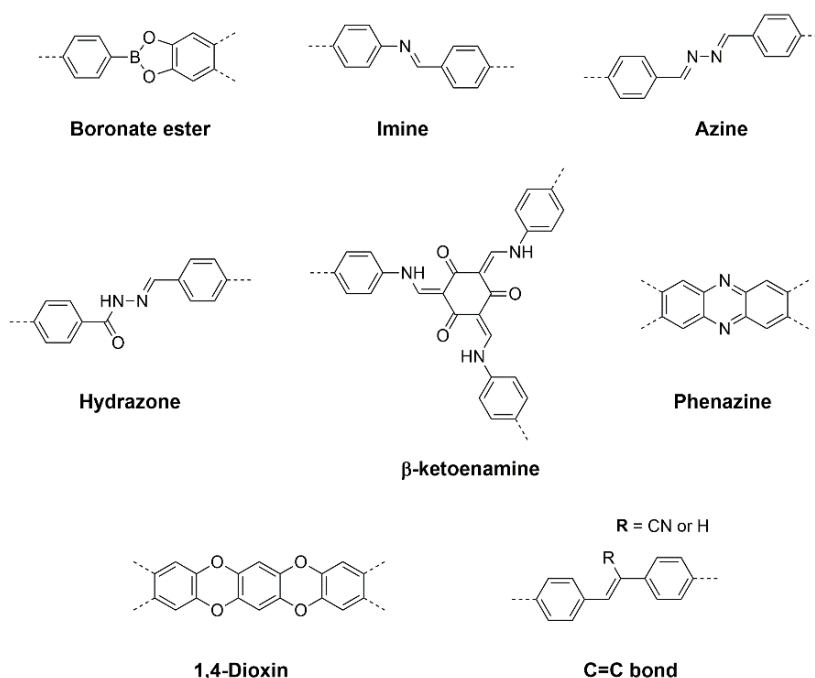


**Figure 3.** Representation of most common covalent bonds used to make 2D COFs.

### 1.2.2. Water stability of COFs

The reversible nature of the covalent bond formed during the self-assembly of the building blocks is essential to obtain a crystalline and stable COF material. Boroxine- and boronate-ester linkage owing to their planarity and high reversibility yield highly crystalline and thermally stable COF materials.<sup>[17,90]</sup> However, boron-linked COFs exhibit poor hydrolytic and oxidative stability, which limits their application, especially in water medium.

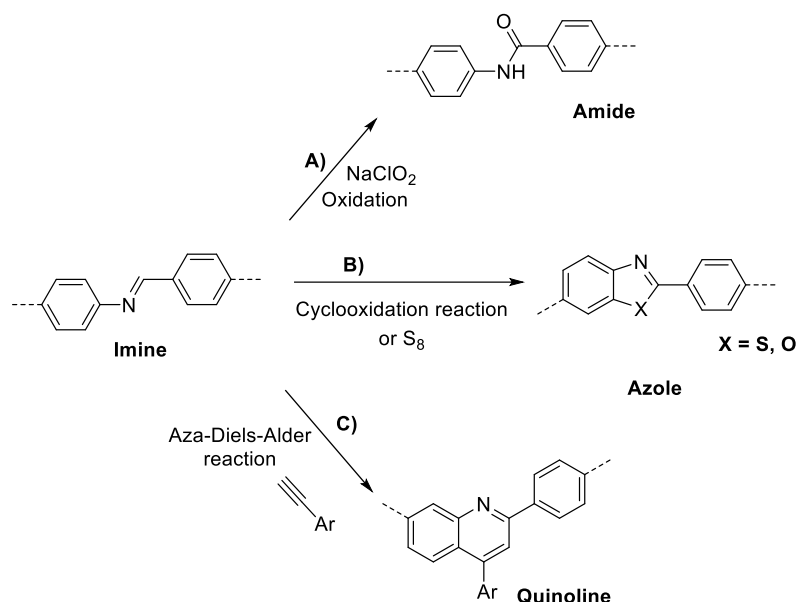
As a way to enhance structural stability, imine linkages have been developed for the synthesis of COFs in presence of acid as catalyst. As opposed to boron-linked COFs, imine-linked COFs offer higher hydrolytic stability, with retention of COF crystallinity.<sup>[17,22,90]</sup> In this way, a plethora of COFs featuring this linkage has been reported for several applications.

Despite the reported stability of imine-linked COFs, several studies have been carried out to improve them even further. Incorporation of an intralayer hydrogen-bonding interaction with the imine nitrogen by positioning a hydroxy group in the  $\alpha$ -position of the

reacting aldehyde has been shown to enhance the hydrolytic COF stability.<sup>[91,92]</sup> More recently, the introduction of interlayer hydrogen bonding interactions has also provided insights on the design of COF materials with enhanced chemical stability.<sup>[93–95]</sup> Hydrolytic stability of COFs has also been enhanced by the incorporation of bulky substituents next to the imine bonds by preventing the access of water molecules to the linkage.<sup>[93,96]</sup>

The azine and hydrazone linkage have shown remarkable water-stability when compared to boronic ester linkage even under acidic and basic conditions, emerging as a possibility to develop new COF materials.<sup>[17,90]</sup> However, their water stability can be compromised in some hydrazone-based COFs (e.g. COF-43)<sup>[67]</sup> due to the relatively weak interlayer interactions observed in some organic solvents, such as dioxane.

Over the years, innovative strategies have emerged to enhance the chemical stability of imine COFs by modifying the linkage post-synthetically (Scheme 1), taking advantage of the high crystallinity of the imine linkage, the reversibility of which is locked in a post-synthetic step, thus resulting in high-quality COFs with high hydrolytic stability. The first example was reported by Yaghi,<sup>[97]</sup> where the imine linkage was converted to amide by treatment with sodium chlorite (Scheme 1A), with highly enhanced aqueous stability, especially under acidic conditions. Lotsch and co-workers converted the imine moieties to thiazole using elemental sulfur (Scheme 1B), under very hard conditions of high temperature, which limit their use to classes of COF materials.<sup>[98]</sup> No losses in crystallinity were observed after treatment with concentrated HCl, hydrazine, or NaBH<sub>4</sub>. Liu and co-workers<sup>[99]</sup> used the Povarov reaction, Lewis-acid catalyzed aza-Diels–Alder cycloaddition, of the imine moiety with phenylacetylene derivatives to gain access to quinoline-linked COFs (Scheme 1C) with enhanced stability not only in acidic and basic medium, but also against oxidation and reducing agents. Further studies on imine linkage functionalization will be discussed in section 1.2.4 in more detail.

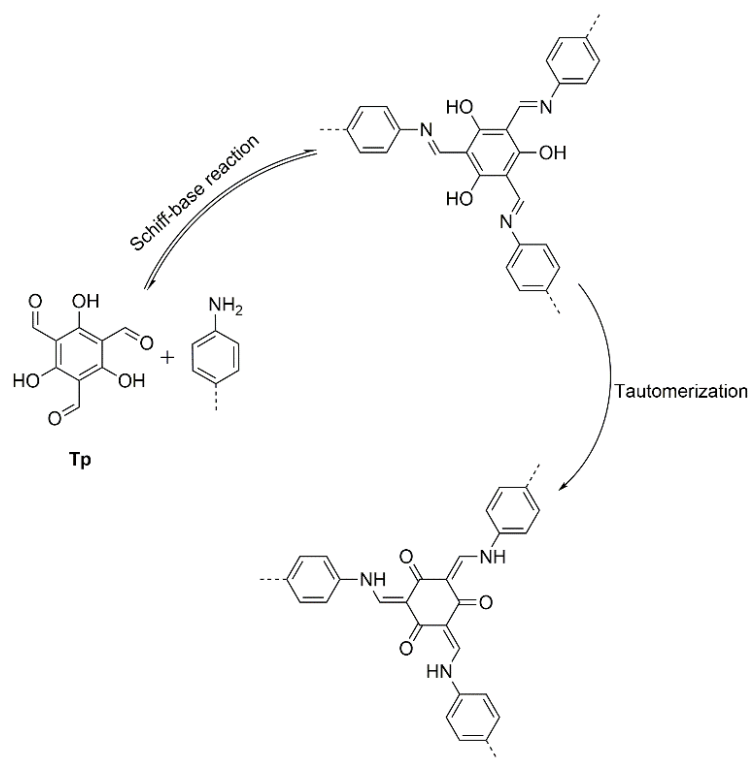


**Scheme 1.** Schematic representation of some of irreversible reactions used to lock and increase stability of imine bond in COFs via chemical conversion to amide (A),<sup>[97]</sup> azole derivatives (B),<sup>[98,100]</sup> and quinoline (C)<sup>[99]</sup> linkages.

The incorporation of a hydroxy group in  $\alpha$ -position to the amine has been also reported as a good strategy to afford ultra-stable benzoxazole COFs.<sup>[101]</sup> The reversible/irreversible sequence of reactions that allows the formation of benzoxazole linkage resulted in highly crystalline and ultrastable benzoxazole-linked COFs in strong acids, such as trifluoroacetic acid, and strong bases. In another study, the formation of a benzimidazole unit through a sequence of reversible imine bond formation followed by an irreversible oxidative aromatization step led to the synthesis of a highly crystalline, thermally and chemically stable benzimidazole-linked COF.<sup>[102]</sup>

In 2012 Banerjee and co-workers<sup>[82]</sup> reported  $\beta$ -ketoenamine linkage featuring outstanding water stability even in aqueous basic and acid medium.  $\beta$ -Ketoenamine-linked COFs are prepared from the condensation of 1,3,5-triformylphloroglucinol (Tp)<sup>[103]</sup> with an amino-functionalized building block (Scheme 2): first, a reversible Schiff-base reaction is responsible for the formation of a crystalline framework, followed by an irreversible enol-to-keto tautomerization ensuring the chemical stability of COF material. The latter irreversible step, which hinders error correction in the COF framework, renders

$\beta$ -ketoenamine COFs commonly less crystalline than their imine counterparts, but imparts them with exceptional hydrolytic stability.



**Scheme 2.** Schematic representation of reversible-irreversible reaction sequence for the formation of water stable  $\beta$ -ketoenamine linkage.

Other water-stable linkages of COFs have been reported, such as the urea-based highly crystalline COF-117<sup>[104]</sup> and COF-118<sup>[104]</sup> obtained by condensation of Tp with 1,4-phenylenediurea and 1,1'-(3,3'-dimethyl-[1,1'-biphenyl]-4,4'-diyl)diurea, respectively, exhibiting excellent stability in water and towards concentrated acids and bases. The phenazine linkage was the first example of irreversible reactions developed for the synthesis of COFs, which owing to its fused planar structure and high stability afforded highly  $\pi$ -conjugated and stable COF structures.<sup>[84]</sup> The 1,4-dioxin linkage is another case of irreversible nucleophilic aromatic substitutions reactions that allowed the formation of a crystalline framework (e.g. COF-316,<sup>[86]</sup> COF-318,<sup>[86]</sup> JUC-506<sup>[87]</sup>), with high chemical stability due to the irreversible nature of linkage. These COFs showed high stability even in concentrated HCl for several days. Recently, olefin (C=C) linked COF materials, despite the lower reversibility when compared to other dynamic linkages such as boron or imine-based

linkages, show remarkably high chemical stability in various media including air, light, acid, basic, and redox conditions.<sup>[89]</sup> Thus,  $sp^2$ -based COFs emerged with outstanding chemical stability, which allied to their high crystallinity and fully extended  $\pi$ -conjugated framework provide 2D COF materials with unique optoelectronic properties. Despite the wide variety of COF structures reported so far, the development of fully conjugated COF structures combining high stability and long-range order still remains a challenge.

### 1.2.3. Supramolecular interactions as driving force for COF synthesis

A deep understanding of the chemistry beyond the molecules, described as supramolecular chemistry, plays an important role in the design of highly complex and functional systems.<sup>[105]</sup> In 2D COFs this influence is mainly governed via non-covalent interactions such as aromatic stacking interactions and van der Waals/dipolar forces between 2D layers that play a critical role in the formation of highly ordered and porous structures.<sup>[106]</sup>

Planarization of COF layers is one of the main reported strategies that have been shown to strongly enhance the overall crystallinity and porosity of COFs. In fact, planar building units tend to stack together driven by favorable interactions such as  $\pi$ - $\pi$  stacking, hydrogen bonding, and dipole-dipole interactions between the COF layers. In 2015, Lotsch and co-workers<sup>[107]</sup> found that the COF crystallinity and porosity of a series of azine-based COFs tend to increase with the increase content of the nitrogen atom on the central phenyl ring of the building block. This result was attributed to the decrease in dihedral angle of the central ring due to the absence of biphenyl-like steric hindrance between the C-H moieties, which led to more favorable stacking interactions between the COF layers. Similar effect was also found for a hydrazone-based COF (TFPT-COF),<sup>[81]</sup> in which by replacement of the triphenylbenzene based monomer of structural analog COF-43<sup>[80]</sup> by a triazine derivative, an improvement of co-facial stacking interactions was observed resulting in an increase in the surface area by a factor of two. This same concept was also applied in imine-based COFs,<sup>[108]</sup> showing the generality of this strategy to give access to COFs with enhanced crystallinity and porosity.

Typically most non-planar building blocks decrease COF crystallinity.<sup>[78,109,110]</sup> However, new studies have emerged that contradict this paradigm, showing the synthesis of highly crystalline COFs containing non-planar building blocks that stack onto each other in favorable conformations.<sup>[106]</sup> Bein and co-workers, inspired by the rigid propeller- and armchair-shaped conformation of tetraphenylethylene<sup>[111]</sup> and tetraphenylpyrene<sup>[112]</sup> building units, respectively, were able to synthesize highly-ordered COFs incorporating these units. They serve as docking sites for further molecules during crystal growth, resulting in high long-range order within the COF materials. Recently, Mateo-Alonso and co-workers<sup>[113]</sup> synthesized a core-twisted non-planar polycyclic aromatic hydrocarbon molecule, which stacks in alternating directions giving access to a chair-like COF structure with high order. To this end, planarity of the building units is not a key factor for the formation of highly ordered structure, but rather the right selection of building units that can stack properly to maximize interlayer interactions can also lead to crystalline COF structures.

The integration of intralayer<sup>[91,92]</sup> and interlayer<sup>[114]</sup> hydrogen-bonding interactions into a COF structure was also shown to enhance their crystallinity and porosity, through enhancement of structure planarity.

Another effective strategy to improve COF crystallinity and porosity has been the incorporation of fluorine units into COF building blocks as a way to enhance interlayer interactions in the framework.<sup>[106]</sup> The first evidence of this strategy, reported by Jiang and co-workers,<sup>[115]</sup> has been demonstrated using a mixture of 1:1 arene and perfluoroarene dialdehyde derivatives. The enhanced quality of COF material stems from the integration of self-complementary  $\pi$ - $\pi$  interactions, which increase the total stacking energy through removal of the electron density from the ring, and consequently decreasing the repulsion of stacked geometry. Afterwards, Smaldone and co-workers, who compared a non-fluorinated azine-linked COF with fluorinated derivatives, found fluorination of the central ring of the three-fold building blocks to result in higher enhancement in surface area and crystallinity than peripheral fluorination.<sup>[116]</sup> This was attributed to enhanced favorable cofacial stacking interactions between the COF layers due to the increased electron-deficient character. Thereafter, through incorporation of different ratios of peripherally



fluorinated and non-fluorinated building units for the synthesis of a series of azine-based COFs, the importance of aromatic stacking interactions between 2D layers was evidenced.<sup>[117]</sup> It became clear that increasing the content of the fluorinated building block present in the mixture led to an increase in the surface area and crystallinity of COFs, emphasizing that the incorporation of electron-deficient aromatic rings into framework may lead to higher COF quality. Recently, a similar strategy was reported to improve the crystallinity of imine-based COFs.<sup>[118]</sup> Partial fluorination of building units seems to favor strong interlayer interactions with the non-fluorinated portion of the building unit, maximizing the alternating phenyl/perfluorophenyl stacking interactions. An enhancement of surface area and crystallinity of imine-based COF when compared to the fully fluorinated face-to-face stacked counterpart was reported.

In 2016 at INL, dipole moment was incorporated into COF building blocks as a supramolecular strategy to afford COFs with improved crystallinity and porosity.<sup>[75]</sup> A pyrene-4,5-dione unit, with a large dipole moment of over 6 D, stacks in an antiparallel manner within the COF walls, favoring columnar stacking interactions resulting in a highly crystalline COF. An increase of surface area of nearly twice the value reported for the non-dipole-moment-bearing pyrene COF was obtained when using pyrene-4,5-dione as building block. Quantum mechanical calculations showed that the antiparallel arrangement of pyrene-4,5-dione stacking is more favorable by over 7 kcal mol<sup>-1</sup> than that of pyrene unit, and 5.5 kcal mol<sup>-1</sup> more than the parallel arrangement of pyrene-4,5-dione.

#### 1.2.4. Functionalization of COFs

Pore surface functionalization of COFs plays a pivotal role in the affinity and selectivity of specific target molecules to the COF pores. The structural functionalization of COFs is mainly based on direct conversion of pre-functionalized building units through a so-called bottom-up approach (Figure 4).<sup>[119,120]</sup> Despite the wide variety of COFs synthesized to date based on this synthetic approach, the introduction of more robust linkages or bulky functional groups into the pore walls is still a challenge. In this perspective, the post-synthetic modification (PSM, Figure 4) approach is a straightforward way to incorporate a wide variety of functional groups into the pores walls of COFs, allowing for

structural and chemical fine-tuning of COF properties without comprising their structural integrity.<sup>[21,119,120]</sup> Functionalization of COFs by PSM relies on the presence of reactive functional groups or active sites on the COF backbone, which are available for further chemical modifications from covalent bond formation to linkage conversion.<sup>[21,120]</sup> To achieve an efficient PSM approach the linkage of pristine COF must be stable under PSM conditions, as well as the target PSM reaction should have minimum side reactions avoiding the formation of side products, otherwise difficult to separate.<sup>[21]</sup> Taking this into account, in an optimal functionalization scenario, PSM should be carried out under mild conditions, such as low temperature and short reaction time, as well in the absence of catalysts or aggressive reagents.

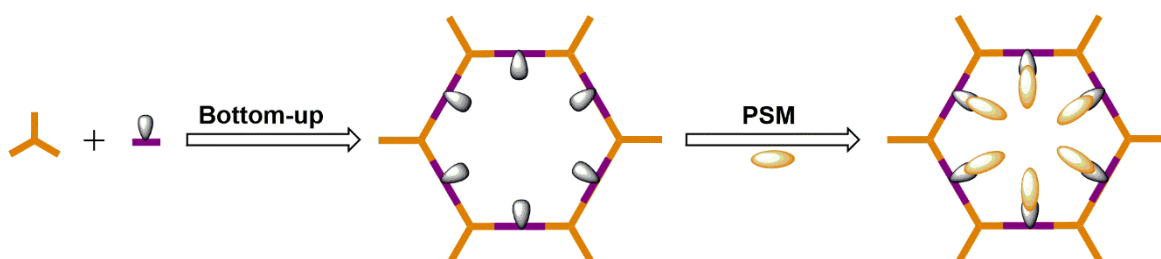


**Figure 4.** Representation of two main functionalization approaches in 2D COFs: bottom-up and PSM approach.

So far, Cu(I) catalyzed azide–alkyne cycloaddition reaction has been the most commonly used method for pore surface functionalization of COFs materials with enhanced performance on gas separation,<sup>[121]</sup> as organocatalyst,<sup>[122][123]</sup> and for adsorption applications.<sup>[43][124,125]</sup> The incorporation of azide<sup>[121,126]</sup> and terminal alkyne<sup>[43,122–125,127]</sup> functional groups into COFs is quite straightforward, which, allied to the high yields and method simplicity reported, make this reaction very attractive for PSM. However, a high degree of functionalization of the pore walls is usually associated with a reduction in porosity and sometimes crystallinity of the COF material.<sup>[121,122,126,127]</sup> Indeed, an optimal balance between the level of post-synthetic functionalization and COF properties needs to be achieved.

The incorporation of hydroxy functional groups into COFs, due to their high reactivity as well as easy availability in many building units, has also emerged as a versatile approach

to promote PSM in an extended way. Through reaction with succinic anhydride,<sup>[128][129]</sup> isothiocyanate derivatives,<sup>[130][131]</sup> and halide ionic liquids,<sup>[132]</sup> the functionalization of COFs with ester, *o*-thiocarbamate, and ether chemical bonds, respectively, have been successfully applied, while maintaining their porosity and crystallinity, otherwise very difficult by direct polymerization. A carboxy-functionalized 3D-COF obtained by PSM of a hydroxy-appended 3D COF with succinic anhydride via ester bond formation, displayed high metal loading capacities promoted by a strong interaction between COF carboxy groups and metal ions, when compared to pristine hydroxy-based 3D COF.<sup>[129]</sup> Similarly, a 2D hydroxy-functionalized COF was successfully functionalized with carboxy groups for enhanced ion adsorption and permeation for seawater desalination.<sup>[133]</sup> These strategies highlight the potential of PSM to impart COF materials as an excellent scaffold for environmental applications.

In 2016, Medina, Bein, and co-workers<sup>[58]</sup> took advantage of the high chemical stability of  $\beta$ -ketoenamine COFs by reporting a two-step PSM method for the synthesis of the amide-based TpBD-(NHCOCH<sub>3</sub>)<sub>2</sub> COF. This study emerged from the challenge observed from the direct functionalization of COF pore walls with amide bonds, in which the main pre-designed building blocks are prone to react in a side product reaction, hindering the formation of highly crystalline frameworks.<sup>[48]</sup> In particular, nitro functional groups of TpBD-(NO<sub>2</sub>)<sub>2</sub> were first reduced to amino functionalities to afford TpBD-(NH<sub>2</sub>)<sub>2</sub>, which subsequently, by reaction with acetic anhydride, gave crystalline acetamide-bearing TpBD-(NHCOCH<sub>3</sub>)<sub>2</sub>. Then, these COFs were employed for lactic acid adsorption with the highest affinity up to 6.6 wt% found for TpBD-(NH<sub>2</sub>)<sub>2</sub>, and the lowest for TpBD-(NO<sub>2</sub>)<sub>2</sub> (2.5 wt%), highlighting the success of PSM to enhance and tune affinity of materials towards a specific target molecule. The success of amide functionality incorporation by PSM was also demonstrated by Yaghi and co-workers through nitrile hydrolysis in aq. concentrated 6M NaOH of dioxin-linked COF COF-316 incorporating nitrile pendant groups into the pores walls.<sup>[86]</sup>

More recently, a nitrile-functionalized  $\beta$ -ketoenamine-based COF was treated with hydroxylamine in the presence of trimethylamine as base, affording an amidoxime-functionalized COF,<sup>[51]</sup> which maintained the long-range order and porosity of

the original material. Interestingly, the amidoxime-COF showed higher uranium uptake with  $q_e = 408 \text{ mg g}^{-1}$  when compared to its amorphous counterpart ( $q_e = 355 \text{ mg g}^{-1}$ ), owing to the improved accessibility and affinity of the amidoxime chelating sites in the well-defined COF pores as compared to the disordered network of amorphous counterpart. Likewise, a dioxin-linked COF COF-316 featuring free and reactive nitrile groups on the pore walls was successfully post-synthetically modified using the same methodology, with preservation of crystallinity.<sup>[86]</sup>

Using thiol–ene ‘click’ reaction the introduction of thioether functionalities into COF structures has been successfully achieved. Through PSM of a vinyl-functionalized imine-based COF-V with 1,2-ethanedithiol in the presence of AIBN, a thioether-functionalized COF-S-SH was prepared for efficient mercury removal,<sup>[43]</sup> outperforming the reported thiol- and thioether-functionalized materials,<sup>[134–136]</sup> while maintaining its crystallinity and porosity. Later the same group<sup>[137]</sup> showed a similar procedure to incorporate perfluoroalkyl functional groups within COF-V structure, rendering new superhydrophobic and superoleophilic COF structures, while retaining its long-range order. This COF, immobilized onto a melamine foam substrate, showed rapid oil adsorption from water, highlighting the potential of this class of materials in oil-spill recovery.

Functionalization of pore surface of COFs can also be carried out via reduction and oxidation reactions, as recently demonstrated with a highly stable polyarylether COF bearing nitrile pendant functional groups that was successfully reduced to afford an amine-functionalized COF with high adsorption capacity for tetracycline antibiotics derivatives under alkaline conditions.<sup>[87]</sup> Following a similar strategy, Dichtel and co-workers<sup>[60]</sup> developed a series of imine COFs incorporation varying density of azide functionalities into the pores, which were reduced in the presence of triphenylphosphine to the corresponding amine-functionalized imine COFs, while maintaining high surface area ( $\geq 1000 \text{ m}^2 \text{ g}^{-1}$ ) and long-range order. The COF with an amine loading of 20% showed the highest uptake ( $q_e = 240 \text{ mg g}^{-1}$ ) of ammonium perfluoro-2-propoxypropionate (GenX). This contaminant belongs to the group of per- and polyfluorinated alkyl substances (PFAS) found as contaminants in drinking water worldwide<sup>[138,139]</sup> and it shows carcinogenic and

endocrine disruption activity in humans.<sup>[140,141]</sup> The interaction of GenX with the amine-functionalized COFs was postulated to arise from favorable interactions of the polar amino groups of COFs with the anionic headgroup of GenX. More recently, a Suzuki-Miyaura cross-coupling reaction was reported as a versatile and efficient post-synthetic strategy to functionalize COFs.<sup>[142]</sup> Brominated imine-COFs (BrCOFs) were post-synthetically modified by reaction with a variety of phenylboronic acids bearing electron-donating and electron-withdrawing functional groups, while the crystallinity and porosity was well-retained.

Functionalization of COFs can also be performed through chemical transformation of the linkages, which are typically stable but, in some cases, can be reactive under specific conditions. This is a very effective approach to incorporate new linkages into a pre-formed COF structure, which are otherwise difficult or even impossible to synthesize *de novo*, while maintaining their inherent properties of crystallinity and porosity. To date, imine linkage have been the most widely transformed.<sup>[143]</sup>

Under controlled oxidation reactions imine-linked COFs were successfully converted to amide-linked materials, with remarkably chemical stability and crystallinity, as already discussed in section 1.2.2.<sup>[97,144]</sup> In addition, by following a building block exchange PSM of imine-based TzBA COF the counterpart amide-based JNU-1 COF was synthesized with enhanced crystallinity when compared to pristine COF material.<sup>[145]</sup> Owing to the reversibility of imine bond formation, the building block exchange strategy has been used in imine-linked COFs allowing for framework-to-framework transformation. The conversion to the amide linkage greatly enhanced COF stability in organic and aqueous media, as well as in concentrated HCl and NaOH. Amide-based JNU-1 COF showed a large adsorption capacity ( $q_{\max} = 1124 \pm 10 \text{ mg g}^{-1}$ ) and high selectivity for gold recovery. In another study, the irreversible reduction of 2D imine-based COF-366 in presence of  $\text{NaBH}_4$  as reducing agent led to the formation of amine-linked COF-366-AR, with improved chemical stability when compared to the pristine imine-based COF.<sup>[146]</sup>

Taking advantage of the high reactivity of imine linkage, the aza-Diels-Alder Povarov cycloaddition reaction has also been used to convert imine-linked COFs to the

corresponding quinoline-based materials.<sup>[99]</sup> Despite the low yield of linkage conversion around 20–30%, the high crystallinity and enhanced stability of the resulting COFs upon exposure to aggressive chemicals make this transformation very useful to obtain new COF materials with enhanced properties. Recently, the Strecker reaction have been employed to modify the imine-based TPB-DMTP-COF to the corresponding  $\alpha$ -aminonitrile-based COF material under solvothermal conditions.<sup>[147]</sup> A similar crystallinity was observed when compared to the same COF material synthesized through the multi-component one-pot *in situ* Strecker reaction. Multicomponent one-pot *in situ* reaction has been demonstrated as a new strategy to overcome some of the issues faced with PSM in COF synthesis. The versatility of imine linkage was also demonstrated by reaction of imine-linked TTI-COF with elemental sulfur which promote oxidation of imine to thioamide, with subsequent oxidative cyclization to afford the thiazole-based TTT-COF with high range order.<sup>[98]</sup> TTT-COF showed improved stability when compared to pristine TTI-COF, even in concentrated HCl. As an alternative strategy, incorporation of thiazole units was also achieved with success following a building block exchange PSM of imine-based COFs.<sup>[100]</sup>

Despite all of this knowledge, to date, most part of the reported PSM strategies require the use of catalysts, such as  $\text{BF}_3 \cdot \text{Et}_2\text{O}$ ,<sup>[99,147]</sup>  $\text{SnCl}_2$ ,<sup>[58]</sup>  $\text{CuI}$ ,<sup>[121–123]</sup>  $\text{Et}_3\text{N}$ ,<sup>[86]</sup>  $\text{K}_2\text{CO}_3$ ,<sup>[87]</sup> additional reagents, such as AIBN,<sup>[43]</sup>  $\text{PPh}_3$ ,<sup>[60]</sup> and harsh reactions conditions involving high temperatures,<sup>[98]</sup> which can limit their application to specific COF materials. Taking this into account new developments on the field of COF PSM are needed to find simpler and more versatile experimental conditions.

### 1.2.5. Structural analysis of COFs

The crystalline structure is one of the most relevant indicators for a successful COF synthesis.<sup>[19]</sup> The evaluation can be done by powder X-ray diffraction (PXRD) or by small-angle X-ray scattering (SAXS), with PXRD being the most commonly used technique. In a typical PXRD pattern, strong and distinct diffraction signals should be observed as an indication of structural periodicity of the framework, which can be combined with computational simulations to predict COF structure. To gain better insight into the COF

stacking behavior *ab initio* quantum calculations including the density functional theory (DFT) are frequently used as prediction methods.<sup>[148]</sup>

Chemical structure of a COF material can be established by Fourier transform infrared spectroscopy (FT-IR), which can offer useful information about the presence of typical functional groups, as well as the existence of specific bonds.<sup>[148]</sup> Thermal stability is an important parameter analyzed by thermogravimetric analysis (TGA), which is directly influenced by the COF's chemical composition.<sup>[148]</sup> Other techniques such as elemental analysis, solid-state nuclear magnetic resonance (NMR) spectroscopy, and X-ray photoelectron (XPS) spectroscopy contribute for a deep insight of the physico-chemical properties of COFs.<sup>[148]</sup> In detail, elemental analysis and XPS could be used to determine the elemental composition of COF material quantitatively and qualitatively, respectively. NMR spectroscopy could give information about the presence of impurities incorporated into the material, as well as is the method of choice to quantify the degree of PSM.<sup>[19]</sup>

Raman spectroscopy is a complementary technique which, besides the information related to the COF chemical structure, can also give additional information about its crystalline nature.<sup>[148]</sup> Electron microscopy (scanning electron microscopy (SEM) and transmission electron microscopy (TEM)) analysis provide information about the surface morphology of COF material, and additional information on the crystal structure, size, and shape of COF crystals, as well as the porous structure, respectively.<sup>[148]</sup>

The surface area and pore volume are assessed by N<sub>2</sub> gas adsorption-desorption isotherm measurements and of utmost importance to determine that the prepared material is in fact porous in nature. Of the adsorption isotherms described by IUPAC (type I, II, III, IV, V, and VI, Figure 5),<sup>[149]</sup> type I<sup>[56,150]</sup> and IV<sup>[125,147]</sup> isotherms are the ones typically reported for COFs, particularly associated with the presence of micropores and mesopores in the framework, respectively. The Brunauer–Emmett-Teller (BET) theory is typically used to establish the specific surface area of a COF material by plotting a linear regression on the pressure range which monotonically increases as a function of relative pressure.<sup>[148,151]</sup> With regard to the pore size distribution, density functional theory (DFT) coupled with Monte Carlo molecular simulations have been used for calculations from isotherm data.

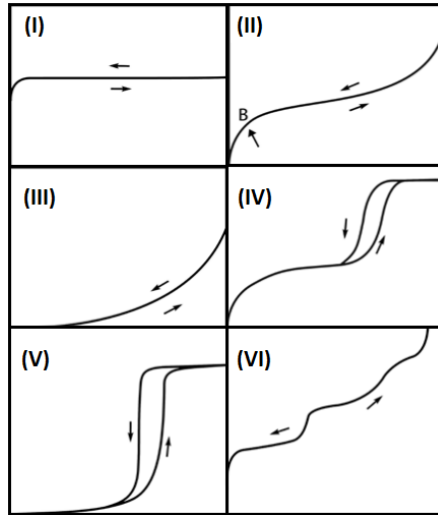


**Figure 5.** Classification of physisorption isotherms by IUPAC.<sup>[149]</sup> Adapted with permission. Copyright, IUPAC & De Gruyter, 2015.

### 1.3. Water quality

Water is of utmost importance for life in earth and the most essential resource for human civilization survival. Technological and industrial growth combined with exponential population growth have emerged as a threat to the quality of water natural sources endangering not only environment but also human health. World Health Organization (WHO)<sup>[152]</sup> estimate that by 2025 half of the world's population will be living in water-stressed areas, due to scarcity of clean drinking water sources.

Since 2000, the European Union has launched directives to establish environmental quality standards in the field of water policy for all the EU member states with the aim of reaching a good ecological and chemical status for water.<sup>[153–158]</sup> Despite the increasing environmental water policies, regulation for the presence of certain hazardous natural and anthropogenic compounds in drinking water is still limited. In December 2020,<sup>[159]</sup> EU council revised the drinking water directive, updating the water quality standards and introducing new emerging pollutants to the watch list of contaminants, such as endocrine disruptors, pharmaceuticals, and microplastics. This directive foresees a synchronisation of the quality standards to be adopted for all the countries in the European Union to protect human health from the adverse effects of water contamination. In fact, defining similar regulatory limits on the EU level is crucial for risk assessment. However, the development



of new and more appropriate and efficient monitoring approaches and methodologies is extremely important. Owing to the high variability and complexity of the water matrix allied with the low concentrations of contaminants that need to be detected, establishing highly efficient water-quality monitoring programs is still a challenge.

In general, contaminants associated with water pollution can be classified in two main groups: inorganic and organic (Figure 6).<sup>[160]</sup> Most part of inorganic contaminants that can be found in water supplies are mainly from agricultural and industrial activities, such as nitrate, chlorine, and heavy metals, such as mercury and arsenic.<sup>[161,162]</sup> Moreover, radiological elements, such as uranium ( $U^{234}$  and  $U^{238}$ ) and radium ( $Ra^{226}$  and  $Ra^{228}$ ), often used in the industry have also been detected.<sup>[163]</sup> The majority of anthropogenic organic water contaminants are pesticides, volatile organic compounds (VOCs), perchlorinated biphenyls (PCBs), and dyes mainly derived from agriculture, industry, and human activity.<sup>[160]</sup> In addition, owing to their recent increasing occurrence in water, the EU has included hazardous substances to the list of emerging contaminants (ECs) that need to be monitored to protect human health.<sup>[159,164,165]</sup> The ECs group includes chemicals such as pharmaceuticals, preservatives, laundry detergents, perfluorinated compounds (PFCs), antibacterial agents, personal care products, fragrances, plasticizers, flame retardants, and surfactants.<sup>[159,166]</sup> To date, the EU has reinforced water quality standards for ECs, providing more transparency at EU level.<sup>[159]</sup> However, more needs to be done to increase the quality of monitoring programs to ensure that the water is wholesome and clean for human consumption.

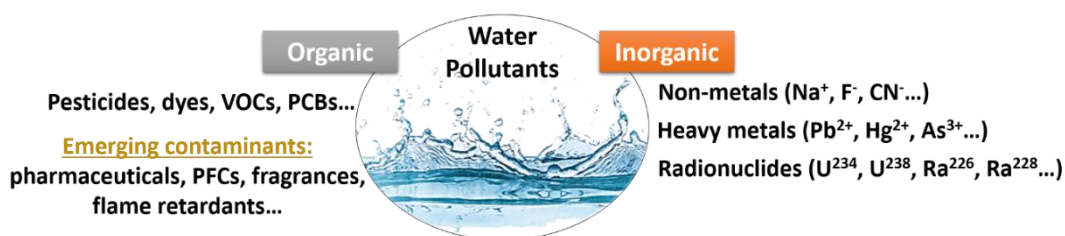


**Figure 6.** Most commonly detected contaminants in water resources (PCBs: polychlorinated biphenyls; PFCs: perfluorinated compounds; VOCs: volatile organic compounds).

### 1.3.1. Biotoxins

Microalgae in marine and cyanobacteria in both marine and freshwaters, are very important photosynthetic organisms since they are primary producers, the base of food webs, and play an important role as CO<sub>2</sub> sinks and carbon transporters to deep waters. Most of these organisms at regular levels are harmless, however some species can cause harmful algal blooms (HABs) events when they grow massively in aquatic environment, under certain circumstances, causing taste and odor problems in the water, as well as anoxia for other species in the water column.<sup>[160,167]</sup> The occurrence and severity of HABs have increased in recent decades, which is mainly attributed to the serious anthropogenic hypertrophication of surface water. In addition, some HAB-producing species (microalgae and cyanobacteria) may produce toxins that are harmful to human health.<sup>[167,168]</sup>

Phycotoxins, naturally produced by microalgae, may produce toxic effects even at low concentrations and are known to accumulate in other organisms, such as fish and shellfish.<sup>[169]</sup> Diarrhetic shellfish poisoning (DSP) is a foodborne intoxication caused by the ingestion of shellfish, such as mussels, contaminated with DSP toxins, including the okadaic acid (OA, Figure 7) group of toxins, with OA being considered the parental compound.<sup>[169]</sup> OA is a lipophilic polyether-type molecule, and a powerful inhibitor of the serine/threonine protein phosphatase (PP) enzymes, particularly PP1 and PP2A, by blocking their catalytic site and consequently their activity.<sup>[169,170]</sup> The most characteristic toxic effects of OA are related to the PP inhibition that leads to a dramatic increase of phosphorylation of a number of proteins, resulting in important cell alterations at the DNA and cellular level. In order to protect consumers from acute intoxications, the European Commission lays down maximum levels of 160 µg of OA per kg of mollusc flesh for the commercialisation of shellfish.<sup>[171]</sup> Throughout Europe,<sup>[172,173]</sup> Asia,<sup>[174,175]</sup> and America<sup>[176,177]</sup> the occurrence of OA has been documented over the years, including Portuguese west coast.<sup>[178–180]</sup> The Portuguese Institute of the Sea and Atmosphere (IPMA) has developed a specific monitoring program for marine biotoxins, in which consecutive monitoring of the amount of lipophilic biotoxins, such as OA, is documented throughout the year, in order to manage the periods of permission/interdiction for bivalves harvesting, following the European legislation.

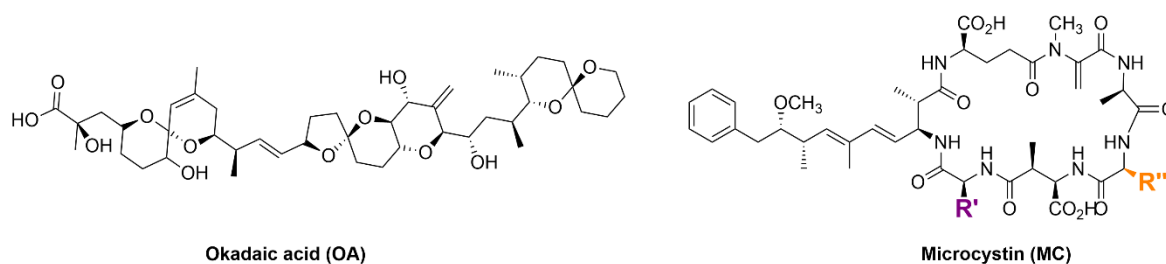


**Figure 7.** Chemical structures of okadaic acid (OA) and microcystins (MC).

Cyanotoxins, produced by cyanobacteria, are commonly found in many water ecosystems and can be classified as neurotoxins (i.e. anatoxins, saxitoxins), cytotoxins (i.e. lingbyatoxin), and hepatotoxins (i.e. microcystins, nodularin).<sup>[181]</sup> Among them, microcystins (MCs, Figure 7) are the most commonly detected in freshwater environments.<sup>[182,183]</sup> MCs induce acute hepatotoxicity, displaying LD<sub>50</sub> values in the range of 50–600  $\mu\text{g kg}^{-1}$ , and chronic exposure to concentrations as low as 0.01  $\mu\text{g mL}^{-1}$  can activate a cascade of apoptotic pathways in cells that increase the risk of cancer development.<sup>[184,185]</sup> Structurally, MCs are monocyclic heptapeptides with a molecular weight in the range of  $\approx 800$ –1100 Da, with high stability and resistance to extreme pH and temperature up to 300 °C.<sup>[182,186]</sup> They possess a common general structure with five amino acids: alanine, methyl isoaspartic acid, glutamic acid, *N*-methyldehydroalanine, and the unusual Adda amino acid, typical of microcystins, which is often associated with the toxicity of these molecules.<sup>[182,183,186]</sup> In addition, MCs have two variable amino acids (Figure 7, R' and R'', being e.g., arginine (R), leucine (L), alanine (A), and tyrosine (Y)), which influence their structural and chemical properties and consequently their toxicity.<sup>[182,183,186]</sup> Up to now, more than 100 MCs have been identified, with MC-LR, MC-RR, and MC-YR being the most commonly observed.<sup>[182,183,186]</sup> In addition to being the most abundant, MC-LR and MC-RR are also the most toxic derivatives. Similarly to OA, MCs are known as potent inhibitors of the protein serine/threonine phosphatases 1 and 2A.<sup>[186,187]</sup> Exposure to MCs can cause severe liver damage, haemorrhage, and even death owing to hyperphosphorylation induced by PP inhibition. MC-producing cyanoHABs have been reported all over the world in various studies.<sup>[183,188]</sup> In Portugal, for example, Sobrino et al.<sup>[189]</sup> showed the presence of five MC variants in the Guadiana estuary in concentrations

above  $1 \mu\text{g MC-LR equiv L}^{-1}$ . Thus, the WHO, as a consequence of MCs toxicity, distribution, and thermal and chemical stability, has established a provisional guideline value of  $1 \mu\text{g L}^{-1}$  of MC-LR in drinking water as a preventive step to protect the public health.<sup>[159,186]</sup> Additionally, MCs were also included in the list of emerging substances by the NORMAN network to be incorporated into the routine monitoring programs at the EU level.<sup>[165]</sup> Recently, in beginning of 2021, European Union launched a new Drinking Water Directive, in which MCs were added as priority substances that need to be monitored with a maximum allowed concentration of  $1 \mu\text{g L}^{-1}$ .<sup>[159]</sup>

### 1.3.2. Pharmaceutical pollutants

Pharmaceutical contaminants have been found in nearly all types of water matrices on every continent, being mainly derived from human and veterinary use.<sup>[190,191]</sup> Their persistence in the environment, allied to their ability to elicit biological effects at very low concentrations make them at the fore of recent environmental European legislation as contaminants of emerging concern.<sup>[159,192,193]</sup> From the beginning of 2021, the EU<sup>[159]</sup> launched a new Drinking Water Directive, in which pharmaceuticals were included as emerging pollutants. In addition, the need of preparation of an environmental risk assessment report for all new pharmaceuticals products found in water was defined as a strategic approach to mitigate their risk to the human health.

Worldwide, a wide variety of pharmaceutical compounds have been detected in water matrices, from antibiotics (i.e. ciprofloxacin, tetracyclines, sulfonamides),  $\beta$ -blockers (i.e. atenolol, propranolol), anticonvulsants (i.e. carbamazepine), antidepressants (benzodiazepines), lipid regulators (i.e. fibrates), to anti-inflammatory and analgesic drugs (i.e. ibuprofen, diclofenac, paracetamol).<sup>[190,191]</sup> Among all these pharmaceuticals, antibiotics and analgesics are the most commonly detected. However, the level of detection varies from country to country.

In Portugal, a preliminary study carried out in 2016 found the presence of at least 1–8 pharmaceutical compounds out of the selected 11 most consumed pharmaceuticals, in 15 chosen wastewater treatment plants (WWTPs) from north to south. Paracetamol was the

pharmaceutical with the highest average concentration found in water of around  $41 \mu\text{g L}^{-1}$ , with increased frequency during the winter season.<sup>[194]</sup> More recently, a broad range of 66 human and veterinary pharmaceuticals were detected in surface waters of the Tagus Estuary, with high incidence of the non-steroidal anti-inflammatory drug diclofenac of around  $52 \text{ ng L}^{-1}$ .<sup>[195]</sup> In addition, other less common pharmaceutical substances, such as the antidepressant sertraline ( $304 \text{ ng L}^{-1}$ ), the lipid regulator gemfibrozil ( $77 \text{ ng L}^{-1}$ ), the antihypertensive ibersartan ( $162 \text{ ng L}^{-1}$ ), and the antibiotic doxycycline ( $128 \text{ ng L}^{-1}$ ), were detected above the threshold of  $10 \text{ ng L}^{-1}$  defined by the guidelines of the European Medicine Agency for individual pharmaceuticals.<sup>[196]</sup>

This well-documented emerging presence of contaminants in water environment highlights the importance of developing efficient risk management strategies and monitoring programs which will help to identify reference points of potential environmental and human risk.

### **1.3.3. Water monitoring and treatment**

Based on the growing demand for clean water, governments and organizations around the world have improved water pollution regulations as a strategy to ensure, in the first instance, public and environmental safety.<sup>[159]</sup> Allied to this, the search for more efficient, cost-efficient, and robust water and wastewater treatment technologies has increased, with the aim to not compromise the environment and not jeopardize human health through the treatment itself. To date, a wide variety of techniques have been described for the removal of toxic contaminants from water, from coagulation, chlorination, advanced oxidation processes (AOPs), ozonation, nanofiltration, and reverse-osmosis membrane process to biological methods.<sup>[160,190,197]</sup> Most of these methods present some drawbacks in their application in terms of limited efficiency, high energy requirement, high investment costs and toxic sludge and by-product generation.<sup>[190]</sup> Therefore, for the selection of the most appropriate technique it is crucial have a deep knowledge about the physico-chemical properties of the target contaminants.<sup>[197]</sup>

On the other hand, the development of analytical monitoring techniques to detect and quantify the occurrence of contaminants in water is also of fundamental importance. Due to the low concentrations (ppm or even ppb) and limits of detection and quantification of the analytical methods, clean-up and pre-concentration steps are always needed, which are usually based on solid-phase extraction (SPE), which through incorporation of a column system filled with a resin can retain a wide range of contaminants.<sup>[198]</sup>

Within the different water-treatment methods developed in the last few decades, adsorption is one of the most common and promising options offering several advantages, such as simplicity, low cost, and in some cases the option of regeneration and reuse of the adsorbent.<sup>[199]</sup> In addition, undesirable by-products are not produced, which is an advantage when compared to other techniques such as AOPs.

Thus, adsorption appeared as one of the most efficient and economic techniques for the removal of contaminants from water and for their pre-concentration for monitoring applications. It is a surface phenomenon of interaction between an adsorbate (target molecule to be adsorbed during the adsorption process) and an adsorbent (material surface where the adsorbate will be retained), which can be governed by non-covalent interactions (physisorption), such as lipophilic/hydrophilic effects and hydrogen-bonding interactions, and/or by covalent bonding (chemisorption).<sup>[160,200]</sup>

For the design and/or selection of an adsorbent for water treatment, several physicochemical properties of the water matrix need to be considered. Temperature of natural water may vary from  $-2\text{ }^{\circ}\text{C}$  in seawater to  $40\text{ }^{\circ}\text{C}$  in any kind of water matrix, which can play an important role in adsorption process. Water salinity can range from less than 0.05% in freshwaters to 4.5% in seawater, and pH from  $-3.6$  in mining drainage waters to 9.6 in seawater.<sup>[201]</sup> The pH of the medium can influence the surface charge distribution of the adsorbent and adsorbate molecule, affecting directly the efficiency of adsorption.<sup>[202]</sup> Therefore, it is of utmost importance obtaining robust and stable adsorbents, which can be used in a broad range of conditions.

Another important pre-requisite for adsorbents is the reversibility of the interaction with the adsorbate molecules, which is essential to allow the recovery of the adsorbed

contaminants for further analysis. This feature is also crucial to allow for recycling of the adsorbent, thus saving production costs, and reducing the carbon footprint in view of sustainability. Therefore, weak non-covalent interactions are preferable as driving forces for the adsorption of water contaminants.

Owing to the complexity of natural waters and the low concentrations of the contaminants, preferential adsorption of the target molecules, or even selectivity, is a key quality parameter for the selection of adsorbent material. In these regards, pore surface functionalization, pore uniformity and size, and surface area are very important parameters to define adsorbent efficiency of an adsorbent. When compared to non-porous adsorbent materials, adsorption process is enhanced in the presence of porous materials, where a faster and more efficient adsorbate adsorption can occur.<sup>[200,203]</sup> Micro- (pore size < 2 nm) and mesoporous (pore size between 2–50 nm) materials feature pores in the appropriate range of sizes for contaminant capture, with pore size lower than 5 nm excluding most part of particulate organic matter present in natural water. However, pore sizes below 1 nm could be too restrictive for most contaminants.

At the equilibrium of adsorption, the amount of adsorbate adsorbed by adsorbent ( $q_e$ ) can be determined by following equation 1.<sup>[200]</sup>

**Equation 1:** 
$$q_e = \frac{V(C_0 - C_e)}{m}$$

where  $V$  is the volume of solution (L),  $m$  is the mass of adsorbent (g), and  $C_0$  and  $C_e$  are the initial and equilibrium concentration of adsorbate, respectively.

In the adsorption process, adsorbate partition between the liquid phase and the adsorbent implies a dynamic phase equilibrium based on thermodynamics principles. This equilibrium, also called adsorption isotherm, can be described by the quantity of adsorbate adsorbed in equilibrium,  $q_e$  ( $\text{mg g}^{-1}$ ), as a function of the concentration of adsorbent,  $C_e$  ( $\text{mg L}^{-1}$ ). A linear isotherm is usually attributed to adsorbents with a homogeneous surface. This type of adsorption data is commonly fitted using Langmuir (equation 2) and Freundlich (equation 4) models.<sup>[200,203]</sup>

**Equation 2:**

$$\frac{C_e}{q_e} = \left(\frac{1}{q_m}\right) C_e + \frac{1}{q_m K_L}$$

where  $q_e$  is the amount of adsorbate adsorbed onto the adsorbent in equilibrium ( $\text{mg g}^{-1}$ ),  $C_e$  is the concentration of adsorbate in the equilibrium state ( $\text{mg L}^{-1}$ ),  $q_m$  is the maximum adsorption capacity ( $\text{mg g}^{-1}$ ), and  $K_L$  is the characteristic Langmuir model constant. The main characteristics of the Langmuir isotherm can be expressed by a dimensionless constant described as the separation factor  $R_L$ , which is an important equilibrium parameter.

**Equation 3:**

$$R_L = \frac{1}{1 + K_L C_0}$$

where  $C_0$  is the initial and highest concentration of the adsorbate in solution ( $\text{mg L}^{-1}$ ).  $R_L > 1$  indicates unfavorable adsorption,  $R_L = 1$  is linear,  $0 < R_L < 1$  is favorable, and  $R_L = 0$  is irreversible.<sup>[203]</sup>

The Freundlich isotherm is determined by

**Equation 4:**

$$\log q_e = \left(\frac{1}{n}\right) \log C_e + \log K_F$$

where  $n$  and  $K_F$  are characteristics constants. The  $n$  constant is related with the energetic heterogeneity of the adsorbent, and determines the curvature of the isotherm. The lower the  $n$  value is, more concave with respect to the x axis of concentration is the isotherm shape, while  $n = 1$  shows a linear isotherm, and  $n > 1$  indicates a favorable adsorption process.  $K_F$  is an indicator of the adsorption capacity in the Freundlich theory. This constant is a parameter used to evaluate the efficiency of the adsorption process, where the higher the value of  $K_F$  is, the higher is the adsorption capacity of the adsorbent.<sup>[203]</sup> The maximum adsorption capacity ( $q_m$ ) can be calculated from the following equation:

**Equation 5:**

$$q_m = K_F C_0^{1/n}$$

Normally adsorption equilibrium is not reached instantaneously, especially for porous adsorbents, where the mass transferred from the solution to the adsorption sites within the adsorbent is constrained by mass transfer resistance, which influences the time required to reach the state of equilibrium. This time progress of the adsorption process is



defined as adsorption kinetics.<sup>[203]</sup> In the adsorption kinetics studies, the differences in the concentration of the adsorbate in solution are measured over time, which can be translated into a decrease of initial concentration of adsorbate,  $C_0$ , to an equilibrium point of maximum adsorption,  $C_e$ . To date, there are two main mathematic models that describe the adsorption kinetics, the pseudo first-order (equation 6) and second-order (equation 7) kinetics of Lagergren. The pseudo-first order model is the most used to evaluate adsorption kinetics in liquid–solid systems and assumes that the rate of adsorption of the adsorbate over time is proportional to the number of active sites on the adsorbent.

**Equation 6:** 
$$\log(q_e - q_t) = \log q_e - \frac{K_1}{2.303} t$$

**Equation 7:** 
$$\frac{t}{q_t} = \frac{1}{K_2 q_e^2} + \frac{1}{q_e} t$$

where  $q_t$  is the amount of adsorbate adsorbed ( $\text{mg g}^{-1}$ ) at specific time,  $t$  (min),  $q_e$  is the amount of adsorbate adsorbed in equilibrium ( $\text{mg g}^{-1}$ ),  $K_1$  and  $K_2$  are the first-order and second-order kinetic constants ( $\text{min}^{-1}$ ), respectively.

#### 1.3.4. State-of-the-art adsorbents for biotoxins and pharmaceuticals

In the last decades, adsorption has been developed for *in situ* passive concentration of contaminants present in water for posterior analysis in the laboratory. Polar organic chemical integrative samplers (POCISs), consisting of a sequestration medium enclosed within hydrophilic microporous polyethersulfone membranes, have been successfully used to sample polar organic compounds in aquatic environments.<sup>[204–207]</sup> Other kind of semi-permeable membrane devices have been used for the monitoring of polycyclic aromatic hydrocarbons.<sup>[208]</sup> Recently, McKay and co-workers,<sup>[209]</sup> described the use of samplers comprising hollow, cylindrical microporous polyethylene tubes (MPTs) containing polymeric sorbent phases of strata-X and strata-X in agarose. These were deployed in the influent stream of a municipal wastewater treatment plant for the quantitative estimation of the concentration of pharmaceuticals and personal care products. Notwithstanding the promise MPTs show for monitoring some of the compounds, having to extract, analyze,

and evaluate the samplers at regular intervals of deployment implies a considerable work-load and costs.

For the removal of pharmaceuticals from water matrices, adsorption has been widely explored through the use of a wide range of adsorbents, including activated carbon (AC),<sup>[210][211]</sup> clays,<sup>[211]</sup> silica and polymer-based materials,<sup>[211]</sup> as well as zeolites.<sup>[211]</sup> AC is the dominantly studied adsorbent for the removal of pharmaceuticals from water mainly due to its high surface area, high availability in the market, and low cost, however its low selectivity is one of its drawbacks.<sup>[166,210]</sup> In addition, although many forms of AC are currently used in water treatment featuring relatively high removal efficiencies, adsorption of hydrophilic contaminants is quite limited.<sup>[212]</sup> Similarly, to activated carbon, zeolites have been widely used, however their low selectivity allied to lower values of adsorption capacity obtained when compared to AC limit their use in the environmental field.

More recently, materials such as MOFs,<sup>[213]</sup> molecularly imprinted polymers (MIPs),<sup>[214]</sup> hybrid membranes<sup>[215]</sup>, and COFs<sup>[216][217]</sup> have been reported for the mitigation of pharmaceutical pollutants in water matrices. MIPs, which have been extensively used in solid-phase extraction systems, offer a highly selective and specific option for pre-concentration and purification of target molecules.<sup>[218]</sup> However, their surface areas are typically in a much lower range than those of other adsorbents, and their fabrication is expensive, which hinders the extensive application of MIPs for *in situ* capture of water contaminants. Additionally, their high selectivity can even be a limitation when targeting the adsorption of broader families of compounds, analogues, and metabolites that are regularly found as mixtures in water.<sup>[198]</sup> On the other hand, MOFs, crystalline materials formed through the linkage of metal ions or clusters with organic building units, with high crystallinity, high surface area, permanent porosity, and tunable pore structure, have been reported as efficient and selective adsorbents,<sup>[213]</sup> as well as photocatalysts<sup>[219]</sup> for water remediation. However, the stability in water of some derivatives, especially under extreme pH conditions, can be an issue.<sup>[220]</sup>

Despite the wide variety of adsorbents reported, the lack of appropriate materials featuring not only well-defined pore geometry and sorbate-selective functionalities, as well

as outstanding stability and reusability, are limiting factors for the efficient removal of contaminants from polluted water.<sup>[221]</sup> COFs with their uniform and restricted pore size (typically 1–5 nm in diameter), high surface area, and tunable pore surface could be suitable materials to address this deficit.<sup>[13,17,21,24]</sup> Despite the similar properties to those of MOFs, COF building blocks composed of light-weight elements are linked by strong covalent bonds, which confer high thermal and chemical stability as compared to the coordinative bonds in MOFs.<sup>[17,222]</sup> In addition, several strategies have recently emerged to produce COFs with water stability, without compromising crystallinity and porosity, and giving access to a wide range of options to functionalize their pore surface, further enhancing the potential of this class of materials for contaminant capture.<sup>[15]</sup>

Additionally, solid phase-based methodologies, such as solid-phase extraction (SPE), solid-phase microextraction (SPME), and solid-phase adsorption toxin tracking (SPATT) systems, are considered efficient, low-cost, and environmentally friendly techniques for the pre-concentration, extraction, and monitoring of water contaminants.<sup>[223]</sup> For microorganisms-produced toxins, passive SPATT systems have been widely studied and their usefulness has been demonstrated in concentrating toxins such as okadaic acid, dinophysistoxins, and microcystins.<sup>[223–225]</sup> The SPATT system consists of batches of hydrated adsorbent resins within a polyester mesh, sown with polyester thread.<sup>[226,227]</sup> The bags are installed in a frame attached to a weighted line at different locations and depths. The nature, properties, and behaviour of the solid-phase adsorbents are of utmost importance in the development of SPATT devices. To date, several polymeric resins have been investigated for the adsorption of lipophilic and hydrophilic toxins, such as OA and some MC derivatives, including styrene-divinylbenzene-based polymer resins, such as Diaion HP-20, Sepabeads SP850, SP825L, SP-700, and SP20.<sup>[223,227]</sup> Some studies showed that HP-20 SPATT devices allowed the detection of toxins in a similar time frame than when detected in shellfish tissues by LC-MS analysis in regulatory centers.<sup>[228]</sup> However, in order to empower the aquaculture industry with an efficient tool to remove the seafood from seawater before contamination occurs, a forecast level of weeks is required. In this perspective, the development of more efficient adsorbents is essential to allow for the

prediction of HABs in advance, and to obtain a practical early warning system for DSP outbreaks in aquaculture sites.

### 1.3.5. COFs for adsorption applications

COFs, in virtue of their advantageous structural and chemical properties, discussed in the previous sections, have emerged as promising adsorbents for water contaminants,<sup>[7,8,216,229,230]</sup> such as organic dyes,<sup>[38–42,231–233]</sup> metal ions (heavy metals and radionuclides),<sup>[49,51,52,234–238]</sup> perfluoroalkyl substances,<sup>[60,239–242]</sup> flame retardants,<sup>[243,244]</sup> and pesticides.<sup>[64,245]</sup> At the time of starting this thesis, the use of COFs as adsorbents for the removal of organic pollutants from water, in particular biotoxins and pharmaceuticals, had not been yet explored.

COFs are usually obtained as low-density powders featuring polydisperse particles with sizes in the micrometre range. Although such powder can be directly applied for adsorption of contaminants in water using different modalities, such as direct dispersion in sample matrices<sup>[60–62,246–250]</sup> or packing into columns,<sup>[251,252]</sup> using the bulk material could lead to material losses, high column backpressure, and difficulties in its isolation from the sample matrix. These are serious limitations, which can hinder the use of COFs in environmental applications. Although COFs can feature fascinating properties, these crystalline materials need to be further engineered to harness their full potential for practical applications.<sup>[15]</sup>

COF powders can be transformed or molded into specific geometric shapes, such as pellets,<sup>[253]</sup> beads,<sup>[254]</sup> and cylinders,<sup>[255]</sup> improving their mechanical strength, durability, and permeability for adsorption applications, while maintaining their crystallinity and porosity. Immobilization of COFs on solid substrates, resulting in the so-called COF composites, can also help in overcoming the issues faced with bulk COF powder material. Such composites can feature improved stability, dispersibility, and/or material retention, while taking advantage of the properties of all materials present in the composite. In the last few years, different materials have been used as substrates for crystalline COF composites for adsorption in water, such as magnetic nanoparticles (NPs),<sup>[59,64,256–259]</sup> silica<sup>[260–264]</sup> and polystyrene beads,<sup>[265]</sup> and mixed matrix membranes (MMMs)<sup>[266–269]</sup>

(Table 1). Recent progresses in the development of COFs as thin films<sup>[270–272]</sup> have been made, increasing the scope of these materials for different applications such as membranes.<sup>[14,273]</sup>

**Table 1.** Some of the reported COF-based composites used for adsorption of pollutants from water.

COF	Solid substrate	Surface area (m <sup>2</sup> g <sup>-1</sup> )	Target	Ref
LZU-1	Magnetic NPs	872	Iodine	[258]
TpBD	Magnetic NPs	273	Bisphenols	[259]
TpPa-1	Magnetic NPs	248	PAHs <sup>[c]</sup>	[59]
CTF	Silica beads	359	Mono-substituted benzenes, nonpolar PAHs, phenols, anilines and bases	[260]
TpBD	Silica beads	385	Separation of neutral, acid, and basic molecules	[262]
BtaMth	Silica beads	n/a	Separation of isomers	[263]
COF-300	Silica beads	431	Separation of isomers	[264]
TbBD	Polystyrene beads	404	Ibuprofen	[265]
TpPa-2	Polysulfone matrix	535	n/a	[267]
TpPa-1	Polyacrylonitrile	300	Orange GII, Methyl blue, Congo red and Alcian blue	[268]
TAPB-PDA	Polyethersulfone	n/a	Rhodamine-WT	[274]
TpPa-1	Polysulfone	n/a	Congo red	[275]

#### 1.4. Objectives

The main goal of this thesis is to demonstrate that through a rational design, fabrication and tailoring of 2D COFs, these materials can be very valuable for efficient adsorption and/or degradation of emerging water contaminants, offering promising alternatives for water remediation or monitoring.

This general objective is divided in the following two specific ones:

- Tailoring COFs for the adsorption of waterborne emerging contaminants and biotoxins: Tp-based 2D COFs, incorporating a robust and water-stable  $\beta$ -ketoenamine linkage will be fabricated for the preferential adsorption of the marine and freshwater biotoxins okadaic acid and microcystins, respectively, and for the broad range adsorption of pharmaceuticals.

- Expanding chemical synthesis of  $sp^2$ -based COFs and exploring their application for photocatalytic degradation of water pollutants; the synthesis of  $sp^2$ -based COFs will be explored and their performance will be evaluated as photocatalyst for the degradation of organic dyes methylene blue and methyl orange as initial models for other organic pollutants.

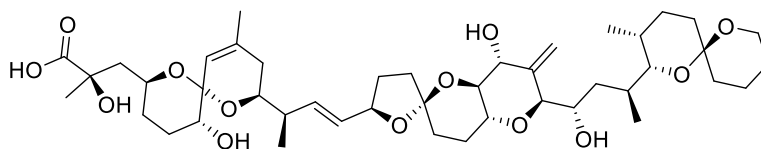
## Chapter 2 – Tailoring COFs for the adsorption of hazardous compounds

### 2.1. COFs for the adsorption of biotoxins

#### 2.1.1. Okadaic acid<sup>[246]</sup>

Okadaic acid (Figure 8) as one of the most relevant marine toxins produced by marine microalgae species during a HAB, occurs broadly<sup>[173,175,176]</sup> around the world. Its acute toxicity ( $LD_{50} = 192 \mu\text{g kg}^{-1}$ , in mice) raises environmental and public health concerns, highlighting the importance of its monitoring in water environment. OA is a highly lipophilic ( $\log K_{ow} = 5.05$ )<sup>[276]</sup> polyether monocarboxylic acid molecule of a  $C_{38}$  fatty acid.<sup>[277]</sup> It is highly thermally stable, as well as stable in a wide pH range from mildly acidic to strongly basic solutions.<sup>[169,170,278]</sup> However, under treatment with hardly strong mineral acids, such as HCl, it rapidly degrades.

In virtue of its harmful impact on human health, OA early monitoring is important to improve human safety, and therefore several techniques have been developed for its capture from water. To date, solid-phase adsorption technique have been demonstrated as a very useful technique for OA extraction, with Diaion HP-20 resin showing the best performance with a maximum adsorption capacity reported of  $1.639 \text{ mg g}^{-1}$  for OA.<sup>[279]</sup> Notwithstanding its efficiency to track lipophilic toxins as compared to other resins, Diaion HP-20 with a pore size of 26 nm suffer of low selectivity, which can affect its efficiency in environmental field. Thus, the development of more efficient adsorbents is crucial.



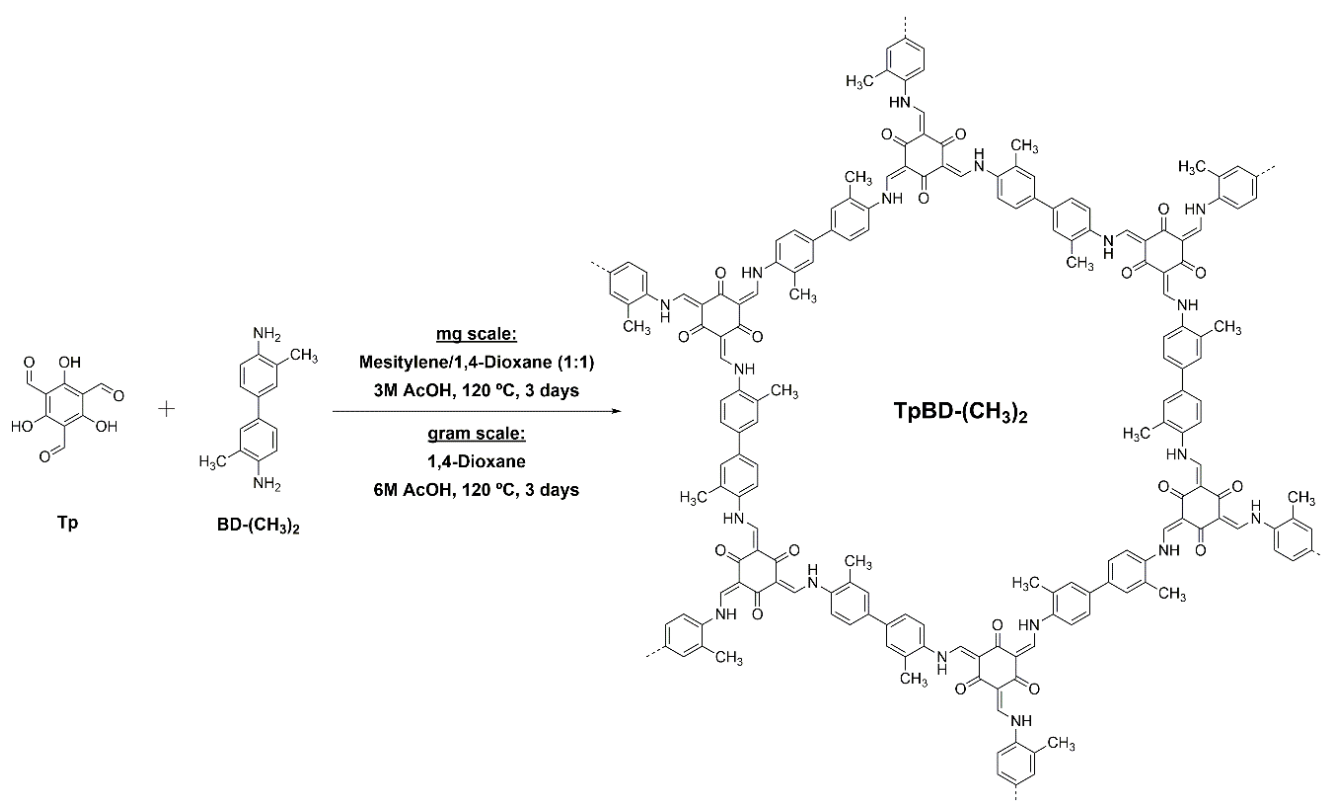
**Okadaic acid (OA)**

**MW ( $\text{g mol}^{-1}$ ) = 805.02**

**$LD_{50}$  ( $\mu\text{g kg}^{-1}$ , in mice) = 192**

**Figure 8.** Chemical structure of OA. Molecular weight and  $LD_{50}$  values.

Due to the lipophilic nature of OA, the literature-known water-stable TpBD-(CH<sub>3</sub>)<sub>2</sub> COF (Scheme 3) was chosen to be tested as adsorbent for OA capture from seawater. Hydrolytic stability<sup>[8]</sup> of the adsorbent material is fundamental and COFs based on Tp, first reported by Banerjee and co-workers,<sup>[82]</sup> have showed outstanding water stability in a wide pH range. Thus, we selected Tp-based COFs as the class to test for the adsorption of OA from water. In addition, the hydrophobic nature of the pores of TpBD-(CH<sub>3</sub>)<sub>2</sub> featuring methyl groups of building block *o*-tolidine (BD-(CH<sub>3</sub>)<sub>2</sub>) was expected to favor the adsorption of the lipophilic OA.



**Scheme 3.** Synthesis of TpBD-(CH<sub>3</sub>)<sub>2</sub> through reaction of Tp and *o*-tolidine (BD-(CH<sub>3</sub>)<sub>2</sub>).

First, the three-fold symmetric building block Tp was synthesized following a literature-known procedure<sup>[103]</sup> starting from phloroglucinol and hexamethylenetetramine in high degree of purity (31%), as assessed by <sup>1</sup>H NMR (for more details, see experimental section 5.2.1 and 5.4.1). Then, TpBD-(CH<sub>3</sub>)<sub>2</sub> was prepared on a milligram scale, in 83% yield, following a procedure reported by Banerjee and co-workers.<sup>[65]</sup> To this end, Tp and *o*-tolidine (BD-(CH<sub>3</sub>)<sub>2</sub>) were reacted in a 1:1 mixture of mesitylene and 1,4-dioxane at 120 °C for 3 days, in presence of 3M AcOH as catalyst (Scheme 3, for more details, see



experimental section 5.2.2). As revealed by SAXS (Figure 9A, red), a crystalline COF material was obtained exhibiting three main reflections at  $q = 2.4, 4.2,$  and  $18.5 \text{ nm}^{-1}$ , which correspond to  $d = 2.6, 1.5,$  and  $0.3 \text{ nm}$ , in good agreement with the reported data.<sup>[65]</sup> Nitrogen sorption measurements at 77 K gave a type I isotherm (Figure 9B, red) with a BET surface area of  $610 \text{ m}^2 \text{ g}^{-1}$  (Figure 84A, experimental section 5.4.2). The pore size distribution calculated using quenched-solid density functional theory (QSDFT) showed a large contribution of mesopores at  $2.0 \text{ nm}$  (Figure 84B, experimental section 5.4.2). These results are in good agreement with those reported for this COF material.<sup>[65]</sup> Further characterization was performed, in which by FT-IR (Figure 92, red curve, experimental section 5.4.3) the formation of  $\beta$ -ketoenamine linkage was confirmed through the appearance of typical bands of C=O, C=C, and C–N bonds at  $1618, 1578,$  and  $1252 \text{ cm}^{-1}$ , respectively. In addition, by TGA (Figure 97, experimental section 5.4.4) TpBD-(CH<sub>3</sub>)<sub>2</sub> was shown to exhibit high thermal stability up to  $300 \text{ }^\circ\text{C}$ .

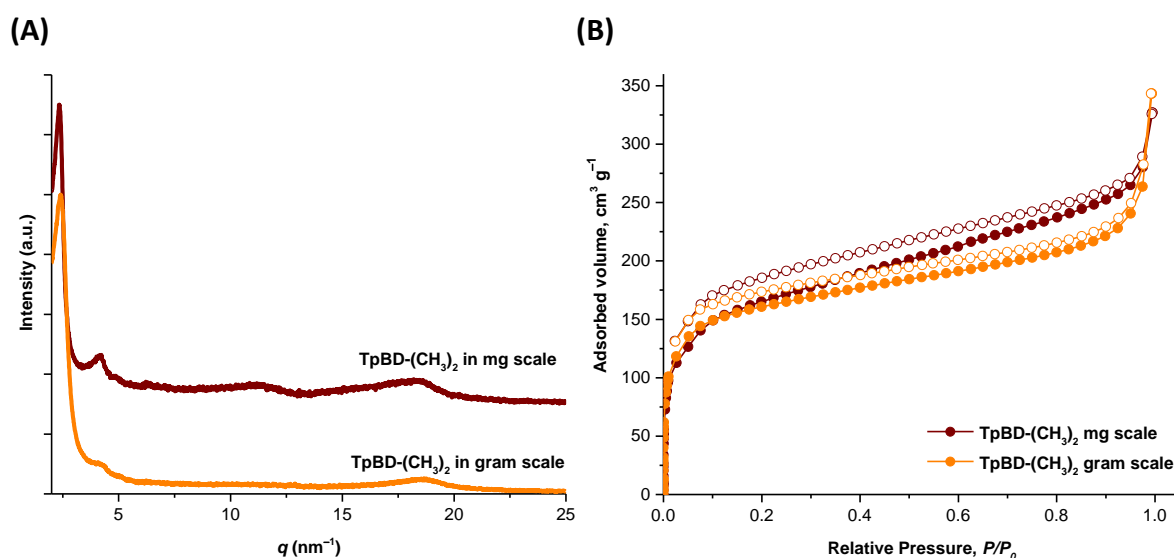


**Figure 9.** (A) SAXS pattern of TpBD-(CH<sub>3</sub>)<sub>2</sub> prepared in mg (red curve) and gram scale (orange curve). (B) N<sub>2</sub> adsorption (filled spheres) and desorption (hollow spheres) isotherm profiles measured at 77 K of the TpBD-(CH<sub>3</sub>)<sub>2</sub> prepared in mg (red curve) and gram scale (orange curve).

Afterwards, the synthesis of TpBD-(CH<sub>3</sub>)<sub>2</sub> was optimized to give access to the material on a gram scale. Changing the solvent to 1,4-dioxane and using 6M AcOH (3.1 equiv) as

catalyst (Scheme 3, for more details, see experimental section 5.2.3) resulted in crystalline material on a gram scale, in 40% yield (Figure 9A, orange curve). In SAXS, three main reflections at  $q = 2.4, 4.3,$  and  $18.8 \text{ nm}^{-1}$  were observed in good agreement with the reported data.<sup>[65]</sup> Similarly to its counterpart prepared in milligram scale, TpBD-(CH<sub>3</sub>)<sub>2</sub> showed by nitrogen sorption measurements at 77 K a type I isotherm (Figure 9B, orange curve), with a BET surface area of  $620 \text{ m}^2 \text{ g}^{-1}$  (Figure 85A, experimental section 5.4.2). Using QSDFT model, a large contribution of micropores at 1.1 and 1.5 nm were observed (Figure 85B, experimental section 5.4.2). By FT-IR the success of Schiff-base reaction formation was confirmed through the appearance of typical bands at 1620, 1580, and  $1258 \text{ cm}^{-1}$  attributed to C=O, C=C, and C–N linkages, respectively (Figure 92, orange curve, experimental section 5.4.3). Likewise to its counterpart prepared in milligram scale, TpBD-(CH<sub>3</sub>)<sub>2</sub> revealed high thermal stability up to 320 °C (Figure 98, experimental section 5.4.4). Thus, the access to TpBD-(CH<sub>3</sub>)<sub>2</sub> in gram scale with retention of the properties of the material is an advantage in view of application in the environmental field.

After the demonstrated quality of the synthesized COF, TpBD-(CH<sub>3</sub>)<sub>2</sub> was subjected to adsorption experiments with OA in synthetic seawater. Notwithstanding the reported water-stability of Tp-based COFs,<sup>[82]</sup> assessing the stability of TpBD-(CH<sub>3</sub>)<sub>2</sub> in seawater is very important to allow its use as adsorbent. The stability was studied by soaking the material in both ultrapure water and synthetic seawater for seven days (for more details, see experimental section 5.1.4). The SAXS patterns (Figure 10) compared to the pristine COF showed that the material is stable under these conditions, with crystallinity retained even when immersed in seawater. In addition, by SEM analysis, no evident morphological changes upon soaking were observed, with the wire-like morphology dominating in all samples (Figure 11).

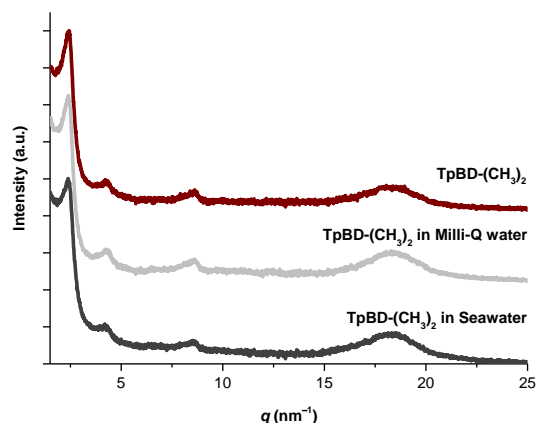


**Figure 10.** SAXS pattern comparison of pristine TpBD-(CH<sub>3</sub>)<sub>2</sub> (red curve), and after soaking for 7 days in ultrapure water (light grey curve) and synthetic seawater (dark grey curve).

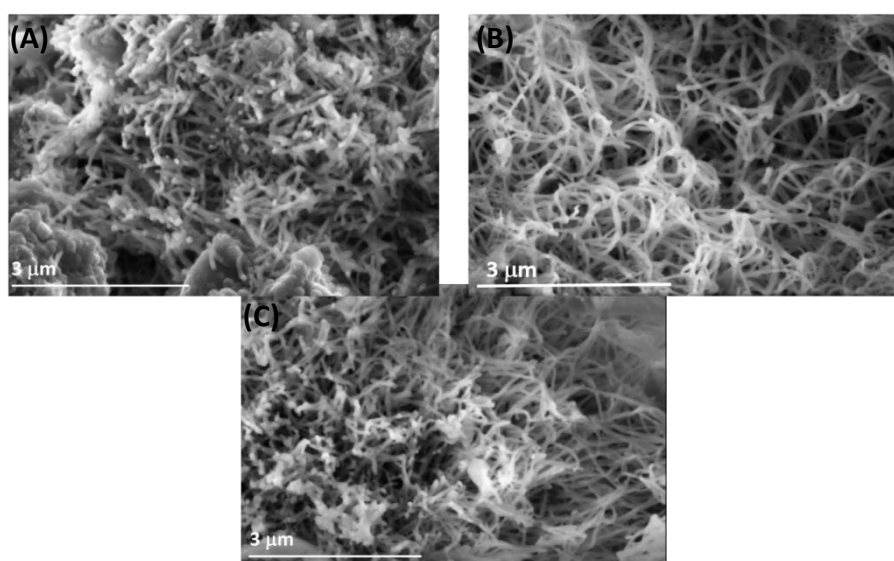


**Figure 11.** SEM images of TpBD-(CH<sub>3</sub>)<sub>2</sub> as synthesized (A), and after soaking for 7 days in ultrapure water (B) and in synthetic seawater (C).

Adsorption experiments using dispersions of 1 mg mL<sup>-1</sup> of TpBD-(CH<sub>3</sub>)<sub>2</sub> in synthetic seawater were performed with OA concentrations of 10, 15, 50, and 100 μmol L<sup>-1</sup>. Mixtures were incubated at different times of 0.5, 60, 240, and 480 min at 19 °C (for more details, see experimental section 5.3.1.3). The kinetic curves (Figure 12) show a fast adsorption phase during the first 60 min, which can be explained by the large initial surface area available for adsorption.<sup>[279]</sup> Thereafter, the adsorption reaches equilibrium between adsorption and desorption due to the process dynamics, as seen by the flattening of the curve. For a constant temperature, a higher initial concentration of adsorbate is expected

to imply a higher amount adsorbed,<sup>[280]</sup> which is the case of OA adsorption onto TpBD-(CH<sub>3</sub>)<sub>2</sub>. The adsorption is almost instantaneous, with half of the equilibrium amount of OA adsorbed within the first 15 min. Although the kinetic curves obtained in other studies on the adsorption of OA using chromatographic resins show the same profile as observed in this study for TpBD-(CH<sub>3</sub>)<sub>2</sub>, adsorption equilibrium was reached at 225 min using the HP-20 resin,<sup>[281]</sup> showing that adsorption by TpBD-(CH<sub>3</sub>)<sub>2</sub> is very fast.

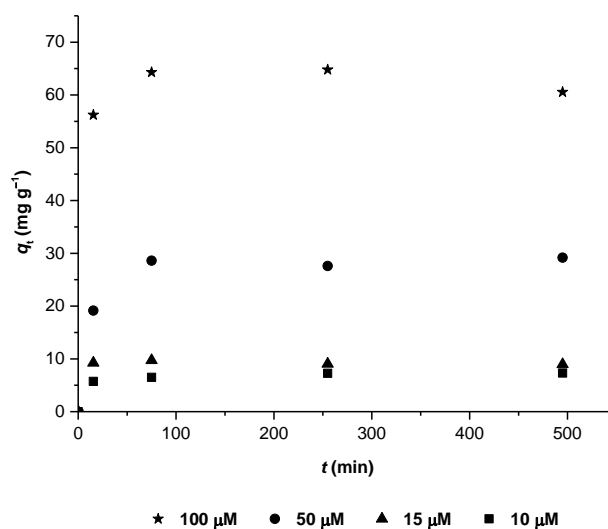


**Figure 12.** Adsorption kinetic curves of TpBD-(CH<sub>3</sub>)<sub>2</sub> expressed as quantity adsorbed,  $q_t$  (mg g<sup>-1</sup>), for initial OA concentrations of 10, 15, 50, and 100 μmol L<sup>-1</sup>, at 19 °C in synthetic seawater [ $C_0(\text{TpBD}-(\text{CH}_3)_2) = 1 \text{ mg mL}^{-1}$ ].

The adsorption isotherm at 19 °C was obtained by plotting the amount absorbed in equilibrium,  $q_e$ , against the concentration of OA in solution at equilibrium,  $C_e$ , (Figure 13A). The best fitting of the experimental data was found with the Freundlich model, with a correlation coefficient close to 1 (Figure 13B, Table 2). The constant  $n$  that reflects the degree of heterogeneity of the surface is higher than 1, indicating a favorable adsorption process. In addition,  $K_F$  is an indicator of adsorption capacity, so that the higher the value of  $K_F$ , the higher the maximum adsorption capacity. This constant decreases with increasing temperature,<sup>[280]</sup> and is also related to the strength of adsorbate–sorber interaction.<sup>[282]</sup> A  $K_F$  value of 22.08 mg<sup>0.421</sup> g<sup>-1</sup> L<sup>0.579</sup> was obtained for TpBD-(CH<sub>3</sub>)<sub>2</sub>. For HP-20,  $K_F$  of 27.46 μg<sup>0.112</sup> g<sup>-1</sup> L<sup>0.888</sup> was reported,<sup>[279]</sup> with different  $n$  values hindering the comparison

between the results.<sup>[283]</sup> The linear tendency of the isotherm indicates that the adsorbed amount is proportional to the equilibrium concentration of the solute in the solution. A linear isotherm is characteristic of homogeneous adsorbent surfaces and occurs at a low concentration. It also suggests that all the pores have the same affinity to OA.<sup>[279]</sup> Scarcity and high cost of the OA toxin standard prevented the expansion of the isotherm to higher concentrations to further confirm the applicability of the Freundlich model. The previously reported maximum capacities for OA adsorption of 1.639 and 1.088 mg g<sup>-1</sup> with the resins HP-20 and SP700, respectively, were calculated using equation 5 (for more details, see chapter 1, section 1.3.4). From the kinetic curve (Figure 12), a value of 60.6 mg g<sup>-1</sup> was obtained as the maximum amount of OA adsorbed when using the highest initial concentration of 100 μmol L<sup>-1</sup>, showing that TpBD-(CH<sub>3</sub>)<sub>2</sub> can adsorb 38 times more OA than HP-20. Using equation 5, a maximum adsorption capacity ( $q_m$ ) of 279 mg g<sup>-1</sup> was obtained for TpBD-(CH<sub>3</sub>)<sub>2</sub>, resulting in a 200-fold increase in comparison to previously reported value with styrene-based resin HP-20.<sup>[279]</sup>

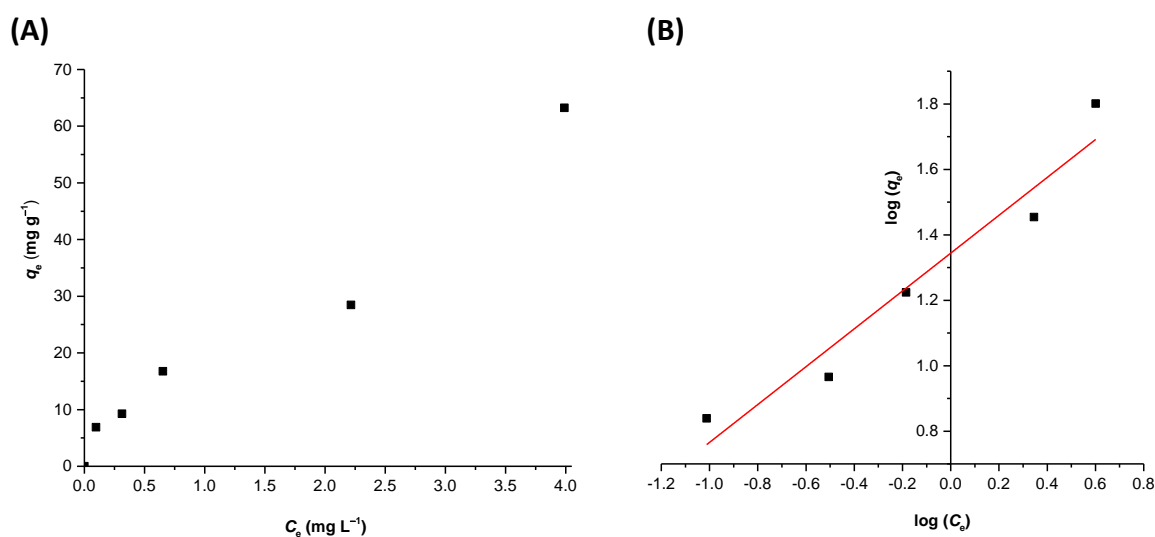


**Figure 13.** (A) Amount of OA adsorbed in equilibrium,  $q_e$  (mg g<sup>-1</sup>), as a function of OA concentration in equilibrium,  $C_e$  (mg L<sup>-1</sup>); (B) linear regression of the Freundlich isotherm for the experimental adsorption of OA by TpBD-(CH<sub>3</sub>)<sub>2</sub>.

**Table 2.** Freundlich isotherm equation constant and correlation coefficient derived from the graph in Figure 13B.

<i>Freundlich model</i>	
Regression equation	$\log q_e = (0.579 \pm 0.082)\log C_e + (1.344 \pm 0.049)$
$K_F$ ( $\text{mg}^{1-1/n} \text{g}^{-1} \text{L}^{1/n}$ )	$22.080 \pm 1.120$
$1/n$	$0.579 \pm 0.082$
$n$	1.727
$R^2$	0.9241

In order to be able to use TpBD-(CH<sub>3</sub>)<sub>2</sub> for OA monitoring, efficient desorption is of utmost importance. To this end, 70% ethanol was tested as solvent for desorption due to its chemical compatibility with both OA and TpBD-(CH<sub>3</sub>)<sub>2</sub>, resulting in about 80% of the adsorbed OA being recovered after a single incubation. Furthermore, desorption kinetic assays (for more details, see experimental section 5.3.1.4) showed that equilibrium is reached after 60 min of incubation (Figure 14), highlighting the suitability of the COF material as adsorbent in the SPATT application.

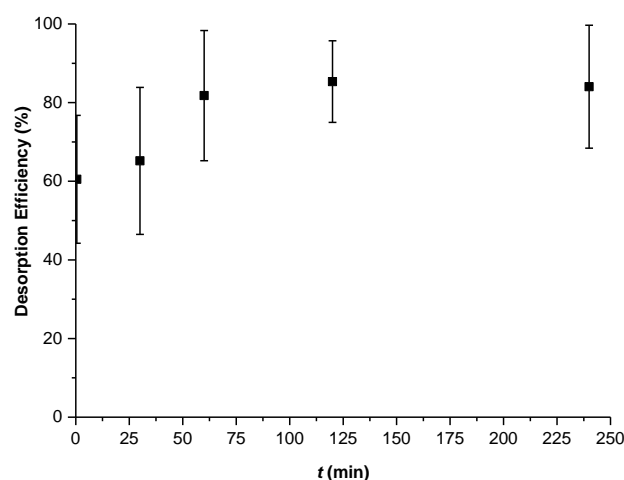


**Figure 14.** Desorption kinetic of OA from TpBD-(CH<sub>3</sub>)<sub>2</sub>, expressed in %, as an average of two independent experiments, performed in duplicates, in ethanol 70% at 4 °C [ $C_0(\text{TpBD}-(\text{CH}_3)_2) = 1 \text{ mg mL}^{-1}$ ;  $C_0(\text{OA}) = 10 \mu\text{mol L}^{-1}$ ]. Error bars correspond to the standard deviation of the mean.

To ascertain that the COF material can be reused is of utmost importance for environmental monitoring applications. To date, very few reports exist on the regeneration of resins used for toxin adsorption,<sup>[284]</sup> most probably due to the relatively low cost of the resins and the difficulties in performing cleaning efficiently. However, investigate their regeneration to allow for their implementation in monitoring programs was underlined.<sup>[285]</sup> Therefore, the reusability of TpBD-(CH<sub>3</sub>)<sub>2</sub> in consecutive cycles of OA adsorption/desorption was studied with an OA concentration of 10 μmol L<sup>-1</sup> using ethanol 70% as solvent for desorption (Figure 15, for more details, see experimental section 5.3.1.5). The amount of OA adsorbed by TpBD-(CH<sub>3</sub>)<sub>2</sub> remained stable at around 6 mg g<sup>-1</sup> in the first two cycles and was reduced to around 5.5 mg g<sup>-1</sup> in the third cycle, indicating a reduction in efficiency of merely 8%.

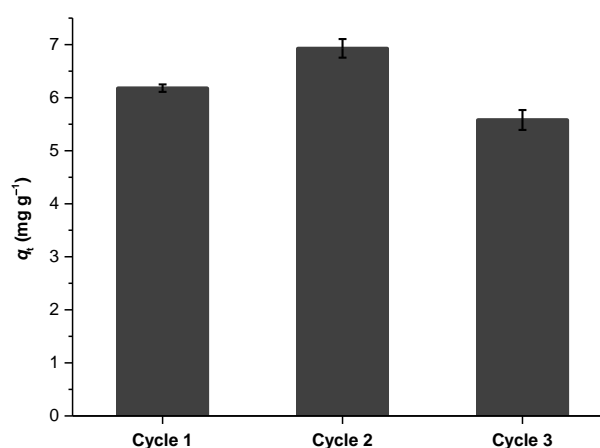


**Figure 15.** Reusability of TpBD-(CH<sub>3</sub>)<sub>2</sub> for OA, expressed as quantity adsorbed,  $q_t$  (mg g<sup>-1</sup>), in three consecutive cycles of adsorption/desorption, with an initial OA concentration of 10 μmol L<sup>-1</sup> in each of the adsorption cycles (seawater at 19 °C). Desorption was carried out using ethanol 70%. Results are expressed as the mean of duplicates. Error bars correspond to the standard deviation of the mean.

In conclusion, with this study the potential of COFs as efficient adsorbents for toxins in seawater was shown for the first time. TpBD-(CH<sub>3</sub>)<sub>2</sub> showed unprecedented performance in OA adsorption, as evidenced by the fast OA adsorption kinetics and the values for  $K_F$  and  $n$  constants obtained from the Freundlich isotherm in seawater. Additionally, OA was easily and efficiently desorbed from the COF, allowing the reuse of the material for at least three

cycles. Consequently, it was hypothesized that TpBD-(CH<sub>3</sub>)<sub>2</sub> could be used as a promising new adsorbent for the *in situ* concentration of OA dissolved in seawater to predict toxic outbreaks.

### 2.1.2. Microcystin (MC)<sup>[249]</sup>

MCs are the most commonly detected cyanotoxins in freshwater, and due to their toxicity, worldwide distribution, and persistence in water, an improvement in the monitoring programs for their early detection and removal from water is necessary.<sup>[183,188,189]</sup> To date, MC-LA, MC-LR, MC-RR, and MC-YR (Figure 16) have been identified as the most toxic and the most abundant in water worldwide.<sup>[183,188,189]</sup> Despite the diversity of the adsorbents reported, most studies focus only on the parental compound, MC-LR, leaving an important gap in the comprehensive understanding of the adsorption capacities for other highly relevant, frequent, and toxic analogues such as MC-RR, MC-YR, and MC-LA.<sup>[176,183]</sup> In addition, no relevant information have been reported on rational selection and performance evaluation of COFs for the adsorption and recovery of different molecules from water. To this end, the four most relevant MC analogues mentioned above were selected as target compounds to understand how COF functionalization can influence their adsorption process. All four chosen MCs have two ionizable carboxy groups ( $pK_a = 2.09, 2.19$ , Figure 16) and two variable amino acids (R' and R'', Figure 16). Arginine with one ionizable amino group ( $pK_a = 12.48$ ) is present in MC-LR, MC-RR, and MC-YR. At neutral pH, MC-LA, MC-LR, and MC-YR are anionic species, while MC-RR is zwitterionic. Furthermore, at this pH, MC-LA is the most lipophilic of the toxins ( $\log D_{pH7} = 0.67$ ) and MC-RR the most hydrophilic one ( $\log D_{pH7} = -0.68$ ). MCs were described to bind to the protein serine/threonine phosphatase, their cellular target, mainly through hydrogen bonding, which is of relevance for the choice of the COF functional groups.



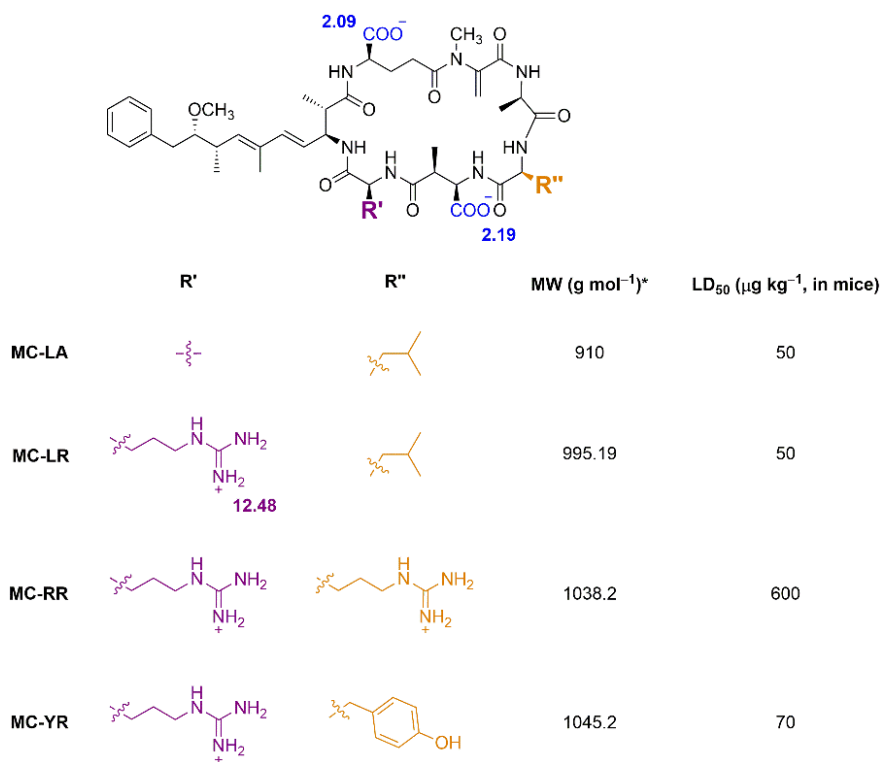


**Figure 16.** Chemical structures of MC-LA, -LR, -RR, -YR at neutral pH. Molecular weight and LD<sub>50</sub><sup>[184,185]</sup> values. \*Molecular weight of MCs at zero net charge.

In order to provide insight into COF–MCs interactions, three Tp-based COFs (Figure 17), TpBD-(CF<sub>3</sub>)<sub>2</sub>, TpBD-(NO<sub>2</sub>)<sub>2</sub>, and TpBD-(NH<sub>2</sub>)<sub>2</sub> were chosen as adsorbents for the adsorption of MC-LR, MC-LA, MC-RR, and MC-YR, from water. These three COFs were selected with the aim to cover both hydrophobic [TpBD-(CF<sub>3</sub>)<sub>2</sub>] and hydrophilic [TpBD-(NO<sub>2</sub>)<sub>2</sub>, and TpBD-(NH<sub>2</sub>)<sub>2</sub>] properties of materials, as well as to feature both hydrogen-bond-donating [TpBD-(NH<sub>2</sub>)<sub>2</sub>] and -accepting substituents [TpBD-(NO<sub>2</sub>)<sub>2</sub>].

The novel fluorine-bearing COF, TpBD-(CF<sub>3</sub>)<sub>2</sub>,<sup>[61]</sup> was designed and prepared from 3,3'-bis(trifluoromethyl)benzidine (BD-(CF<sub>3</sub>)<sub>2</sub>) and Tp (Scheme 4). In comparison to hydrogen in TpBD-(CH<sub>3</sub>)<sub>2</sub>, the high electronegativity and low polarizability of fluorine can result in dramatically different material properties,<sup>[286]</sup> such as enhanced light and air stability and low surface tension. In addition, fluorination of an aromatic ring with perfluoroalkyl groups, such as CF<sub>3</sub> groups, was shown to increase lipophilicity of molecules relative to hydrogen at the same position.<sup>[287]</sup> Facing the different lipophilic nature of

selected MCs, the synthesis of TpBD-(CF<sub>3</sub>)<sub>2</sub> was envisioned to obtain a COF material with higher lipophilic pore surface.

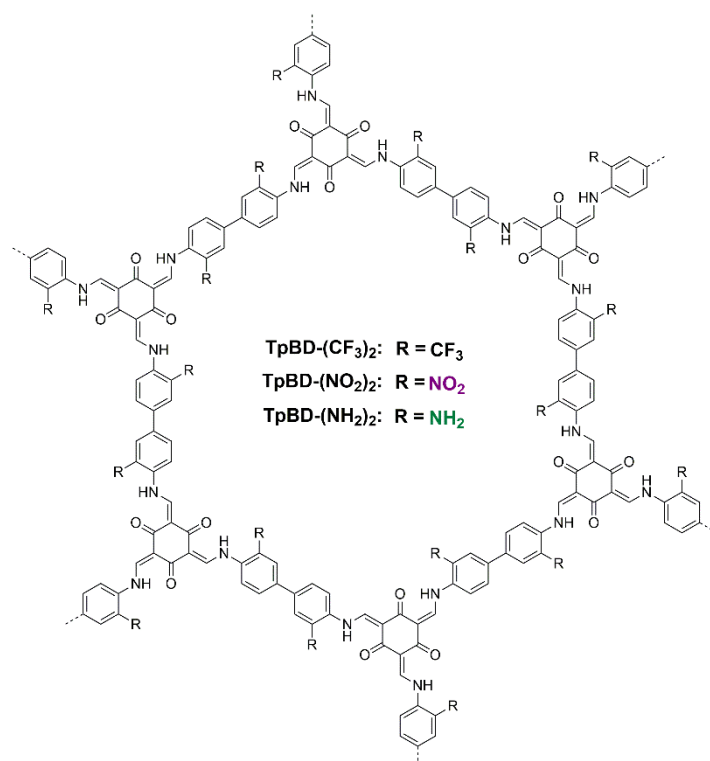
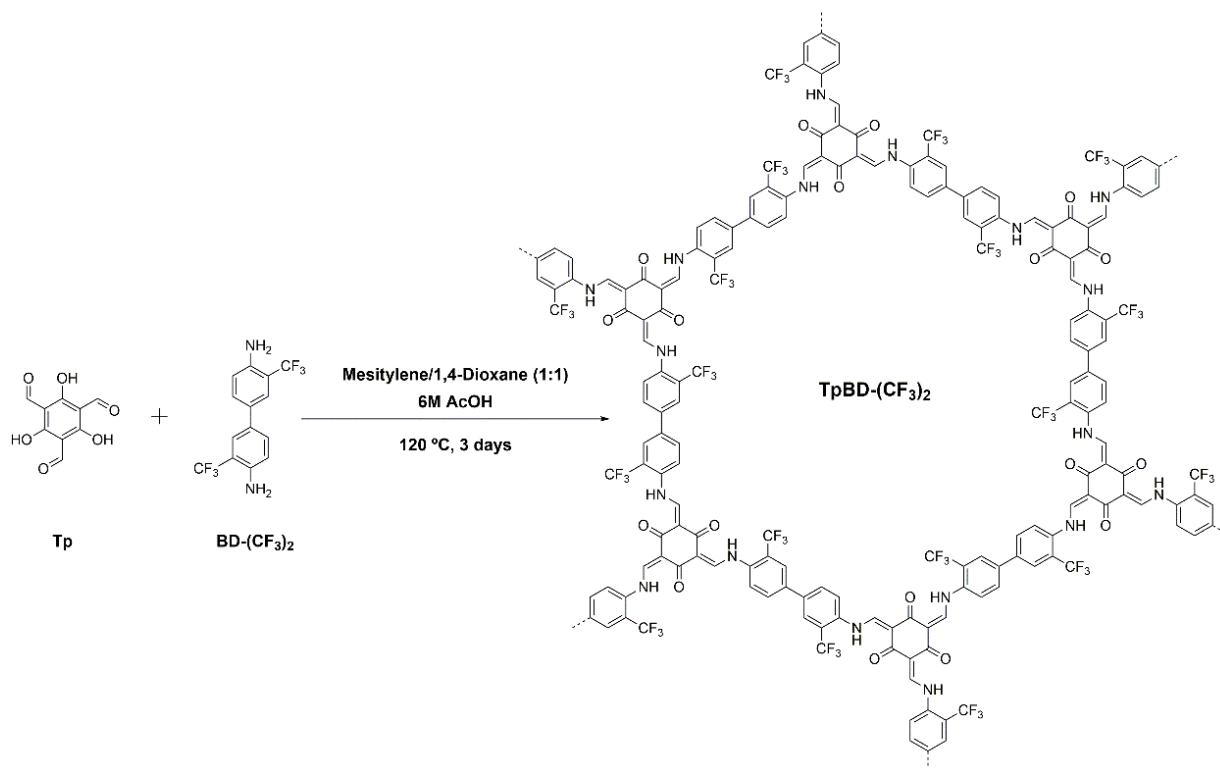


**Figure 17.** The structure of TpBD-(CF<sub>3</sub>)<sub>2</sub>, TpBD-(NO<sub>2</sub>)<sub>2</sub> and TpBD-(NH<sub>2</sub>)<sub>2</sub>.

TpBD-(CF<sub>3</sub>)<sub>2</sub> was synthesized from reaction of Tp with 1.5 equiv of 3,3'-bis(trifluoromethyl)benzidine (BD-(CF<sub>3</sub>)<sub>2</sub>), in 74% yield, from an equal mixture of mesitylene and 1,4-dioxane with aqueous 6M AcOH as catalyst at 120 °C for 3 days (Scheme 4, for more details, see experimental section 5.2.6). The PXRD pattern of TpBD-(CF<sub>3</sub>)<sub>2</sub> indicated the formation of an ordered porous structure (Figure 18A), with evident reflection at  $2\theta = 3.6^\circ$ , which is in good agreement with related COFs exhibiting similar pore dimensions and eclipsed AA COF layer arrangement.<sup>[58,65]</sup> In addition, we observed two broad reflections at about  $2\theta = 6^\circ$  and  $25^\circ$ , the latter of which is attributed to the interlayer distance.

Based on the functional groups and the geometry of TpBD-(CF<sub>3</sub>)<sub>2</sub>, precursor molecules and considering eclipsed AA COF layer arrangement, the possible unit cell and the corresponding powder diffraction pattern were simulated (carried out by collaborator

Dr. Medina at LMU Munich). The simulated unit cell (Figure 19) was constructed with the visualization environment of Materials Studio and the geometry was optimized using force field methods. The simulated diffraction pattern corresponds well with the experimental PXRD data (Figure 20).



**Scheme 4.** Synthesis of TpBD-(CF<sub>3</sub>)<sub>2</sub> from Tp and 3,3'-bis(trifluoromethyl)benzidine (BD-(CF<sub>3</sub>)<sub>2</sub>).

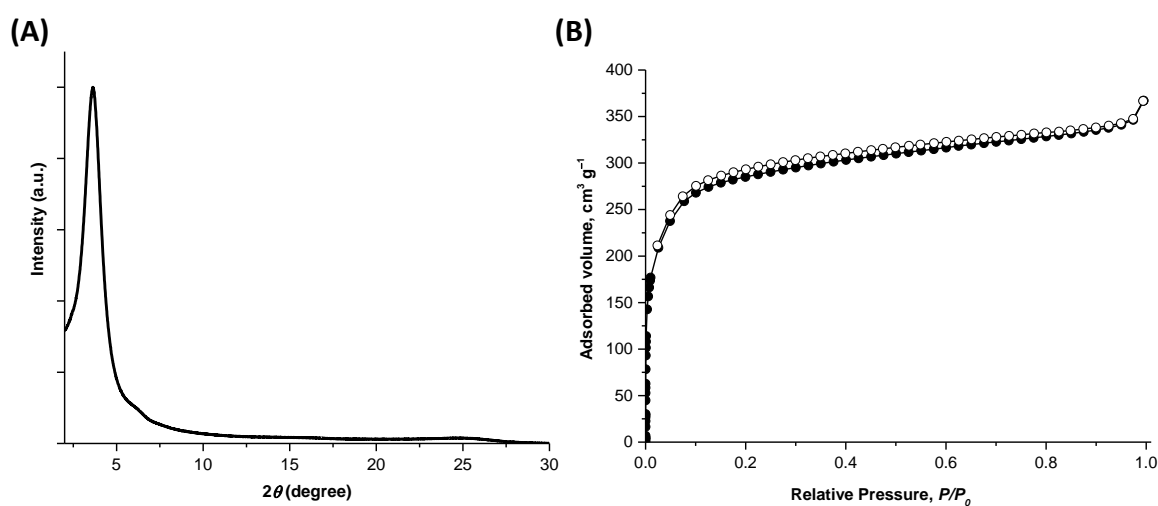


**Figure 18.** (A) PXRD pattern of TpBD-(CF<sub>3</sub>)<sub>2</sub>. (B) N<sub>2</sub> adsorption (filled spheres) and desorption (hollow spheres) isotherm profiles measured at 77 K of TpBD-(CF<sub>3</sub>)<sub>2</sub>.

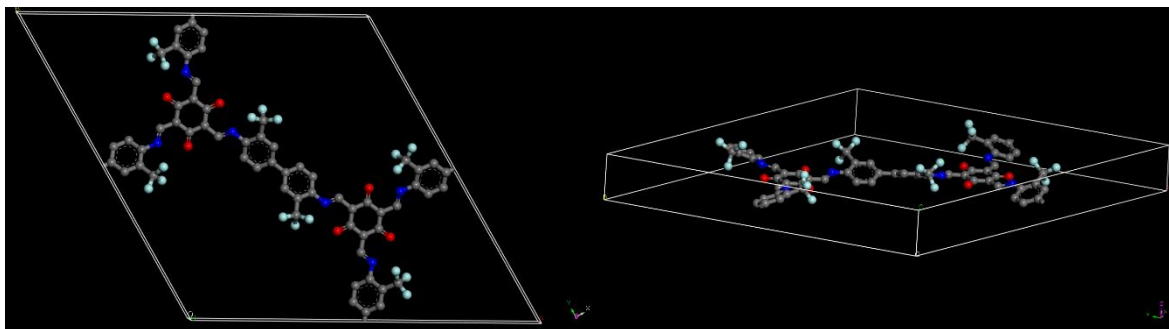


**Figure 19.** Simulation of the crystal unit cell calculated in an eclipsed AA arrangement in the P6 space group. Top: view on ab-plane; bottom: view along b-axis.

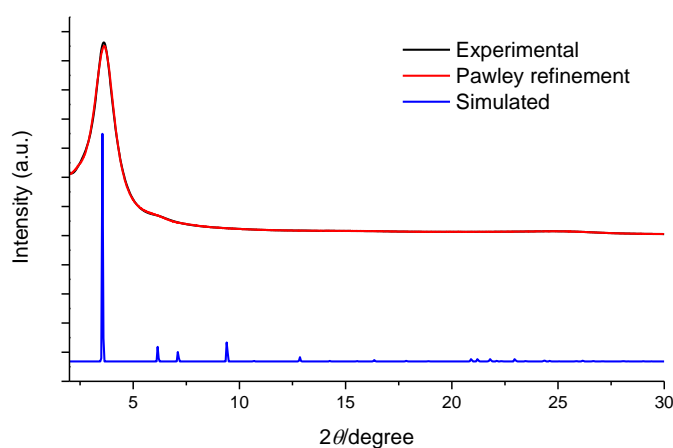


**Figure 20.** The experimentally obtained PXRD pattern of TpBD-(CF<sub>3</sub>)<sub>2</sub> (black), Pawley refinement (red), and the simulated PXRD pattern obtained by the Reflex module in Materials Studio based on an eclipsed AA arrangement.

Nitrogen sorption measurements at 77 K showed a rapid N<sub>2</sub> uptake at low pressures ( $P/P_0 < 0.05$ ), evidencing the microporosity of TpBD-(CF<sub>3</sub>)<sub>2</sub>. The COF showed a type I isotherm (Figure 18B) with a BET surface area of 870 m<sup>2</sup> g<sup>-1</sup> (Figure 88A, experimental section 5.4.2) and a pore volume of 0.50 cm<sup>3</sup> g<sup>-1</sup>. Pore size distribution calculated using QSDFT model showed a large micropore contribution (Figure 88B, experimental section 5.4.2). In the FT-IR spectrum of TpBD-(CF<sub>3</sub>)<sub>2</sub> bands were identified for C=O at 1626, for C=C at 1578, and for C–N at 1230 cm<sup>-1</sup> (Figure 94, black curve, experimental section 5.4.3), indicating the formation of the β-keto-enamine<sup>[103]</sup> linkage. In addition, the material showed thermal stability up to 307 °C under inert atmosphere (Figure 101, experimental

section 5.4.4). By water contact angle measurements a value of  $133^\circ$  (Figure 107A, experimental section 5.4.5) was found, highlighting the higher lipophilicity of TpBD-(CF<sub>3</sub>)<sub>2</sub> as compared to TpBD-(CH<sub>3</sub>)<sub>2</sub> (Figure 105, experimental section 5.4.5). In terms of surface morphology, by SEM TpBD-(CF<sub>3</sub>)<sub>2</sub> showed the presence of round-shaped particles, which could be agglomerates of smaller ones (Figure 21A).

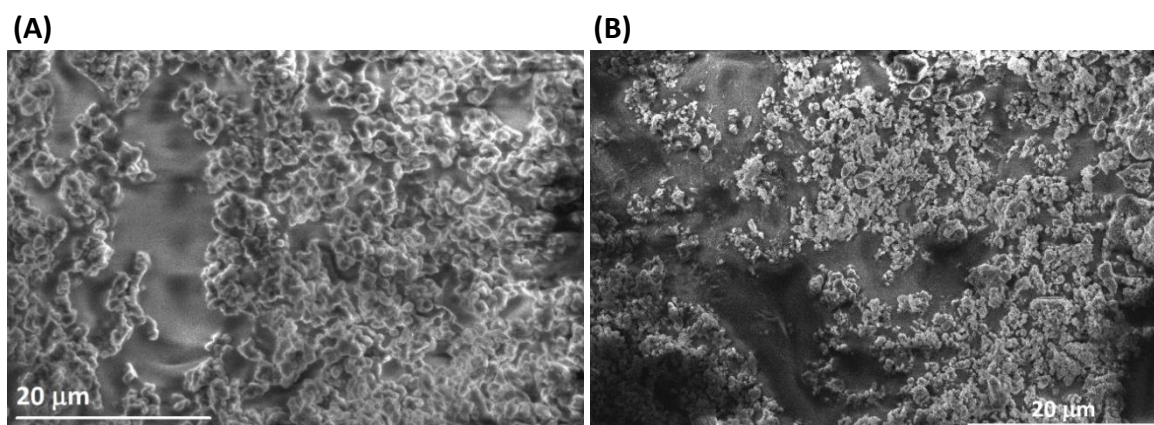


**Figure 21.** SEM images of TpBD-(CF<sub>3</sub>)<sub>2</sub> prepared in mg scale (A) and TpBD-(CF<sub>3</sub>)<sub>2</sub> prepared in gram scale (B).

Following the same conditions described above for mg scale synthesis, TpBD-(CF<sub>3</sub>)<sub>2</sub> was prepared on a gram scale, in 95% yield (for more details, see experimental section 5.2.7). SAXS analysis proved the formation of a crystalline COF structure (Figure 22A) through the appearance of two main reflections at scattering vector  $q = 2.5$  and  $17.6 \text{ nm}^{-1}$ , corresponding to  $d = 2.5$  and  $0.36 \text{ nm}$ , in good agreement with the data observed by PXRD on the mg scale. The material showed a type I isotherm (Figure 22B) with a BET surface area of  $987 \text{ m}^2 \text{ g}^{-1}$  and a pore volume of  $0.49 \text{ cm}^3 \text{ g}^{-1}$  (Figure 89A, experimental section 5.4.2). The pore size distribution calculated using QSDFT model showed a large contribution of micropores at  $0.5$  and  $1.2 \text{ nm}$ , as well as the presence of mesopores at  $2.0 \text{ nm}$  (Figure 89B, experimental section 5.4.2). This observation agrees with the values reported for its counterpart. FT-IR (Figure 94, blue curve, experimental section 5.4.3) evidenced the formation of the  $\beta$ -keto-enamine linkage. High thermal stability up to  $340^\circ \text{C}$  was found (Figure 102, experimental section 5.4.4) by TGA analysis. The high lipophilicity of TpBD-(CF<sub>3</sub>)<sub>2</sub> was reflected by the value of  $126^\circ$  in water contact angle measurements

(Figure 107B, experimental section 5.4.5). SEM images are in good agreement with the observed round-shaped structure of its counterpart (Figure 21B).

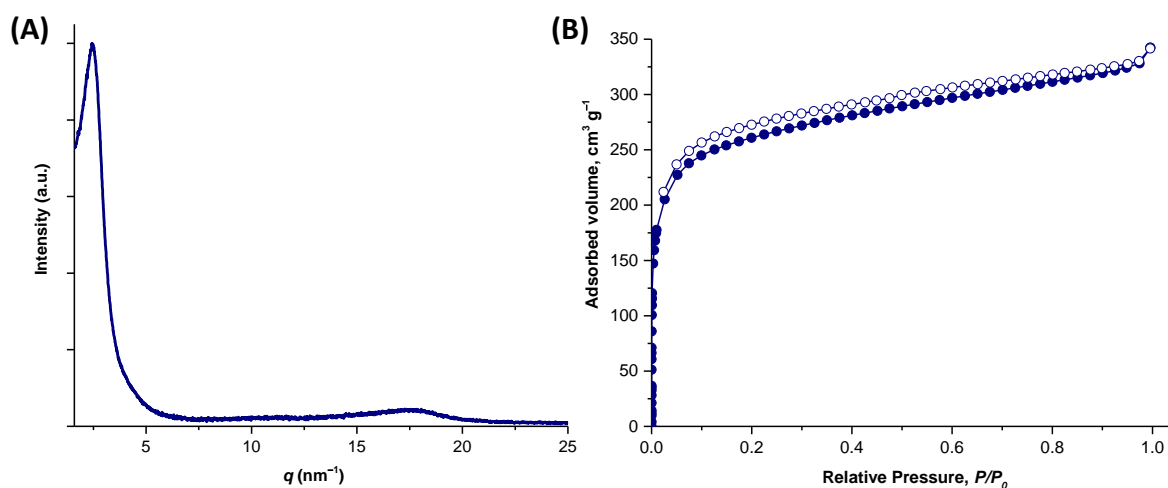
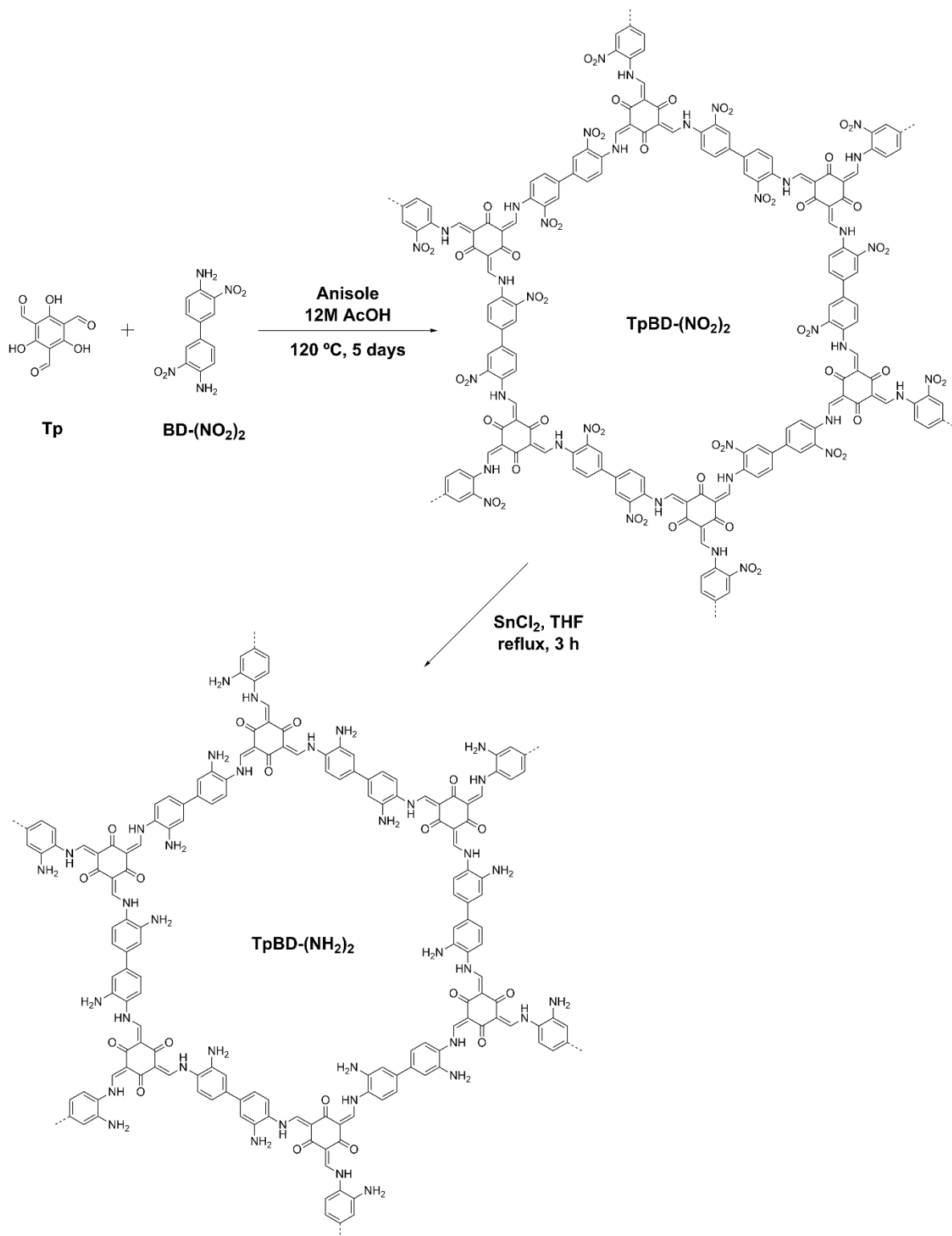


**Figure 22.** (A) SAXS pattern of  $\text{TpBD}-(\text{CF}_3)_2$  synthesized on a gram scale. (B)  $\text{N}_2$  adsorption (filled spheres) and desorption (hollow spheres) isotherm profiles measured at 77 K.

After optimization of  $\text{TpBD}-(\text{CF}_3)_2$  synthesis,  $\text{TpBD}-(\text{NO}_2)_2$  and  $\text{TpBD}-(\text{NH}_2)_2$  were targeted, envisioning the formation of hydrophilic COF materials as compared to  $\text{TpBD}-(\text{CF}_3)_2$ .  $\text{TpBD}-(\text{NO}_2)_2$  was prepared following a reported procedure<sup>[58]</sup> by reaction of Tp with 3,3'-dinitrobenzidine ( $\text{BD}-(\text{NO}_2)_2$ ) in anisole at 120 °C for 5 days, in 81% yield (Scheme 5, for more details, see experimental section 5.2.4). Then, as previously described,<sup>[58]</sup> by subsequent reduction of the nitro groups using  $\text{SnCl}_2$ ,  $\text{TpBD}-(\text{NH}_2)_2$  was obtained in 70% yield (Scheme 5, for more details, see experimental section 5.2.5).

As assessed by SAXS (Figure 23A), crystalline  $\text{TpBD}-(\text{NO}_2)_2$  and  $\text{TpBD}-(\text{NH}_2)_2$  materials were obtained. Four main reflections at scattering vector  $q = 2.4, 3.9, 6.8,$  and  $18.7 \text{ nm}^{-1}$  were obtained, corresponding to  $d = 2.62, 1.61, 0.92,$  and  $0.34 \text{ nm}$ , in good agreement with the reported data.<sup>[58]</sup>



**Scheme 5.** Synthesis of TpBD-(NO<sub>2</sub>)<sub>2</sub> from Tp and 3,3'-dinitrobenzidine (BD-(NO<sub>2</sub>)<sub>2</sub>), followed by a PSM reduction reaction to afford TpBD-(NH<sub>2</sub>)<sub>2</sub>.

Nitrogen sorption measurements at 77 K showed a rapid N<sub>2</sub> uptake at low pressure ( $P/P_0 < 0.05$ ), evidencing the microporosity of TpBD-(NO<sub>2</sub>)<sub>2</sub> and TpBD-(NH<sub>2</sub>)<sub>2</sub> (Figure 23B). BET surface areas of 439 and 391 m<sup>2</sup> g<sup>-1</sup> were obtained for TpBD-(NO<sub>2</sub>)<sub>2</sub> and TpBD-(NH<sub>2</sub>)<sub>2</sub>, respectively (Figure 86A and 87A, respectively for TpBD-(NO<sub>2</sub>)<sub>2</sub> and TpBD-(NH<sub>2</sub>)<sub>2</sub>, experimental section 5.4.2). By using QSDFT model, the pore size distribution was calculated showing a large micropores contribution and the presence of mesopores at 1.5 and 2.3 nm for TpBD-(NO<sub>2</sub>)<sub>2</sub>, and at 1.8 and 2.7 nm for TpBD-(NH<sub>2</sub>)<sub>2</sub> (Figure 86B and 87B, respectively for TpBD-(NO<sub>2</sub>)<sub>2</sub> and TpBD-(NH<sub>2</sub>)<sub>2</sub>, experimental section 5.4.2). These results are in agreement with those reported.<sup>[58]</sup>

The success of the reduction of the nitro groups of TpBD-(NO<sub>2</sub>)<sub>2</sub> was confirmed by FT-IR, where a strong decrease in the typical bands of NO<sub>2</sub> stretching vibrations at 1512 and 1336 cm<sup>-1</sup> was observed for TpBD-(NH<sub>2</sub>)<sub>2</sub>, with the appearance of an additional signal at 1255 cm<sup>-1</sup> attributed to the C–N stretching of the primary amine, confirming that the reduction had taken place (Figure 93, experimental section 5.4.3). Afterwards, the high hydrophilicity of TpBD-(NO<sub>2</sub>)<sub>2</sub> and TpBD-(NH<sub>2</sub>)<sub>2</sub>, when compared to the highly lipophilic TpBD-(CF<sub>3</sub>)<sub>2</sub>, was demonstrated by the values of 15° and 6.3°, respectively, obtained in water contact angle measurements (Figure 106A and 106B, respectively for TpBD-(NO<sub>2</sub>)<sub>2</sub> and TpBD-(NH<sub>2</sub>)<sub>2</sub>, experimental section 5.4.5). Moreover, by TGA, TpBD-(NO<sub>2</sub>)<sub>2</sub> and TpBD-(NH<sub>2</sub>)<sub>2</sub> showed a thermal stability up to 300 and 280 °C, respectively, under inert atmosphere (Figure 99 and 100, respectively for TpBD-(NO<sub>2</sub>)<sub>2</sub> and TpBD-(NH<sub>2</sub>)<sub>2</sub>, experimental section 5.4.4). In addition, SEM images showed the presence of ribbon-like structures for both COFs (Figure 108A and 108B, respectively for TpBD-(NO<sub>2</sub>)<sub>2</sub> and TpBD-(NH<sub>2</sub>)<sub>2</sub>, experimental section 5.4.6).



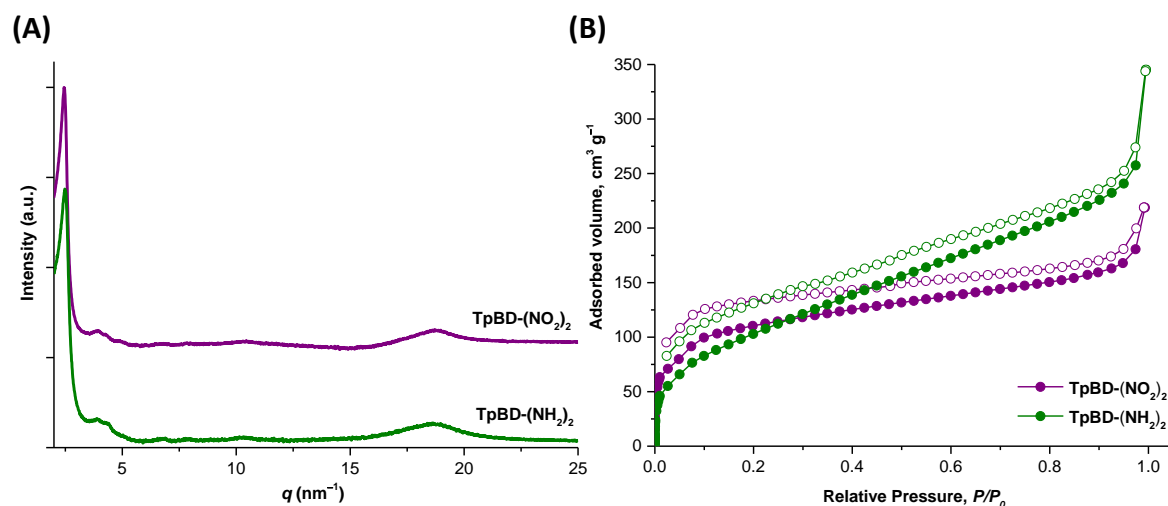


**Figure 23.** (A) SAXS pattern of TpBD-(NO<sub>2</sub>)<sub>2</sub> (purple curve) and TpBD-(NH<sub>2</sub>)<sub>2</sub> (green curve). (B) N<sub>2</sub> adsorption (filled spheres) and desorption (hollow spheres) isotherm profiles measured at 77 K of TpBD-(NO<sub>2</sub>)<sub>2</sub> (purple curve) and TpBD-(NH<sub>2</sub>)<sub>2</sub> (green curve).

After having in hand crystalline TpBD-(CF<sub>3</sub>)<sub>2</sub>, TpBD-(NO<sub>2</sub>)<sub>2</sub>, and TpBD-(NH<sub>2</sub>)<sub>2</sub> materials, adsorption experiments of MC-LA, MC-LR, MC-RR, or MC-YR from water were performed. First, the adsorption capacity,  $q_e$  ( $\text{mg g}^{-1}$ , Table 3), was experimentally determined by performing independent adsorption tests using aqueous dispersions of 1  $\text{mg mL}^{-1}$  of TpBD-(CF<sub>3</sub>)<sub>2</sub>, TpBD-(NO<sub>2</sub>)<sub>2</sub>, or TpBD-(NH<sub>2</sub>)<sub>2</sub>, spiked with 10  $\mu\text{mol L}^{-1}$  of MC-LA, MC-LR, MC-RR, or MC-YR. Individual mixtures were incubated at 19 °C under constant shaking at 1400 rpm for 4 h to ensure that equilibrium was reached (for more details, see experimental section 5.3.2.4). The results (Figure 24A) revealed that MC-LR (red) and MC-YR (purple) are efficiently adsorbed from water by all three COF derivatives, with adsorption efficiencies above 75%. In the case of MC-LA (grey), the adsorption efficiency decreases in the following order: TpBD-(NH<sub>2</sub>)<sub>2</sub> (94%) > TpBD-(CF<sub>3</sub>)<sub>2</sub> (73%) > TpBD-(NO<sub>2</sub>)<sub>2</sub> (40%). The lower efficiency of TpBD-(NO<sub>2</sub>)<sub>2</sub> could stem from electrostatic repulsions between the COF surface and the only charged moieties in MC-LA, the backbone carboxylic groups. In contrast, such repulsion would not be present in TpBD-(NH<sub>2</sub>)<sub>2</sub>, possibly justifying the higher adsorption efficiency exhibited by this COF derivative. MC-RR (blue) was much more efficiently adsorbed by TpBD-(NO<sub>2</sub>)<sub>2</sub> (69%) than by TpBD-(CF<sub>3</sub>)<sub>2</sub> (30%) or TpBD-(NH<sub>2</sub>)<sub>2</sub> (22%). This preference could result from the formation of hydrogen bonds between the

nitro groups of TpBD-(NO<sub>2</sub>)<sub>2</sub> and the guanidinium moieties of MC-RR. In fact, all tested MCs with arginine residues showed good adsorption efficiencies (68–85%) with TpBD-(NO<sub>2</sub>)<sub>2</sub>, supporting this hypothesis.

**Table 3.** Amount of MC-LA, MC-LR, MC-RR, and MC-YR adsorbed and desorbed in equilibrium,  $q_e$  (mg g<sup>-1</sup>), by TpBD-(CF<sub>3</sub>)<sub>2</sub>, TpBD-(NO<sub>2</sub>)<sub>2</sub>, and TpBD-(NH<sub>2</sub>)<sub>2</sub> COF.

	MC-LA		MC-LR		MC-RR		MC-YR	
	Adsorption $q_e$	Desorption $q_e$	Adsorption $q_e$	Desorption $q_e$	Adsorption $q_e$	Desorption $q_e$	Adsorption $q_e$	Desorption $q_e$
<b>TpBD-(CF<sub>3</sub>)<sub>2</sub></b>	6.62 ± 0.3	1.38 ± 0.47	7.76 ± 0.38	2.01 ± 1.3	3.43 ± 0.49	1.35 ± 0.47	9.24 ± 0.34	7.41 ± 1.01
<b>TpBD-(NO<sub>2</sub>)<sub>2</sub></b>	3.62 ± 1.42	0.93 ± 0.62	8.29 ± 0.17	1.81 ± 1.42	7.12 ± 0.59	0.06 ± 0.04	8.85 ± 0.29	2.52 ± 1.44
<b>TpBD-(NH<sub>2</sub>)<sub>2</sub></b>	8.58 ± 0.07	5.71 ± 1.28	8.82 ± 0.06	3.69 ± 1.73	2.26 ± 0.89	0.21 ± 0.04	9.62 ± 0.1	7.84 ± 1.06

To gain an understanding of the interaction mechanism between the COFs and the MCs, molecular dynamics simulations were performed (carried out by collaborator Dr. Kovář and Dr. Pšenička at Charles University, in Czech Republic; for more details, see experimental section 5.1.3.1). Due to the opposite behavior they showed in the adsorption on the COFs, the interactions in the systems of MC-LA and MC-RR with TpBD-(CF<sub>3</sub>)<sub>2</sub>, TpBD-(NO<sub>2</sub>)<sub>2</sub>, and TpBD-(NH<sub>2</sub>)<sub>2</sub> were chosen to be studied. For each system, a set of independent models was built and the corresponding value of adsorption energy (Table 4, for more details, see experimental section 5.1.3.1) was calculated and compared to the experimentally obtained  $q_e$  values (Table 3).

In all MC-LA model systems, quite a tight arrangement of the toxin on the COF structure was found, with the shortest distance of about 2–3 Å between MC-LA and the COF atoms. Of all COFs studied, the lowest adsorption energy value of –16.41 kcal mol<sup>-1</sup> (Table 4) was observed for MC-LA with TpBD-(NH<sub>2</sub>)<sub>2</sub>. This value correlates with the highest adsorption efficiency found for MC-LA ( $q_e = 8.58$  mg g<sup>-1</sup>) with TpBD-(NH<sub>2</sub>)<sub>2</sub>. In the computational model, MC-LA has the tendency to be oriented on the surface of TpBD-(NH<sub>2</sub>)<sub>2</sub> above the Tp linker and partially in the cavity formed by NH<sub>2</sub>, Tp, and NH

moieties of the COF (Figure 110, experimental section 5.4.7), at a closest distance of about 2 Å.

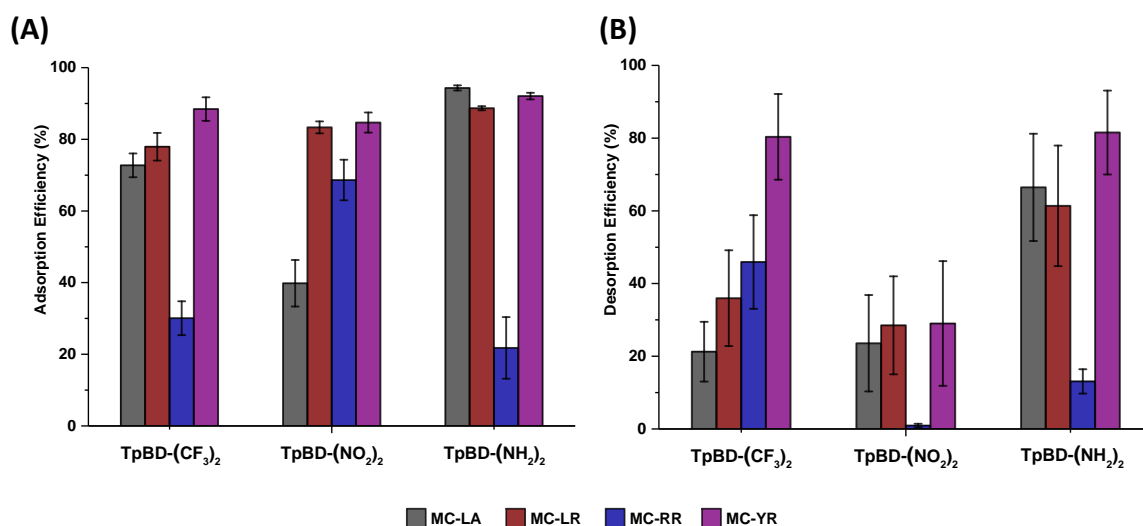


**Figure 24.** Quantification of the MC-LA, MC-LR, MC-RR, and MC-YR adsorption (A) and desorption (B) efficiencies (%) onto TpBD-(CF<sub>3</sub>)<sub>2</sub>, TpBD-(NO<sub>2</sub>)<sub>2</sub>, and TpBD-(NH<sub>2</sub>)<sub>2</sub>, as an average of three independent experiments, performed in duplicates, in ultrapure water at 19 °C and pH 6–7 and propan-2-ol at 4 °C, respectively ( $C_0(\text{COF}) = 1 \text{ mg mL}^{-1}$ ;  $C_0(\text{MCs}) = 10 \text{ } \mu\text{mol L}^{-1}$ ). Error bars correspond to the standard deviation of the mean.

Hydrogen bonds are formed between the carbonyl groups of MC-LA and amino moieties of the COF pore (Figure 25). Models with partial or full immersion of MC-LA into the COF pore exhibited by 4–6 kcal mol<sup>-1</sup> higher adsorption energy than the model with MC-LA preferentially oriented on the COF surface, suggesting that the toxin is mainly interacting with the COF surface without penetrating the pores. However, the adsorption energy of the partially/fully immersed model of MC-LA is still negative enough for a part of the toxin molecules to possibly reside within the COF pores (Figure 110, experimental section 5.4.7). In the case of TpBD-(CF<sub>3</sub>)<sub>2</sub>, very similar adsorption energy values were found for models with MC-LA on the surface and inside the COF pore. The least favorable adsorption energy was found for MC-LA with TpBD-(NO<sub>2</sub>)<sub>2</sub> (−9.35 kcal mol<sup>-1</sup>), which correlates with the experimentally observed lowest amount adsorbed ( $q_e = 3.62 \text{ mg g}^{-1}$ ). In the computational model, the polar groups of MC-LA were located on the COF surface and

the less polar chain containing the phenyl ring is immersed in the COF pore. For the model where no part of MC-LA is located on the COF surface and practically the whole toxin is immersed in the COF pore, the calculated adsorption energy is close to 0 (ca.  $-1 \text{ kcal mol}^{-1}$ ), indicating that MC-LA preferentially resides on the surface of TpBD-(NO<sub>2</sub>)<sub>2</sub>.

**Table 4.** Adsorption energy values ( $\text{kcal mol}^{-1}$ ) of the MC-LA and MC-RR models with TpBD-(CF<sub>3</sub>)<sub>2</sub>, TpBD-(NO<sub>2</sub>)<sub>2</sub>, and TpBD-(NH<sub>2</sub>)<sub>2</sub>.<sup>a</sup>

Model system		$E_{\text{ads}}$ ( $\text{Kcal mol}^{-1}$ )	$q_e$ ( $\text{mg g}^{-1}$ )
COF	MCs		
TpBD-(CF <sub>3</sub> ) <sub>2</sub>	MC-LA	-11.31	6.62
TpBD-(NO <sub>2</sub> ) <sub>2</sub>	MC-LA	-9.35	3.62
TpBD-(NH <sub>2</sub> ) <sub>2</sub>	MC-LA	-16.41	8.58
TpBD-(CF <sub>3</sub> ) <sub>2</sub>	MC-RR	-8.81	3.43
TpBD-(NO <sub>2</sub> ) <sub>2</sub>	MC-RR	-14.21	7.12
TpBD-(NH <sub>2</sub> ) <sub>2</sub>	MC-RR	-4.51	2.26

<sup>a</sup>A correlation coefficient between the experimentally observed amount adsorbed,  $q_e$ , by each model and the corresponding adsorption energy is  $\approx 0.95$ .

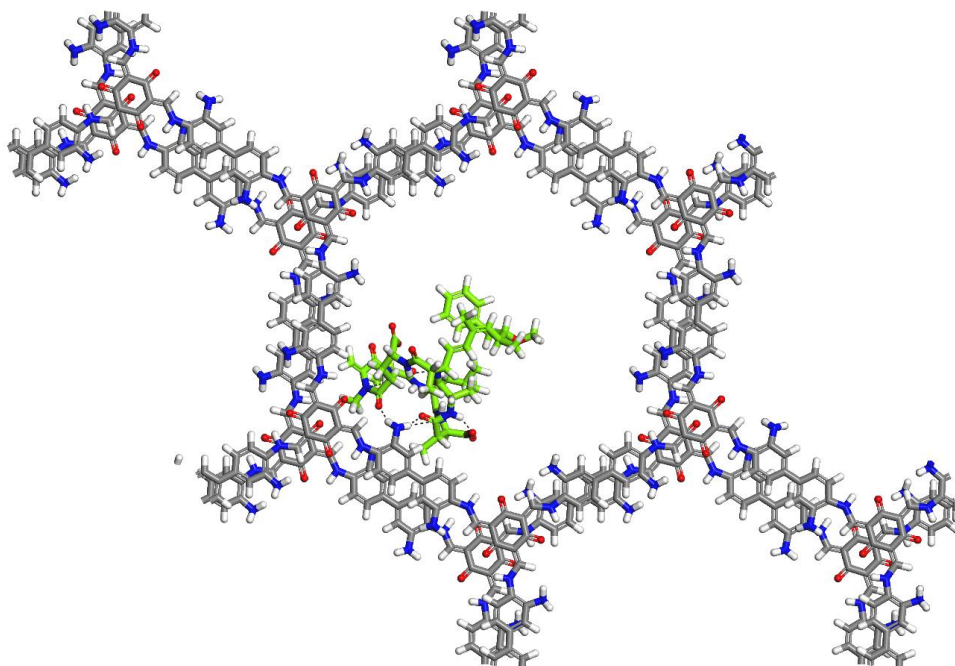


**Figure 25.** A top view along z axis of the atomistic model of MC-LA with TpBD-(NH<sub>2</sub>)<sub>2</sub>. Reprinted with permission from Ref. [249]. Copyright 2021, American Chemical Society.

Regarding MC-RR adsorption mechanism, from all simulated MC-RR model systems, the most favorable adsorption energy value of  $-14.21 \text{ kcal mol}^{-1}$  (Table 4) was obtained with TpBD-(NO<sub>2</sub>)<sub>2</sub>, which agrees with the experimentally observed highest amount adsorbed from water ( $q_e = 7.12 \text{ mg g}^{-1}$ ). Calculations showed that the arginine moieties of MC-RR are located on the COF surface (Figure 26) with the tendency to interact with the nitro functional groups of the COF, with the closest distance of about 2.5 Å between the functional groups. The less polar chain of the toxin containing the phenyl ring is immersed in the COF pore. The adsorption energy is less favorable by about 3 kcal mol<sup>-1</sup> when MC-RR is completely immersed in the COF pore, indicating that the toxins will be located mainly on the COF surface, possibly partially residing in the COF pores with the tendency to interact with TpBD-(NO<sub>2</sub>)<sub>2</sub> through hydrogen-bonding interactions (Figure 111, experimental section 5.4.7). For TpBD-(CF<sub>3</sub>)<sub>2</sub> and TpBD-(NH<sub>2</sub>)<sub>2</sub>, MC-RR tends to be located mainly in the COF pore, with none or rather few contacts between the arginine moieties of MC and the fluorine or amino functional group of the COFs, with lowest affinity ( $-8.81 \text{ kcal mol}^{-1}$  and  $-4.51 \text{ kcal mol}^{-1}$  for TpBD-(CF<sub>3</sub>)<sub>2</sub> and TpBD-(NH<sub>2</sub>)<sub>2</sub>, respectively). The observed least favorable adsorption energies correlate with the experimentally observed lowest amount adsorbed of 3.43 and 2.26 mg g<sup>-1</sup> for TpBD-(CF<sub>3</sub>)<sub>2</sub> and TpBD-(NH<sub>2</sub>)<sub>2</sub>, respectively. The adsorption energy of MC-RR stems nearly completely from van der Waals interactions.

Afterwards, as TpBD-(CF<sub>3</sub>)<sub>2</sub> adsorbed efficiently all four MC analogues, kinetic studies of adsorption were performed at different contact times,  $t$  (min), and concentrations of MCs of 1, 5, 10, and 15 μmol L<sup>-1</sup> at 19 °C in ultrapure water (for more details, see experimental section 5.3.2.3). For the parental compound MC-LR, an increase in the initial concentration of MC-LR from 10 to 15 and 25 μmol L<sup>-1</sup> resulted in a decrease of almost 30% of the adsorption efficiency (Figure 27A), with the equilibrium reached in 100 min. The fastest adsorption rate was obtained for MC-YR with equilibrium reached after 10 min (Figure 57C, experimental section 5.3.2.3, and Table 5), while all other toxins showed a slow initial phase of adsorption reaching equilibrium only after 100–120 min. After, considering that TpBD-(NO<sub>2</sub>)<sub>2</sub> and TpBD-(NH<sub>2</sub>)<sub>2</sub> had the best performance in the adsorption of MC-RR and MC-LA, respectively, kinetic studies of adsorption were performed as described above. In the case of MC-LA with TpBD-(NH<sub>2</sub>)<sub>2</sub>, at all concentrations tested, equilibrium was

reached very quickly, in 10 min, with more than 90% adsorbed at concentrations of 1, 5, and 10  $\mu\text{mol L}^{-1}$  (Figure 27B). The increase in the initial concentration of the adsorbate was directly proportional to the amount adsorbed, with high adsorption efficiencies observed at 15  $\mu\text{mol L}^{-1}$  and even at 25  $\mu\text{mol L}^{-1}$  of MC-LA, with more than 70% of MC-LA adsorbed in equilibrium, indicating that saturation of the adsorbent was not attained.

For TpBD-(NO<sub>2</sub>)<sub>2</sub>, at low MC-RR concentration of 1  $\mu\text{mol L}^{-1}$ , the equilibrium was reached very fast (5 min) (Figure 27C). At higher initial concentrations, the time needed to reach the equilibrium increased to 100 min and adsorption efficiency decreased progressively to 57% and 35% for 15 and 25  $\mu\text{mol L}^{-1}$ , respectively, indicating that the saturation of the adsorbent was nearly attained. In virtue of the much faster adsorption process of MC-LA with TpBD-(NH<sub>2</sub>)<sub>2</sub> as compared to that of MC-RR with TpBD-(NO<sub>2</sub>)<sub>2</sub>, we calculated the interaction energies in microcystin-water models, in order to understand this phenomenon. In the case of MC-LA, the interaction energy with water was  $-386 \pm 7 \text{ kcal mol}^{-1}$ , while for MC-RR a value of about  $-420 \pm 7 \text{ kcal mol}^{-1}$  was obtained, indicating a higher tendency of MC-RR to be solvated by water. This difference in the interaction energy with water together with the slightly higher adsorption energy value of MC-LA with TpBD-(NH<sub>2</sub>)<sub>2</sub> could account for the higher rate of MC-LA adsorption onto the COF.

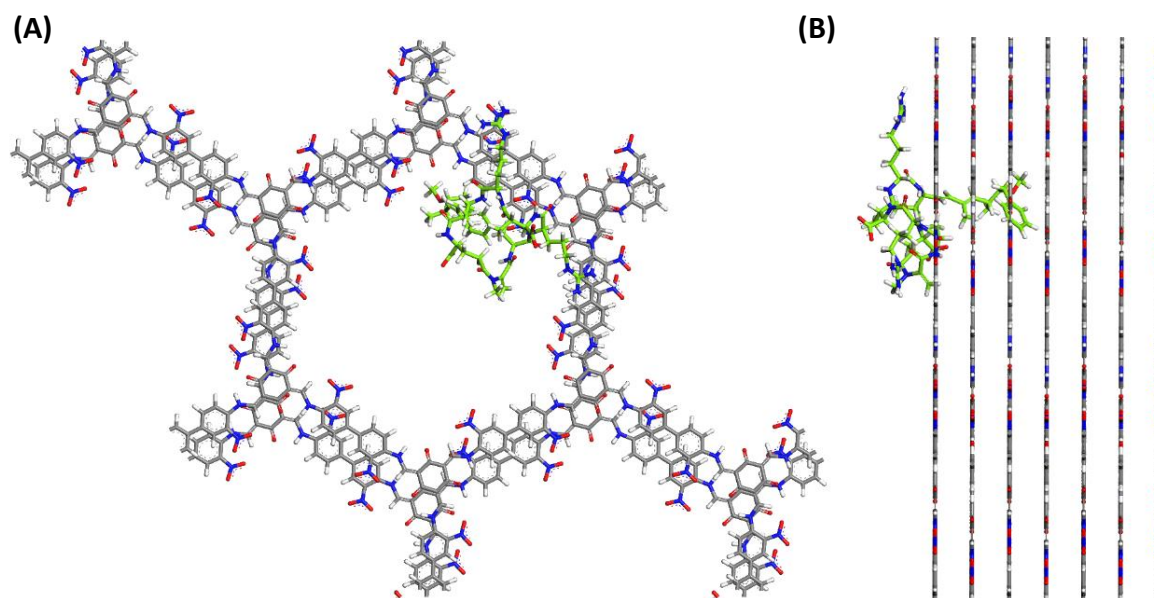


**Figure 26.** A top view along z axis (A) and side view along x axis (B) of the atomistic model of MC-RR with TpBD-(NO<sub>2</sub>)<sub>2</sub>, located on the surface of COF. Reprinted with permission from Ref. [249]. Copyright 2021, American Chemical Society.

**Table 5.** Rate of adsorption of MC-LA, MC-LR, MC-RR, and MC-YR in COF derivatives until reaching the equilibrium of adsorption.

	TpBD-(CF <sub>3</sub> ) <sub>2</sub>		TpBD-(NO <sub>2</sub> ) <sub>2</sub>		TpBD-(NH <sub>2</sub> ) <sub>2</sub>	
	Equilibrium time (min)	Slope initial adsorption	Equilibrium time (min)	Slope initial adsorption	Equilibrium time (min)	Slope initial adsorption
MC-LA	120	0.01772 ± 0.00067			10	0.03798 ± 0.00121
MC-LR	100	0.04152 ± 0.00454				
MC-RR	100	0.03287 ± 0.0059	100	0.04372 ± 0.01064		
MC-YR	10	0.06691 ± 0.02807				

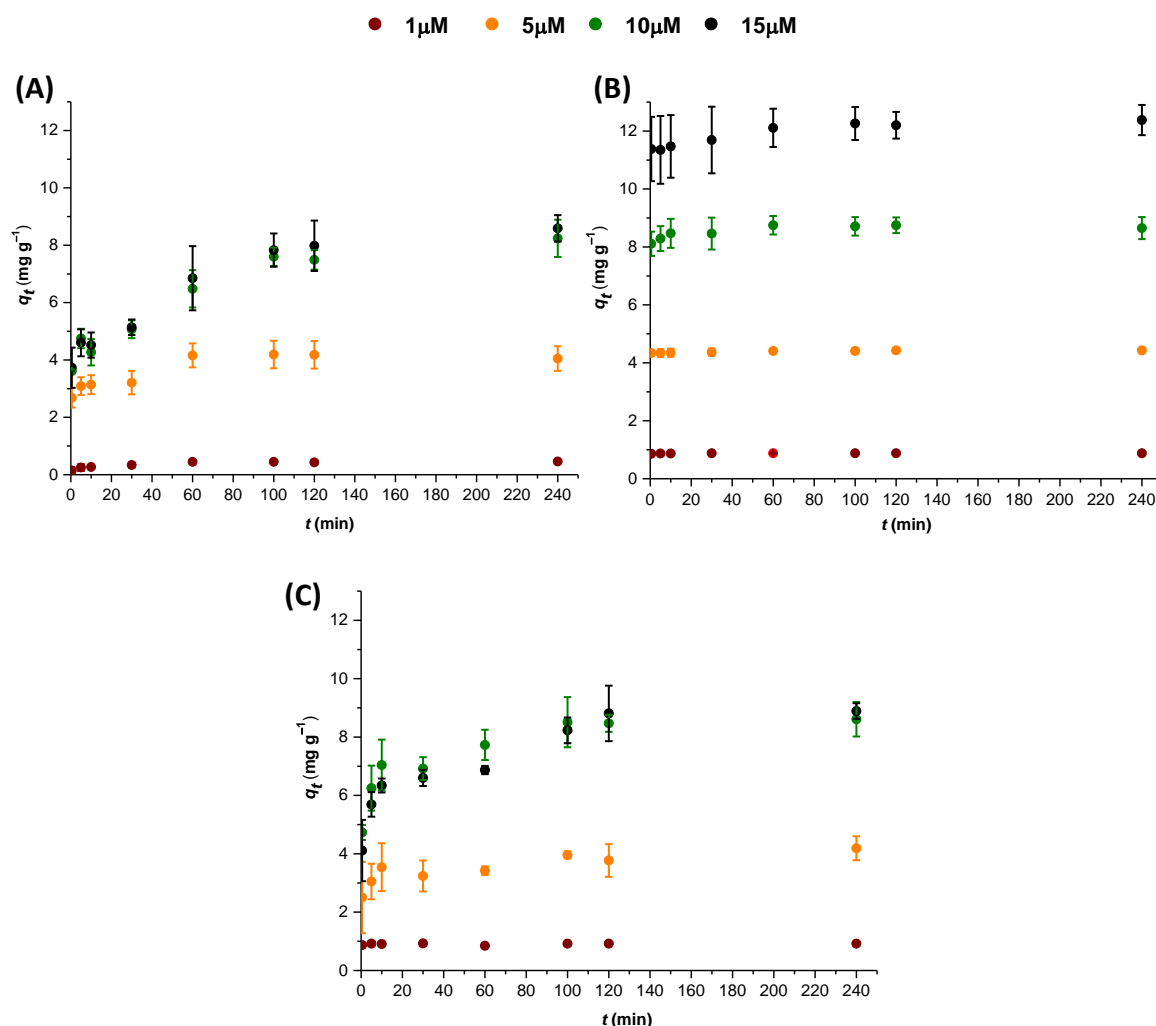


**Figure 27.** Adsorption kinetics of: (A) MC-LR onto TpBD-(CF<sub>3</sub>)<sub>2</sub>; (B) MC-LA onto TpBD-(NH<sub>2</sub>)<sub>2</sub>; and (C) MC-RR onto TpBD-(NO<sub>2</sub>)<sub>2</sub> expressed as quantity adsorbed,  $q_t$  (mg g<sup>-1</sup>), for initial MCs concentrations of 1, 5, 10, and 15 μmol L<sup>-1</sup>, at 19 °C in ultrapure water at pH 6–7 [ $C_0(\text{COF}) = 1 \text{ mg mL}^{-1}$ ]. Results are expressed as the mean of three independent experiments with measurements performed in duplicates. Error bars correspond to the standard deviation of the mean.

The adsorption isotherms of MC-LR, MC-LA, and MC-RR with TpBD-(CF<sub>3</sub>)<sub>2</sub>, TpBD-(NH<sub>2</sub>)<sub>2</sub>, and TpBD-(NO<sub>2</sub>)<sub>2</sub>, respectively, at 19 °C were obtained by fitting the experimental data to the Freundlich and Langmuir models (Figure 58 and 59, experimental section 5.3.2.5, and Table 6). The best fit was found with the Freundlich model, with correlation coefficients close to 1, as shown in Table 6.  $K_F$  values of 1.021 mg<sup>0.071</sup> g<sup>-1</sup> L<sup>0.929</sup>



for MC-LA in TpBD-(NH<sub>2</sub>)<sub>2</sub>, 0.546 mg<sup>-0.037</sup> g<sup>-1</sup> L<sup>1.037</sup> for MC-LR in TpBD-(CF<sub>3</sub>)<sub>2</sub>, and 1.015 mg<sup>0.233</sup> g<sup>-1</sup> L<sup>0.767</sup> for MC-RR in TpBD-(NO<sub>2</sub>)<sub>2</sub> were obtained, highlighting the high adsorption capacity of MC-LA in TpBD-(NH<sub>2</sub>)<sub>2</sub> and MC-RR in TpBD-(NO<sub>2</sub>)<sub>2</sub> ( $K_F > 1$ ).

Maximum adsorption capacity,  $q_m$ , calculated from the adsorption isotherm, gave values of 18.6 mg g<sup>-1</sup>, 15.3 mg g<sup>-1</sup>, and 12.3 mg g<sup>-1</sup> for MC-LA with TpBD-(NH<sub>2</sub>)<sub>2</sub>, MC-LR with TpBD-(CF<sub>3</sub>)<sub>2</sub>, and MC-RR with TpBD-(NO<sub>2</sub>)<sub>2</sub>, respectively. With this result, TpBD-(CF<sub>3</sub>)<sub>2</sub> outperforms the most commonly used resins reported for the capture of MC-LR from water (A860,<sup>[288]</sup> HP20, and SP700<sup>[289]</sup>), carbon and silica composites,<sup>[290–294]</sup> graphene oxide,<sup>[295]</sup> and MOF<sup>[296]</sup> adsorbent materials (Table 7). Nonetheless, despite the good performance of TpBD-(CF<sub>3</sub>)<sub>2</sub>, some reported iron-based and ordered mesoporous carbon materials showed higher adsorption capacities. However, due to its long-range order and small pore size, TpBD-(CF<sub>3</sub>)<sub>2</sub> can offer higher selectivity for MC-LR making it more attractive for environmental water adsorption applications. Related to MC-RR, TpBD-(NO<sub>2</sub>)<sub>2</sub> outperforms the previously reported adsorbent materials by an order of magnitude, highlighting its potential to be used as efficient adsorbent for this MC analogue. Furthermore, to date, this is the first study reported on the efficient adsorption of MC-LA.

Based on the results obtained, interesting approaches for the selective capture of MC analogues using COFs were postulated based on the different adsorption efficiencies and speeds. For instance, for the preferential capture of MC-LA and MC-YR from a complex mixture of analogues, the use of TpBD-(NH<sub>2</sub>)<sub>2</sub> and TpBD-(CF<sub>3</sub>)<sub>2</sub>, respectively, during 5 min could be explored, while TpBD-(NO<sub>2</sub>)<sub>2</sub> could be used to maximize the extraction of MC-RR. Then, TpBD-(CF<sub>3</sub>)<sub>2</sub> could be used for the efficient but slower removal of all the remaining analogues.

**Table 6.** Freundlich and Langmuir isotherm equation constants and correlation coefficient obtained for MC-LR in TpBD-(CF<sub>3</sub>)<sub>2</sub>, for MC-LA in TpBD-(NH<sub>2</sub>)<sub>2</sub>, and for MC-RR in TpBD-(NO<sub>2</sub>)<sub>2</sub>.

<b>MC-LR onto TpBD-(CF<sub>3</sub>)<sub>2</sub></b>	
<b>Freundlich model</b>	
Regression equation	$\log q_e = (1.037 \pm 0.132)\log C_e - (0.263 \pm 0.129)$
$K_F$ (mg <sup>1-1/n</sup> g <sup>-1</sup> L <sup>1/n</sup> )	0.546
1/n	1.037 ± 0.132
n	0.964
R <sup>2</sup>	0.938
<b>Langmuir model</b>	
Regression equation	$\frac{C_e}{q_e} = (0.0097 \pm 0.02958)C_e + (1.6505 \pm 0.41127)$
$K_L$ (L mg <sup>-1</sup> )	0.006
R <sup>2</sup>	-0.287
<b>MC-LA onto TpBD-(NH<sub>2</sub>)<sub>2</sub></b>	
<b>Freundlich model</b>	
Regression equation	$\log q_e = (0.9294 \pm 0.04343)\log C_e + (0.0092 \pm 0.04113)$
$K_F$ (mg <sup>1-1/n</sup> g <sup>-1</sup> L <sup>1/n</sup> )	1.021
1/n	0.929 ± 0.043
n	1.076
R <sup>2</sup>	0.991
<b>Langmuir model</b>	
Regression equation	$\frac{C_e}{q_e} = (0.0168 \pm 0.00417)C_e + (0.9545 \pm 0.05302)$
$K_L$ (L mg <sup>-1</sup> )	0.018
R <sup>2</sup>	0.791
<b>MC-RR onto TpBD-(NO<sub>2</sub>)<sub>2</sub></b>	
<b>Freundlich model</b>	
Regression equation	$\log q_e = (0.7667 \pm 0.10926)\log C_e + (0.0065 \pm 0.10889)$
$K_F$ (mg <sup>1-1/n</sup> g <sup>-1</sup> L <sup>1/n</sup> )	1.015
1/n	0.767 ± 0.10926
n	1.304
R <sup>2</sup>	0.923
<b>Langmuir model</b>	
Regression equation	$\frac{C_e}{q_e} = (0.0682 \pm 0.01514)C_e + (0.8793 \pm 0.21956)$
$K_L$ (L mg <sup>-1</sup> )	0.078
R <sup>2</sup>	0.923

**Table 7.** Reported performance of most commonly used MCs adsorbents.  $q_m$  as the maximum adsorption capacity, in  $\text{mg g}^{-1}$ , and  $t_{eq}$  as the time needed to reach the equilibrium, in minutes.

Adsorbent ( $\text{mg mL}^{-1}$ )	MCs ( $\text{mg L}^{-1}$ )	$q_m$ ( $\text{mg g}^{-1}$ )	$t_{eq}$ (min)	Reference
<b>MC-LR</b>				
Purolite® A860 resin (0.2 $\text{mg mL}^{-1}$ )	0.025	0.13	40	[288]
HP20 resin	148.86	3.3	30	[289]
SP700 resin (50 $\text{mg mL}^{-1}$ )		2.5	15	
$\text{Fe}_3\text{O}_4@PDA@ \gamma\text{-CDP}$ (0.2 $\text{mg mL}^{-1}$ )	0.05	0.34	30	[291]
$\text{Fe}_3\text{O}_4@SiO_2@ \beta\text{-CDP}$ (2 $\text{mg mL}^{-1}$ )	0.025	0.24	30	[290]
Microgel-Fe(III) complex (0.15 $\text{mg mL}^{-1}$ )	10	164.47	12	[297]
Macroporous magnetic-silica composite (3 $\text{mg mL}^{-1}$ )	0.010	0.0033	10	[293]
m- $\text{Fe}_3\text{O}_4@C\text{-NPs}$	0.05	0.17	60	[292]
mesoporous- $\text{Si}@Fe_3O_4\text{-NPs}$	0.013	0.10		
$\text{Fe}_3\text{O}_4/\text{Chitosan}$ (25 $\text{mg mL}^{-1}$ )	6.47	0.59	180	[294]
MIL-100(Al) xerogel (1 $\text{mg mL}^{-1}$ )	10	7.13	60	[296]
Graphene oxide (0.5 $\text{mg mL}^{-1}$ )	0.5	1.70	5	[295]
Granular activated carbon (0.5 $\text{mg mL}^{-1}$ )	0.5	1.48	n.d	[295]
PAC-Fe(III) (0.15 $\text{mg mL}^{-1}$ )	10	126.61	120	[298]
Ordered Mesoporous carbon (0.01 $\text{mg mL}^{-1}$ )	10	87–526	240	[299]
Functionalized mesoporous materials (0.1 $\text{mg mL}^{-1}$ )	1	23.03–37.87	250	[300]

<b>TpBD-(CF<sub>3</sub>)<sub>2</sub> COF</b> (1 mg mL <sup>-1</sup> )	24.9	15.31	100	<b>This work</b>
<b>MC-RR</b>				
Fe <sub>3</sub> O <sub>4</sub> @PDA@γ-CDP (0.2 mg mL <sup>-1</sup> )	0.05	0.37	30	[291]
Fe <sub>3</sub> O <sub>4</sub> @SiO <sub>2</sub> @β-CDP (2 mg mL <sup>-1</sup> )	0.025	0.24	30	[290]
Graphene oxide (0.5 mg mL <sup>-1</sup> )	0.50	1.88	5	[295]
Granular activated carbon (0.5 mg mL <sup>-1</sup> )	0.5	1.03	-	[295]
<b>TpBD-(NO<sub>2</sub>)<sub>2</sub> COF</b> (1 mg mL <sup>-1</sup> )	25.96	12.32	100	<b>This work</b>
<b>MC-YR</b>				
Fe <sub>3</sub> O <sub>4</sub> @PDA@γ-CDP (0.2 mg mL <sup>-1</sup> )	0.05	0.35	30	[291]
Fe <sub>3</sub> O <sub>4</sub> @SiO <sub>2</sub> @β-CDP (2 mg mL <sup>-1</sup> )	0.025	0.21	30	[290]
<b>MC-LA</b>				
<b>TpBD-(NH<sub>2</sub>)<sub>2</sub> COF</b> (1 mg mL <sup>-1</sup> )	22.75	18.64	10	<b>This work</b>

Afterwards to confirm that the toxins can be efficiently recovered from COF materials, desorption experiments were conducted by immersion of COFs in propan-2-ol at 4 °C overnight (Figure 24B; for more details, see experimental section 5.3.2.4). The obtained maximum desorption efficiency,  $q_e$  (mg g<sup>-1</sup>) (Table 3), showed large differences between the MC–COF combinations, highlighting the differences in the interactions of the COF derivatives with the MC analogues. Desorption efficiency above 60% was achieved for MC–YR from TpBD-(CF<sub>3</sub>)<sub>2</sub> and TpBD-(NH<sub>2</sub>)<sub>2</sub>, and for MC-LR and MC-LA from TpBD-(NH<sub>2</sub>)<sub>2</sub>. In all other cases, values below 50% were obtained. Interestingly, MC-LR, which was efficiently adsorbed by all three COF derivatives, was only efficiently desorbed (>60%) from TpBD-(NH<sub>2</sub>)<sub>2</sub>. MC-YR, on the other hand, was efficiently desorbed (>80%) from TpBD-(NH<sub>2</sub>)<sub>2</sub> and TpBD-(CF<sub>3</sub>)<sub>2</sub>, whereas from TpBD-(NO<sub>2</sub>)<sub>2</sub>, merely 29% were recovered. Remarkably, in

the case of MC-RR, efficiently adsorbed by TpBD-(NO<sub>2</sub>)<sub>2</sub>, a very low amount (1%) was desorbed, indicating the presence of a strong interaction between the adsorbent and the adsorbate. With this model system in particular, an interaction energy of  $-92 \text{ kcal mol}^{-1}$  was obtained by calculations when MC-RR is immersed in the COF pore. This interaction is twice as strong as when MC-RR is located only in the COF surface ( $-47 \text{ kcal mol}^{-1}$ ), which could explain the lowest desorption efficiency observed experimentally. On the other hand, MC-LA was efficiently recovered (66%) from TpBD-(NH<sub>2</sub>)<sub>2</sub>, while a low recovery (20%) was observed from both TpBD-(CF<sub>3</sub>)<sub>2</sub> and TpBD-(NO<sub>2</sub>)<sub>2</sub>, suggesting a stronger interaction of MC-LA with TpBD-(CF<sub>3</sub>)<sub>2</sub>, which could be attributed to the higher lipophilicity of that COF.

Furthermore, to ascertain that the COF materials are recyclable, we evaluated the reusability of TpBD-(CF<sub>3</sub>)<sub>2</sub> for the efficiently adsorbed MC-LR and MC-YR, as well as TpBD-(NO<sub>2</sub>)<sub>2</sub> and TpBD-(NH<sub>2</sub>)<sub>2</sub> for the preferential capture of MC-RR and MC-LA, respectively. Due to the low desorption efficiencies observed for some of these combinations using propan-2-ol, we carried out adsorption–desorption cycles at a concentration of  $10 \text{ } \mu\text{mol L}^{-1}$  of MC using methanol/water (1:1), methanol/formic acid (pH 2.7), and methanol/ammonium hydroxide (pH 9.7) as desorption solvents (data not shown). These solvent mixtures were selected due to the surface properties of the MC analogues, as well as of the COFs, which could be protonated and deprotonated at different pH values. Data presented in the following corresponds to the cycles using the solvent with which the highest desorption efficiency for the MC–COF combination was found. Using methanol/ammonium hydroxide mixture for desorption, we obtained an adsorption efficiency for MC-LR with TpBD-(CF<sub>3</sub>)<sub>2</sub> of 60% in cycles 2 and 3 (Figure 28), only slightly lower than what was found in the first cycle (78%), indicating that the basic mixture is a much more efficient desorption solvent than propan-2-ol (desorption efficiency 20%, Figure 24B). Using the same solvent mixture, the adsorption efficiency of MC-YR was found to be 90% in all three cycles tested, without loss of adsorption capacity by TpBD-(CF<sub>3</sub>)<sub>2</sub>. The efficient regeneration of the COF in basic medium may stem from electrostatic repulsions between the negatively charged surface of MC-LR and MC-YR and TpBD-(CF<sub>3</sub>)<sub>2</sub> ( $\text{pH}_{\text{pzc}} = 3.86$ , Figure 112, experimental section 5.4.8).

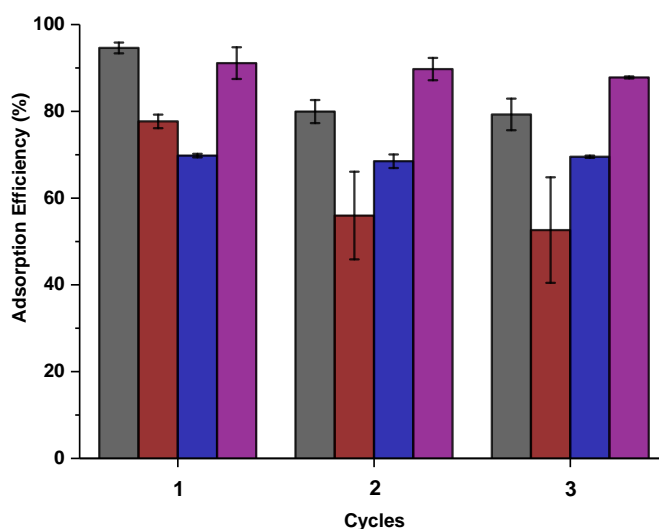


**Figure 28.** Reusability of TpBD-(CF<sub>3</sub>)<sub>2</sub> for MC-LR and MC-YR, TpBD-(NO<sub>2</sub>)<sub>2</sub> for MC-RR, and TpBD-(NH<sub>2</sub>)<sub>2</sub> for MC-LA, in three consecutive cycles of adsorption-desorption, with an initial MC concentration of 10 μmol L<sup>-1</sup> in each of the adsorption cycles (ultrapure water at 19 °C and pH 6–7). Desorption was carried out using methanol/ammonium hydroxide mixture at pH 9.7 for MC-LR, MC-YR, and MC-RR, and methanol/formic acid mixture at pH 2.7 for MC-LA. Results are expressed as the mean of duplicates. Error bars correspond to the standard deviation of the mean.

For MC-RR from TpBD-(NO<sub>2</sub>)<sub>2</sub>, a low desorption efficiency was found with propan-2-ol (1%, Figure 24B). Using methanol/ammonium hydroxide mixture at pH 9.7, the adsorption capacity of TpBD-(NO<sub>2</sub>)<sub>2</sub> was retained at 70% up to three cycles (Figure 28), indicating that this mixture is adequate for its regeneration. This could be due to the disruption of hydrogen bonds between the toxin and the adsorbent under alkaline conditions. In order to test the reusability of TpBD-(NH<sub>2</sub>)<sub>2</sub> with MC-LA, a methanol/formic acid mixture at pH 2.7 was used as regeneration solvent between the adsorption cycles. The amount of MC-LA adsorbed in the first cycle was around 95% (Figure 28), followed by a slight reduction in adsorption efficiency of 15% in the next two cycles. It was postulated that the desorption could be enhanced by electrostatic repulsions between TpBD-(NH<sub>2</sub>)<sub>2</sub> and MC-LA at acidic pH.

In summary, a comprehensive study on how COF functionalization can influence the adsorption rate and efficiency for diverse microcystin analogues was carried out. Large differences were observed in adsorption and desorption efficiencies, as well as in kinetics. Theoretical calculations gave a deep insight into some of the tendencies observed, highlighting their importance as a guide to design new and more selective adsorbents. TpBD-(NO<sub>2</sub>)<sub>2</sub> was found to outperform the reported adsorbent materials for the capture of MC-RR, resulting in an increase in the maximum adsorption capacity by one order of magnitude. TpBD-(NH<sub>2</sub>)<sub>2</sub> was demonstrated as the first efficient adsorbent material for the capture of MC-LA. In addition, the fast adsorption kinetics observed for MC-YR with TpBD-(CF<sub>3</sub>)<sub>2</sub> and MC-LA with TpBD-(NH<sub>2</sub>)<sub>2</sub> indicate that analogue-preferential strategies can be designed by selecting the time of contact. This study highlights that careful choice of COF functionalities can lead to strong preferences for one analogue over the others, indicating that COF structures can potentially be designed for selective contaminant capture, which would facilitate purification and analytical methods for quantification of the different analogues. Finally, the selected COFs can be efficiently regenerated with loss of adsorption efficiencies ≤15% in three consecutive cycles, stressing their potential utility for MC recovery and analysis.

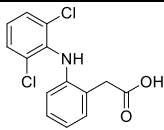
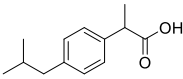
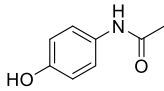
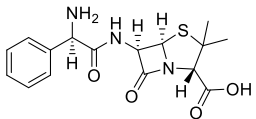
## **2.2. COFs for the adsorption of pharmaceutical pollutants**

### **2.2.1 Pharmaceutical pollutants<sup>[61]</sup>**

To probe the efficiency of COFs for the capture of pharmaceuticals, ibuprofen was chosen as target compound (Table 8). It is among the most widely used pharmaceuticals in the world, and due to its inefficient removal by conventional wastewater treatment, it can be found in natural surface waters<sup>[191]</sup> as well as in wastewater<sup>[301]</sup> at high concentrations (> 1 ppb), making it an attractive molecule to probe adsorption capacity by COFs. The low solubility of ibuprofen in water, 21 mg L<sup>-1</sup>,<sup>[302]</sup> and the reported octanol/water partition coefficient log*P* value at pH 7.4 of 1.07<sup>[303]</sup> reflect the lipophilic character of the pharmaceutical. Taking this into account, the selection of COF material is crucial to promote the adsorption of ibuprofen from water. In this respect, as demonstrated in section 2.1.2, the novel fluorine-bearing COF, TpBD-(CF<sub>3</sub>)<sub>2</sub> (Scheme 4) was successfully prepared. Due to

its highly lipophilic nature, as evidenced by contact angle measurements (133°, Figure 107A, experimental section 5.4.5), this material was chosen as a potential candidate for the capture of the lipophilic ibuprofen. For further information related to the synthesis and characterization data of TpBD-(CF<sub>3</sub>)<sub>2</sub>, see section 2.1.2, as well as experimental section 5.4.2, 5.4.3, and 5.4.4.

**Table 8.** The properties of the studied pharmaceuticals. <sup>a</sup>pH 7.4. Dimensions of pharmaceuticals were obtained by measuring the furthest distances of C, N, or O atoms from the X-ray crystal structures obtained from the Cambridge Structural Database (CSD) with the following codes: <sup>b</sup>CCDC-1102110, <sup>c</sup>CCDC-1041382, <sup>d</sup>CCDC-150969, <sup>e</sup>CCDC-298547.

Pharmaceutical	log <i>P</i>	Dimensions (Å)	MW (g mol <sup>-1</sup> )	p <i>K</i> <sub>a</sub>
 <b>Diclofenac</b>	<sup>a</sup> 1.22 <sup>[303]</sup>	<sup>b</sup> 7.5 x 6.4 x 5.4	296.15	4.5 <sup>[303]</sup>
 <b>Ibuprofen</b>	<sup>a</sup> 1.07 <sup>[303]</sup>	<sup>c</sup> 8.8 x 4.5 x 2.4	206.28	5.2 <sup>[303]</sup>
 <b>Acetaminophen</b>	<sup>a</sup> 0.51 <sup>[303]</sup>	<sup>d</sup> 7.9 x 2.4 x 0.8	151.16	9.5 <sup>[304]</sup>
 <b>Ampicillin</b>	-1.13 <sup>[305]</sup>	<sup>e</sup> 10.9 x 5.5 x 4.9	403.45	2.5, 7.2 <sup>[306]</sup>

The adsorption capacity of TpBD-(CF<sub>3</sub>)<sub>2</sub> for ibuprofen in equilibrium, *q<sub>e</sub>* (mg g<sup>-1</sup>), was evaluated at 21 °C in ultrapure water at pH 6–7, for 120 min to ensure that equilibrium was reached (*C*<sub>0</sub>(TpBD-(CF<sub>3</sub>)<sub>2</sub>) = 100 mg L<sup>-1</sup>, *C*<sub>0</sub>(ibuprofen) = 20 mg g<sup>-1</sup>, for more details, see experimental section 5.3.3.3). TpBD-(CF<sub>3</sub>)<sub>2</sub> was found to adsorb ibuprofen very efficiently



with  $q_e$  of  $119 \text{ mg g}^{-1}$  (Figure 29, black). With this value the COF material outperforms MOFs<sup>[307,308]</sup> and is comparable to reported activated carbon materials.<sup>[210,308]</sup> Then, kinetic studies were conducted at different contact times,  $t$  (min, for more details, see experimental section 5.3.3.2), and equilibrium was found to be reached at around 60 min (Figure 29, black).

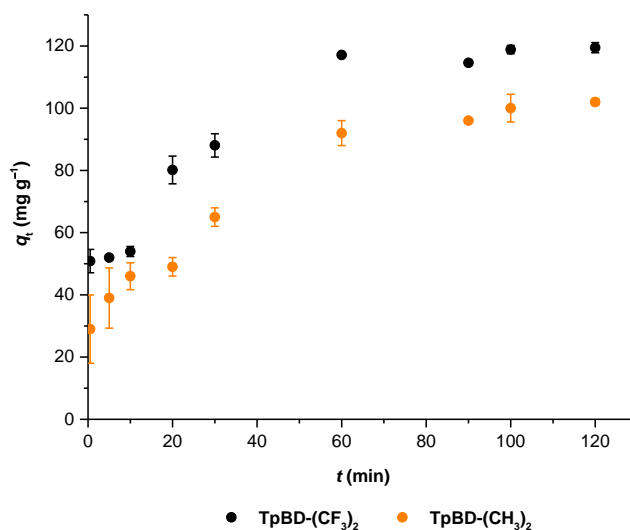


**Figure 29.** Ibuprofen adsorption kinetics expressed as quantity adsorbed,  $q_t$  ( $\text{mg g}^{-1}$ ), by TpBD-(CF<sub>3</sub>)<sub>2</sub> (black) and TpBD-(CH<sub>3</sub>)<sub>2</sub> (orange) at 21 °C in ultrapure water at pH 6–7 ( $C_0(\text{ibuprofen}) = 20 \text{ mg L}^{-1}$ ;  $C_0(\text{COF}) = 100 \text{ mg L}^{-1}$ ). Results are expressed as the mean of two separate experiments with measurements performed in duplicate. Error bars correspond to the standard deviation of the mean.

The adsorption kinetics of ibuprofen with TpBD-(CF<sub>3</sub>)<sub>2</sub> were obtained by fitting the experimental data to the pseudo-first-order and the pseudo-second-order kinetic models (Figure 60A and 60B, experimental section 5.3.3.2, and Table 9). The pseudo-second-order kinetic model gives a coefficient of determination close to 1, suggesting that this model is adequate to describe the adsorption process, as has been shown to be the case for most nanomaterials. In addition, the calculated  $q_e$  of  $127.7 \text{ mg g}^{-1}$  is very close to the experimental value ( $q_e = 119 \text{ mg g}^{-1}$ ), further corroborating the adequacy of this model.

**Table 9.** The rate constants, amount of adsorbed pharmaceutical in equilibrium, and the coefficient of determination obtained using the kinetic models.

<b><i>Pseudo-first-order model</i></b>	
Regression equation	$\log(q_e - q_t) = \log q_e - \frac{K_1}{2.303} t$
$K_1$ (min <sup>-1</sup> )	0.0450
$q_e$ (mg g <sup>-1</sup> )	91.46
$R^2$	0.887
<b><i>Pseudo-second-order model</i></b>	
Regression equation	$\frac{t}{q_t} = \frac{1}{K_2 q_e^2} + \frac{1}{q_e} t$
$K_2$ (mg g <sup>-1</sup> min <sup>-1</sup> )	0.0009
$q_e$ (mg g <sup>-1</sup> )	127.71
$R^2$	0.9905

In order to verify the reusability of TpBD-(CF<sub>3</sub>)<sub>2</sub> for ibuprofen adsorption, adsorption-desorption experiments were conducted at the same concentrations on a larger scale ( $m(\text{TpBD}-(\text{CF}_3)_2) = 12.5 \text{ mg}$ ,  $C_0(\text{TpBD}-(\text{CF}_3)_2) = 100 \text{ mg L}^{-1}$ ,  $C_0(\text{ibuprofen}) = 20 \text{ mg g}^{-1}$ ; for more details, see experimental section 5.3.3.3). Desorption by immersion of TpBD-(CF<sub>3</sub>)<sub>2</sub> in propan-2-ol resulted in the recovery of 79% of the adsorbed ibuprofen, showing promise for the reuse of the COF material.

To gain further insight into the adsorption of ibuprofen with TpBD-(CF<sub>3</sub>)<sub>2</sub> during and after adsorption and to allow for complete characterization, the adsorption-desorption cycle was repeated using 200 mg of COF as adsorbent at the same concentrations ( $C_0(\text{TpBD}-(\text{CF}_3)_2) = 100 \text{ mg L}^{-1}$ ,  $C_0(\text{ibuprofen}) = 20 \text{ mg g}^{-1}$ , for more details, see experimental section 5.3.3.3). The crystallinity of the COF was found retained after one cycle of adsorption and desorption of ibuprofen (Figure 30A, cyan and grey, respectively). The N<sub>2</sub> sorption measurements at 77 K after ibuprofen adsorption showed a decrease in surface area to 590 m<sup>2</sup> g<sup>-1</sup>, corresponding to a drop of 32% as compared with pristine COF, which could indicate that the pharmaceutical is adsorbed within the pores of the material (Figure 30B, cyan). After desorption, the surface area recovers to 830 m<sup>2</sup> g<sup>-1</sup> (Figure 30B, grey),

corresponding to 95% of the original surface area. This result highlights the possibility of reusing the material, an important aspect in view of cost-efficiency for adsorbents.

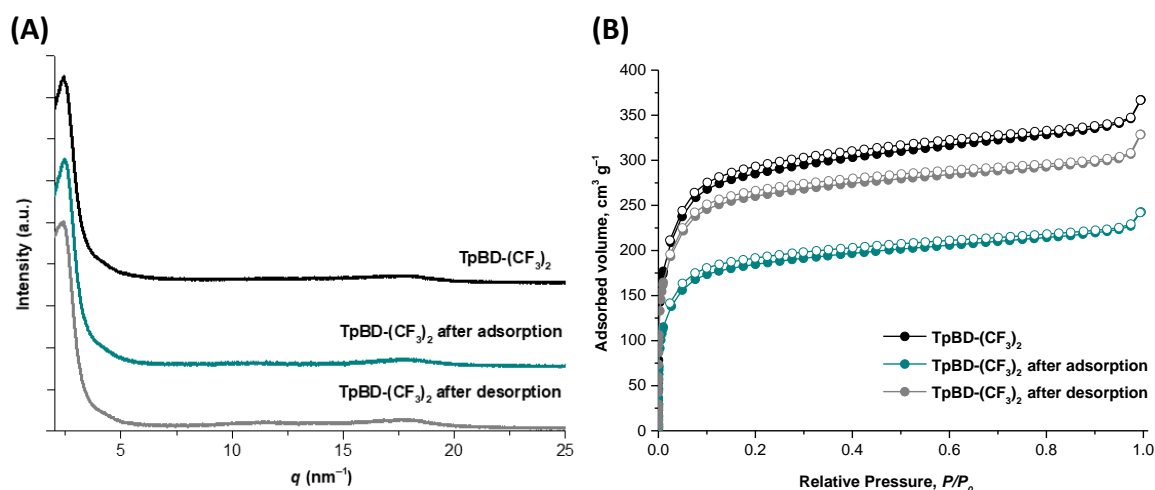


**Figure 30.** (A) SAXS pattern and (B) N<sub>2</sub> adsorption (filled spheres) and desorption (hollow spheres) isotherm profiles measured at 77 K of TpBD-(CF<sub>3</sub>)<sub>2</sub> as-synthesized (black), after adsorption of ibuprofen (cyan), and after desorption (grey).

In the FT-IR spectrum of TpBD-(CF<sub>3</sub>)<sub>2</sub>, after ibuprofen adsorption, the presence of the pharmaceutical is evident from the appearance of a vibration at  $\approx 1720$  cm<sup>-1</sup> (Figure 31A), which was attributed to the C=O stretching of the ibuprofen carboxylic acid moiety. The slight blueshift from 1705 cm<sup>-1</sup> of free ibuprofen could be indicative of a change in hydrogen-bonding environment upon adsorption. After desorption, this vibration disappears and the spectrum corresponds to the as-synthesized one. By TGA measurements after adsorption, an additional weight-loss contribution between 197 and 330 °C can be attributed to ibuprofen (Figure 31B). Notably, decomposition of pure ibuprofen, not surrounded by the COF pores, occurs at a much lower temperature of  $\approx 115$  °C. After desorption, the TGA curve corresponds to the as-synthesized one. Additionally, no changes in the COF morphology were observed in the SEM images after desorption of ibuprofen (Figure 109, experimental section 5.4.6).

Ibuprofen, with a  $pK_a$  of 5.2 (Table 8),<sup>[303]</sup> features a carboxylic acid moiety, which is partially negatively charged at the studied pH 6–7. Thus, in order to establish if this moiety plays a role in the capture of the pharmaceutical, adsorption capacity of COF at low pH of

2 and at the high pH of 10 was measured (Figure 32A, red). An increase in the captured quantity was found at pH 2, suggesting that protonation of ibuprofen leads to some favorable interactions with the COF adsorbent. Additionally, the octanol/water distribution coefficient  $\log D$  of ibuprofen is  $\approx 3.5$  at pH 2, indicating an enhanced preference for a lipophilic environment. A drastic drop in affinity at pH 10 could stem from repulsions of the ionic carboxylic acid moiety with the negatively charged surface of TpBD-(CF<sub>3</sub>)<sub>2</sub> ( $\text{pH}_{\text{pzc}} = 3.86$ , Figure 112, experimental section 5.4.8). Similar results have been reported with activated carbon<sup>[309]</sup> and graphene oxide.<sup>[310]</sup>

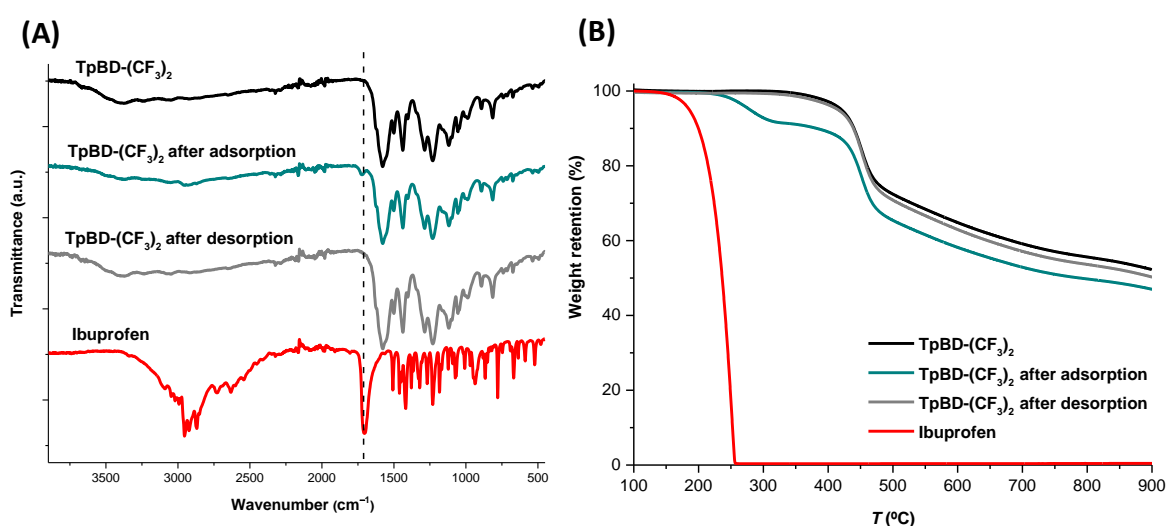


**Figure 31.** FT-IR spectra (A) and TGA data (B) of ibuprofen (red) and of TpBD-(CF<sub>3</sub>)<sub>2</sub> as-synthesized (black), after adsorption of ibuprofen (cyan), and after desorption of ibuprofen (grey).

In order to establish the preference of TpBD-(CF<sub>3</sub>)<sub>2</sub> towards lipophilic pharmaceuticals, we chosen two other potential pollutants, acetaminophen and ampicillin (Table 8), which are both more hydrophilic in nature than ibuprofen, with  $\log P$  values of 0.51<sup>[303]</sup> and  $-1.13$ <sup>[305]</sup> for acetaminophen and ampicillin, respectively. At neutral pH a dramatic reduction in the adsorbed amount,  $q_t$  (mg g<sup>-1</sup>), was found with increasing hydrophilicity, with ibuprofen adsorbed by TpBD-(CF<sub>3</sub>)<sub>2</sub> more efficiently by a factor of  $\approx 10$  and  $\approx 100$  in comparison to acetaminophen and ampicillin, respectively (Figure 32, blue for acetaminophen and orange for ampicillin).

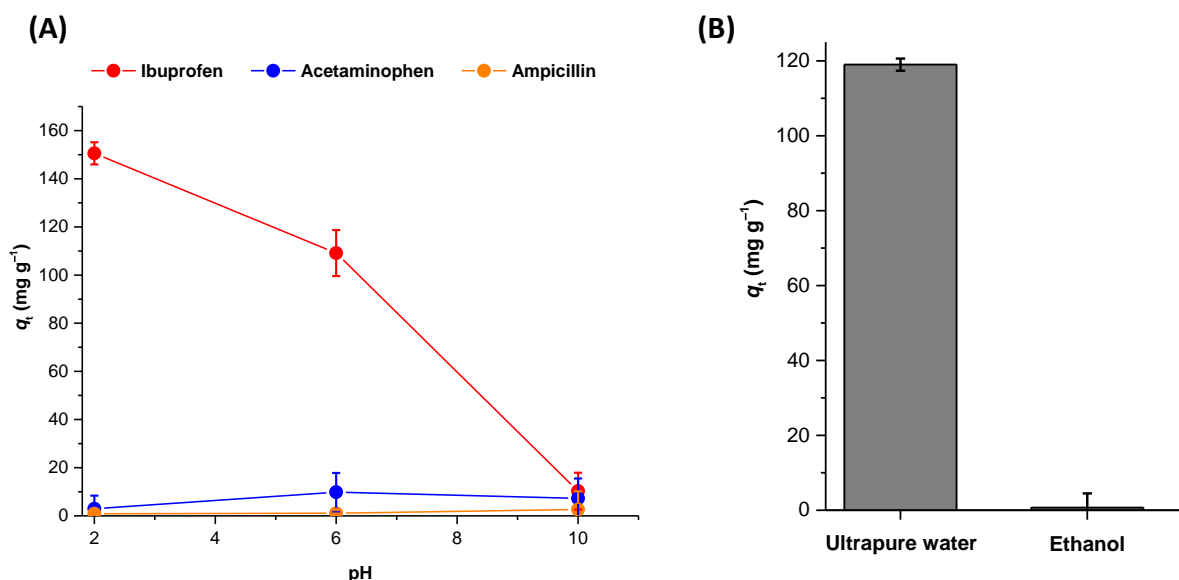


**Figure 32.** (A) The adsorbed quantities of the ibuprofen, acetaminophen, and ampicillin by TpBD-(CF<sub>3</sub>)<sub>2</sub> as a function of pH (pH 6 denotes ultrapure water,  $C_0(\text{pharmaceutical}) = 20 \text{ mg L}^{-1}$ ,  $C_0(\text{TpBD}-(\text{CF}_3)_2) = 100 \text{ mg L}^{-1}$ ,  $t = 120 \text{ min}$ ). (B) The adsorbed quantities of ibuprofen by TpBD-(CF<sub>3</sub>)<sub>2</sub> as a function of solvent polarity (water and ethanol as selected solvents,  $C_0(\text{pharmaceutical}) = 20 \text{ mg L}^{-1}$ ,  $C_0(\text{TpBD}-(\text{CF}_3)_2) = 100 \text{ mg L}^{-1}$ ,  $t = 120 \text{ min}$ ). Results are expressed as the mean of two separate experiments with measurements performed in duplicate. Error bars correspond to the standard deviation of the mean.

To demonstrate the influence of solvent polarity on the adsorption, adsorption experiments were performed in the less polar ethanol solvent (Figure 32B, for more details, see experimental section 5.3.3.5), resulting in a dramatic reduction in adsorption capacity for ibuprofen down to the level of acetaminophen, indicating that hydrophobic interactions play a role in the pharmaceutical adsorption. However, the large differences in the electrostatic potential surfaces (Figure 33 and 34) of the pharmaceuticals, as well as of model system of TpBD-(CF<sub>3</sub>)<sub>2</sub>, indicate that electrostatics may contribute to the differences observed in the adsorption as well.

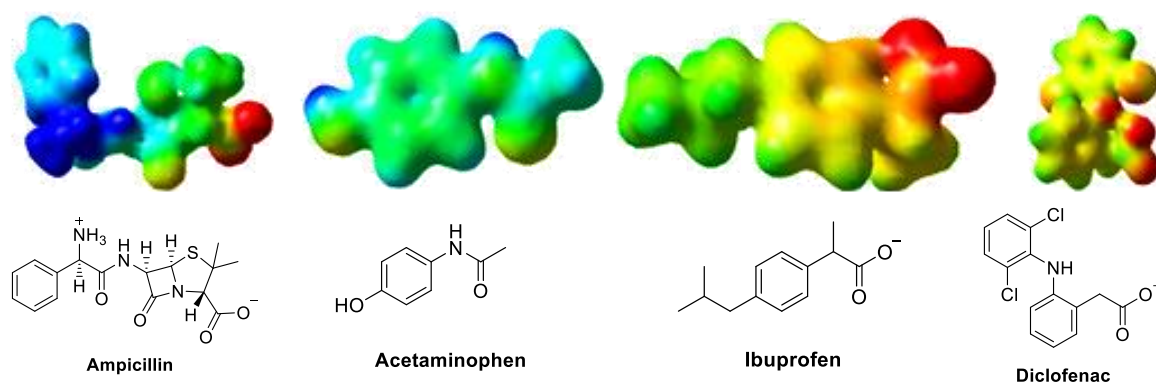


**Figure 33.** Electrostatic potential (ESP) surfaces of the studied pharmaceuticals generated at the HF/STO-3G level of theory using an isovalue of 0.02 with scale from  $-0.2$  red to  $0.2$  blue. The geometry of the molecules resembles those of the X-ray crystal structures, obtained from the Cambridge Structural Database (CSD) with the following codes: diclofenac: CCDC-1102110, ibuprofen: CCDC-1041382, acetaminophen: CCDC-150969, ampicillin: CCDC-298547. The charges are expressed as found at pH 6.

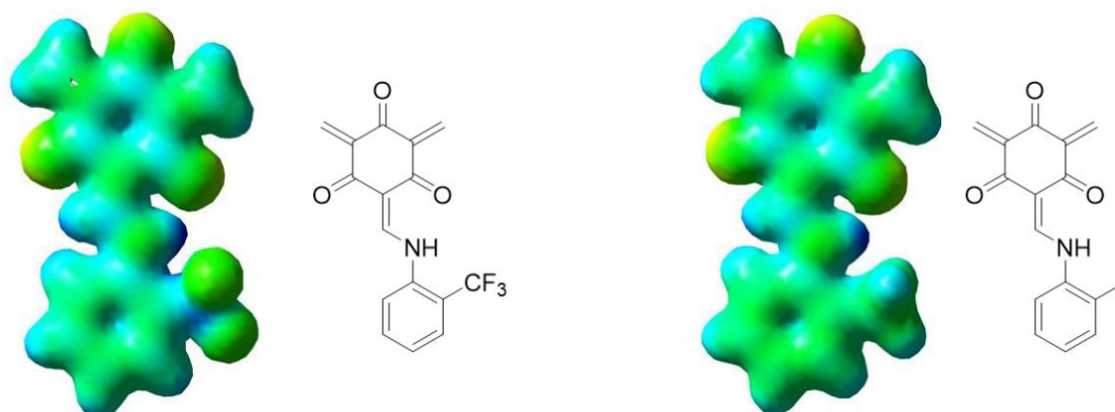


**Figure 34.** ESP surfaces of truncated model system TpBD-(CF<sub>3</sub>)<sub>2</sub> (left) and TpBD-(CH<sub>3</sub>)<sub>2</sub> (right), where the more electronegative character of the CF<sub>3</sub> moiety is evident.

To further confirm the tendency of TpBD-(CF<sub>3</sub>)<sub>2</sub> to adsorb lipophilic pharmaceuticals, we tested diclofenac, another potential pharmaceutical pollutant, which with  $\log P = 1.22$ <sup>[303]</sup> is more lipophilic in nature than ibuprofen. A very high adsorption capacity of  $18 \text{ mg g}^{-1}$  was found ( $C_0(\text{diclofenac}) = 2.4 \text{ mg L}^{-1}$ ,  $C_0(\text{TpBD}-(\text{CF}_3)_2) = 100 \text{ mg L}^{-1}$ ,  $t = 120 \text{ min}$ , for more details, see experimental section 5.3.3.6), corresponding to an

adsorption efficiency of 77% in relation to the added amount, suggesting that COF pore surfaces can be designed to target a contaminant class from water. In the particular case of highly lipophilic COF materials, such as TpBD-(CF<sub>3</sub>)<sub>2</sub>, the efficient capture of hydrophobic pharmaceutical pollutants from water can be addressed as compared to more hydrophilic ones.

Afterwards, to demonstrate the importance of the lipophilic nature of TpBD-(CF<sub>3</sub>)<sub>2</sub> on the adsorption of lipophilic pharmaceutical pollutants, TpBD-(CH<sub>3</sub>)<sub>2</sub> was used as comparison for the adsorption of the studied pharmaceuticals. TpBD-(CH<sub>3</sub>)<sub>2</sub> (Scheme 3) was successfully prepared as described in section 2.1.1 (for more details on synthesis and characterization, see experimental sections 5.2.3 and 5.4). The higher lipophilicity of TpBD-(CF<sub>3</sub>)<sub>2</sub> as compared to TpBD-(CH<sub>3</sub>)<sub>2</sub> was supported by water contact angle measurements with values of 133° and 18° found, respectively for TpBD-(CF<sub>3</sub>)<sub>2</sub> and TpBD-(CH<sub>3</sub>)<sub>2</sub> (Figure 105 and 107A, experimental section 5.4.5). The adsorption followed the trend of TpBD-(CF<sub>3</sub>)<sub>2</sub> with a reduction of 20% in capture efficiency to a maximum in equilibrium,  $q_e$ , of 100 mg g<sup>-1</sup> reached at around 60 min (Figures 29, orange), which could be attributed to the lower lipophilicity of TpBD-(CH<sub>3</sub>)<sub>2</sub>. In addition, as ascertained by SAXS (Figure 35A), TpBD-(CH<sub>3</sub>)<sub>2</sub> also retains its crystalline nature after desorption of ibuprofen. Similarly, to TpBD-(CF<sub>3</sub>)<sub>2</sub>, an increase in the amount of ibuprofen adsorbed was found at pH 2, followed by a drastic drop in adsorption efficiency at pH 10 (Figure 35B).

With this study, at the moment it was performed, it was demonstrated for the first time that COFs can be used to adsorb pharmaceutical pollutants from water. The new fluorine-bearing COF TpBD-(CF<sub>3</sub>)<sub>2</sub> captured ibuprofen with high efficiency at both neutral and acidic pH. The pharmaceutical can be recovered with high yield with the structural integrity and properties of the COF remaining intact after desorption. Compared to more hydrophilic pharmaceutical contaminants, ibuprofen is adsorbed much more efficiently, showing the potential of COF materials to be designed for selective contaminant capture.

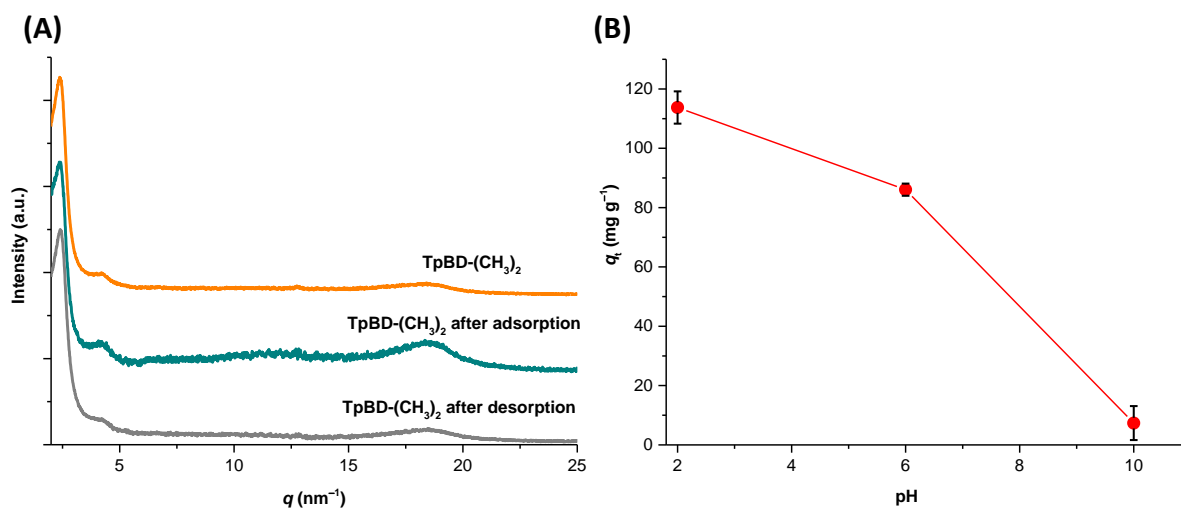


**Figure 35.** (A) SAXS pattern of TpBD-(CH<sub>3</sub>)<sub>2</sub> as synthesized (orange), after adsorption of ibuprofen (cyan), and after desorption (grey). (B) The adsorbed quantity of the ibuprofen by TpBD-(CH<sub>3</sub>)<sub>2</sub> as a function of pH (pH 6 denotes ultrapure water,  $C_0(\text{ibuprofen}) = 20 \text{ mg L}^{-1}$ ,  $C_0(\text{TpBD}-(\text{CH}_3)_2) = 100 \text{ mg L}^{-1}$ ,  $t = 120 \text{ min}$ ).

### 2.2.2. Ibuprofen adsorption from natural waters samples<sup>[248]</sup>

Followed by the demonstrated high efficiency of novel fluorine-based TpBD-(CF<sub>3</sub>)<sub>2</sub> to adsorb lipophilic pharmaceutical pollutants ibuprofen and diclofenac from ultrapure water, is of utmost importance to understand its performance in the environmental field. There, the adsorption process can be affected by the nature of the adsorbent, but also by the physicochemical properties of the water matrix, such as temperature, pH, and salinity.<sup>[199]</sup> Ubiquitous in the water environment, natural organic matter (NOM), which is composed of a complex mixture of organic compounds, such as humic and fulvic acids, can also influence the adsorption process.<sup>[311]</sup>

In this perspective, TpBD-(CF<sub>3</sub>)<sub>2</sub> was tested to extract pharmaceutical pollutant ibuprofen from natural water samples to gain insight into its adsorption efficiency in different water environments and to compare with the adsorption efficiencies found in ultrapure water, as presented in section 2.2.1. Natural water samples were collected from lake, river, and estuary in the region of Viana do Castelo, in Northern Portugal, on the 6<sup>th</sup> of May of 2017, between 15 and 16 h. High tide was at 13.13 h and low tide at 19.16 h;



however, a limited influence of seawater was expected as the samples were collected in the first 1 m of the water column. River water sample was collected from Lima river in Viana do Castelo (41°41'17.7" N 8°47'23.9"W), lake water sample from lake of São Pedro de Arcos in Ponte de Lima (41°45'52.5"N 8°38'13.60"W), and estuary water from Lima river near the mouth of the river (41°40'58.14"N 8°49'35.67"W).

The samples were found to feature different physical-chemical properties (Table 10). The pH of the water samples was found to vary from slightly acidic in lake water with pH 6.5 to slightly alkaline in the river and estuary waters with pH 7.7 and 7.8, respectively. High contents of ions such as calcium and magnesium were measured in lake water giving a total hardness GH of 8°, corresponding to a concentration of about 143 mg L<sup>-1</sup>, whereas in river water the value was below 1°. On the other hand, in river and estuary water, the content of carbonate ions, KH, detected was 7°, 125 mg L<sup>-1</sup>, which is 40% more than that registered in the lake water, explaining its lower pH.

**Table 10.** Physical-chemical parameters of river, lake and estuary water collected. GH = Total hardness; KH = carbonate hardness; LOD = Limit of detection; n/a = not applicable.

	Water sample		
	Lake	River	Estuary
<b>pH</b>	6.5	7.7	7.8
<b>GH (dGH)</b>	8	<LOD	n/a
<b>KH (dKH)</b>	4	7	7
<b>NH<sub>4</sub> (mg L<sup>-1</sup>)</b>	0.50	<0.50	<0.50
<b>NH<sub>3</sub> (mg L<sup>-1</sup>)</b>	<0.003	0.03	0.03
<b>NO<sub>2</sub> (mg L<sup>-1</sup>)</b>	0.00	0.00	1.00
<b>NO<sub>3</sub> (mg L<sup>-1</sup>)</b>	0.00	0.00	10.00
<b>PO<sub>4</sub> (mg L<sup>-1</sup>)</b>	1.00	2.00	1.00
<b>Fe (mg L<sup>-1</sup>)</b>	0.50	0.00	0.00

TpBD-(CF<sub>3</sub>)<sub>2</sub> was prepared as described in section 2.1.2 (for more details about synthesis and characterization data, see experimental sections 5.2.7 and 5.4). To determine

its adsorption efficiency towards ibuprofen in lake, river, and estuary waters, adsorption experiments were performed over 120 min to ensure that equilibrium was reached, at 21 °C under constant shaking at 1400 rpm ( $C_0(\text{TpBD}-(\text{CF}_3)_2) = 330 \text{ mg L}^{-1}$ , for more details, see experimental section 5.3.4.3). The natural water samples were spiked with ibuprofen at concentrations of 50  $\mu\text{M}$  and 100  $\mu\text{M}$ , the latter corresponding to the solubility limit of the compound in water. These concentrations, despite being much higher than expected of a contamination with pharmaceuticals in nature, where values between few  $\text{ng L}^{-1}$  to  $\mu\text{g L}^{-1}$  in locations close to wastewater effluents can be observed,<sup>[192,312]</sup> will allow us to compare the maximum capacity of the adsorbent previously observed in ultrapure water with the results obtained in this study.

At 100  $\mu\text{M}$ , the adsorption capacities,  $q_t$  ( $\text{mg g}^{-1}$ ) of  $\text{TpBD}-(\text{CF}_3)_2$  for ibuprofen were found to be 42, 27, and 14  $\text{mg g}^{-1}$  in lake, river, and estuary water, respectively (Table 11). By comparison, in our previous study in ultrapure water,  $q_e$  of 119  $\text{mg g}^{-1}$  was found with a lower COF loading of 100  $\text{mg L}^{-1}$ , corresponding to decreases of 65%, 77%, and 88%, for lake, river, and estuary waters, respectively. Such a reduction in adsorption capacity can be expected due to the complexity of natural water samples and could stem from the different physical-chemical parameters of the water samples, as well as due to the presence of dissolved organic matter or competing molecules.<sup>[311,313]</sup> Previous studies with COFs have indicated that the presence of humic acid can severely affect the extraction efficiency of organic contaminants, with a reduction of adsorption efficiency up to 40%.<sup>[59]</sup>

**Table 11.** Adsorption capacity,  $q_t$  ( $\text{mg g}^{-1}$ ), of ibuprofen by  $\text{TpBD}-(\text{CF}_3)_2$  at 21 °C in lake, river, and estuary water. ( $C_0(\text{TpBD}-(\text{CF}_3)_2) = 330 \text{ mg L}^{-1}$ ,  $C_0(\text{ibuprofen}) = 10.31$  and  $20.63 \text{ mg L}^{-1}$ ,  $t = 120 \text{ min}$ ).

	Lake	River	Estuary
<b>[<math>\mu\text{M}</math>]</b>	<b><math>q_t</math> (<math>\text{mg g}^{-1}</math>)</b>	<b><math>q_t</math> (<math>\text{mg g}^{-1}</math>)</b>	<b><math>q_t</math> (<math>\text{mg g}^{-1}</math>)</b>
<b>50</b>	26.2 $\pm$ 0.2	6.2 $\pm$ 2.1	9.7 $\pm$ 9.3
<b>100</b>	42.3 $\pm$ 0.3	27.2 $\pm$ 6.0	14.1 $\pm$ 2.6

The highest adsorption efficiency, 85%, was found in lake water (Figure 36), whereas in river and estuary water the efficiency was below 50%. This could be due to the lower pH of lake water as compared to the other water samples. This observation is supported by our previous results in section 2.2.1, where was found that adsorption of ibuprofen was enhanced by 25% when moving from neutral pH to pH 2, which was attributed to the higher lipophilicity of the compound at lower pH upon protonation of the carboxylic acid moiety. For ibuprofen with  $pK_a$  of 5.2, approximately 5% and 0.3% of the molecules are protonated at pH 6.5 and 7.7, respectively,<sup>[303]</sup> which could partially explain the increased adsorption capacity in lake water. On the other hand, the amount of organic matter can be expected to be higher in lake and estuary waters as compared to river water, which could also affect the adsorption of ibuprofen. Additionally, the higher salinity of estuary water as compared to river or lake water can hinder the adsorption of ibuprofen, as demonstrated in a recent study,<sup>[314]</sup> where the presence of  $CaCl_2$  and  $NaCl$  was found to significantly lower the adsorption capacity of a COF towards diclofenac, which was attributed to the cations competing for the adsorption sites with the pharmaceutical. However, a limited influence of this parameter was expected as the samples from estuary were collected from the first 1 m in the water column, which is mainly constituted by the river water. However, the day before the collection of samples a strong precipitation was registered, opening the possibility to the influence of organic matter and other ions from the outflow in the matrix effect.<sup>[315]</sup>

In order to gain insight into the differences of affinity of ibuprofen to  $TpBD-(CF_3)_2$  in the natural water samples, theoretical calculations on COF–ibuprofen interactions were carried out by collaborators Dr. Kovář and Dr. Pšenička from Charles University, in Czech Republic (for more details, see experimental section 5.1.3.2). Both protonated and deprotonated forms of ibuprofen were calculated to shed light on the differences in the adsorption efficiencies at different pH. In vacuo, both forms tend to adopt a very similar orientation in the COF pore (Figure 37A) with six molecules with a supercell containing one entire pore. The longitudinal axes of the molecules are mostly oriented along the COF pore axis and can also adopt a tilted arrangement with respect to the COF pore axis during the simulation. The binding area extends over the oxygen atoms of Tp and neighboring  $CF_3$  and

NH moieties of the COF, with the carboxy group located between the COF layers (Figure 37B).

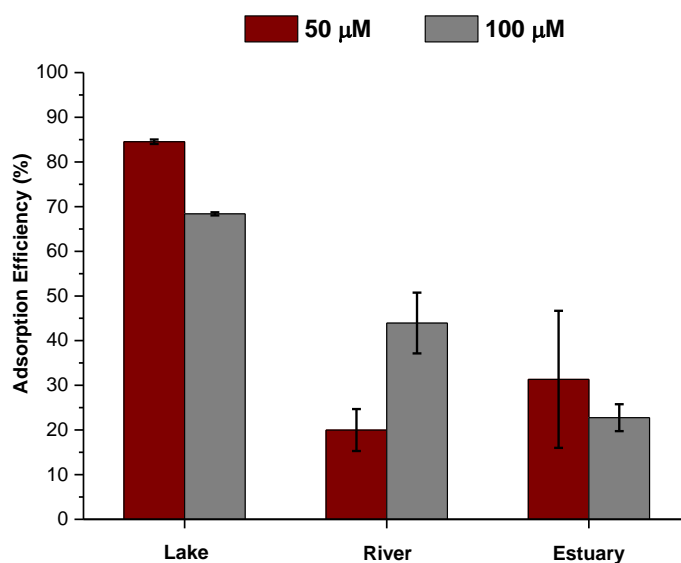


**Figure 36.** Adsorption efficiency (%) of ibuprofen by TpBD-(CF<sub>3</sub>)<sub>2</sub> in natural water samples collected from lake, river, and estuary ( $C_0(\text{TpBD}-(\text{CF}_3)_2) = 330 \text{ mg L}^{-1}$ ,  $C_0(\text{ibuprofen}) = 10.31$  and  $20.63 \text{ mg L}^{-1}$ ,  $t = 120 \text{ min}$ ).

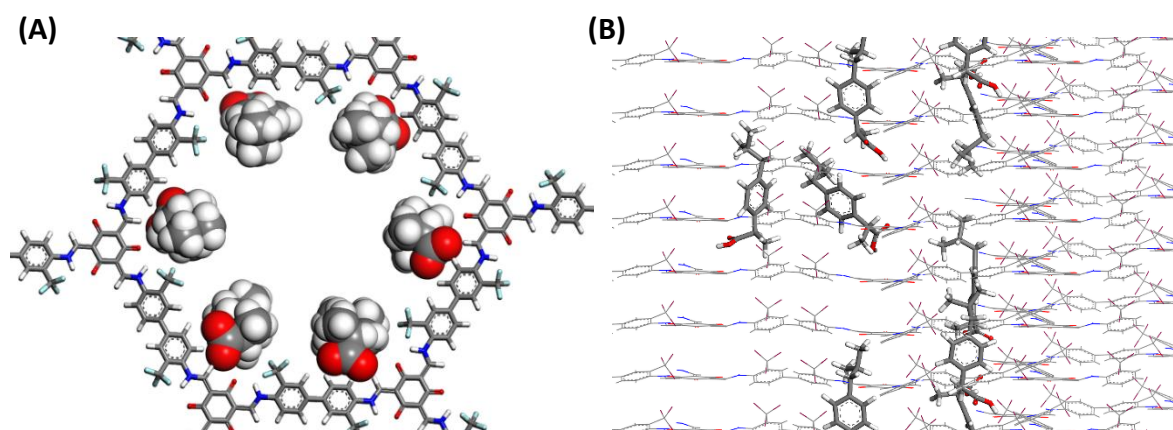


**Figure 37.** (A) A view along the TpBD-(CF<sub>3</sub>)<sub>2</sub> pore axis showing the orientations of six deprotonated ibuprofen molecules. (B) A view perpendicular to the TpBD-(CF<sub>3</sub>)<sub>2</sub> pore axis showing the protonated ibuprofen in tilted and parallel orientation with respect to the TpBD-(CF<sub>3</sub>)<sub>2</sub> pore axis.

Next, models were created with water containing two ibuprofen molecules in protonated or deprotonated form and they were located on the TpBD-(CF<sub>3</sub>)<sub>2</sub> surface or in the COF pore. The results showed that in all cases the molecules had the tendency to move into the COF pore. Thereafter, models were created by locating two ibuprofen molecules in protonated and deprotonated form each in the COF pore. This corresponds to a situation found at pH 5.2, where half of the molecules are protonated. Both protonated (Figure 38A) and deprotonated (Figure 38B) forms exhibit a very similar trend: they are located in the same binding area, in the corner of the COF pore formed by Tp, as in the case of models without water, and their longitudinal axes are nearly parallel to the COF pore axis. However, the carboxyl group of deprotonated ibuprofen faces the water environment, whereas protonation causes the molecule to flip and interact via hydrogen bonds with O atoms of Tp and NH moieties or form short contacts with the fluorine atoms of the CF<sub>3</sub> moiety. The average distance between the hydrogen atoms of the carboxy group and a fluorine or O atom of the COF is 2.7 Å.

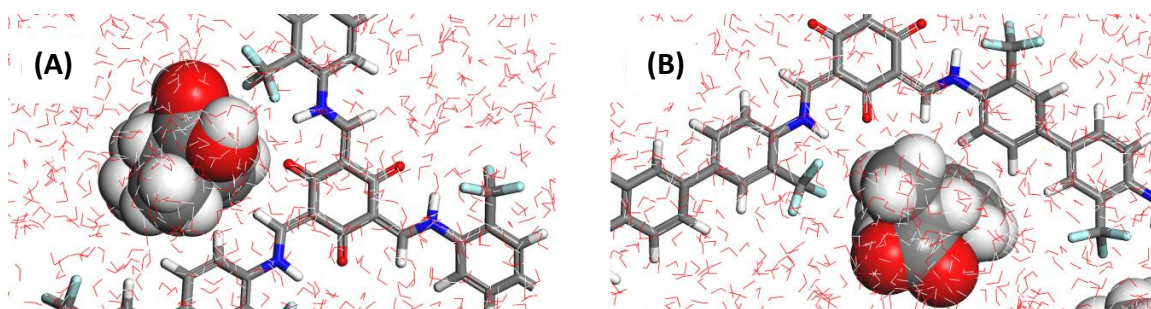


**Figure 38.** A view along the COF pore axis showing the orientations of protonated (A) and deprotonated (B) ibuprofen in water environment.

In the models with two ibuprofen molecules in the COF pore the average interaction per one ibuprofen molecule between the deprotonated form and the COF structure was  $-19 \text{ kcal mol}^{-1}$ , whereas for the protonated form a slightly enhanced value of  $-21 \text{ kcal mol}^{-1}$  was found. The main driving force was found to be van der Waals interactions with ca. 90%. A large difference in the interactions between water and the two ibuprofen forms was observed. In the protonated form, the interaction energy with water was comparable to that with the COF; i.e.,  $-20 \text{ kcal mol}^{-1}$ . However, a dramatic

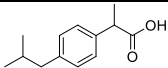
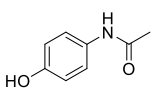
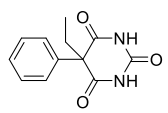
enhancement of interaction energy with water was found for the deprotonated form, giving an average value of  $-160 \text{ kcal mol}^{-1}$  per ibuprofen molecule. In the model at pH 5.2, this interaction was 7–8 times stronger compared to that of the protonated form. Therefore, ibuprofen in the deprotonated form has a much higher tendency to be solvated by water than to be adsorbed on the COF, which could account for the experimental results obtained with the natural water samples. With decreasing pH, the quantity of protonated ibuprofen increases, leading to enhanced tendency of the pharmaceutical to be adsorbed within the COF pores. Overall, according to theoretical calculations, ibuprofen interacts more favorably with the COF pores in the protonated form, which may partially account for the enhanced adsorption efficiency found in lake water.

In order to evaluate the effect of the presence of competing pharmaceuticals on ibuprofen adsorption, adsorption of binary mixtures of the compound with acetaminophen and phenobarbital was studied. Phenobarbital and acetaminophen were chosen due to their broad use and different physico-chemical properties (Table 12). Phenobarbital is still one of the most widely used antiepileptic drugs worldwide<sup>[316]</sup> and one of the active ingredients of the anticonvulsant primidone. Phenobarbital has been found in urban wastewater effluents at  $0.09\text{--}0.21 \mu\text{g L}^{-1}$  and at concentrations of  $\leq 0.05 \mu\text{g L}^{-1}$  in downstream surface waters.<sup>[317]</sup> On the other hand, acetaminophen is also frequently found in natural and drinking water worldwide, reaching concentrations of over  $500 \text{ ng L}^{-1}$  in river waters.<sup>[191,192,195,318]</sup> In our previous study in ultrapure water in section 2.1, acetaminophen was not efficiently adsorbed by TpBD-(CF<sub>3</sub>)<sub>2</sub>, which was attributed to its higher hydrophilicity ( $\log D_{6.0} = 0.34$ )<sup>[319]</sup> as compared to ibuprofen ( $\log D_{6.0} = 2.12$ ).<sup>[319]</sup> Phenobarbital, on the other hand, is more lipophilic than acetaminophen, but less than ibuprofen ( $\log D_{6.0} = 1.66$ ).<sup>[319]</sup>

First, the adsorption capacity of TpBD-(CF<sub>3</sub>)<sub>2</sub> for acetaminophen and phenobarbital was evaluated independently by spiking lake water with 50, 100, or 150  $\mu\text{M}$  of acetaminophen or phenobarbital. In virtue of the highest value found for ibuprofen adsorption in lake water (85%), lake water samples were selected to perform the additional tests using other pharmaceuticals. Adsorption experiment was conducted over 120 min to ensure that equilibrium was reached, at 21 °C under constant shaking at 1400 rpm

( $C_0(\text{TpBD}-(\text{CF}_3)_2) = 330 \text{ mg L}^{-1}$ , for more details, see experimental section 5.3.4.3). As expected, very low adsorption efficiency was found for acetaminophen, with values of 0.3%, 32%, and 28% recorded for 50, 100, and 150  $\mu\text{M}$ , respectively (Figure 39, green). The adsorption capacity of  $19 \text{ mg g}^{-1}$ , obtained at the highest concentration (Table 13), was similar to that found in our previous study, albeit with a lower COF loading. Phenobarbital showed low adsorption efficiencies, around 5%, at all concentrations tested (Figure 39, blue).

**Table 12.** The properties of the studied pharmaceuticals. Dimensions of pharmaceuticals were obtained by measuring the furthest distances of C, N, or O atoms from the X-ray crystal structures obtained from the Cambridge Structural Database (CSD) with the following codes: <sup>b</sup>CCDC-1041382, <sup>c</sup>CCDC-150969, <sup>d</sup>CCDC-1149948. <sup>a</sup>for more informations check also Table 8.

Pharmaceutical	$\log D_{6.0}$ <sup>[319]</sup>	Dimensions (Å)	Water solubility ( $\text{g L}^{-1}$ )	$\text{p}K_a$
 <b>Ibuprofen<sup>a</sup></b>	2.12	<sup>b</sup> 8.8 x 4.5 x 2.4	0.021 <sup>[302]</sup>	5.2 <sup>[303]</sup>
 <b>Acetaminophen<sup>a</sup></b>	0.34	<sup>c</sup> 7.9 x 2.4 x 0.8	14 <sup>[302]</sup>	9.5 <sup>[304]</sup>
 <b>Phenobarbital</b>	1.66	<sup>d</sup> 6.5 x 4.5 x 4.3	1 <sup>[320]</sup>	7.3 <sup>[320]</sup>

**Table 13.** Adsorption capacity,  $q_t$  ( $\text{mg g}^{-1}$ ), of TpBD-( $\text{CF}_3$ )<sub>2</sub> in binary mixtures of ibuprofen and acetaminophen or phenobarbital (concentration ratios of pharmaceuticals 50/150 and 100/100  $\mu\text{M}$ ,  $C(\text{TpBD-(CF}_3)_2) = 330 \text{ mg L}^{-1}$ ,  $t = 120 \text{ min}$ ).

[ $\mu\text{M}$ ]	Individual Pharmaceutical		Binary mixture
	Ibuprofen	Acetaminophen	Ibuprofen/Acetaminophen
50/150	$26.2 \pm 0.2$	$19.1 \pm 2.1$	$27.3 \pm 0.2 / 19.6 \pm 1.9$
100/100	$42.3 \pm 0.3$	$14.6 \pm 5.5$	$58.1 \pm 0.3 / 5.5 \pm 0.1$
[ $\mu\text{M}$ ]	Ibuprofen	Phenobarbital	Ibuprofen/Phenobarbital
	50/150	$26.2 \pm 0.2$	$6.6 \pm 2.4$
100/100	$42.3 \pm 0.3$	$3.3 \pm 3.5$	$57.3 \pm 0.1 / 1.3 \pm 1.2$

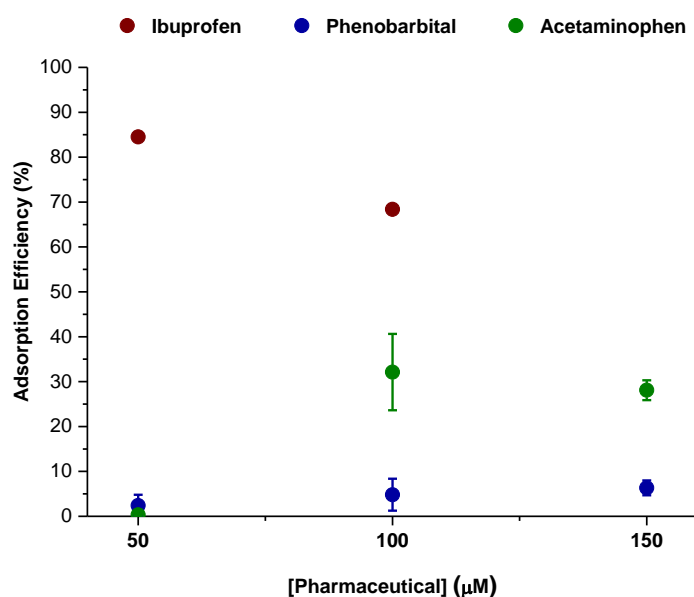


**Figure 39.** Adsorption efficiency (%) of ibuprofen (red) at concentrations of 50 and 100  $\mu\text{M}$ , and acetaminophen (green) and phenobarbital (blue) at concentrations of 50, 100, and 150  $\mu\text{M}$  by TpBD-( $\text{CF}_3$ )<sub>2</sub> in lake water. The experiment was performed in duplicate. ( $C_0(\text{TpBD-(CF}_3)_2) = 330 \text{ mg L}^{-1}$ ,  $t = 120 \text{ min}$ ).

After establishing the independent adsorption efficiency of all pharmaceuticals, adsorption experiments on binary mixtures were carried out. The total concentration of spiked pharmaceuticals was kept at 200  $\mu\text{M}$ , using ratios of 50/150 and 100/100  $\mu\text{M}$  for



each binary mixture under the same incubation conditions as described above (for more details, see experimental section 5.3.4.4).

When ibuprofen was combined with either acetaminophen or phenobarbital at 50/150  $\mu\text{M}$  ratio, the quantity of ibuprofen adsorbed by TpBD-(CF<sub>3</sub>)<sub>2</sub> remained the same (Figure 40, Table 13). In addition, the values of adsorption of acetaminophen and phenobarbital were not influenced as compared to the individual adsorption tests (Table 13). At a 100/100  $\mu\text{M}$  ratio, however, an increase of over 10  $\text{mg g}^{-1}$  was found for ibuprofen (Table 13), whereas decreases were observed for both acetaminophen and phenobarbital of about 38% and 40%, respectively (Figure 40). The reduction can be explained by the competitive adsorption of ibuprofen, a compound with high affinity to TpBD-(CF<sub>3</sub>)<sub>2</sub>, which hinders the adsorption of the other two pharmaceuticals. Many previous studies have reported how the presence of competing molecules can enhance the uptake of an adsorbate with higher affinity for the adsorbent.<sup>[321]</sup> However, the differential interference exerted by the NOM and different ions present in the water sample on each pharmaceutical cannot be ruled out in this study.

In summary, it was demonstrated that TpBD-(CF<sub>3</sub>)<sub>2</sub> can be used as an efficient adsorbent of ibuprofen even in natural water samples. The physical-chemical properties of the water determined the adsorption efficiency, and pH was identified as the key parameter. In agreement with the theoretical calculations, which showed the protonated form of ibuprofen to preferentially interact with the COF pores, the highest affinity of the COF adsorbent was found in lake water that featured slightly acidic pH. Finally, the results of competitive adsorption with other commonly found pharmaceuticals in water, acetaminophen and phenobarbital, tested as binary mixtures, showed that the adsorption efficiency of ibuprofen is not hindered, but enhanced by the presence of other lower affinity pharmaceuticals.

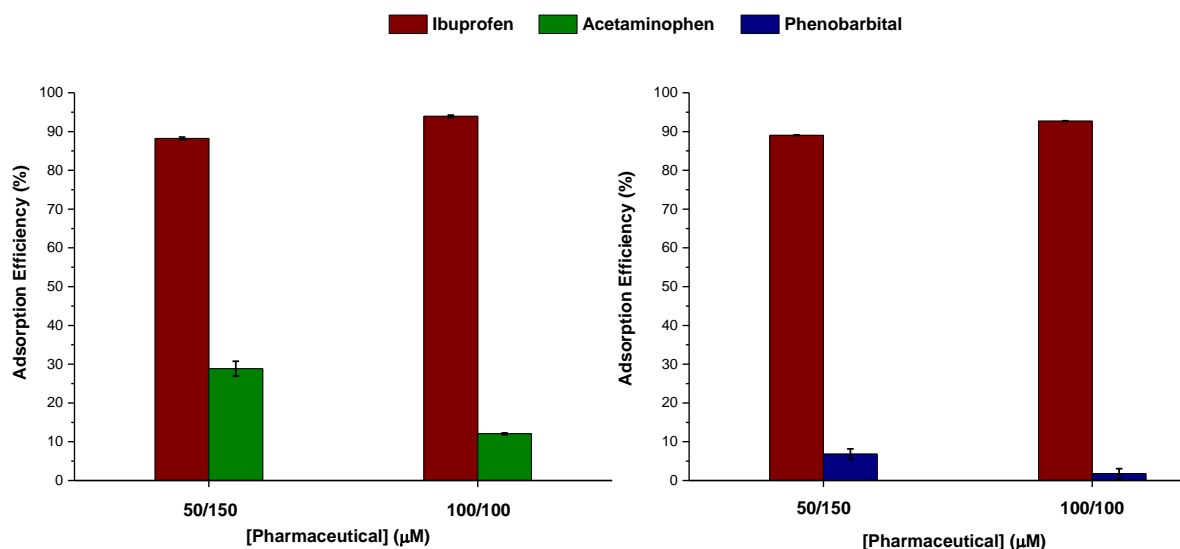


**Figure 40.** Adsorption efficiency (%) of binary mixtures of ibuprofen and acetaminophen or phenobarbital, at concentration ratios of 50/150 and 100/100  $\mu\text{M}$ , by  $\text{TpBD}-(\text{CF}_3)_2$  ( $C_0 = 330 \text{ mg L}^{-1}$ ) in lake water samples. ( $C_0(\text{TpBD}-(\text{CF}_3)_2) = 330 \text{ mg L}^{-1}$ ,  $t = 120 \text{ min}$ ).

### 2.2.3. Screening of pharmaceutical pollutants in Tagus estuary using COF as adsorbent – an environmental case study<sup>[250]</sup>

To date, tracking the presence of pharmaceutical pollutants in natural waters is still a challenge because of low analyte concentrations and complex matrix effects, particularly in estuarine and marine waters. Thus, preparation steps are often required to both concentrate and purify samples, and isolate analytes from the potential confounding effects of natural environmental matrices. Due to the low concentrations and limits of detection and quantification of the analytical methods, clean-up and pre-concentration steps are always needed. Usually, this is attained by SPE columns filled with broad-spectrum resins, which can retain both hydrophilic and hydrophobic molecules. Using this approach, in a recent study 32 pharmaceuticals of different classes were found in the Tagus estuary in Portugal, associated with direct input from urban wastewater treatment outfalls and indirect input via river discharge, highlighting the need of efficient monitoring programs.<sup>[195]</sup>

In the previous studies<sup>[61,248]</sup> detailed in sections 2.2.1 and 2.2.2, it was demonstrated that  $\text{TpBD}-(\text{CF}_3)_2$  can capture single pharmaceutical pollutants, i.e. ibuprofen, from

ultrapure water with high efficiency, allowing for the recovery of both the adsorbent and the pharmaceutical by a simple solvent exchange, with the material displaying good stability in the different organic solvents and water. In addition, it was demonstrated that ibuprofen can be efficiently extracted from spiked natural water samples, also in competition with other pharmaceuticals, although with slightly reduced adsorption efficiency in the real environmental water as compared to ultrapure water. Taking these results into consideration and in collaboration with Dr. Vanessa Fonseca and Dr. Patrick Reis-Santos at Marine and Environmental Sciences Centre (MARE) of University of Lisbon, the potential of COFs as passive adsorbents to be used for the screening of pharmaceuticals in unspiked real water samples was evaluated for the first time to corroborate if their use *in situ* as passive sampler could substitute and simplify the water sample collection and treatment in the laboratory.

The selected COF TpBD-(CF<sub>3</sub>)<sub>2</sub> was prepared as described on section 2.1.2, and successfully characterized to ascertain its high quality (for more details see experimental sections 5.2.7 and 5.4). Then, TpBD-(CF<sub>3</sub>)<sub>2</sub> was used for environmental monitoring of pharmaceutical pollutants present in natural water samples of Tagus estuary and the obtained results were benchmarked against state-of-the-art SPE method. The effect of acidification of the water samples as well as filtration procedures were also studied.

Water samples (500 mL) were collected for analysis on the 18<sup>th</sup> of June of 2019, in the Tagus estuary from the vicinity of a wastewater treatment outfall that serves a large urban area (38°78'72.3''N, -9°09'09.98''W). Water samples' physical and chemical parameters were measured upon collection, and mean and standard deviation of water salinity, temperature (°C), and pH levels were 4.7 ± 0.6, 24.1 ± 0.04, and 8.1 ± 0.1, respectively.

A pharmaceutical extraction methodology based on a standard SPE procedure was carried out as described<sup>[195]</sup> with some modifications (Figure 41, for more details, see experimental section 5.3.5.1). For benchmarking, standard SPE adsorption experiments were performed using OASIS HLB cartridges. To evaluate the efficiency of the COF, three different methods were employed. To mimic the conditions of the standard method, in

Method 1 (Figure 41), the water samples were acidified to pH 2, filtered, and subjected to passive adsorption by COF for 4 h with a subsequent desorption of the extracted compounds by soaking the COF in propan-2-ol. In Method 2 (Figure 41), the same steps were followed but without acidification. Finally, to test the influence of acidification on the regular procedure, in Method 3 (Figure 41) the water samples without acidification were subjected to SPE by OASIS HLB cartridges. The water samples were analyzed by UHPLC-TOF-MS (for more details, see experimental section 5.3.5.2) after treatment with the COF (*adsorption efficiency*, Table 14), as well as the desorption solution after elution from the COF using propan-2-ol (*detected*, Table 14).

Results show that 19 out of the 23 pharmaceuticals (Figure 42 and 43) recovered from the water by the SPE standard procedure were also detected when applying passive adsorption with the COF with or without acidification (Method 1 and 2, respectively, Table 14). Furthermore, detection efficiencies of >50% (Table 14, asterisk) as compared with the SPE standard procedure were found for 10 pharmaceuticals in Method 1 (COF) and 6 pharmaceuticals in Method 2 (COF without acidification). Finally, in 5 cases the passive adsorption of pharmaceuticals by the COF outperformed the standard SPE (Table 14, in bold).

Passive adsorption by the COF worked particularly well for antibacterial antibiotics sulfamethoxazole and sulfapyridine, which were recovered by the COF at efficiencies of 430% and 3387%, respectively, when the water samples were not acidified (Figure 42 and Table 14). Interestingly, the detection efficiency is significantly decreased with Method 1. A similar trend is observed with SPE upon comparing Method 3 with the SPE standard procedure. At pH 2, the amino group of sulfapyridine is partially positively charged ( $pK_a = 2.2$ ),<sup>[322]</sup> which could hamper the interaction with the adsorbents, thus explaining the reduction in adsorbed quantity. We measured the point of zero charge of the COF to be  $pH_{pzc} = 3.86$  (Figure 112, for more details, see experimental section 5.4.8), indicating that at pH 2 the positive charge of the surface could lead to repulsions with sulfapyridine. Of particular interest is the case of topiramate, as with  $154 \text{ ng L}^{-1}$  its concentration is among the highest for pharmaceutical residues measured in the waters of the Tagus estuary using

SPE, but also because acidification significantly increased the efficiency with which it was recovered by the COF material (125% for Method 1).

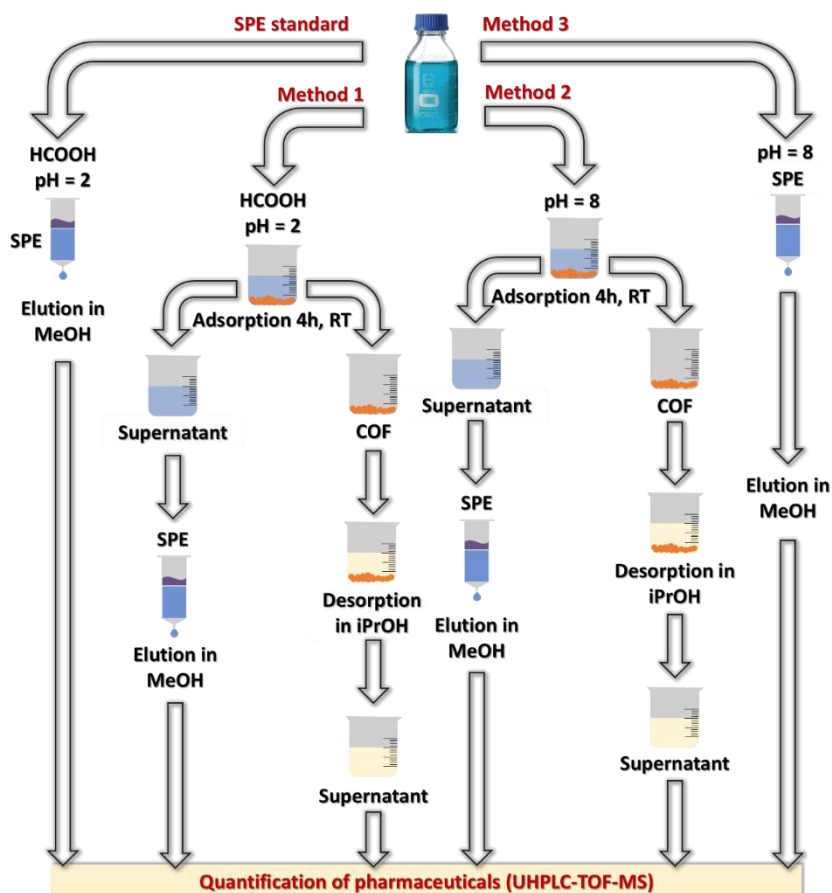


**Figure 41.** Overview of the studied methods.

In contrast, higher efficiency in detection of topiramate was observed without acidification in the SPE resin (Method 3). Topiramate features a sulfonamide moiety with a  $pK_a$  of 8.6, which is partially deprotonated at the pH 8 of Methods 2 and 3. At this pH, the COF surface has a partial negative charge, which could prevent more efficient adsorption of topiramate due to electrostatic repulsions when the media was not acidified.

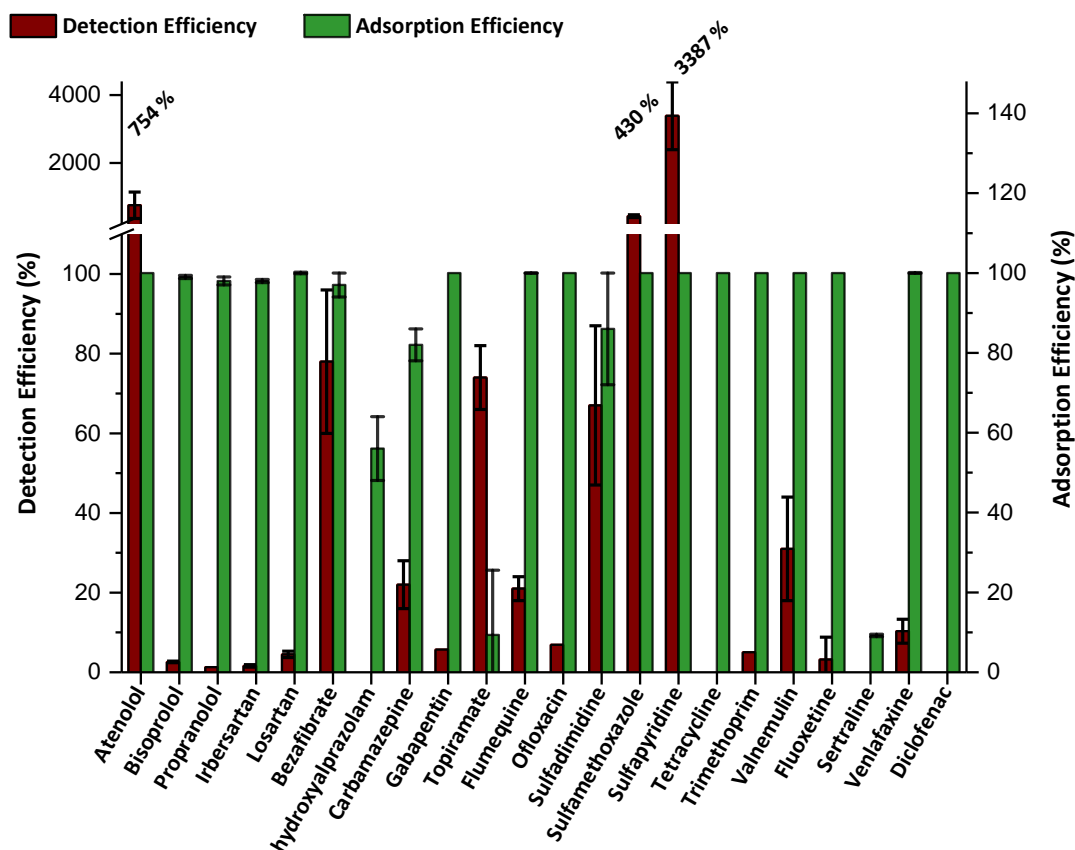


**Figure 42.** Detection and adsorption efficiencies (%) obtained for all identified pharmaceuticals with Method 2 in Tagus estuary. Results are the average of 5 samples collected in the same site.

When analyzing the adsorption efficiency of the COF in Method 2, which takes into account the amount of pharmaceuticals remaining in the water after adsorption, it can be observed that all drugs except  $\alpha$ -hydroxyalprazolam, topiramate, and sertraline were extracted from the water with efficiencies above 80%. In fact, out of the 22 pharmaceuticals, 17 show an adsorption efficiency of >96%. This is a highly promising result considering that passive adsorption was used instead of forcing the sample through the adsorbent, as in the case of the SPE. However, low detection efficiencies were observed for bisoprolol, propranolol, irbesartan, losartan, gabapentin, flumequine, ofloxacin, tetracycline, trimethoprim, valnemulin, fluoxetine, venlafaxine, and diclofenac. In our first study in ultrapure water described on section 2.2.1, TpBD-(CF<sub>3</sub>)<sub>2</sub> adsorbed diclofenac with high efficiency, and therefore we postulated that the desorption method based on

propan-2-ol used herein was not efficient to recover these pharmaceuticals from the COF material. In fact, 8 of the above-mentioned 13 pharmaceuticals feature  $\log P$  values  $>2$ , suggesting that lipophilicity could play a role in the inefficient desorption. To corroborate this, we performed sequential desorption of three samples with acetonitrile, acetone, and dichloromethane, and quantified the detection efficiencies for diclofenac. Large quantities of the pharmaceutical were found in acetonitrile ( $10,123 \pm 847 \text{ ng L}^{-1}$ ) and acetone ( $7124 \pm 1114 \text{ ng L}^{-1}$ ), whereas in the last desorption with dichloromethane, no further release of diclofenac was detected. The total concentration of diclofenac found,  $17,247 \pm 1610 \text{ ng L}^{-1}$ , is already above the range of micropollutants in natural water samples and nearing those of heavy metals.<sup>[323]</sup> It should be taken into account that the data in Table 14 were obtained using UHPLC-TOF-MS with electrospray ion source in positive mode (for more details, see experimental section 5.3.5.2), whereas the desorption data of diclofenac was obtained in negative mode (for more details, see experimental section 5.3.5.4), therefore preventing the direct comparison of these results. To corroborate this result, Palma and co-workers<sup>[318]</sup> have recently reported a high concentration of diclofenac in Guadiana river basin of up to  $4806 \text{ ng L}^{-1}$  using negative electrospray ionization with UPLC-HR-QTOF-MS. An integrated analysis of the detection results obtained with all the methods reveals that 11 of the 23 pharmaceuticals recovered with the standard SPE method are underestimated (Table 14, in bold), four of them heavily (Table 14, asterisk). Interestingly, Method 3 outperformed the standard SPE in 10 out of the 23 pharmaceuticals found in the water samples, to a maximum increase of 4128% in the detection of sulfapyridine. This demonstrates that acidification of the samples can heavily jeopardize the estimation of the pharmaceutical occurrence in water, with major implications in environmental and human health risk assessment.

The WHO has established a maximum level of  $10 \text{ ng L}^{-1}$  as a general safe threshold for the presence of pharmaceuticals in natural waters.<sup>[167]</sup> Above this limit, the ecotoxicity, bioaccumulation, and persistence of the drug needs to be studied to perform a proper risk evaluation. In this study, atenolol, sulfamethoxazole, and sulfapyridine appeared at a higher concentration than the established threshold in Method 3 (75, 13, and  $118 \text{ ng L}^{-1}$ , respectively), but not when using the regular procedure. Considering the current problems

with antimicrobial resistance,<sup>[324]</sup> unreported high levels of antibiotics, such as sulfapyridine and sulfamethoxazole, in surface waters could help to explain some of the observed effects and stress the necessity of taking a closer look into this issue.<sup>[325]</sup> Antibiotic concentrations in aquatic environments have generally been found to range from  $\text{ng L}^{-1}$  to low  $\mu\text{g L}^{-1}$  levels.<sup>[326][327][328]</sup>

To conclude, with this study the utility of COFs for the passive adsorption of pharmaceuticals found in unspiked natural water samples was demonstrated for the first time. Of the 23 pharmaceuticals detected in the water samples from the Tagus river estuary using state-of-the-art SPE, 22 were also detected (adsorbed and recovered for analysis) using the COF as the adsorbent material with adsorption efficiency over 80% for nearly all compounds. In the case of  $\alpha$ -hydroxyalprazolam and diclofenac, the COF outperformed the SPE procedure in the recovery efficiency. In specific cases, acidification of the water samples was identified to lead to a dramatic loss of extraction efficiency, underlining the effect of sample pre-treatment on the results. *In situ* passive adsorption would simplify sample collection and processing, opening interesting alternatives for regular monitoring programs of emerging contaminants in water. However, establishing efficient desorption strategies is crucial to allow for the use of COFs for this purpose, as indicated by the results with diclofenac. Finally, it is very important to stress that many of the pharmaceuticals found exceeded the precautionary maximum concentration established by the WHO ( $10 \text{ ng L}^{-1}$ ), indicating, once again, that a revision of the monitoring programs for priority substances should be implemented.



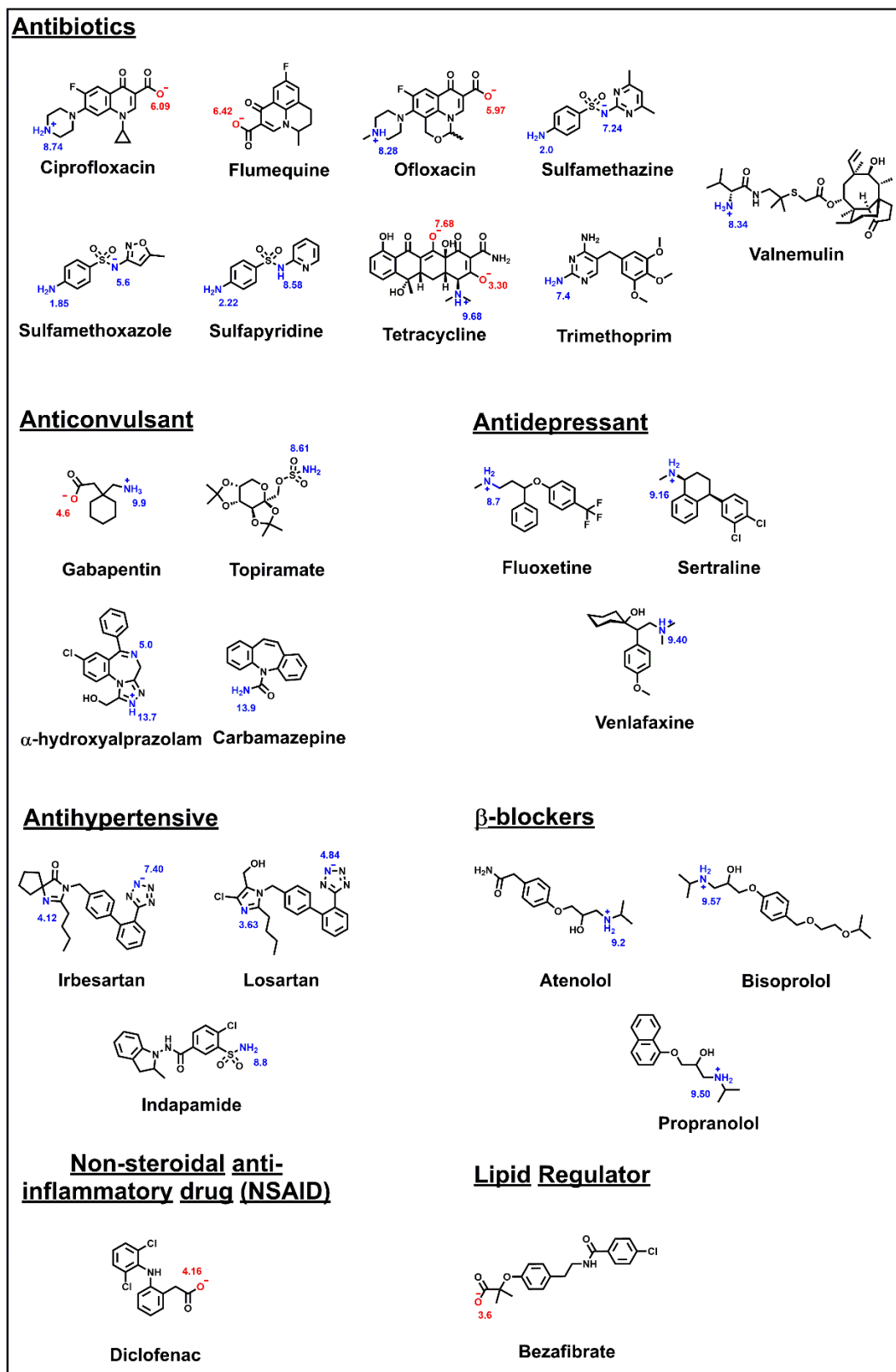


**Figure 43.** The structures of the pharmaceuticals at pH 8. The pK<sub>a</sub> values of the relevant functional groups are presented in the figures in red and blue.

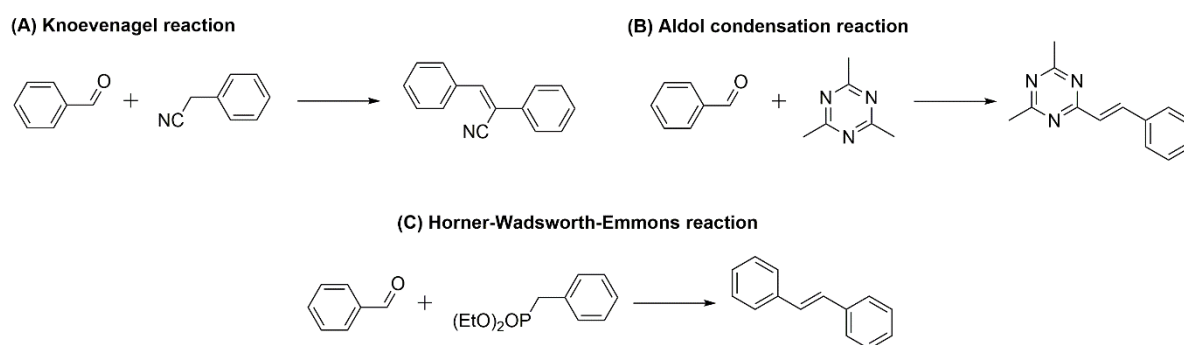
## Chapter 2 – Tailoring COFs for the adsorption of hazardous compounds

**Table 14.** Pharmaceutical occurrence found in waters collected in the Tagus river estuary. LOQ: limit of quantification; nd: not detected. The pharmaceuticals detected with an efficiency >50% of the SPE are marked with \*; results outperforming standard SPE are indicated in boldface. Concentrations and % are expressed as average values of the 5 samples ± standard deviation. In brackets: the detected interval in the 5 samples.

Therapeutic group	Pharmaceutical	SPE standard	Method 1			Method 2			Method 3	
		[ng L <sup>-1</sup> ]	[ng L <sup>-1</sup> ]	Detected (%)	Adsorption Efficiency (%)	[ng L <sup>-1</sup> ]	Detected (%)	Adsorption Efficiency (%)	[ng L <sup>-1</sup> ]	Detected (%)
<b>β-blocker</b>	Atenolol	6.6 ± 1.9 [3.4–8.2]	4.7 ± 1.1 [3.8–6.6]	81 ± 32*	100 ± 0.0	42.3 ± 6.5 [34.7–49.7]	<b>754 ± 390*</b>	100 ± 0.0	75.1 ± 20.4 [54.9–106.1]	<b>1425 ± 1003*</b>
	Bisoprolol	53.3 ± 1.4 [51.5–55.4]	22.1 ± 1.53 [20.74–24.6]	42 ± 3	96 ± 3	1.4 ± 0.1 [1.3–1.5]	2.6 ± 0.2	99 ± 0.4	66.9 ± 9.1 [57.8–79.2]	<b>125 ± 16*</b>
	Propranolol	4.7 ± 0.4 [4.2–5.2]	1.4 ± 0.1 [1.2–1.6]	29 ± 3	95 ± 5	< LOQ	< LOQ	98 ± 1	3.7 ± 0.9 [2.2–4.6]	79 ± 17**
<b>Antihypertensive</b>	Irbesartan	628.2 ± 49.3 [574.2–687.6]	6.1 ± 0.9 [5.2–7.3]	1 ± 0.1	99 ± 0.9	10.1 ± 1.5 [8.2–11.6]	1.6 ± 0.3	98 ± 0.4	251.1 ± 66.7 [135.9–295.3]	40 ± 9.8#
	Losartan	34.7 ± 2.8 [31.5–37.9]	0.3 ± 0.1 [0.3–0.5]	0.9 ± 0.2	88 ± 16	1.6 ± 0.2 [1.4–1.8]	4.5 ± 0.8	100 ± 0.2	18.5 ± 3.1 [14–22.4]	53 ± 7#
	Indapamide	nd	nd	nd	nd	nd	nd	nd	2.6 ± 1.0 [1.7–4.2]	nd
<b>Lipid regulator</b>	Bezafibrate	15.6 ± 2.5 [12.9–19.7]	nd	nd	4.1 ± 7.2	11.8 ± 1.4 [9.8–13.8]	78 ± 18*	97 ± 3	23.5 ± 4.3 [18–29.9]	<b>152 ± 26*</b>
<b>Anticonvulsant</b>	α-hydroxyalprazolam	4.3 ± 0.5 [3.6–4.8]	4.7 ± 0.4 [4.3–5.2]	<b>110 ± 18*</b>	100 ± 0.0	nd	nd	56 ± 8	4.2 ± 0.6 [3.4–4.9]	102 ± 26*
	Carbamazepine	214.4 ± 12.8 [201.8–231.10]	109.6 ± 10.3 [95.2–123.4]	51 ± 2*	56 ± 6	46.7 ± 10.3 [36.4–62.3]	22 ± 6	82 ± 4	216.5 ± 33.7 [171.7–265.9]	101 ± 15*
	Gabapentin	14.2 ± 5.3 [5.5–18.5]	7.9 ± 3.9 [4.3–14.6]	62 ± 29*	100 ± 0.0	< LOQ	< LOQ	100 ± 0.0	< LOQ	< LOQ
<b>Antibiotic</b>	Topiramate	153.5 ± 4.7 [149.6–161.3]	190.6 ± 25.1 [148.6–214.9]	<b>125 ± 19*</b>	59 ± 3	113 ± 14.9 [91.7–131.5]	74 ± 8*	9.3 ± 16.2	222.5 ± 35.9 [174.2–275.4]	<b>145 ± 23*</b>
	Ciprofloxacin	< LOQ	< LOQ	< LOQ	< LOQ	< LOQ	< LOQ	< LOQ	< LOQ	< LOQ
	Flumequine	240.1 ± 18.3 [221.7–266.6]	29.5 ± 4.1 [23.6–34.6]	12 ± 1	91 ± 6	49.9 ± 8.3 [38.2–61.5]	21 ± 3	100 ± 0.04	179.5 ± 41.6 [137.5–246.2]	75 ± 14**
	Ofloxacin	14.3 ± 2.2 [11.9–17.3]	< LOQ	< LOQ	100 ± 0.0	< LOQ	< LOQ	100 ± 0.0	4.6 ± 0.8 [3.4–5.6]	32 ± 2#
	Sulfadimidine/ Sulfamethazine	28.3 ± 3.1 [23.5–31.4]	5.5 ± 1.0 [3.8–6.5]	20 ± 5	57 ± 25	18.7 ± 5.4 [13.2–26.9]	67 ± 20*	86 ± 14	21.5 ± 6.8 [14.6–28.6]	76 ± 23**
	Sulfamethoxazole	1.6 ± 0.3 [1.33–1.99]	nd	nd	100 ± 0.0	6.8 ± 1.7 [5.3–9.7]	<b>430 ± 41*</b>	100 ± 0.0	12.5 ± 11.9 [2.8–32.9]	<b>808 ± 753*</b>
	Sulfapyridine	2.2 ± 1.5 [1.7–3.7]	3.1 ± 1.1 [2.2–4.9]	<b>143 ± 0.6*</b>	92 ± 14	90.44 ± 9.7 [81.4–103.9]	<b>3387 ± 997*</b>	100 ± 0.0	118.2 ± 38.2 [72.6–166.2]	<b>4128 ± 794*</b>
<b>Antidepressant</b>	Tetracycline	8.8 ± 1.5 [7.3–11.3]	4.9 ± 1.01 [3.3–5.8]	57 ± 11*	100 ± 0.0	nd	nd	100 ± 0.0	nd	nd#
	Trimethoprim	15.9 ± 0.9 [14.8–16.8]	13.4 ± 0.3 [13.06–13.8]	85 ± 3*	100 ± 0.0	< LOQ	< LOQ	100 ± 0.0	19 ± 3.5 [15.5–23.9]	<b>120 ± 19*</b>
	Valnemulin	12.1 ± 0.7 [11.2–13.0]	6.5 ± 0.7 [6.0–7.7]	54 ± 9*	100 ± 0.0	3.7 ± 1.4 [1.7–5.6]	31 ± 13	100 ± 0.0	13.4 ± 1.6 [11.4–15.9]	<b>110 ± 10*</b>
	Fluoxetine	3.0 ± 0.24 [2.6–3.2]	0.5 ± 0.1 [0.3–0.7]	18 ± 5	100 ± 0.0	0.1 ± 0.2 [3.2–5.6]	3.2 ± 5.6	100 ± 0.0	0.24 ± 0.2 [0.2–0.4]	8.4 ± 5.7#
	Sertraline	3.1 ± 0.7 [2.0–3.7]	nd	nd	100 ± 0.0	nd	nd	9.2 ± 0.3	nd	nd#
<b>NSAID</b>	Venlafaxine	151.7 ± 1.9 [148.4–153.4]	142.9 ± 8.2 [132.3–154.2]	94 ± 5*	100 ± 0.3	15.6 ± 4.8 [8.6–20.9]	10.3 ± 3	100 ± 0.1	181.7 ± 28.5 [152.2–219.1]	<b>119 ± 18*</b>
	Diclofenac	60.7 ± 8.5 [50.7–73.8]	nd	nd	31 ± 19	nd	nd	100 ± 0.0	198.2 ± 23.4 [166.7–231.0]	<b>329 ± 41*</b>

### Chapter 3 – Expanding chemical synthesis of sp<sup>2</sup>-based COFs

Since the first report in 2016,<sup>[88]</sup> the variety of 2D sp<sup>2</sup>-based COFs expanded due to their incomparable features of high  $\pi$ -conjugation, crystallinity, permanent porosity, outstanding chemical stability, and unique optoelectronic properties.<sup>[89,329]</sup> Over the past five years some progresses in chemistry have been done to expand the development of sp<sup>2</sup>-based COFs, however more research need to be performed to disclose its design principles and synthetic routes. To date, for the synthesis of sp<sup>2</sup>-based COFs, Knoevenagel condensation (Scheme 6A),<sup>[88,330–332]</sup> aldol condensation (Scheme 6B),<sup>[333–335]</sup> as well as, more recently, the Horner–Wadsworth–Emmons (Scheme 6C)<sup>[336]</sup> reaction have been used for the formation of C=C bonds. The Knoevenagel condensation reaction gives access to a structural diversity of cyano-substituted sp<sup>2</sup>-based COFs with high crystallinity, while aldol condensation, as well as the Horner–Wadsworth–Emmons reaction, can yield unsubstituted sp<sup>2</sup>-based COFs with thus far limited scope due to the restricted building block selection.<sup>[89,329]</sup> Cyano-substituted sp<sup>2</sup>-based COFs despite their high quality and permanent porosity, have shown low hydrolytic stability arising from the strong electron-withdrawing cyano groups appended to C=C bonds which by steric hindrance induce structural twisting of the linkage, leading to a decrease on their crystallinity.<sup>[89]</sup> On the other hand, unsubstituted sp<sup>2</sup>-based COFs, such as the first reported COF-701,<sup>[334]</sup> feature enhanced stability, even in the presence of strong acids like BF<sub>3</sub>•OEt<sub>2</sub>, bases, as well as organolithium reagents.



**Scheme 6.** Representation of synthetic strategies reported for the synthesis of sp<sup>2</sup>-based COFs.

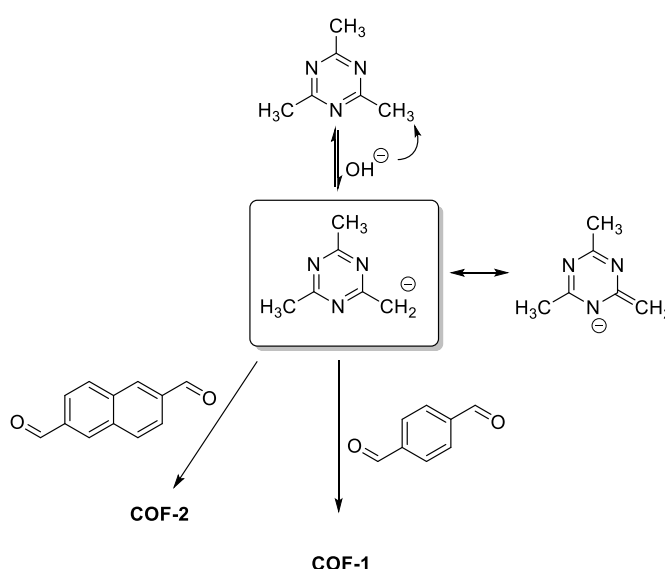
Similarly to other type of COF derivatives, the formation of crystalline sp<sup>2</sup>-based COFs is highly dependent of synthetic conditions which modulate the thermodynamic equilibrium of C=C covalent bond formation.<sup>[89,329]</sup> So far, solvothermal conditions have been employed with reaction times ranging from 3 to 5 days, at temperatures between 80 and 180 °C, with the aid of catalysts, most commonly bases (e.g. Cs<sub>2</sub>CO<sub>3</sub>,<sup>[88,337]</sup> NaOH,<sup>[330,338]</sup> KOH,<sup>[331]</sup> DBU,<sup>[339]</sup> and piperidine<sup>[335,340]</sup>). More recently, the use of acids (e.g. trifluoroacetic acid<sup>[334,341]</sup>) as catalyst in aldol condensation has been reported as an alternative approach; however still very few sp<sup>2</sup>-based COFs structures have been described using this approach.

In virtue of their unparalleled combination of structural features, sp<sup>2</sup>-based COFs have been exploited in applications, such as energy storage,<sup>[88,337,340]</sup> photocatalysis,<sup>[335,339,342–346]</sup> and adsorption, mainly on radionuclides sequestration.<sup>[51,52,54,79,347–350]</sup> Owing to their fully conjugated backbone, sp<sup>2</sup>-based COFs exhibit high  $\pi$ -electron delocalization along the 2D lattice, which enhances charge carrier transport across the network. The combination of outstanding optical properties and high chemical stability make sp<sup>2</sup>-based COFs very interesting for photocatalytic degradation of contaminants. To date, a triazine-based unsubstituted sp<sup>2</sup>-based COF (TTO-COF) with high chemical stability under harsh conditions and broad light absorption with an optical bandgap of 2.46 eV has been reported for efficient photocatalytic degradation of organic dyes methyl orange (MO) and methylene blue (MB) in aqueous medium, outperforming its counterpart imine-linked COF.<sup>[341]</sup> Thus, further exploration of novel sp<sup>2</sup>-based COFs for photocatalytic degradation of organic pollutants is a very interesting field of research.

### 3.1. Selection of building block units – model system preparation

For the synthesis of high-quality sp<sup>2</sup>-based COFs, the selection of monomers is very important, which should incorporate oriented and very reactive functional groups. Recently, the combination of aryl aldehydes with electron-deficient mesitylene monomers (e.g. triazine derivatives) or phosphonates have been explored as an efficient strategy to develop new sp<sup>2</sup>-based COFs (Scheme 6B and C).<sup>[89,329]</sup> First, it has been demonstrated that the acidity of methyl groups placed on an electron-deficient heterocycle unit (e.g. triazine

unit) have tendency to increase<sup>[334,341]</sup>, which favors the deprotonation of the methyl groups under basic conditions, so they can react with aldehyde counterparts eventually forming a C=C bond.<sup>[333]</sup> This strategy was proven with the synthesis of the two crystalline COF-1 and COF-2 in 2019 by Perepichka (Scheme 7).<sup>[333]</sup> Similarly, through an acid-catalyzed aldol condensation reaction between the reactive methyl groups of a triazine derivative and aryl aldehydes, the synthesis of sp<sup>2</sup>-based COFs was also successfully achieved, as demonstrated for 2D COF-701.<sup>[334]</sup> To this end, the goal in this thesis was to expand the building block selection that can be used to construct sp<sup>2</sup>-based COFs.



**Scheme 7.** Synthesis of COF-1 and COF-2<sup>[333]</sup> via aldol condensation of trimethyltriazine with reactive aldehyde derivatives terephthalaldehyde and naphthalene-2,6-dicarbaldehyde, respectively, under basic conditions.

Several methyl-bearing electron-deficient heterocycles were chosen to be tested for C=C bond formation (Figure 44). 4,7-Phenanthroline derivatives, featuring an extended and electron-poor  $\pi$ -conjugated system,<sup>[351]</sup> have shown on single crystal structure ability to establish  $\pi$ - $\pi$  interactions, hypothesizing its relevance during COF nucleation process.<sup>[352]</sup> 1,3,4-Thiadiazole and 1,2,4,5-tetrazine are very electron deficient due to the electron-withdrawing effect of the nitrogen atoms, which increases the acidity of the methyl groups (Figure 44).<sup>[353]</sup> Likewise, 1,2,4,5-tetrafluorobenzene has a very electron-deficient aromatic system owing to the presence of highly electronegative

fluorine units, which should enrich the reactivity of methyl groups (Figure 44).<sup>[286,354]</sup> To date, no COFs have been reported incorporating these kind of functional building blocks. With this in mind, the synthesis of novel sp<sup>2</sup>-based COFs was explored using 3,8-dimethyl-4,7-phenanthroline (Phen), 2,5-dimethyl-1,3,4-thiadiazole (Tda), 3,6-dimethyl-1,2,4,5-tetrazine (Tz), and 2,3,5,6-tetrafluoro-*p*-xylene (Tf) (Figure 44) as the reactive methylated electron-deficient building units, and 1,3,5-triformylbenzene (TFB) as the aldehyde counterpart. Prior to COF formation, studies on the synthesis of the molecular model compounds were performed by aldol condensation of the selected electron-deficient building blocks (Figure 44) with benzaldehyde (**1**), in order to optimize the experimental conditions.

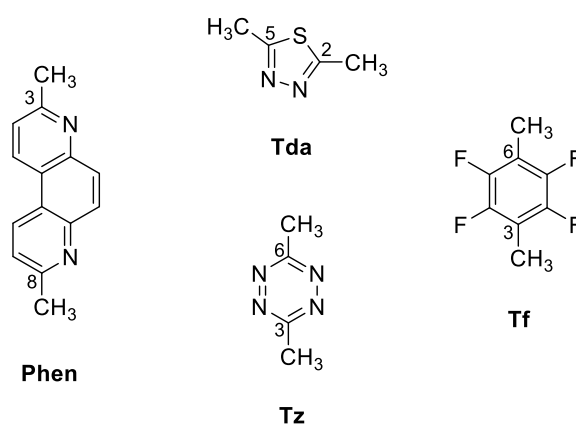
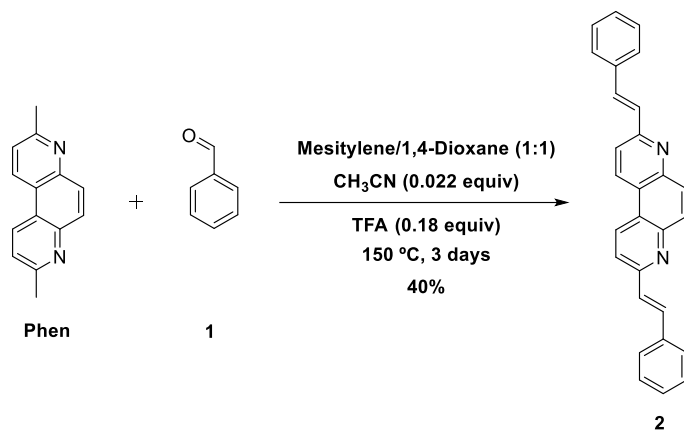


**Figure 44.** Electron-deficient building blocks selected to be tested for the synthesis of sp<sup>2</sup>-based COFs.

First, the synthesis of model compound **2** was explored by reacting Phen with benzaldehyde (**1**) (Scheme 8). The conditions<sup>[333]</sup> tested first were those typically used for this type of aldol condensation, where Phen was reacted with 6 equiv of benzaldehyde in 1,4-dioxane using aqueous 2 M KOH as catalyst (Table 15, entry 1). No formation of model compound **2** was observed, and only the presence of a mixture of starting materials was seen by <sup>1</sup>H NMR analysis. Similarly, replacement nucleophilic KOH base by the non-nucleophilic strong base KO<sup>t</sup>Bu also did not result in the formation of model compound **2** (Table 15, entry 2). Increasing the solvent polarity by using highly polar solvents DMF and DMSO with two different bases, KO<sup>t</sup>Bu and piperidine (Table 15,

entries 3–5), did also not yield the desired model compound. Finally, following acid-catalyzed aldol condensation conditions described by Yaghi<sup>[334]</sup> for the synthesis of COF-701, model compound **2** was successfully prepared in 40% yield in a mixture of mesitylene, 1,4-dioxane, and acetonitrile, using trifluoroacetic acid (TFA) as catalyst (Table 15, entry 6, for more details on the synthesis and characterization, see experimental sections 5.2.8, 5.4.1, and 5.4.3).



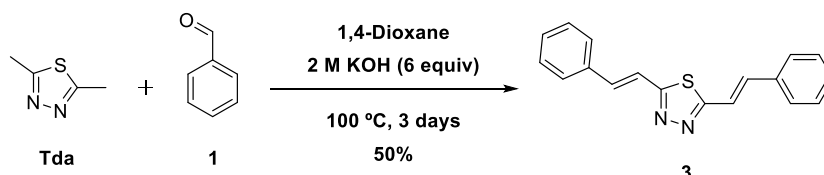
**Scheme 8.** Synthesis of model compound **2** in 40% yield from reaction of Phen with benzaldehyde (**1**).

**Table 15.** Experimental conditions tested for the synthesis of model compound **2**.

Entry	Solvents	Catalyst (equiv)	T (°C)	Product <sup>a</sup>
1	1,4-Dioxane	2 M KOH (6.0)	100	– <sup>b</sup>
2	1,4-Dioxane	KOtBu (1.0)	100	– <sup>b</sup>
3	DMSO	KOtBu (1.0)	150	– <sup>c</sup>
4	DMF	KOtBu (1.0)	150	– <sup>c</sup>
5	DMF	Piperidine (6.0)	150	– <sup>b</sup>
6	1,4-Dioxane/Mesitylene/CH <sub>3</sub> CN (1:1:0.022 equiv)	TFA (0.18)	150	40% <sup>d</sup>

<sup>a</sup>Product formation evaluated by <sup>1</sup>H NMR. <sup>b</sup>The presence of a mixture of 3,8-dimethyl-4,7-phenanthroline and benzaldehyde was seen in the <sup>1</sup>H NMR spectrum. <sup>c</sup>The presence of a mixture of 3,8-dimethyl-4,7-phenanthroline and unidentified impurities was seen in the <sup>1</sup>H NMR spectrum. <sup>d</sup>Very soluble.

The synthesis of model compound **3** incorporating the Tda electron-deficient building unit was successful in 50% yield by direct condensation with 6 equiv of benzaldehyde (**1**) in 1,4-dioxane using 6 equiv of aqueous 2 M KOH as catalyst at 100 °C for 3 days (Scheme 9, for more details on the synthesis and characterization, see experimental sections 5.2.9, 5.4.1, and 5.4.3).



**Scheme 9.** Synthesis of model compound **3** in 50% yield from reaction of Tda with benzaldehyde (**1**).

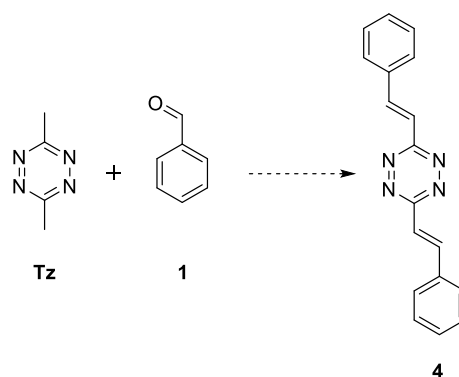
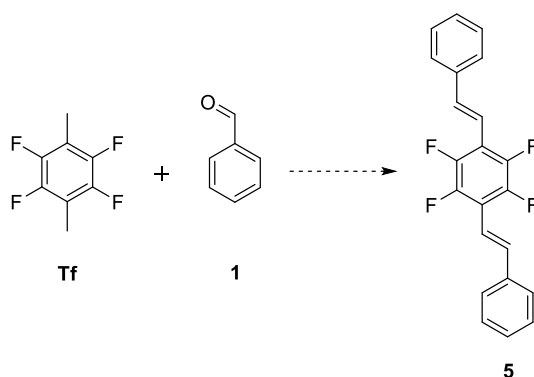
The reactivity of Tz and Tf building blocks was explored through the synthesis of model compounds **4** (Scheme 10) and **5** (Scheme 11), respectively. First, Tz and Tf were individually reacted with 6 equiv of benzaldehyde in 1,4-dioxane using aqueous 2 M KOH as catalyst at 100 °C for 3 days (Table 16, entry 1). However, no formation of model compounds was observed, and only the presence of a mixture of starting materials was observed by <sup>1</sup>H NMR analysis. Next, the influence of the non-nucleophilic base 1,8-diazabicyclo[5.4.0]undec-7-ene (DBU) was evaluated (Table 16, entry 2) however, no product formation was observed by <sup>1</sup>H NMR analysis. The acid-catalyzed aldol condensation conditions applied for model compound **2** did also not yield the desired model compounds (Table 16, entry 3). Therefore, due to time restrictions, it was decided not to pursue further the synthesis of these target compounds.



**Table 16.** Experimental conditions tested for the synthesis of model compounds **4** and **5**.

Entry	Solvents	Catalyst (equiv)	T (°C)	Product <sup>a</sup>
1	1,4-Dioxane	2 M KOH (6.0)	100	– <sup>b</sup>
2	1,4-Dioxane	DBU (6.0)	100	– <sup>b</sup>
3	1,4-Dioxane/Mesitylene/CH <sub>3</sub> CN (1:1:0.022 equiv)	TFA (0.18)	150	– <sup>b</sup>

<sup>a</sup>Product formation evaluated by <sup>1</sup>H NMR. <sup>b</sup>The presence of a mixture of 3,8-dimethyl-4,7-phenanthroline and benzaldehyde was seen in the <sup>1</sup>H NMR spectrum.

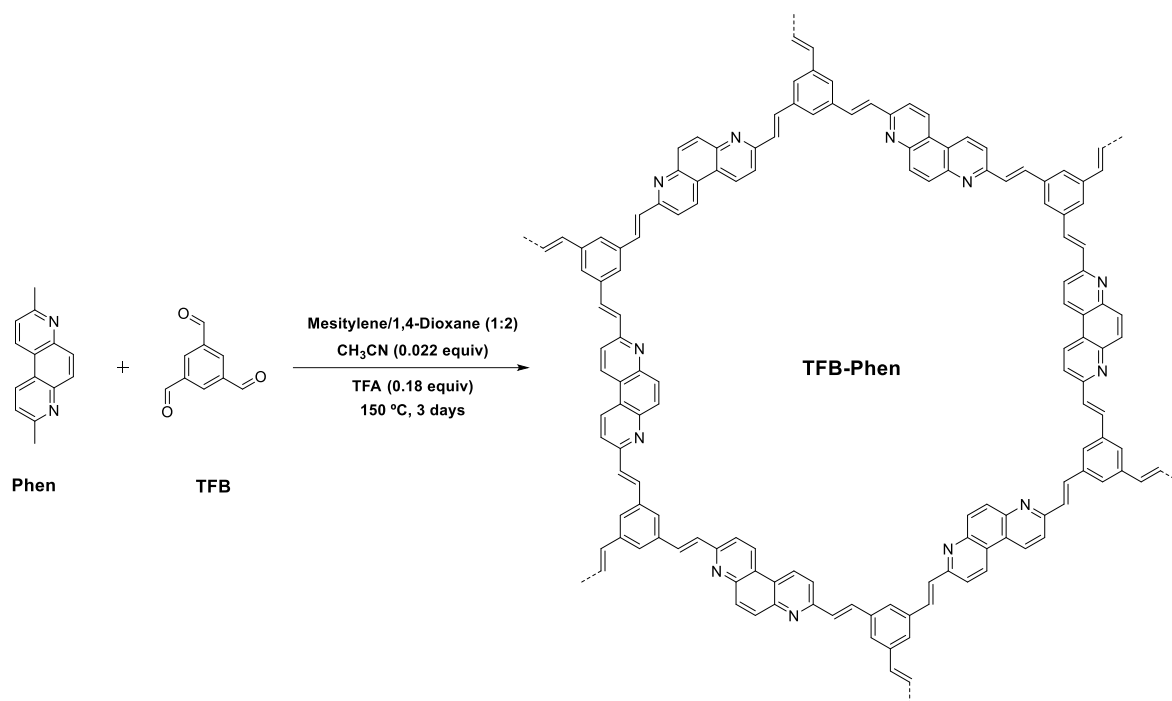
**Scheme 10.** Synthesis of model compound **4** from reaction of Tz with benzaldehyde (**1**).**Scheme 11.** Synthesis of model compound **5** from reaction of Tf with benzaldehyde (**1**).

### 3.2. Synthesis of sp<sup>2</sup>-based COFs – preliminary tests

To understand the impact of best conditions found for the synthesis of molecular model compounds **2** and **3**, the synthesis of novel sp<sup>2</sup>-based COF was explored by reaction of the three-fold 1,3,5-triformylbenzene (TFB) building block with the electron-deficient building units Phen and Tda.

Considering the highly efficient conditions found for the synthesis of model compound **3**, the synthesis of sp<sup>2</sup>-based TFB-Tda COF was explored. However, using the same conditions as for the model system resulted in the formation of amorphous material. Next, the influence of solvent polarity was evaluated in different polar and apolar solvents, such as DMAc, *o*-DCB, ethanol, and mesitylene, in different ratios; however, amorphous material was obtained in all tested conditions. The use of acid-catalyzed aldol condensation conditions were also tested for the synthesis of TFB-Tda without success. Finally, due to time constraints, it was decided not to pursue the synthesis of TFB-Tda COF further.

Then, the synthesis of sp<sup>2</sup>-based TFB-Phen COF (Scheme 12) was evaluated using the same conditions used for the successful synthesis of the model compound **2** (Table 17, entry 1). However, amorphous material was obtained, which could stem from insufficient reversibility under those reaction conditions (Figure 45A, black pattern). The influence of the amount of acetonitrile and TFA on the synthesis of TFB-Phen COF was evaluated, and omitting acetonitrile (Table 17, entry 2) still resulted in an amorphous material (Figure 45A, blue pattern), while increasing the amount of acetonitrile and TFA to 0.5 equiv resulted in full solubility of building blocks (Table 17, entry 3 and 4). Decreasing the amount of TFA from 0.18 to 0.05 equiv (Table 17, entry 5) resulted in the formation of an amorphous material (Figure 45A, green pattern). Then, replacing the TFA catalyst by oxalic acid or *p*-toluenesulfonic acid (Table 17, entries 11 and 12) also yielded amorphous material.



**Scheme 12.** Synthesis of sp<sup>2</sup>-based TFB-Phen COF from TFB and Phen.

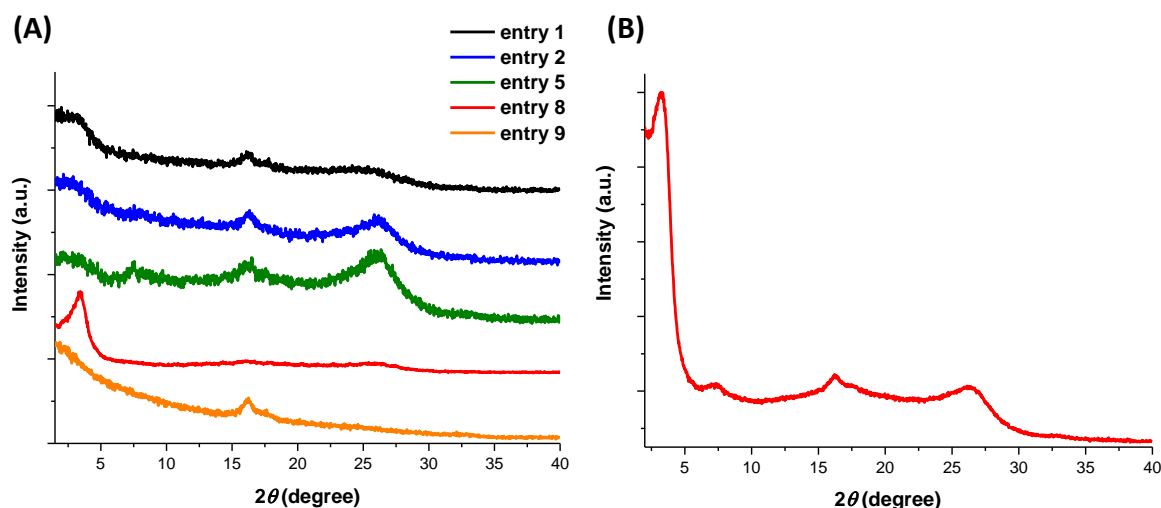


**Figure 45.** (A) PXRD patterns of selected experimental conditions tested for the synthesis of sp<sup>2</sup>-based TFB-Phen COF. (B) PXRD pattern of TFB-Phen prepared following the optimal conditions.

Next, the influence of the apolar solvent mesitylene on the synthesis of TFB-Phen COF was evaluated, and increasing its content in reaction medium led to the full solubility of the building blocks (Table 17, entries 6 and 7), whereas increasing the content of the polar

solvent 1,4-dioxane (Table 17, entry 9) yielded amorphous material (Figure 45A, orange pattern). Then, reaction medium of intermediate polarity was explored using a mixture of mesitylene and 1,4-dioxane in a ratio of 2:1 (Table 17, entry 8), which resulted in the formation of a crystalline framework of TFB-Phen COF after 3 days of reaction (Figure 45, red pattern). Under the same conditions with 5 days of reaction time (Table 17, entry 10) no differences were observed in the PXRD pattern, and therefore, the conditions of mesitylene and 1,4-dioxane in the ratio of 2:1 with 0.02 equiv of acetonitrile and 0.18 equiv of TFA as catalyst, at 150 °C for 3 days were chosen as optimum, resulting in the formation of the novel sp<sup>2</sup>-based TFB-Phen COF, in 35% yield (Scheme 12, for more details on synthesis, see experimental section 5.2.10).

**Table 17.** Experimental conditions tested for the synthesis of sp<sup>2</sup>-based TFB-Phen COF at 150 °C.

Entry	Solvents (equiv)	Catalyst (equiv)	t (days)	Crystallinity <sup>a</sup>
1	1,4-Dioxane/Mesitylene/ CH <sub>3</sub> CN (1:1:0.02)	TFA (0.18)	3	No
2	1,4-Dioxane/Mesitylene (1:1)	TFA (0.18)	3	No
3	1,4-Dioxane/Mesitylene/ CH <sub>3</sub> CN (1:1:0.5)	TFA (0.18)	3	No <sup>b</sup>
4	1,4-Dioxane/Mesitylene/ CH <sub>3</sub> CN (1:1:0.02)	TFA (0.5)	3	No <sup>b</sup>
5	1,4-Dioxane/Mesitylene/ CH <sub>3</sub> CN (1:1:0.02)	TFA (0.05)	3	No
6	Mesitylene/ CH <sub>3</sub> CN (1:0.02)	TFA (0.18)	3	No <sup>b</sup>
7	1,4-Dioxane/Mesitylene/ CH <sub>3</sub> CN (1:9:0.02)	TFA (0.18)	3	No <sup>b</sup>
8	1,4-Dioxane/Mesitylene/ CH <sub>3</sub> CN (1:2:0.02)	TFA (0.18)	3	High
9	1,4-Dioxane/Mesitylene/ CH <sub>3</sub> CN (2:1:0.02)	TFA (0.18)	3	No
10	1,4-Dioxane/Mesitylene/ CH <sub>3</sub> CN (1:2:0.02)	TFA (0.18)	5	High
11	1,4-Dioxane/Mesitylene/ CH <sub>3</sub> CN (1:2:0.02)	Oxalic acid (0.18)	3	No
12	1,4-Dioxane/Mesitylene/ CH <sub>3</sub> CN (1:2:0.02)	pTsOH (0.18)	3	No

<sup>a</sup>Product formation evaluated by PXRD. <sup>b</sup>After 3 days of reaction, no solid was seen.

The crystallinity of sp<sup>2</sup>-based TFB-Phen COF was confirmed by PXRD technique (Figure 45B), which showed the formation of an ordered porous structure, with four main reflections observed at  $2\theta = 3.2^\circ$ ,  $7.2^\circ$ ,  $16.2^\circ$ , and  $26.3^\circ$ . Preliminary calculations were carried out by our collaborator Dr. Melle-Franco from CICECO indicating that the simulated AA stacking diffraction pattern corresponds well with the experimental PXRD data. Nitrogen sorption measurements at 77 K showed a type I isotherm (Figure 46A) with high N<sub>2</sub> uptake in the low-pressure region ( $P/P_0 < 0.05$ ), indicating the microporosity of TFB-Phen COF. The BET surface area calculated was 485 m<sup>2</sup> g<sup>-1</sup> (Figure 46B), with a total pore volume of 0.347 cm<sup>3</sup> g<sup>-1</sup>. Pore size distribution was derived from the QSDFT model for cylindrical pores (adsorption branch), which showed a maximum at 1.1 nm, and a small contribution at 1.5 nm (Figure 46C).

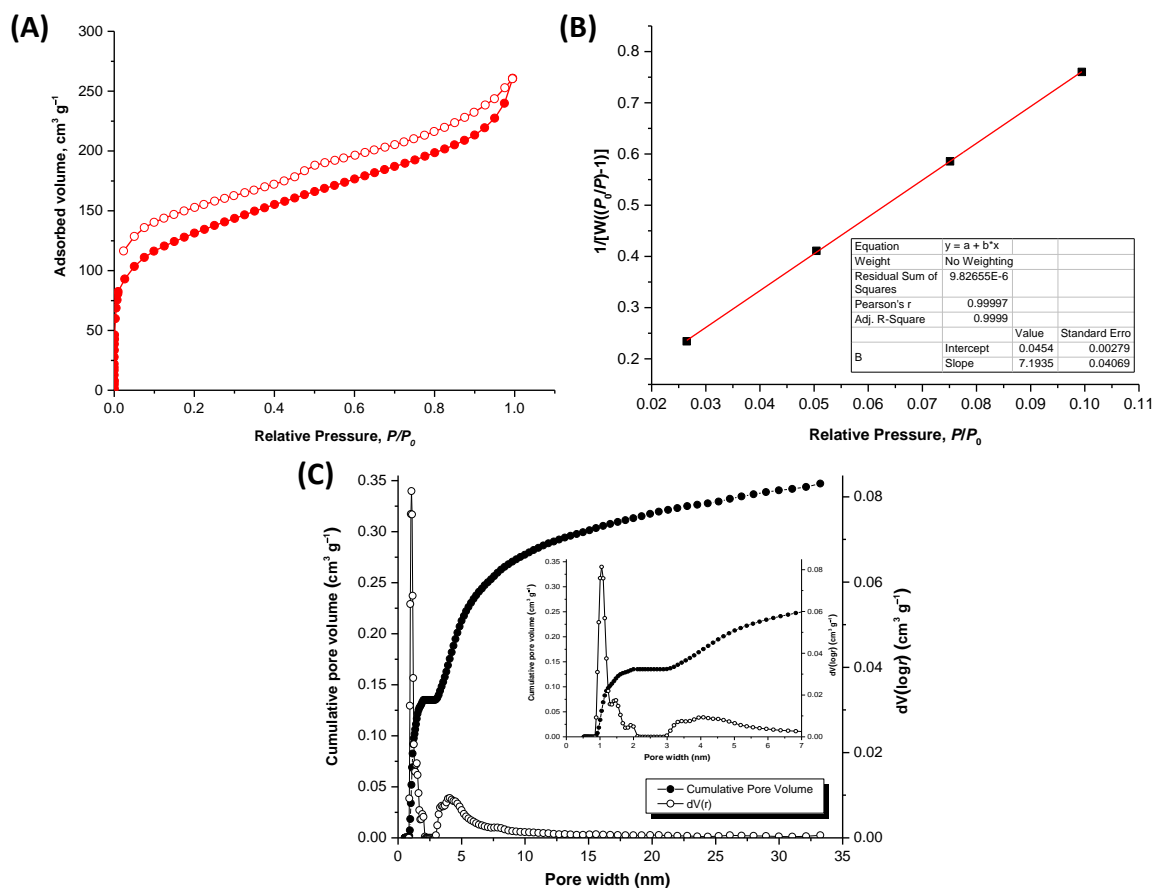


**Figure 46.** (A) N<sub>2</sub> adsorption (filled spheres) and desorption (hollow spheres) isotherm profiles measured at 77 K of TFB-Phen COF. (B) Multi-point BET plot and linear fit of TFB-Phen COF. (C) Pore size distribution (hollow spheres) and cumulative pore volume (filled spheres) profile of TFB-Phen COF.

The success of condensation reaction was also supported by FT-IR spectroscopy (Figure 47), where the typical band of carbonyl group of TFB at 1693 cm<sup>-1</sup> almost disappeared completely, and a new vibration peak appeared at 1627 cm<sup>-1</sup>, supporting the formation of C=C bond in TFB-Phen COF. In addition, the high resemblance of the FT-IR spectra of model compound **2** and TFB-Phen COF confirms the formation of a sp<sup>2</sup>-linkage structure (Figure 47). According to the thermogravimetric analysis (TGA) curves (Figure 48), the synthesized TFB-Phen COF possess around 10% of unreactive Phen, which could be mainly located within the pores. This result is an indication that additional washes needed to be performed to improve COF purity.

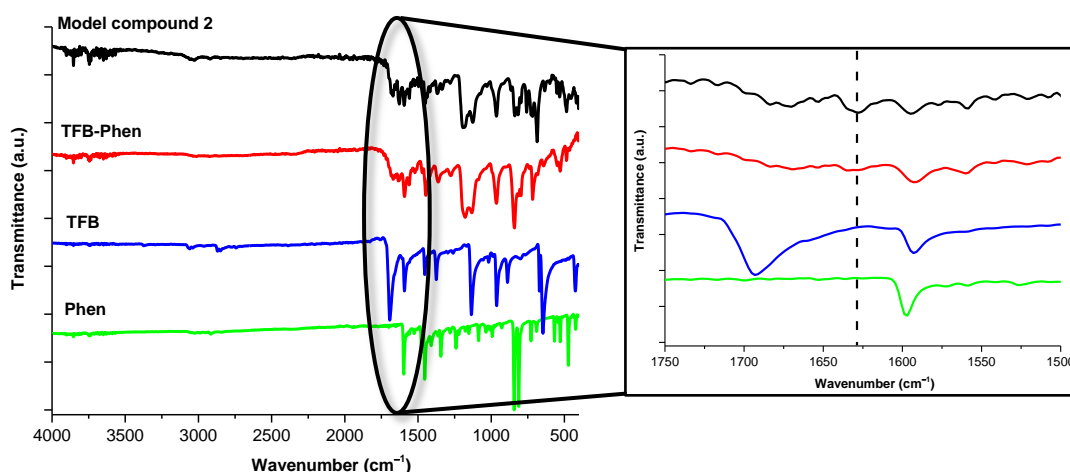


**Figure 47.** FT-IR spectra of model compound **2** (black), 1,3,5-triformylbenze (blue), 3,8-dimethyl-4,7-phenanthroline (green), and TFB-Phen COF (red).

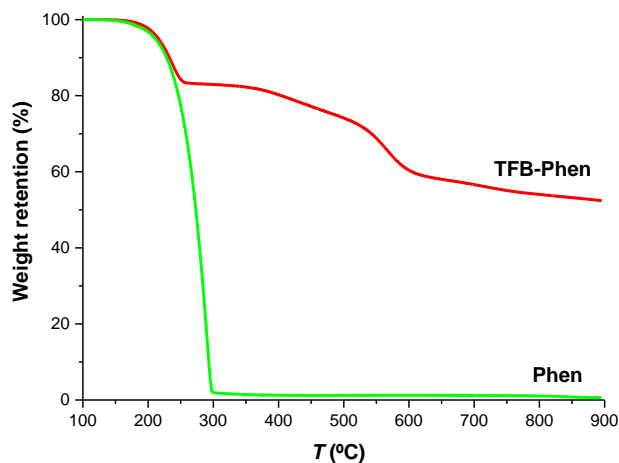


**Figure 48.** TGA data of TFB-Phen COF (red) and 3,8-dimethyl-4,7-phenanthroline (green).

The electronic properties of TFB-Phen COF were investigated by photophysical measurements. The ultraviolet/visible diffuse reflectance spectrum (UV/vis DRS) showed a broad adsorption band covering both UV and visible-light regions, with a maximum peak at around 510 nm (Figure 49A). The optical band gap was calculated to be 1.96 eV according to the Kubelka-Munk (K–M) function (Figure 49B), which is slightly narrower than the band gap value obtained for some of the reported sp<sup>2</sup>-based COFs (Table 18).

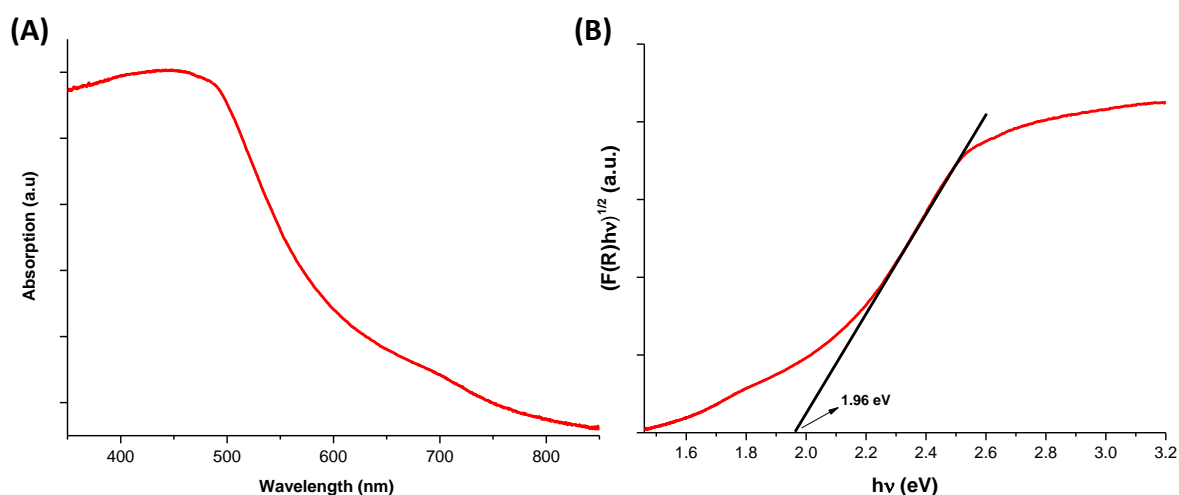


**Figure 49.** (A) UV/vis diffuse reflectance spectra (DRS) of TFB-Phen COF, and (B) band gap determined from the Kubelka–Munk-transformed reflectance spectra.

**Table 18.** Band gap value of some of the reported sp<sup>2</sup>-based COFs.

COFs	$E_g$ (eV)	Reference
2DPPV	2.10	[88]
sp <sup>2</sup> c-COF	1.90	[330]
sp <sup>2</sup> c-COF-2	2.07	[331]
sp <sup>2</sup> c-COF-3	2.12	
g-C <sub>54</sub> N <sub>6</sub> -COF	2.03	[355]
g-C <sub>52</sub> N <sub>6</sub> -COF	2.15	
2D-PPQV1	2.20	[336]
2D-PPQV2	2.23	
2D CCP-Th	2.05	[342]
2D CCP-BD	2.40	

### 3.3. Photocatalytic degradation of dyes by TFB-Phen COF – preliminary tests

Taking into account the interesting optical properties of TFB-Phen COF, it was next explored as photocatalyst for the degradation of the organic dyes, MB and MO (Figure 50). To date, TFO-COF<sup>[341]</sup> with a slightly higher bandgap of 2.46 eV than that obtained for TFB-Phen COF is the only sp<sup>2</sup>-based COF reported for the photocatalytic degradation of dyes. However, comparing with other reported COF materials used as photocatalysts for the degradation of dyes, TFB-Phen COF features a very similar bandgap, highlighting its potential to be used as photocatalyst for degradation of pollutants (Table 19).

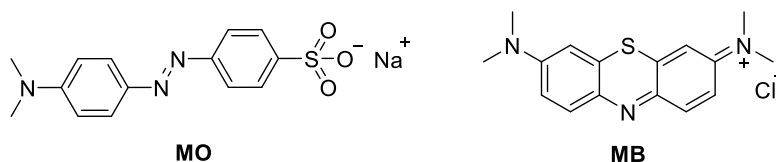


**Figure 50.** Chemical structure of MO and MB at neutral pH.

The use of TFB-Phen COF as a non-metallic organic photocatalyst for degradation of MO and MB under the irradiation of visible light was explored by first subjecting 1 mg mL<sup>-1</sup> of the photocatalyst to an aqueous dye solution of 10 mg L<sup>-1</sup> in darkness for 60 min at room temperature to reach adsorption equilibrium prior to the photodegradation experiments. The degradation of MO was nearly complete (>90%) within 90 min in the presence of TFB-Phen COF (Figure 51A, green curve). In the case of MB, a longer time of 360 min was required to reach a degradation efficiency of 90% (Figure 51A, black curve). To better describe the photocatalytic degradation process by the TFB-Phen COF, MO concentrations during the photocatalytic process were fitted, with pseudo-second-order reaction model (Figure 51B) giving the best fitting. The MO photocatalytic degradation rate by TFB-Phen COF ( $K = 4.39 \times 10^{-3} \text{ min}^{-1}$ , Table 19) was lower than the degradation rate of the reported TFO-COF<sup>[341]</sup> ( $K = 4.42 \times 10^{-5} \text{ min}^{-1}$ , Table 19). On the other hand, comparing with other Tp-based COFs (TpMa,  $K = 1.02 \times 10^{-1} \text{ min}^{-1}$ , Table 19),<sup>[356]</sup> TFB-Phen COF showed better performance. These results have shown the capacity of TFB-Phen COF to be used as photocatalyst, however due to time constrains, it was decided not to pursue with further studies.



**Table 19.** Reported performance of COF materials as photocatalysts for degradation of organic pollutants.

COFs	$E_g$ (eV)	Light irradiation (nm)	[COF] mg mL <sup>-1</sup>	[dye] mg L <sup>-1</sup>	$K$ (min <sup>-1</sup> ) <sup>a</sup>	Reference
TTO-COF	2.46	> 420 nm	0.3	10 (MO and MB)	MO: $4.42 \times 10^{-5}$ MB: $5.38 \times 10^{-5}$	[341]
TFB-Phen	1.96	> 420 nm	1.0	10 (MO and MB)	MO: $4.39 \times 10^{-3}$	<b>This work</b>
Tp-Mela	2.04				$2.53 \times 10^{-1}$	
Tp-Tab	1.59	> 420 nm	0.17	100 (RhB)	$8.0 \times 10^{-3}$	[357]
Tp-Tapt	1.88				$9.2 \times 10^{-2}$	
COF-PDZ	2.31				$1.28 \times 10^{-1}$	
COF-PMD	2.22				$8.70 \times 10^{-2}$	
COF-PZ	2.11	> 400 nm	0.3	5.0 (paracetamol)	$9.20 \times 10^{-2}$	[358]
COF-PD	2.18				$1.60 \times 10^{-2}$	
COF-1	2.15				$5.00 \times 10^{-3}$	
TpMA	2.3	> 420 nm	0.6	10 (MO)	$1.02 \times 10^{-1}$	[356]

<sup>a</sup>Kinetic linear constant obtained to evaluate the photocatalytic degradation rate of COFs.

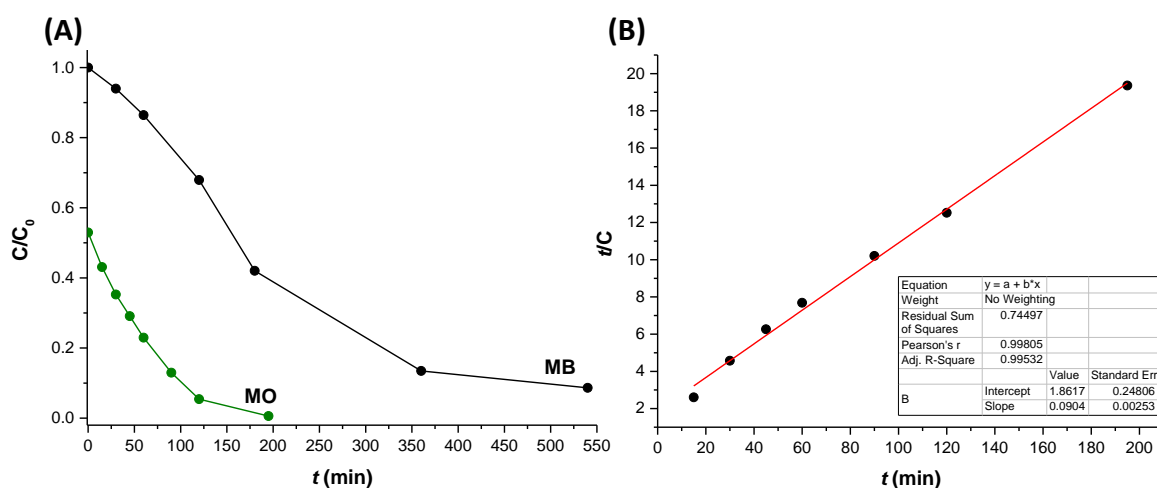


**Figure 51.** (A) Photocatalytic degradation of 10 ppm MO (green) and MB (black) over TFB-Phen. (B) Kinetic linear simulation curve of MO photodegradation over TFB-Phen. The data fitted well to the pseudo-second-order kinetics model.



### Chapter 4 – Conclusions and outlook

In this thesis, the potential of COFs as efficient adsorbents for biotoxins, as well as for pharmaceuticals even in naturally contaminated water samples was demonstrated.

In the case of biotoxins, TpBD-(CH<sub>3</sub>)<sub>2</sub> showed high efficiency for OA adsorption, with a maximum adsorption capacity,  $q_m$ , of 279 mg g<sup>-1</sup>, resulting in a 200-fold increase in comparison to the previously reported styrene-based resins. In addition, OA was efficiently desorbed from the COF, allowing for the reuse of the material for at least three cycles, while maintaining its structural integrity. The results demonstrate that COF materials are promising candidates for solid-phase adsorption in water monitoring devices. Later, a comprehensive study was performed on the impact of the COF pore functionality on the preferential adsorption of diverse microcystin analogues which only differ in one moiety. The influence of COF functionalization on the adsorption rate and efficiency of diverse microcystin analogues (MC-LR, -LA, -RR, and -YR) was established, providing insight into the design of more efficient and selective adsorbent materials. TpBD-(NO<sub>2</sub>)<sub>2</sub> outperformed the commonly used adsorbent materials for the capture of MC-RR, with an increase in the maximum adsorption capacity by one order of magnitude, while TpBD-(NH<sub>2</sub>)<sub>2</sub> was shown as the first efficient adsorbent material for the capture of MC-LA. Furthermore, theoretical calculations were performed that allowed a deeper understanding of some of the tendencies that guide the adsorption process. In addition, large differences in adsorption efficiencies but also in kinetics and desorption efficiencies were observed. It was found that the novel-fluorine TpBD-(CF<sub>3</sub>)<sub>2</sub> and TpBD-(NH<sub>2</sub>)<sub>2</sub> adsorb, respectively, MC-YR and MC-LA, very fast (5 min), indicating that preferential analogue strategies can be designed by selecting the time of contact. The potential of the selected COFs to be reused was demonstrated, with losses in adsorption efficiencies ≤15% in three consecutive cycles of adsorption-desorption. With this study was demonstrated that by careful choice of COF functionalities, specific compounds can be targeted or excluded from a group of analogues, providing insight into the design of more efficient and selective adsorbent materials.

For pharmaceuticals, TpBD-(CF<sub>3</sub>)<sub>2</sub> showed high efficiency for the adsorption of ibuprofen from water at both neutral and acidic pH. The compound could be recovered in

high yield with the structural integrity and properties of TpBD-(CF<sub>3</sub>)<sub>2</sub> remaining intact after desorption. Additionally, ibuprofen was much more efficiently adsorbed than more hydrophilic pharmaceutical contaminants, highlighting the potential of COF materials to be tuned for selective capture of contaminant classes. TpBD-(CF<sub>3</sub>)<sub>2</sub> also proved to be an efficient adsorbent for ibuprofen from natural water samples, with the physical-chemical properties of the water determining the adsorption efficiency. From three different water samples, the highest affinity of TpBD-(CF<sub>3</sub>)<sub>2</sub> for ibuprofen was found in lake water that featured the most acidic pH of the samples. This was rationalized by theoretical calculations, where the protonated form of ibuprofen, which prevails at acidic pH, has higher tendency to interact with the COF pores. Moreover, in competition with other commonly found pharmaceuticals in water, acetaminophen and phenobarbital, tested as binary mixtures, the adsorption efficiency of ibuprofen by TpBD-(CF<sub>3</sub>)<sub>2</sub> was not decreased, but enhanced by more than 10 mg g<sup>-1</sup> at the highest concentration tested. Finally, TpBD-(CF<sub>3</sub>)<sub>2</sub> was tested for the passive adsorption of pharmaceuticals found in unspiked natural water samples of Tagus river estuary. Adsorption efficiencies over 80% were observed for nearly all 22 compounds detected using COF material out of the 23 pharmaceuticals detected using state-of-the-art SPE. TpBD-(CF<sub>3</sub>)<sub>2</sub> outperformed the SPE procedure in the recovery efficiency of  $\alpha$ -hydroxyalprazolam and diclofenac. In some cases, acidification of the water samples led to a dramatic loss of extraction efficiency, underlining the effect of sample pre-treatment on the results. Interestingly, TpBD-(CF<sub>3</sub>)<sub>2</sub> adsorbed with high efficiency 19 pharmaceuticals without acid treatment of the samples, underlining the potential of COFs for *in situ* passive adsorption of pharmaceuticals, making this material suitable to be used in regular water monitoring programs.

Finally, a novel sp<sup>2</sup>-based TFB-Phen COF was prepared following acid-catalyzed aldol condensation conditions. The interesting optical properties of TFB-Phen were found to render it with potential to be used as photocatalyst for the degradation of organic dyes, outperforming some of the commonly used COF materials.

The results described above raise new interesting questions, which could be addressed in follow-up studies. First, studies of adsorption with different co-occurring toxin mixtures (such as OA family and yessotoxins, pectenotoxins or azaspiracids), incorporating

different analogues from the same family, should be carried out to gain insight into the main driving forces that guide the adsorption process in a more complex water media and the preferential adsorption observed for the different compounds in real scenario. This information will allow to further design fit-for-purpose COF materials.

Individual adsorption studies of pharmaceuticals detected in Tagus river estuary by TpBD-(CF<sub>3</sub>)<sub>2</sub> should be performed in order to understand the adsorption mechanism beyond the results obtained. In addition, the influence of organic matter on the adsorption process of the different compounds by TpBD-(CF<sub>3</sub>)<sub>2</sub> should be also investigated. Combination of all these results with computational studies will give better insight into the main interactions involved on the adsorption process.

The synthesis of new sp<sup>2</sup>-based COFs incorporating new electron-deficient heterocycles building units can be explored, in order to enhance COF crystallinity as well as optical band gap. Further, the synthesized materials can be explored for photocatalytic degradation of pharmaceutical contaminants, such as ibuprofen, opening a new perspective for water treatment.

Through this work, we have demonstrated that COFs can be efficiently designed and tailored for adsorption of some water contaminants. The high versatility of COFs structures with the additional possibilities offered by post-synthetic modification, provides virtually infinite combinations that can be explored for many other contaminants. The knowledge gained through this work, pioneer in its area of application, offer new promising pathways for exploring COFs as efficient adsorbent materials to be incorporated in new water monitoring programs.



## Chapter 5 – Experimental

### 5.1. Materials and methods

#### 5.1.1. Reagents and chemicals

Hexamethylenetetramine, 99% and phloroglucinol anhydrous, 99%, used for the synthesis of Tp were purchased from Sigma-Aldrich and Acros Organics. *o*-Tolidine and 3,3'-bis(trifluoromethyl)benzidine were purchased from TCI chemicals and Apollo Scientific, respectively, and used for the synthesis of the correspondent TpBD-(CH<sub>3</sub>)<sub>2</sub> and TpBD-(CF<sub>3</sub>)<sub>2</sub>. Mesitylene 99% extra pure from Fisher Chemical and anhydrous 1,4-dioxane from Acros Organics were used for the synthesis of TpBD-(CH<sub>3</sub>)<sub>2</sub> and TpBD-(CF<sub>3</sub>)<sub>2</sub>. For the synthesis of TpBD-(NO<sub>2</sub>)<sub>2</sub>, 3,3'-dinitrobenzidine and anisole were purchased from TCI Chemicals. Tin(II) chloride dihydrate (>98%) and anhydrous THF were purchased from Acros Organics for the synthesis of TpBD-(NH<sub>2</sub>)<sub>2</sub>.

THF HPLC grade, *N,N*-dimethylformamide HPLC grade from Fisher Chemical, acetone 99.8%, ACS reagent from Honeywell, and dichloromethane 99%, extra pure from Sigma-aldrich were used as received for the washing of the resulting products. Chloroform deuterated, 99.8% for NMR was purchased from Acros Organics. Trifluoroacetic acid for HPLC, 99% was purchased from Fisher Chemical. Aqueous acetic acid and hydrochloric acid were prepared by dilution of commercial acetic acid, ACS reagent, ≥99.8% from Sigma-Aldrich, and the commercial hydrochloric acid, 37% from Fisher Chemical. Sodium sulfate anhydrous, ACS reagent, for analysis, was purchased from Panreac AppliChem. Ultrapure water was produced by Milli-Q Advantage A10 system (Millipore, resistivity: 18.2 MΩ cm<sup>-1</sup>). The pH of the used ultrapure water was measured before the experiments and was found to be always in the range of 6–7.

Okadaic acid from *Prorocentrum* sp. was purchased from Merck-Calbiochem (Darmstadt, Germany). Microcystin-LR, -LA, -RR, and -YR isolated from *Microcystis aeruginosa* sp. were purchased from Enzo Life Sciences. 6,8-Difluoro-4-methylumbelliferylphosphate (DIFMUP) was purchased from Thermo Fisher Scientific. Protein phosphatase-1 catalytic subunit (PP1),  $\alpha$ -isoform from rabbit, 5000–15000 units

mg<sup>-1</sup> of protein was purchased from Sigma-Aldrich. Ibuprofen (≥98%), acetaminophen (98.0–102.0%), ampicillin (96.0–100.5%), and phenobarbital (99.9%) were purchased from Sigma-Aldrich.

### 5.1.2. Characterization techniques

Small-angle X-ray scattering (SAXS) measurements were performed in an Anton Paar SAXSess mc2 instrument operating at 40 kV and 50 mA. Data were collected with an image plate detector. Samples were placed into a holder with Mylar windows for the measurement. Data are background corrected. Powder X-ray diffraction (PXRD) measurements were performed on a PANalytical X'Pert PRO MRD diffractometer operating at 45 Kv and 40 mA.

Nitrogen sorption measurements were performed using a Quantachrome Autosorb IQ2 automated analyser. Prior to the measurements, samples were outgassed by heating to 120 °C (heating rate: 5 °C min<sup>-1</sup>, dwelling time: 720 min). Multipoint Brunauer–Emmett–Teller (BET) method using ASIQwin™ software was used to estimate the surface areas of the obtained powders. Pore size distributions were assessed using quenched-solid density functional theory (QSDFT) equilibrium model for slit pores (N<sub>2</sub> at 77 K on carbon).

Infrared (IR) spectra were recorded on a Bruker VERTEX 80v FT-IR spectrometer in ATR mode. IR data is background corrected and reported in frequency of adsorption (cm<sup>-1</sup>). UV-Vis spectrophotometry analysis was performed using a ThermoScientific NanoDrop 2000c spectrophotometer at 220 nm, 243 nm, 210 nm, and 273 nm for ibuprofen, acetaminophen, ampicillin, and diclofenac, respectively.

Thermogravimetric analyses (TGA) were carried out on a TGA/DSC 1 STAR<sup>e</sup> system (Mettler-Toledo). The samples were heated from 298.15 to 1173.15 K at 283.15 K min<sup>-1</sup> under a continuous Ar flow of 50 mL min<sup>-1</sup>.

The contact angle measurements were performed under air at room temperature (19 °C) with a Drop Shape Analyzer DSA100 from Krüss. COF powders were gently homogenized with pestle and mortar to avoid large aggregates and diminish the effect of



the roughness in the measurements. The COF powder was placed on a transparent tape and pressed against another piece of tape. After peeling the second layer, a uniform layer of each COF was obtained for the contact angle measurements.

Scanning electron microscopy (SEM) studies were performed using a Quanta 650 field-emission scanning electron microscope operating at 3 kV and employing an Everhardt Thornley secondary electrons detector, with a working distance of around 10 mm. The samples were prepared by adhesion of the sample powder directly on a conductive double-sided copper tape attached to SEM pin stub.

Proton nuclear magnetic resonance ( $^1\text{H}$  NMR) spectra were recorded on 400 MHz Bruker Avance II spectrometer at the NMR service of University of Minho in Braga, Portugal. Chemical shifts are given in ppm ( $\delta$ ) and calibrated using residual deuterated solvent peak as internal reference ( $\text{CDCl}_3$ :  $\delta$  7.26;  $(\text{CD}_3)_2\text{SO}$ : 2.5;  $\text{CD}_2\text{Cl}_2$ : 5.32). Multiplicities are reported as follow: s (singlet), d (doublet), t (triplet), m (multiplet), or combinations thereof. Coupling constants  $J$  are given in Hz.

Incubation of COFs with the pharmaceuticals in small volumes (adsorption kinetics and adsorption at different pH) were performed using Thermomixer Comfort Eppendorf MTP at 1400 rpm with a 1.5 mL Block.

pH of natural water samples collected in Viana do Castelo was measured using a benchtop pHmeter (SevenCompact, Mettler Toledo) with an accuracy of  $\pm 0.002$ . All other physical-chemical parameters of water were measured using the Sera Aqua-Test.

HPLC-DAD analysis was performed in an Agilent Technologies 1200 series high-performance liquid chromatograph coupled with a diode-array detector.

### **5.1.3. Theoretical calculations**

#### **5.1.3.1. MC computational studies**

Molecular simulations were used to describe the structure arrangement and the adsorption mechanism of the toxins on TpBD-( $\text{NO}_2$ )<sub>2</sub>, TpBD-( $\text{NH}_2$ )<sub>2</sub>, and TpBD-( $\text{CF}_3$ )<sub>2</sub> COFs. A TpBD COF cell was built in Materials Studio software<sup>[359]</sup> by using the reported parameters

(space group P6/m,  $a = b = 30.5 \text{ \AA}$ ,  $c = 3.4 \text{ \AA}$ ,  $\alpha = \beta = 90^\circ$ ,  $\gamma = 120^\circ$ ).<sup>[65]</sup> The obtained structure was modified to get TpBD-(NO<sub>2</sub>)<sub>2</sub> and TpBD-(NH<sub>2</sub>)<sub>2</sub> COF supercells. The structure of TpBD-(CF<sub>3</sub>)<sub>2</sub> was previously described.<sup>[64]</sup> The cell parameters are  $a = b = 28.67 \text{ \AA}$ ,  $c = 4.25 \text{ \AA}$ ,  $\alpha = \beta = 90^\circ$ ,  $\gamma = 120^\circ$ ; space group is P6. For purposes of molecular simulations, a 3D periodic box with the dimensions of  $a \times a \times c$  was built, with the  $c$  dimension about  $80 \text{ \AA}$ . The box contained 6–8 COF layers simulating a surface with a thickness of about  $28 \text{ \AA}$  and a part of the COF pore (one  $4a \times 4a \times c$  3D periodic box would contain one entire COF pore). To describe the structure of the COF–toxin system, it is necessary to get a structure model ideally giving the lowest value of the adsorption energy. For this purpose, 4 types of structure models were built: COF–water–toxin model, COF–water model, water model, and water–toxin model. All 4 structure models contained about 1800 water molecules to keep the density of  $1000 \text{ kg m}^{-3}$ ; the molar volumes of individual components in the models were kept constant. The molecular simulations were carried out as detailed in the following.

#### *COF–water–toxin models*

At first, the calculations were carried out in vacuum to find the binding sites of the toxins on the COF structure. A set of initial models with different orientations of one toxin molecule placed above the COF surface was built. After a geometry optimization of the starting models 1–2 ns quench dynamics simulation in an NVT statistical ensemble (N – constant number of atoms, V – constant volume, T – constant temperature) at 298 K was done in Materials Studio software. Thereafter, the models with the most different geometry (a set of 3–5 models) were selected for subsequent calculations. The free volume of the periodic box was filled with water molecules and the geometry of the models was optimized in Materials Studio. At this stage all atomic positions in the structure except of water molecules were kept fixed. After the geometry optimization a short molecular dynamics simulation ( $\leq 30 \text{ ps}$ ) was carried out to preequilibrate the positions of water molecules in the simulation box. This simulation was repeated again, this time with free atomic positions of the toxin and water molecules. Thereafter, molecular dynamics

simulations were carried out in the Lammmps simulation package<sup>[360]</sup> with all atomic positions variable except those within the COF structure.

*COF–water models, water models, and water–toxin models*

In all cases, 3 independent structure models with different starting configurations were built and the simulation strategy was very similar as in the COF–water–toxin models. In the COF–water models the atomic positions of the COF were fixed and the positions of water molecules were variable during the simulations. In the water–toxin models all atomic positions were variable except of the geometry optimization of initial models and short molecular dynamic runs carried out in Materials Studio, where all the atomic positions of the toxin molecules were kept fixed. Then, the pre-equilibrated models were used in the Lammmps simulation package.

*Molecular simulations conditions in Lammmps*

At first, a few hundred thousand steps of the dynamics simulation at 300 K were performed, and then the system was heated up to 500 K for 1–2 ns. After the system was cooled down, 1 ns molecular dynamics simulation at 298 K followed. Then, 5 ns blocks of molecular dynamics simulations at 298 K were repeated until the convergence of the total energy value of the structure models was reached. The snapshots were collected every 2000 steps. The molecular simulations were carried out in an NVT statistical ensemble. In all cases (including the geometry optimization and molecular dynamics in Materials Studio), pcff interface forcefield<sup>[361]</sup> was employed in the simulations, the calculations were done in the space group P1. One simulation step was 1 fs, the atomic charges of the COF structure and the parameters for water molecules were incorporated into pcff force field from the Compass forcefield.<sup>[362]</sup> Temperature was controlled by Nosé–Hoover thermostat. Electrostatic interactions were calculated by the PPPM method with the accuracy of  $10^{-6}$  kcal mol<sup>-1</sup> and van der Waals interactions were calculated by using Lennard–Jones potential with a cut-off of 12 Å.

*Adsorption energy calculations*

The individual trajectories of the molecular dynamics simulations for all types of structure models exhibited slight deviations ( $\pm 0.1$  K) of the target average temperature of 298 K. To obtain comparable results, the average value of the total energy for each trajectory was adjusted to 298 K by using the heat capacity of the system calculated during the simulations. In case of water models, water–toxin models and COF–water models, the uncertainty of the average value of the total energy was about  $\pm 0.5$  kcal mol<sup>-1</sup>. In case of COF–water–toxin models the situation was somewhat different, i.e. the models with different geometries exhibited different average values of the total energy. The convergence criterion for each trajectory was reached when the difference between the average values of two successive 5 ns blocks (or between two consecutive 10 ns and 5 ns blocks) was less than 1 kcal mol<sup>-1</sup>. The structure models with the lowest value of average total energy were involved in the adsorption energy ( $\Delta E_{\text{ads}}$ ) calculation presented in Table 4.<sup>[363]</sup>

$$\Delta E_{\text{ads}} = E_{\text{COF-water-toxin}} - E_{\text{water-toxin}} + E_{\text{water}} - E_{\text{COF-water}}$$

*Shift of the COF layers*

To estimate the relative position of two adjacent layers in the investigated models we built a supercell containing two COF layers and one entire COF pore. The position of the layers was estimated by searching for the global minimum of the interaction energy by a systematic shift of one layer with 0.5 Å steps along  $x$  and  $y$  axes direction. In case of TpBD-(NO<sub>2</sub>)<sub>2</sub> the global minimum of the interaction energy was reached for  $x = y = 2$  Å. In case of TpBD-(NH<sub>2</sub>)<sub>2</sub> the relative position of the layers exhibited certain variability with very similar values to the value of the global minimum of the interaction energy. To keep the structure consistency with TpBD-(NO<sub>2</sub>)<sub>2</sub> we adopted the model with the same layer shift. In case of TpBD-(CF<sub>3</sub>)<sub>2</sub> the lowest value of the interaction energy was obtained for an eclipsed arrangement due to non-planarity of the COF layers stemming from the presence of CF<sub>3</sub> substituents.

### 5.1.3.2. Ibuprofen computational studies in natural water samples

For the structure of TpBD-(CF<sub>3</sub>)<sub>2</sub> the cell parameters were defined as  $a = b = 28.67 \text{ \AA}$ ,  $c = 4.25 \text{ \AA}$ ,  $\alpha = \beta = 90^\circ$ ,  $\gamma = 120^\circ$ ; and the space group was P6, as described on section 2.1.2 for the synthesis of TpBD-(CF<sub>3</sub>)<sub>2</sub>. A 3D periodic box with space group P1 and the dimensions  $1a \times 1b \times 1c$  was created from the original cell;  $C \approx 80 \text{ \AA}$ . The box contained six COF layers of a total thickness of ca.  $28 \text{ \AA}$ , simulating the COF surface and a part of its pore. The ibuprofen molecule was built in a Forcite module of Materials Studio modelling environment, version 8<sup>[359]</sup> and its geometry was optimized. Based on the experimental data, both deprotonated and protonated forms of ibuprofen were used. To better understand and describe the behavior of ibuprofen, a series of different calculations was carried out: (i) COF models with the ibuprofen molecules on the COF surface, and (ii) COF models with the ibuprofen molecules in the pore. In both cases, protonated or deprotonated form of the pharmaceutical, and the mixture thereof were used. At first, 1 ns dynamics simulations at 298 K in an NVT statistical ensemble (N – constant number of atoms, V – constant volume, T – constant temperature) were carried out without water to find the binding sites of ibuprofen on the COF structure. The obtained models were used for subsequent calculations. A corresponding amount of water to keep the density of  $1000 \text{ kg m}^{-3}$  was added into the box; the geometry of these models was optimized and pre-equilibrated in Materials Studio software. After this, dynamics simulations were carried out in an NVT statistical ensemble in Lammmps simulation package.<sup>[360]</sup> At first, the systems were heated up to 500 K for 1 ns and after cooling down 2 ns dynamics simulations at 298 K were carried out. The snapshots were collected every 2000 steps and those from the last 1 ns of the simulation were used for the analysis. In all cases one dynamic step was 1 fs, the atomic positions of COF were kept fixed, and all other atomic positions were variable. The calculations were done in pcff force field;<sup>[364]</sup> the atomic charges were assigned by the Compass force field.<sup>[362]</sup> The electrostatic interactions were calculated by PPPM method and van der Waals interactions were calculated by Lennard–Jones potential with a cut-off of  $12 \text{ \AA}$ .

#### 5.1.4. Stability tests

TpBD-(CH<sub>3</sub>)<sub>2</sub> COF (16 mg) was suspended in ultrapure water or synthetic seawater (3 mL) at room temperature for 7 days. Then, the samples were centrifuged (15000 rpm, 15 min, r.t.), and the aqueous medium was removed. The sample suspended in ultrapure water was soaked in acetone for 8 h, centrifuged (15000 rpm, 15 min, r.t.), and the solvent was decanted. The soaking was repeated 3 times in total. The sample was then dried at 120 °C at high vacuum for 9 h. In order to remove salts, the sample suspended in synthetic seawater was first soaked in ultrapure water for 8 h, centrifuged (15000 rpm, 15 min, r.t.), and the solvent was decanted. The soaking was repeated 3 times in total. Thereafter, the sample was treated as the sample suspended in ultrapure water.

## 5.2. Synthetic procedures

### 5.2.1. Synthesis of 2,4,6-trihydroxybenzene-1,3,5-tricarbaldehyde (1,3,5-Triformylphloroglucinol, Tp)

1,3,5-Triformylphloroglucinol (Tp) was synthesized following a literature-known procedure.<sup>[103]</sup> In a round-bottom flask of 500 mL, to a mixture of hexamethylenetetramine (15 g, 107 mmol, 1 equiv) and phloroglucinol (6.07 g, 48.15 mmol, 0.45 equiv) under argon was added trifluoroacetic acid (90 mL). The mixture was magnetically stirred under reflux for 2.5 h. Then, 3M HCl (150 mL) was added, and the mixture was stirred for 1 h. The mixture was cooled down at r.t. and filtered under vacuum. Solution was extracted three times with CH<sub>2</sub>Cl<sub>2</sub>, dried over anhydrous Na<sub>2</sub>SO<sub>4</sub>, and concentrated under reduced pressure to afford **Tp** (3.1 g, 31%) as a beige solid.

<sup>1</sup>H NMR (400 MHz, (CDCl<sub>3</sub>): δ= 14.13 (s, 3H, OH), 10.16 (s, 3H, CHO).

### 5.2.2. Synthesis of TpBD-(CH<sub>3</sub>)<sub>2</sub> (in mg scale)

TpBD-(CH<sub>3</sub>)<sub>2</sub> was synthesized following a literature-known procedure.<sup>[65]</sup> In a 10 mL ampoule (Wheaton, prescored, borosilicate, 19 x 107 mm), to a mixture of Tp (63 mg, 0.30 mmol, 1.0 equiv) and *o*-tolidine (95.6 mg, 0.45 mmol, 1.5 equiv) were added mesitylene (1.5 mL) and 1,4-dioxane (1.5 mL), and an aqueous solution of 3 M acetic acid (0.5 mL). The mixture was sonicated for 10 min at r.t. in order to get a homogeneous dispersion. Then,

the ampoule was flash frozen at 77 K (liquid N<sub>2</sub> bath), sealed off, and heated at 120 °C for 3 days. The solid was collected by filtration and washed with acetone and THF for five times. The resulting solid was dried under vacuum at 120 °C for 4 h, to give TpBD-(CH<sub>3</sub>)<sub>2</sub> (95 mg, 83%) as a red solid.

### 5.2.3. Synthesis of TpBD-(CH<sub>3</sub>)<sub>2</sub> (in gram scale)

Into a 100 mL pressure tube (ACE glass, bushing type back seal, 17.8 cm x 38.1 cm), Tp (1.1 g, 5.21 mmol, 1 equiv) and *o*-tolidine (1.66 g, 7.82 mmol, 1.5 equiv) were dispersed in 1,4-dioxane (50 mL). Then, aqueous 6 M acetic acid (2.70 mL, 16.15 mmol, 3.1 equiv) was added, and the mixture was sonicated at r.t. for 10 min in order to get a homogenous dispersion. The reaction mixture was magnetically stirred at 120 °C for 3 days. Solid was collected by filtration and washed with THF and acetone until a colorless filtrate was observed. The obtained solid was dried under vacuum at 120 °C for 4 h, to give TpBD-(CH<sub>3</sub>)<sub>2</sub> (1150 mg, 40% yield), as a red solid.

### 5.2.4. Synthesis of TpBD-(NO<sub>2</sub>)<sub>2</sub>

TpBD-(NO<sub>2</sub>)<sub>2</sub> was synthesized following a literature-known procedure.<sup>[58]</sup> In a Duran glass bottle (DURAN®, 25 mL, 3.6 cm x 7.0 cm), to a mixture of Tp (52 mg, 0.25 mmol, 1.0 equiv) and 3,3'-dinitrobenzidine (101 mg, 0.37 mmol, 1.5 equiv) was added anisole (8 mL), and an aqueous solution of 12 M acetic acid (2 mL). The mixture was sonicated for 10 min at r.t. to furnish a homogeneous mixture. Then, the reaction mixture, without stirring, was heated at 120 °C for 4 days. The red solid was filtered and washed with acetone (~200 mL). Then, in a Duran glass bottle, the resulting COF powder was re-suspended in anisole (5 mL), heated at 120 °C for 1 day and allowed to reach r.t. Red powder was collected by filtration and washed with acetone (6 x 30 mL) until a colorless filtrate was observed. The obtained powder was dried under high vacuum at 120 °C for 6 h to afford TpBD-(NO<sub>2</sub>)<sub>2</sub> (90 mg, 81%) as a red solid.

### 5.2.5. Synthesis of TpBD-(NH<sub>2</sub>)<sub>2</sub>

TpBD-(NH<sub>2</sub>)<sub>2</sub> was synthesized following a literature-known procedure.<sup>[58]</sup> In a 50 mL round-bottom flask, SnCl<sub>2</sub>·2H<sub>2</sub>O (1500 mg, 6.65 mmol) was dissolved in anhydrous THF (3 mL). To the solution was added TpBD-(NO<sub>2</sub>)<sub>2</sub> (71.2 mg), and the resulting suspension was

heated under reflux for 3 h. The brown powder was collected by filtration and suspended in aqueous 1 M HCl (10 mL, 30 min). Then, the precipitate was collected by filtration and washed with 1 M HCl (10 x 10 mL), water (3 x 10 mL), and THF (3 x 10 mL), with period of 1 h per wash. The resulting solid was dried under high vacuum at 120 °C for 6 h to give TpBD-(NH<sub>2</sub>)<sub>2</sub> (55 mg, 70%) as a brown solid.

#### **5.2.6. Synthesis of TpBD-(CF<sub>3</sub>)<sub>2</sub> (in mg scale)**

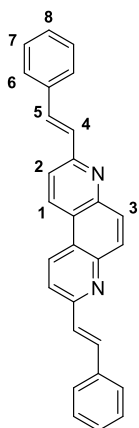
Into a 15 mL pressure tube (ACE glass, bushing type back seal, 10.2 cm x 25.4 cm), Tp (229 mg, 1.09 mmol, 1.0 equiv) and 3,3'-bis(trifluoromethyl)benzidine (523 mg, 1.64 mmol, 1.5 equiv) were suspended in 1,4-dioxane (4.5 mL) and mesitylene (4.5 mL). The suspension was stirred and sonicated at r.t. for 2 min to furnish a homogeneous mixture and aqueous 6M acetic acid (0.91 mL, 5.45 mmol) was added. The suspension was heated in an oil bath to 120 °C with vigorous stirring. At the beginning, solids started to dissolve to some extent but after 5 min a large amount of an orange solid was formed. The reaction mixture was stirred at 120 °C for 3 days, allowed to reach r.t., and filtered. The solid was washed with DMF (3 x 10 mL) until a colorless filtrate was observed. Then, it was washed with H<sub>2</sub>O (2 x 10 mL), acetone (3 x 10 mL), and CH<sub>2</sub>Cl<sub>2</sub> (3x10 mL). The resulting solid was dried under high vacuum at 80 °C to give TpBD-(CF<sub>3</sub>)<sub>2</sub> (396 mg, 74%) as a yellow solid.

#### **5.2.7. Synthesis of TpBD-(CF<sub>3</sub>)<sub>2</sub> (in gram scale)**

TpBD-(CF<sub>3</sub>)<sub>2</sub> was prepared following the procedure optimized for the synthesis in mg scale described above. Tp (370 mg, 1.76 mmol, 1.0 equiv); 3,3'-bis(trifluoromethyl)benzidine (845 mg, 2.64 mmol, 1.5 equiv); 1,4-dioxane and mesitylene (1:1, 12 mL); 6M acetic acid (1.47 mL, 8.8 mmol, 5 equiv). TpBD-(CF<sub>3</sub>)<sub>2</sub> (850 mg, 95%, yellow-orange solid).



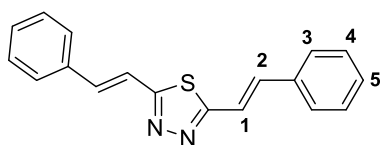
### 5.2.8. Synthesis of model compound 3,8-Di((E)-styryl)-4,7-phenanthroline (2)



In a 15 mL pressure tube (ACE glass, bushing type back seal, 10.2 cm x 25.4 mm), a mixture of Phen (41 mg, 0.20 mmol, 1.0 equiv) and benzaldehyde (1) (30  $\mu$ L, 0.30 mmol, 1.5 equiv) was dispersed in mesitylene (1.8 mL) and 1,4-dioxane (1.8 mL). Then, to the mixture was added trifluoroacetic acid (0.8 mL, 0.18 equiv) and acetonitrile (0.10 mL, 0.02 equiv). It was obtained a greenish solution, which was stirred at 150 °C for 3 days. The solid was collected by centrifugation and washed with 1,4-dioxane for five times. Then, the resulting solid was dried under reduced pressure to afford the model compound **2** (30 mg, 0.08 mmol, 40%) as a brown solid.

$^1\text{H}$  NMR (400 MHz, DMSO- $d_6$ ):  $\delta$ = 9.35 (d,  $J$  = 8.7 Hz, 2H, H-C(1) or H-C(2)), 8.23 (s, 2H, H-C(3)), 8.16 (d,  $J$  = 8.7 Hz, 2H, H-C(1) or H-C(2)), 7.99 (d,  $J$  = 16.3 Hz, 2H, H-C(4) or H-C(5)), 7.78 (d,  $J$  = 7.3 Hz, 4H, H-C(6)), 7.57 (d,  $J$  = 16.3 Hz, 2H, H-C(4) or H-C(5)), 7.47 (t,  $J$  = 7.4 Hz, 4H, H-C(7)), 7.39 (t,  $J$  = 7.2 Hz, 2H, H-C(8)). FT-IR (ATR): 3853, 3745, 3022, 1670, 1628, 1593, 1560, 1450, 1367, 1334, 1279, 1190, 1125, 965, 866, 839, 816, 758, 727, 687, 633, 551, 532  $\text{cm}^{-1}$ .

### 5.2.9. Synthesis of model compound 2,5-Di((E)-styryl)-1,3,4-thiadiazole (3)



In a 100 mL pressure tube (ACE glass, bushing type back seal, 17.8 cm x 38.1 mm), a mixture of Tda (178 mg, 1.56 mmol, 1.0 equiv) and benzaldehyde (1) (945  $\mu$ L, 9.34 mmol, 6 equiv) was dispersed in 1,4-dioxane (10 mL). Then, to the mixture was added 2 M KOH (5 mL). It was obtained a yellow solution, which was stirred at 100 °C for 3 days. The solid was collected by filtration and washed with methanol for five times. The resulting solid was dried under reduced pressure to afford the model compound **3** (226 mg, 0.78 mmol, 50%) as a yellow solid.

$^1\text{H}$  NMR (400 MHz, DMSO- $d_6$ ):  $\delta$ = 7.76 (dd,  $J$  = 8.3 Hz and  $J$  = 1.2 Hz, 4H, H-C(3)), 7.65 (d,  $J$  = 16.3 Hz, 2H, H-C(1) or H-C(2)), 7.56 (d,  $J$  = 16.4 Hz, 2H, H-C(1) or H-C(2)), 7.43 (m, 6H,

H–C(4) or H–C(5)). FT-IR (ATR): 3022, 1628, 1570, 1487, 1450, 1412, 1252, 1068, 972, 947, 856, 748, 687, 640, 577, 506  $\text{cm}^{-1}$ .

### **5.2.10. Synthesis of TFB-Phen COF**

In a 10 mL ampoule (Wheaton, prescored, borosilicate, 19 x 107 mm), to a mixture of TFB (50 mg, 0.31 mmol, 1.0 equiv) and Phen (96.2 mg, 0.46 mmol, 1.5 equiv) were added mesitylene (2 mL), 1,4-dioxane (1 mL), trifluoroacetic acid (0.68 mL, 0.18 equiv), and acetonitrile (0.08 mL, 0.022 equiv). The mixture was sonicated for 10 min at r.t. in order to get a homogeneous dispersion. Then, the ampoule was flash frozen at 77 K (liquid  $\text{N}_2$  bath), sealed off, and heated at 150 °C for 3 days. The solid was collected and washed with THF and  $\text{CH}_2\text{Cl}_2$  using a soxhlet washing procedure for 1 day. The resulting solid was dried under high vacuum at 90 °C to give TFB-Phen (30 mg, 35%) as a light brown solid.

## **5.3. Adsorption procedures**

### **5.3.1. Okadaic acid adsorption procedure**

#### **5.3.1.1. Okadaic acid quantification method**

Aqueous reaction buffer consisted of 20 mM Tris-HCl, 5 mM  $\text{MgCl}_2$ , 1 mM  $\text{MnCl}_2$ , 0.1% (v/v) 2-mercaptoethanol, and 1 mg  $\text{mL}^{-1}$  bovine serum albumin (BSA) adjusted to pH = 8. DIFMUP stock solution was prepared at 40 mM in a solution of 50 mM Tris-HCl at pH = 8. PP1 was reconstituted from the lyophilized product at 3.9 U  $\mu\text{L}^{-1}$  with ultrapure water. OA stock solutions were prepared at 1 mM in absolute ethanol. A separate calibration curve was used for each OA quantification experiment, and carried out in the same microplate as the rest of the samples. OA solutions for the calibration curves were prepared in the corresponding solvent, synthetic seawater for the quantification of the supernatants from the OA adsorption test and 70% ethanol for the quantification of the supernatants from the OA desorption assay. The PP1 inhibition assays were performed in a flat-bottom opaque 96-well microplates with a final volume of 200  $\mu\text{L}$  in each well. More in detail, 10  $\mu\text{L}$  of an intermediate solution of PP1 (0.01 U  $\mu\text{L}^{-1}$ ), prepared by dilution of the stock solution with aqueous buffer, was added to the reaction wells containing 165  $\mu\text{L}$  of reaction buffer. Then, 20  $\mu\text{L}$  of the corresponding solution of OA calibration curve, solvent (blank), or supernatant samples obtained from the adsorption/desorption assays were

added to the wells of microplate. Then, the microplate was incubated for 30 min under constant shaking of 500 rpm at 37 °C for a maximum enzymatic inhibition. Afterward, 5  $\mu\text{L}$  of 8 mM DIFMUP solution, prepared by dilution of the stock solution with aqueous buffer, was added to the wells. Next, the microplate was again incubated under constant shaking of 500 rpm at 37 °C for 2 h. Fluorescence intensity was measured (excitation wavelength 315 nm, emission wavelength 470 nm) in a BioTek Synergy H1 microplate reader. Analytical calculations were provided in duplicates for each experiment.

### 5.3.1.2. Calibration curves for OA quantification

Calibration curves were made using the software Origin9<sup>®</sup> by plotting the known concentrations of serial dilutions against their respective fluorescence read at 470 nm. Then, a non-linear pharmacology dose-response fitting was applied. Calibration curves were made using synthetic seawater or 70% ethanol as the solvent for the OA calibration standard dilutions. Below are examples of calibration curves made for each of the used solvents. The calibration curves for each solvent represent the average fluorescent values from three different experiments. The error bars were calculated as standard deviation (SD).

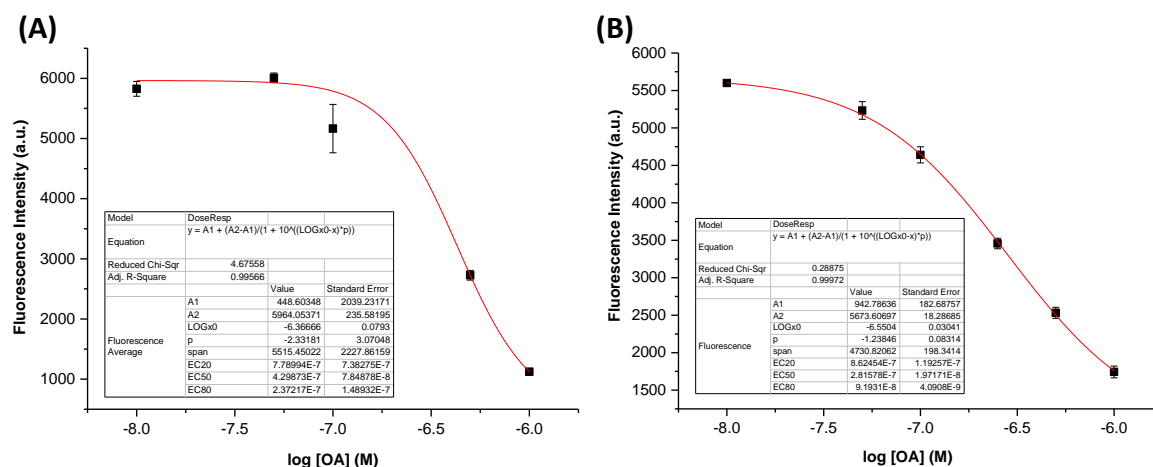


**Figure 52.** OA calibration curve in synthetic seawater (A) and ethanol 70% (B).

### **5.3.1.3. Adsorption kinetics**

Samples of 100  $\mu\text{L}$  of TpBD-(CH<sub>3</sub>)<sub>2</sub> COF dispersion of 1 mg mL<sup>-1</sup> in synthetic seawater were spiked with an OA concentration of 10, 15, 50, and 100  $\mu\text{mol L}^{-1}$ . Mixtures were incubated at 19 °C under constant shaking at 1400 rpm, with incubation times of 0.5, 60, 240, and 480 min. Then, the supernatant of the samples was collected by centrifugation (15 000 rpm, 19 °C, 15 min). The time used for centrifugation was added to the time points as time elapsed, resulting in time points of 15.5, 75, 255, and 495 min, respectively. Supernatants were collected and quantified for OA. Two replicates of each concentration and each time were done.

### **5.3.1.4. Desorption kinetics**

Samples of 100  $\mu\text{L}$  of a TpBD-(CH<sub>3</sub>)<sub>2</sub> COF dispersion of 1 mg mL<sup>-1</sup> in synthetic seawater were spiked with an OA concentration of 10  $\mu\text{mol L}^{-1}$  and incubated at 19 °C under constant shaking at 1400 rpm for each time point. After 240 min of incubation, the samples were centrifuged at 15 000 rpm during 15 min at 19 °C. Desorption kinetics were carried out using the pellets, which were suspended in 200  $\mu\text{L}$  of ethanol 70% and incubated during 5, 30, 60, 120, or 240 min at 19 °C under constant shaking at 1400 rpm. The samples were then centrifuged at 15 000 rpm for 15 min at 19 °C. Supernatants were recovered and analyzed for OA quantification. In the case of the samples for 5 minutes of incubation the volumes were increased (500  $\mu\text{L}$  for adsorption tests and 1000  $\mu\text{L}$  for desorption), maintaining OA and COF concentrations (10  $\mu\text{mol L}^{-1}$  and 1 mg mL<sup>-1</sup>, respectively). COF was separated from the supernatant by filtration through a 0.2  $\mu\text{m}$  PES syringe filter after the 5 minutes incubation in order to avoid the centrifugation time lapse.

### **5.3.1.5. Recycling tests**

First, the adsorption assays were carried out with an OA concentration of 10  $\mu\text{mol L}^{-1}$  in a final volume of 100  $\mu\text{L}$  of TpBD-(CH<sub>3</sub>)<sub>2</sub> in synthetic seawater during 240 min at 19 °C under constant shaking at 1400 rpm. The samples were then centrifuged at 15 000 rpm during 15 min at 19 °C. The supernatants were collected and OA was quantified (cycle 1). The pellets were suspended in ultrapure water and centrifuged at 15 000 rpm during 15

min at 19 °C. The OA was desorbed from the pellets by soaking in 200  $\mu\text{L}$  of ethanol 70% at 4 °C, overnight. The pellets from desorption were suspended in synthetic seawater with an OA concentration of 10  $\mu\text{mol L}^{-1}$ , initiating the adsorption cycle 2. The procedure was repeated for cycle 3.

### **5.3.2. Microcystin adsorption procedure**

#### **5.3.2.1. *Microcystin quantification method***

Aqueous reaction buffer was prepared as described for OA quantification, on section 3.1.1. DIFMUP stock solution was prepared at 40 mM in a solution of 50 mM Tris-HCl at pH = 8. PP1 was reconstituted from the lyophilized product at 1.53 U  $\mu\text{L}^{-1}$  with 20% (v/v) glycerol solution. MC stock solutions were prepared at 1 mM with ultrapure water. Separated calibration curves were used for each quantification experiment of the different microcystins, and performed in the same microplate as the rest of the samples. Microcystin standard solutions for the calibration curves were prepared in the corresponding solvent, ultrapure water for the quantification of the supernatants from the adsorption test and propan-2-ol for the quantification of the supernatants from the desorption assay. The PP1 inhibition assays were performed in a flat-bottom opaque 96-well microplates with a final volume of 200  $\mu\text{L}$  in each well. More in detail, 10  $\mu\text{L}$  of an intermediate solution of PP1 (0.02 U  $\mu\text{L}^{-1}$ ), prepared by dilution of the stock solution with aqueous buffer, was added to the reaction wells containing 165  $\mu\text{L}$  of reaction buffer. Then, 20  $\mu\text{L}$  of the corresponding solution of microcystin calibration curve, solvent (blank), or supernatant samples obtained from the adsorption/desorption assays were added to the wells of microplate. Then, the microplate was incubated for 30 min under constant shaking of 500 rpm at 37 °C for a maximum enzymatic inhibition. Afterward, 5  $\mu\text{L}$  of 8 mM DIFMUP solution, prepared by dilution of the stock solution with aqueous buffer, was added to the wells. Next, the microplate was again incubated under constant shaking of 500 rpm at 37 °C for 2 h. Fluorescence intensity was measured (excitation wavelength 315 nm, emission wavelength 470 nm) in a BioTek Synergy H1 microplate reader. Analytical calculations were provided in duplicates for each experiment.

### 5.3.2.2. Calibration curves for MC quantification

Calibration curves were prepared using the software Origin9®, plotting the known concentration of serial dilutions against their corresponding fluorescence at 470 nm. Then, a non-linear pharmacology dose-response fitting was applied. Calibration curves were prepared using the corresponding solvent, ultrapure water or propan-2-ol, as the solvent for calibration standard solutions. Examples of calibration curves made for each microcystin with the used solvents are presented below. The calibration curves represent the average fluorescent values of three different experiments. The error bars were calculated as standard deviation (SD).

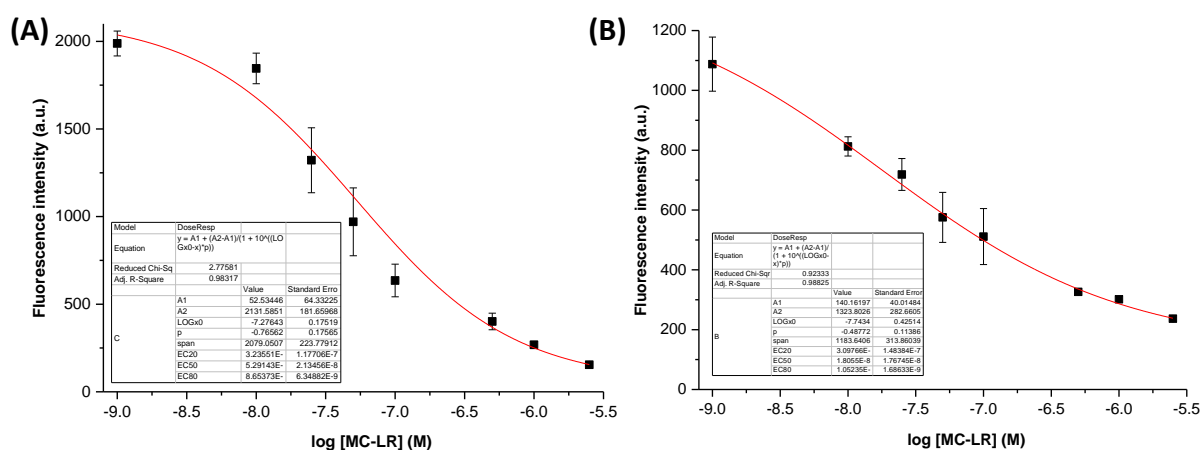


Figure 53. MC-LR calibration curve in ultrapure water (A) and propan-2-ol (B).

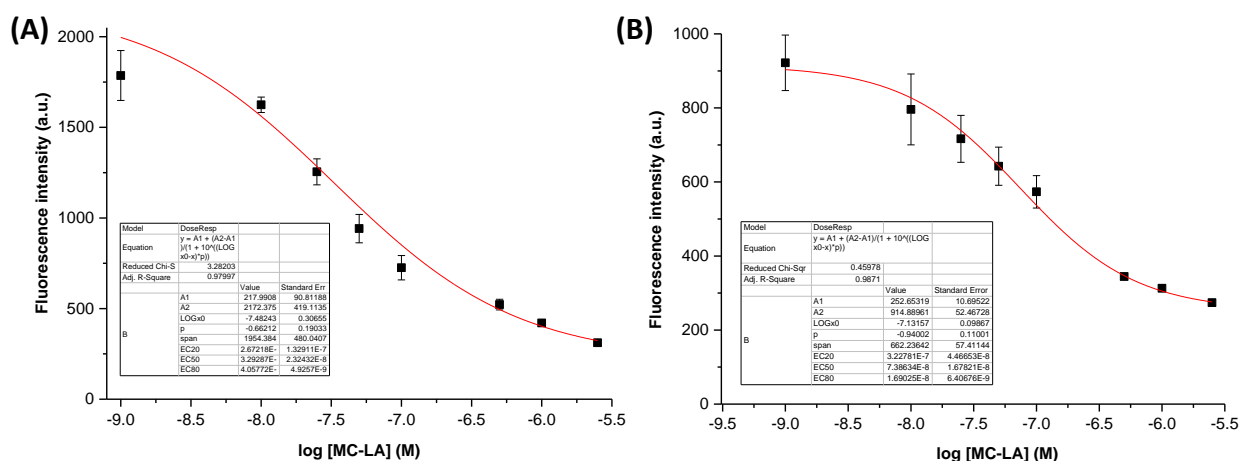


Figure 54. MC-LA calibration curve in ultrapure water (A) and propan-2-ol (B).

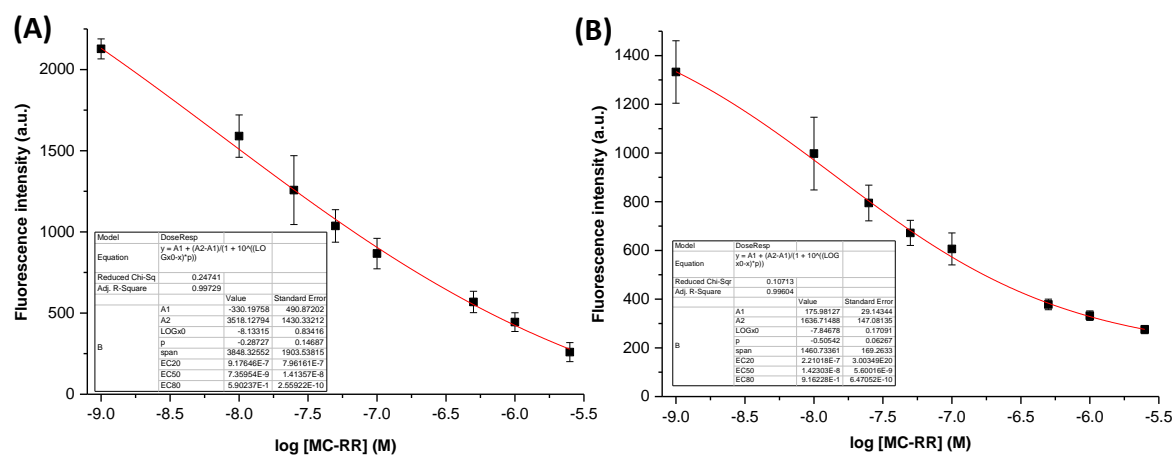


Figure 55. MC-RR calibration curve in ultrapure water (A) and propan-2-ol (B).

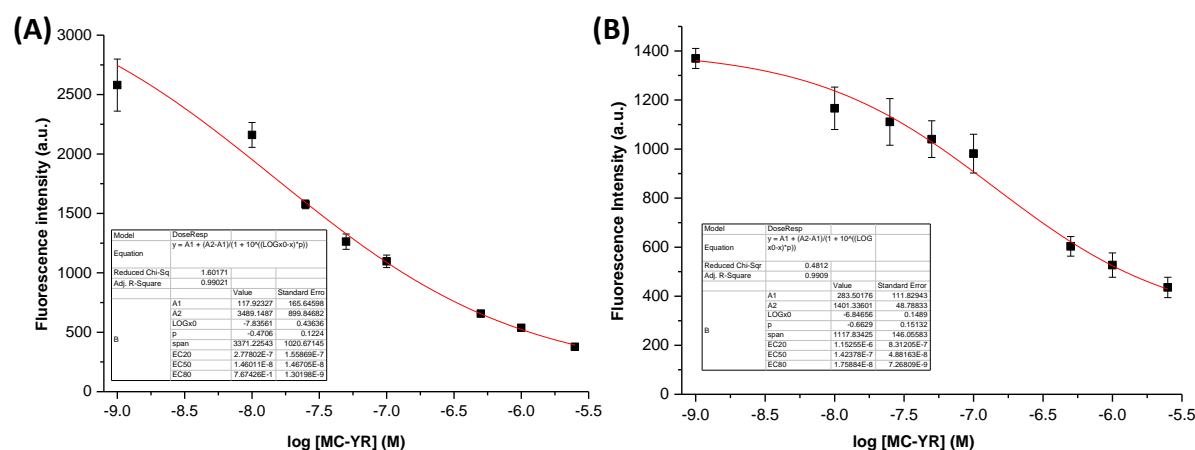
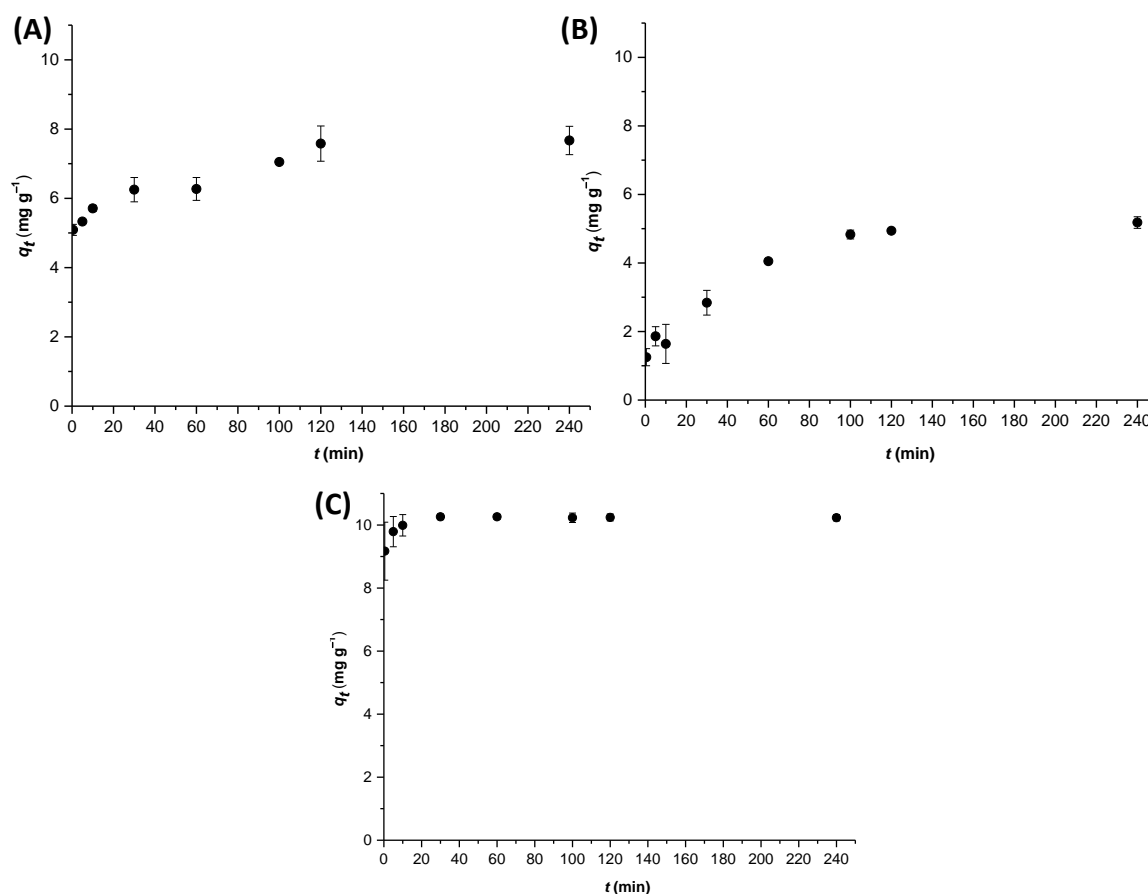


Figure 56. MC-YR calibration curve in ultrapure water (A) and propan-2-ol (B).

### 5.3.2.3. Adsorption kinetics

Samples of 100  $\mu\text{L}$  of a TpBD-(CF<sub>3</sub>)<sub>2</sub>, TpBD-(NO<sub>2</sub>)<sub>2</sub>, or TpBD-(NH<sub>2</sub>)<sub>2</sub> COF dispersion of 1 mg mL<sup>-1</sup> in ultrapure water were spiked with a MC-LR, -LA, -RR, or -YR concentration of 1, 5, 10, 15, and 25  $\mu\text{mol L}^{-1}$ . Mixtures were incubated at 19 °C under constant shaking at 1400 rpm, with incubation times of 0.5, 5, 10, 30, 60, 100, 120, and 240 min. The supernatant of the samples with incubation times of 60, 100, 120, and 240 min were collected by centrifugation (15 000 rpm, 19 °C, 15 min). For the short times of the kinetics (0.5, 5, 10, and 30 min), the isolation of supernatant was performed by filtration (0.22  $\mu\text{m}$  hydrophilic PVDF membrane). Supernatants were collected and quantified for

MC-LR, -LA, -RR, and -YR. Two replicates of each concentration and each time were done. In case of samples with a concentration of  $1 \mu\text{mol L}^{-1}$  of MC, the volume of experiment was increased to  $200 \mu\text{L}$ , maintaining COF and MC concentration.



**Figure 57.** Adsorption kinetics at  $10 \mu\text{mol L}^{-1}$  of: (A) MC-LA; (B) MC-RR; and (C) MC-YR in  $\text{TpBD}-(\text{CF}_3)_2$ , expressed as quantity adsorbed,  $q_t$  ( $\text{mg g}^{-1}$ ) in function of time, 0.5, 5, 10, 30, 60, 100, 120, and 240 min, at  $19^\circ\text{C}$  in ultrapure water at pH 6–7 [ $C_0(\text{COF}) = 1 \text{ mg mL}^{-1}$ ]. Results are expressed as the mean of three independent experiments with measurements performed in duplicates. Error bars correspond to the standard deviation of the mean.

#### 5.3.2.4. Adsorption and desorption assay

For adsorption, two replicates of  $100 \mu\text{L}$  of a  $\text{TpBD}-(\text{CF}_3)_2$ ,  $\text{TpBD}-(\text{NO}_2)_2$ , or  $\text{TpBD}-(\text{NH}_2)_2$  COF dispersion of  $1 \text{ mg mL}^{-1}$  in ultrapure water were spiked with a MC-LR, -LA, -RR, or -YR concentration of  $10 \mu\text{mol L}^{-1}$ . Mixtures were incubated at  $19^\circ\text{C}$  under constant shaking at 1400 rpm for 240 min. After this time, the supernatant of the samples



was collected by centrifugation (15 000 rpm, 19 °C, 15 min), and analyzed for MC quantification. The pellets were washed with ultrapure water (100  $\mu$ L) under constant shaking at 1400 rpm for 10 min, and collected by centrifugation (15 000 rpm, 19 °C, 15 min). With regard to desorption, the pellets obtained from the adsorption assay were suspended in 200  $\mu$ L of propan-2-ol and incubated overnight at 4 °C under constant shaking of 1400 rpm. Then, the samples were centrifuged (15 000 rpm, 19 °C, 15 min), and the supernatants analyzed for MC quantification.

### 5.3.2.5. Adsorption isotherms at 19 °C

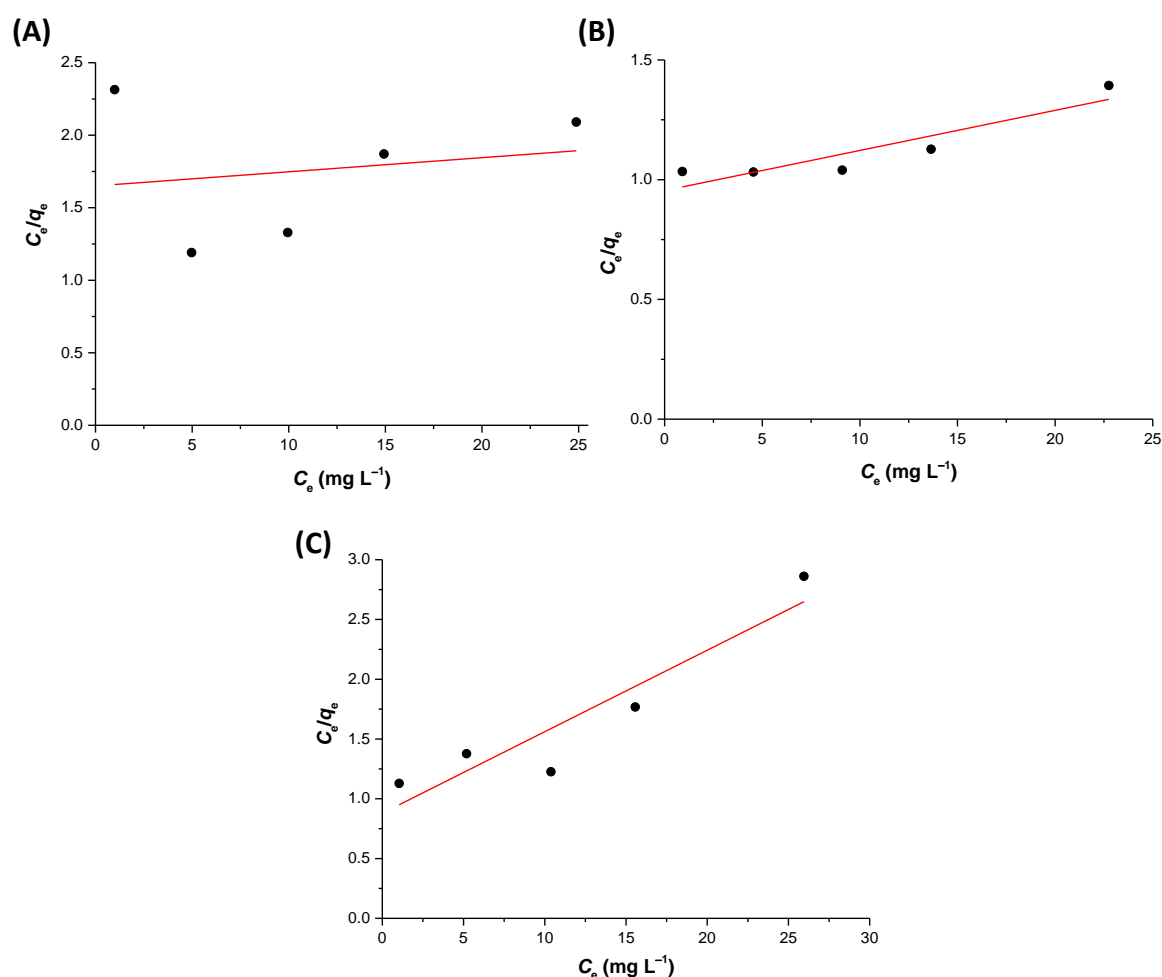


**Figure 58.** Linear regression of the Langmuir isotherm for the experimental adsorption of (A) MC-LR by TpBD-(CF<sub>3</sub>)<sub>2</sub>; (B) MC-LA by TpBD-(NH<sub>2</sub>)<sub>2</sub>; and MC-RR by TpBD-(NO<sub>2</sub>)<sub>2</sub>.

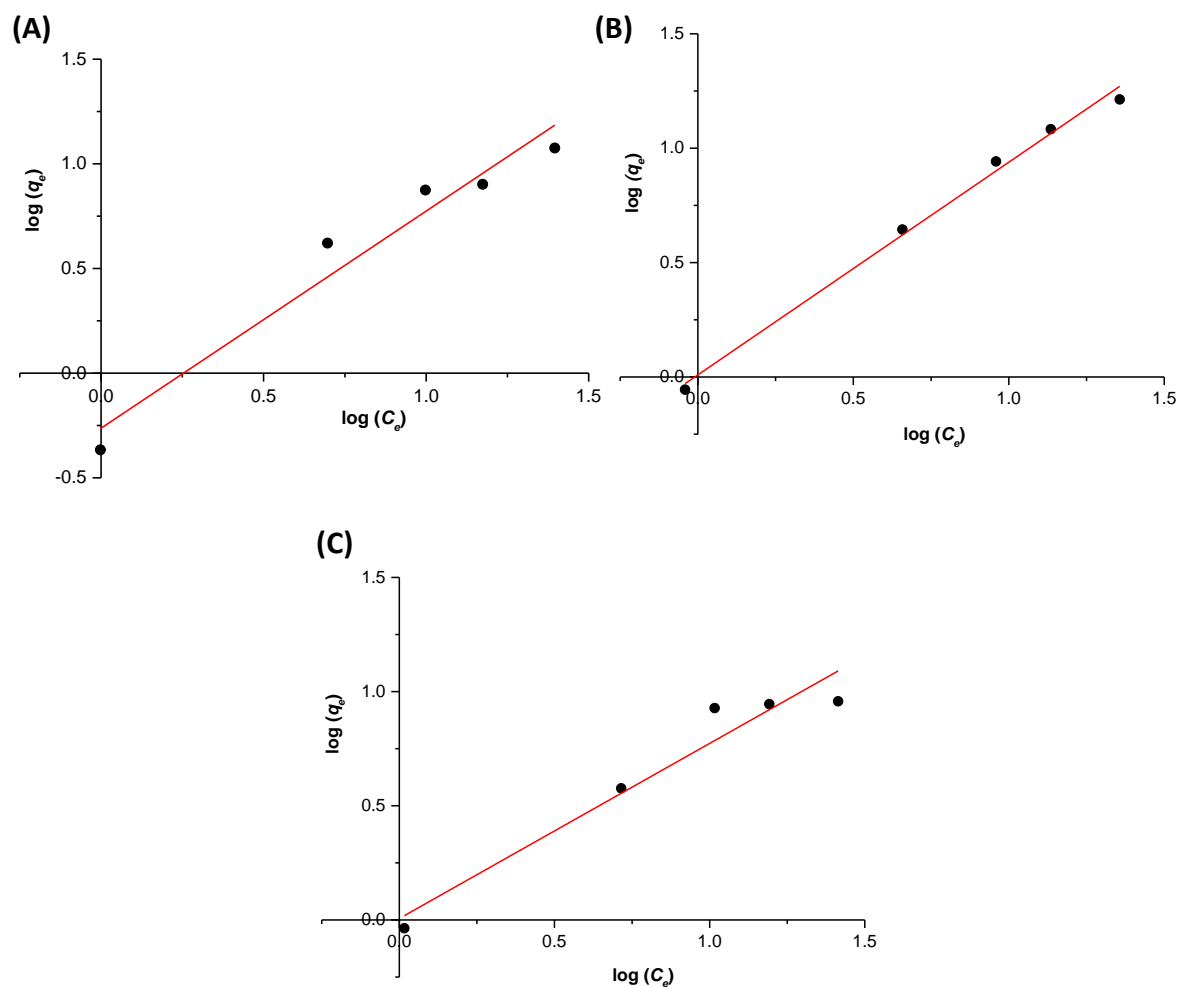


**Figure 59.** Linear regression of the Freundlich isotherm for the experimental adsorption of (A) MC-LR by TpBD-(CF<sub>3</sub>)<sub>2</sub>; (B) MC-LA by TpBD-(NH<sub>2</sub>)<sub>2</sub>; and MC-RR by TpBD-(NO<sub>2</sub>)<sub>2</sub>.

### 5.3.3. Ibuprofen, acetaminophen, and ampicillin adsorption procedure

#### 5.3.3.1. Stock solutions

Stock solutions of the pharmaceuticals were prepared in methanol for ibuprofen and in ultrapure water for acetaminophen and ampicillin. For adsorption kinetics, 40 mg of ibuprofen was added to 2 mL of methanol to obtain a final concentration of 20000 mg L<sup>-1</sup>. For COF stock solution, 5 mg of COF was added to 50 mL of ultrapure water with a final concentration of 100 mg L<sup>-1</sup>. Buffers for the adsorption experiments and different pH were prepared in ultrapure water as follows: pH 2 buffer: 50 mL of aqueous 0.2 M KCl solution

and 13 mL of aqueous 0.2 M HCl solution; pH 10 buffer: 100 mL of aqueous 0.025 M  $\text{Na}_2\text{B}_4\text{O}_7 \cdot 10\text{H}_2\text{O}$  solution and 36.6 mL of aqueous 0.1 M NaOH solution.

### 5.3.3.2. Adsorption kinetics

Adsorption experiments were performed using a batch experimental approach with TpBD-( $\text{CF}_3$ )<sub>2</sub> and TpBD-( $\text{CH}_3$ )<sub>2</sub> as adsorbents and ibuprofen as target compound. Ultrapure water was used as the solvent at pH 6–7. From the ibuprofen stock solution, a sample of 1.5  $\mu\text{L}$  was withdrawn and added to a solution of 1.5 mL of COF stock solution. The mixture was incubated under constant shaking (1400 rpm) at  $21 \pm 2$  °C during a specific time. The supernatant was isolated by centrifugation (15000 rpm, 21 °C, 15 min) and analyzed by UV/Vis spectroscopy ( $\lambda = 220$  nm) to determine the quantity of the pharmaceutical remaining in the solution after adsorption. For the short times of the kinetics (0.5, 5, 10, 20, and 30 min), the isolation of the supernatant was performed by filtration (0.22  $\mu\text{m}$  polysulfone syringe filter). The amount of the pharmaceutical adsorbed onto the COF at a specific time,  $q_t$  ( $\text{mg g}^{-1}$ ), was calculated. For the rest of the adsorption experiments,  $t = 120$  min was chosen to ensure that equilibrium was reached, as inferred from the kinetics studies. The amount of the pharmaceutical adsorbed onto the COF in equilibrium,  $q_e$  ( $\text{mg g}^{-1}$ ), was calculated.

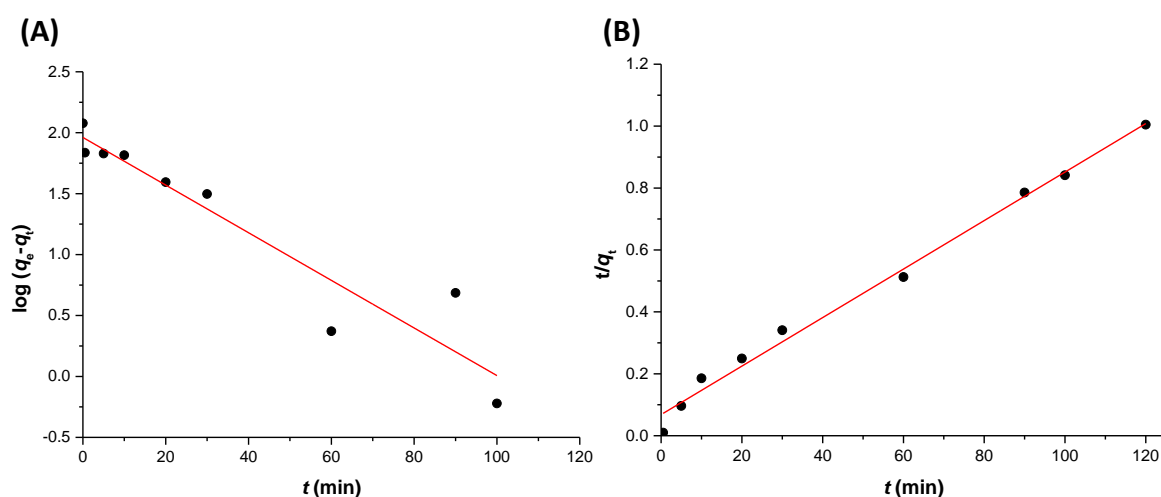


**Figure 60.** (A) Pseudo-first-order adsorption kinetics, and (B) pseudo-second-order adsorption kinetics of ibuprofen onto TpBD-( $\text{CF}_3$ )<sub>2</sub>.

### **5.3.3.3. Adsorption and desorption assay**

For the adsorption and desorption experiments performed, COF (12.5 mg or 200 mg,  $C(\text{COF}) = 100 \text{ mg L}^{-1}$ ) was magnetically stirred in a solution of ibuprofen in water (125 mL or 2 L;  $20 \text{ mg L}^{-1}$ ) at  $21 \text{ }^\circ\text{C}$  for 120 min. The supernatant was isolated by filtration (pore 3 glass filter covered with a Whatman filter paper of 47 mm) and analyzed by UV-Vis spectroscopy ( $\lambda = 220 \text{ nm}$ ) using a NanoDrop 2000C spectrophotometer to determine the quantity of ibuprofen remaining in the solution after adsorption. For desorption, the COF was soaked in propan-2-ol (100 mL) at  $4 \text{ }^\circ\text{C}$  for 16 h under magnetic stirring. The suspension was filtered (pore 3 glass filter covered with a Whatman filter paper of 47 mm), and the supernatant was analyzed by UV-Vis spectroscopy to determine the quantity of ibuprofen desorbed ( $\lambda = 220 \text{ nm}$ ). The full characterization of the material after ibuprofen adsorption and desorption was performed using the COF material from the experiment with 200 mg.

### **5.3.3.4. Adsorption at different pH**

For adsorption at different pH values, 4 mg of the pharmaceutical was added to 2 mL of methanol for ibuprofen and ultrapure water for acetaminophen and ampicillin with a final concentration of  $2000 \text{ mg L}^{-1}$ . For COF stock solution, 0.505 mg of COF was added to 5 mL of ultrapure water (pH 6–7) or buffer at pH 2 or 10 with a final concentration of  $101 \text{ mg L}^{-1}$ . From the stock solution of pharmaceutical, 6  $\mu\text{L}$  were withdrawn to a solution of 594  $\mu\text{L}$  of stock solution of COF. The mixture was incubated under constant shaking (1400 rpm) at  $21 \text{ }^\circ\text{C}$  for 120 min. Then, the supernatant was analyzed by UV-Vis spectroscopy in NanoDrop, with wavelengths of analysis of 220 nm, 243 nm, and 210 nm for ibuprofen, acetaminophen, and ampicillin, respectively.

### **5.3.3.5. Adsorption of ibuprofen in ethanol**

Stock solution of ibuprofen was prepared in pure ethanol with a final concentration of  $2000 \text{ mg L}^{-1}$ . For TpBD-(CF<sub>3</sub>)<sub>2</sub>, a stock solution in ethanol was prepared with a final concentration of  $100 \text{ mg L}^{-1}$ . In the adsorption experiments, from the stock solution of pharmaceuticals 15  $\mu\text{L}$  were withdrawn to a solution of 1485  $\mu\text{L}$  of TpBD-(CF<sub>3</sub>)<sub>2</sub> stock

solution. The mixture was incubated under constant shaking (1400 rpm) at 21 °C for 120 min. Then, the supernatant was analyzed by UV-Vis spectroscopy at 220 nm.

#### **5.3.3.6. Adsorption of diclofenac method**

Stock solution of diclofenac was prepared in pure ethanol with a final concentration of 1.8 mg mL<sup>-1</sup>. For TpBD-(CF<sub>3</sub>)<sub>2</sub>, a stock solution was prepared in water with a final concentration of 100 mg L<sup>-1</sup>. In the adsorption experiments, from the stock solution of diclofenac 2 μL were withdrawn to a solution of 11498 μL of COF stock solution. The mixture was incubated under constant shaking (1400 rpm) at 21 °C for 120 min. Then, the supernatant was analyzed by UV-Vis spectroscopy at a wavelength of 273 nm.

#### **5.3.3.7. Calibration curves for ibuprofen, acetaminophen, and ampicillin quantification**

Calibration curves were prepared using the software Origin9®, plotting the known concentration of serial dilutions against the corresponding absorbance at 220, 243, and 210 nm for ibuprofen, acetaminophen, and ampicillin, respectively. Then, a linear fitting was applied. Calibration curves were prepared using the corresponding solvent, ultrapure water, propan-2-ol, and buffer at pH 2 or 10, as the solvent for calibration standard solutions. Examples of calibration curves made for each pharmaceutical with the used solvents are presented below.

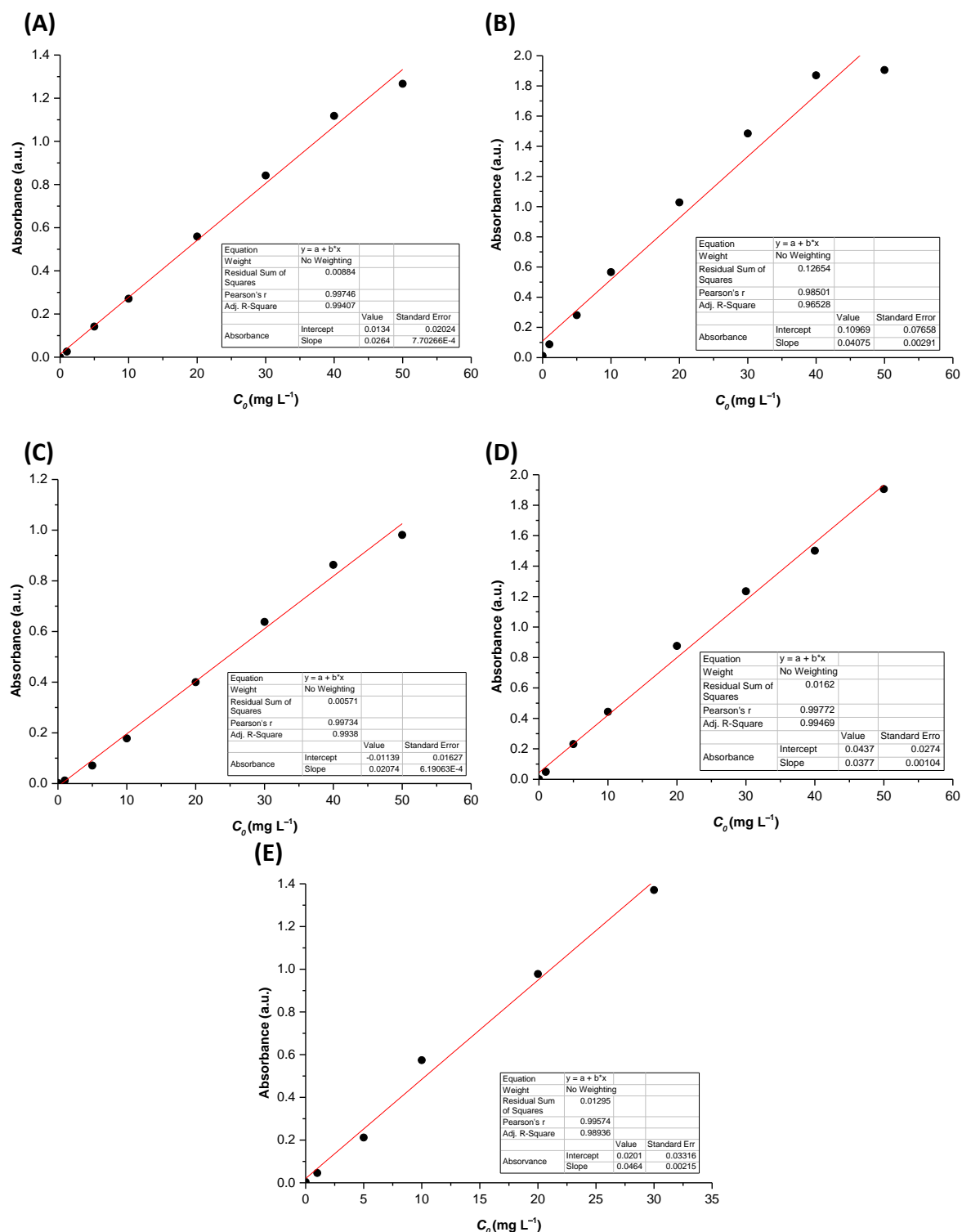


**Figure 61.** Calibration curve of ibuprofen in ultrapure water (A), propan-2-ol (B), buffer at pH 2 (C), buffer at pH 10 (D), and ethanol (E) as measured by UV-Vis spectroscopy at 220 nm.

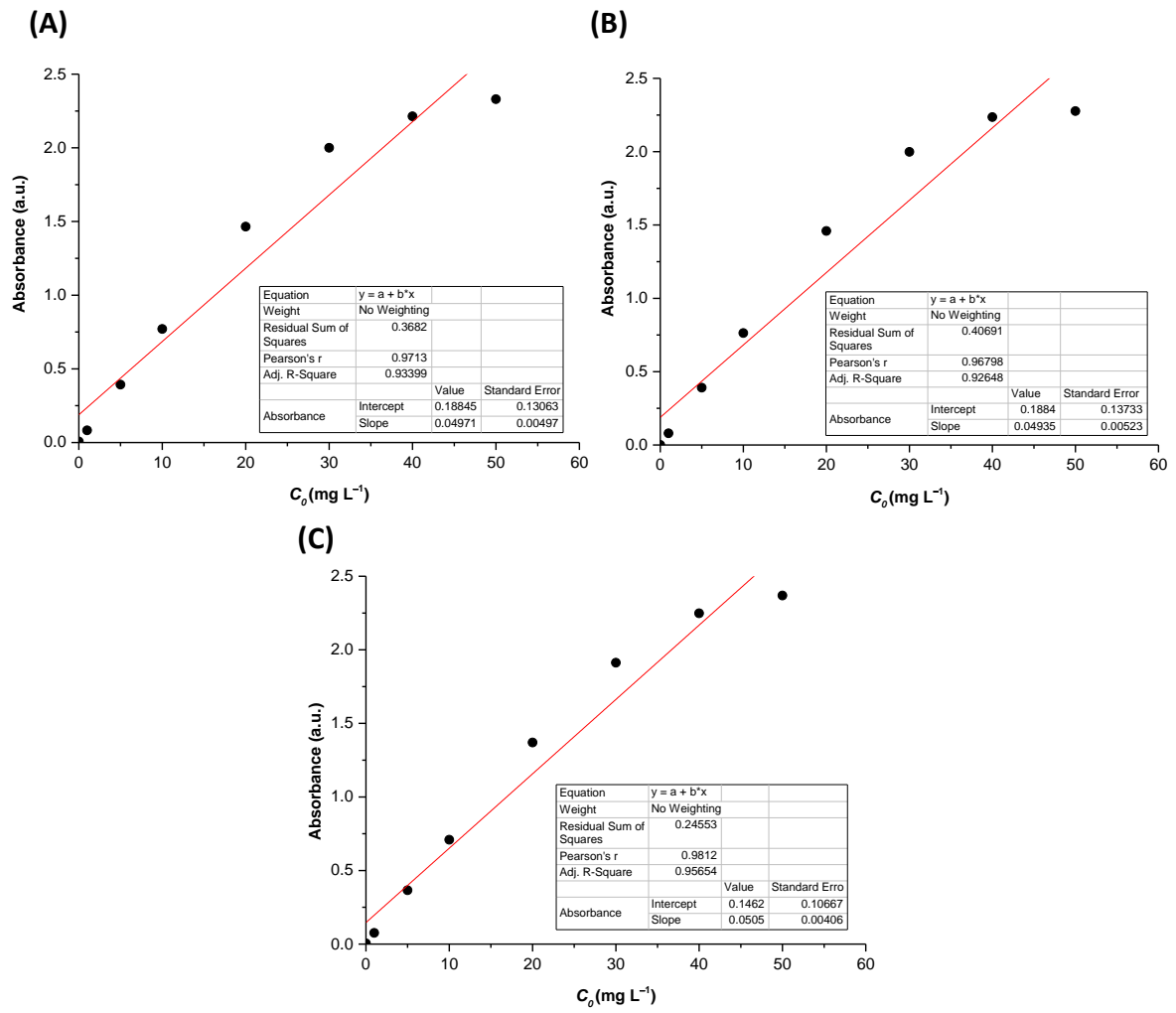


**Figure 62.** Calibration curve of acetaminophen in ultrapure water (A), buffer at pH 2 (B), and buffer at pH 10 (C) as measured by UV-Vis spectroscopy at 243 nm.

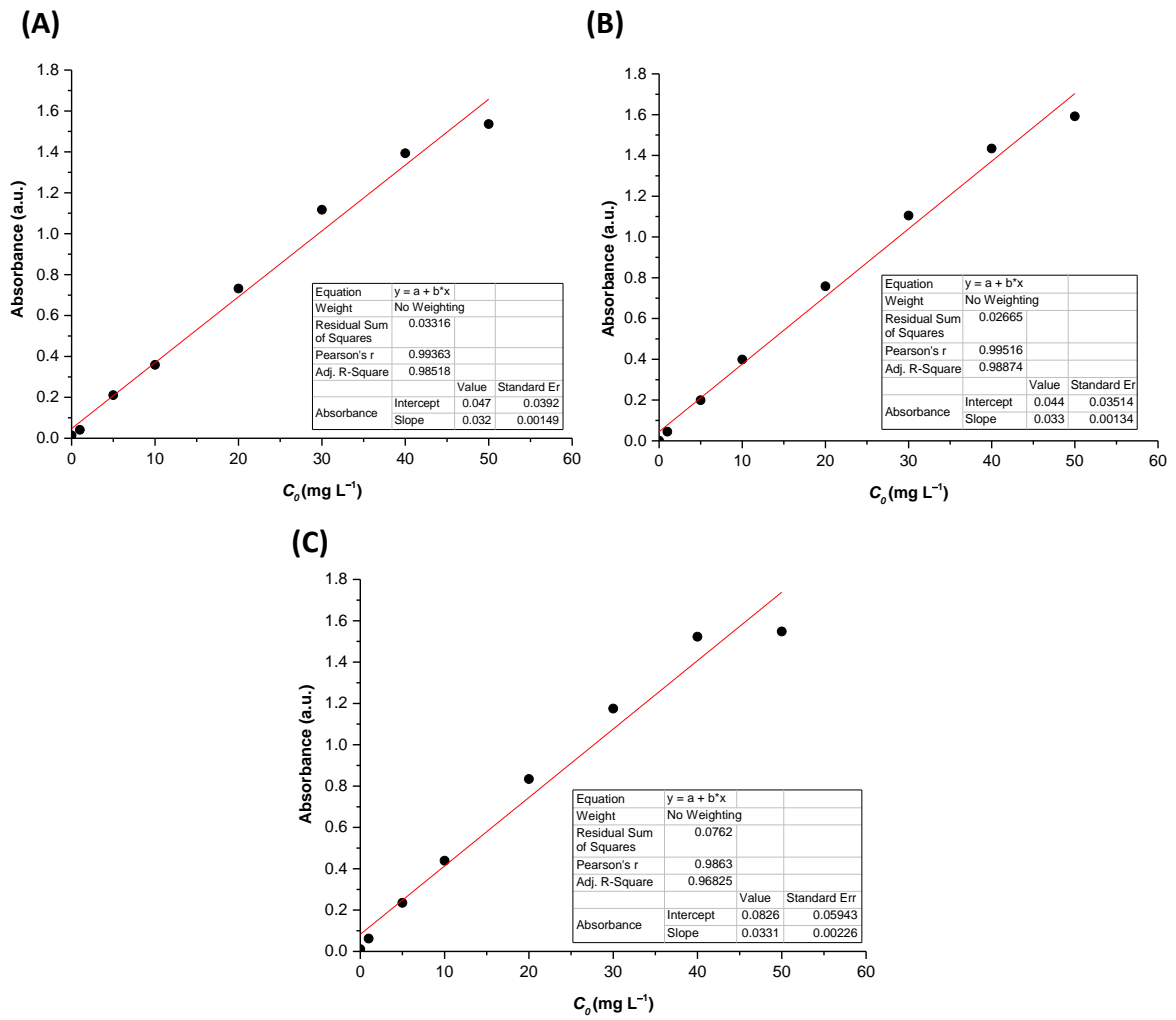


**Figure 63.** Calibration curve of ampicillin in ultrapure water (A), buffer at pH 2 (B), and buffer at pH 10 (C) as measured by UV-Vis spectroscopy at 210 nm.



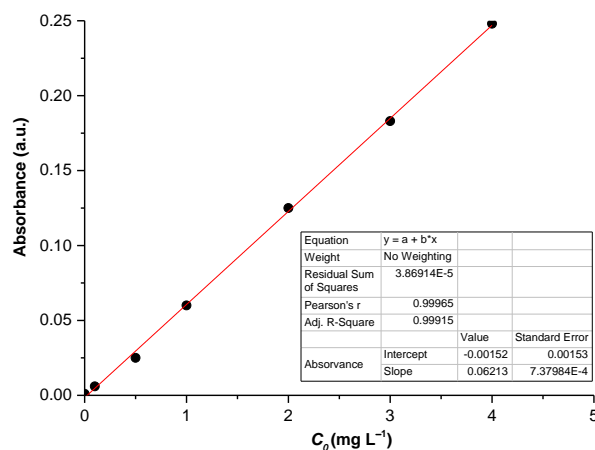


**Figure 64.** Calibration curve of diclofenac in ultrapure water as measured by UV-Vis spectroscopy at 273 nm.

### 5.3.4. Ibuprofen adsorption in natural water samples

#### 5.3.4.1. Stock solutions

Stock solutions of the pharmaceuticals were prepared in methanol, to ensure their solubility, with final concentrations of 1.03 and 2.06 g L<sup>-1</sup> for ibuprofen; 0.76, 1.51, and 2.27 g L<sup>-1</sup> for acetaminophen; and, 1.16, 2.32, and 3.48 g L<sup>-1</sup> for phenobarbital. COF stock solutions were prepared in lake, river, and estuary waters with a final concentration of 336 mg L<sup>-1</sup>.

#### 5.3.4.2. Pharmaceuticals quantification by HPLC

Agilent Technologies (Waldbronn, Germany) 1200 series HPLC system was used for the identification and quantification of the pharmaceuticals in natural water samples of the lake, river, and estuary. HPLC was equipped with a pump module, a vacuum degasser, an autosampler, a thermostatted column compartment, and a diode-array detector (DAD). Data acquisition was performed by Agilent's ChemStation software, version 1.9.0. Reverse phase analysis was carried out with a Kinetex EVO C-18 column purchased from Phenomenex (Madrid, Spain) (reversed phase, particle size of 2.6 μm, pore size of 100 Å, length 100 mm, internal diameter 4.6 mm) at 20 °C. Mobile phase consisted of 0.1% v/v TFA in ultrapure water (phase A) and 0.1% v/v TFA in acetonitrile (phase B). A gradient ratio of 98% of phase A and 2% of phase B was employed for 6 min. Then, during 5 min a gradient

ratio of 70% phase A and 30% phase B was applied. The injection volume was set to 20  $\mu\text{L}$  and a flow rate of 1.25  $\text{mL min}^{-1}$  was maintained during the whole analysis. Detection of ibuprofen was performed at  $\lambda = 220 \text{ nm}$  and a retention time of around 9.5 min; acetaminophen at  $\lambda = 243 \text{ nm}$  with a retention time of around 2.8 min; and phenobarbital at  $\lambda = 210 \text{ nm}$  with a retention time of around 6.1 min.

#### **5.3.4.3. Adsorption of ibuprofen, acetaminophen and phenobarbital**

Adsorption experiments were performed using lake, river, and estuary natural water samples, which were spiked individually with ibuprofen, acetaminophen, and phenobarbital stock solutions. Concentration of methanol in water mixtures was always below 1% of total volume. For adsorption of ibuprofen, 6  $\mu\text{L}$  of pharmaceutical stock solutions was withdrawn and added to a mixture of 594  $\mu\text{L}$  of TpBD-( $\text{CF}_3$ )<sub>2</sub> stock solution prepared in lake, river, and estuary water, respectively, to obtain a final pharmaceutical concentration of 0.05 or 0.10  $\text{mmol L}^{-1}$ . For acetaminophen and phenobarbital adsorption, 6  $\mu\text{L}$  of pharmaceutical stock solutions were withdrawn and added to a mixture of 594  $\mu\text{L}$  of TpBD-( $\text{CF}_3$ )<sub>2</sub> stock solution prepared in lake water, to obtain final pharmaceutical concentrations of 0.05, 0.10, and 0.15  $\text{mmol L}^{-1}$ . The mixtures were prepared as duplicates and incubated under constant shaking at 1400 rpm and  $21 \pm 2 \text{ }^\circ\text{C}$  for 120 min. After this time, the supernatant was isolated by centrifugation (15000 rpm,  $21 \text{ }^\circ\text{C}$ , 15 min) and the supernatant filtered through a 0.22  $\mu\text{m}$  polysulfone syringe filter. Supernatant was analyzed by HPLC-DAD to quantify the amount of pharmaceutical remaining in the solution after adsorption. The characteristic retention time of each pharmaceutical allowed their identification. The surface area of the chromatographic peak was determined using the software OpenLab. The amount of the pharmaceutical adsorbed onto the COF,  $q_t$  ( $\text{mg g}^{-1}$ ), was calculated.

#### **5.3.4.4. Adsorption of binary mixtures of ibuprofen and acetaminophen or phenobarbital**

Adsorption experiments were performed using lake water samples, which were spiked with mixtures of ibuprofen with acetaminophen or phenobarbital, in the ratios of 0.05  $\text{mmol L}^{-1}$  of ibuprofen and 0.15  $\text{mmol L}^{-1}$  of acetaminophen or phenobarbital

(50/150  $\mu\text{M}$ ) and 0.10  $\text{mmol L}^{-1}$  of ibuprofen and 0.10  $\text{mmol L}^{-1}$  of acetaminophen or phenobarbital (100/100  $\mu\text{M}$ ). For the adsorption, 6  $\mu\text{L}$  of ibuprofen stock solution and 6  $\mu\text{L}$  of acetaminophen or phenobarbital stock solution were withdrawn and added to a mixture of 588  $\mu\text{L}$  of TpBD-(CF<sub>3</sub>)<sub>2</sub> stock solution prepared in lake water. The adsorption experiment and analysis were carried out as described above.

**5.3.4.5. Calibration curves for ibuprofen, acetaminophen, and phenobarbital quantification**

Calibration curves of ibuprofen, acetaminophen, and phenobarbital were prepared with concentrations between 0 and 30  $\text{mg L}^{-1}$  in ultrapure water (pH 6–7). The samples were analyzed by HPLC-DAD as described above. The area of the chromatographic peak typical of each pharmaceutical was determined. The peak area ( $\text{mAu s}^{-1}$ ) versus pharmaceutical concentration was plotted and a linear regression was applied (Figure 40).

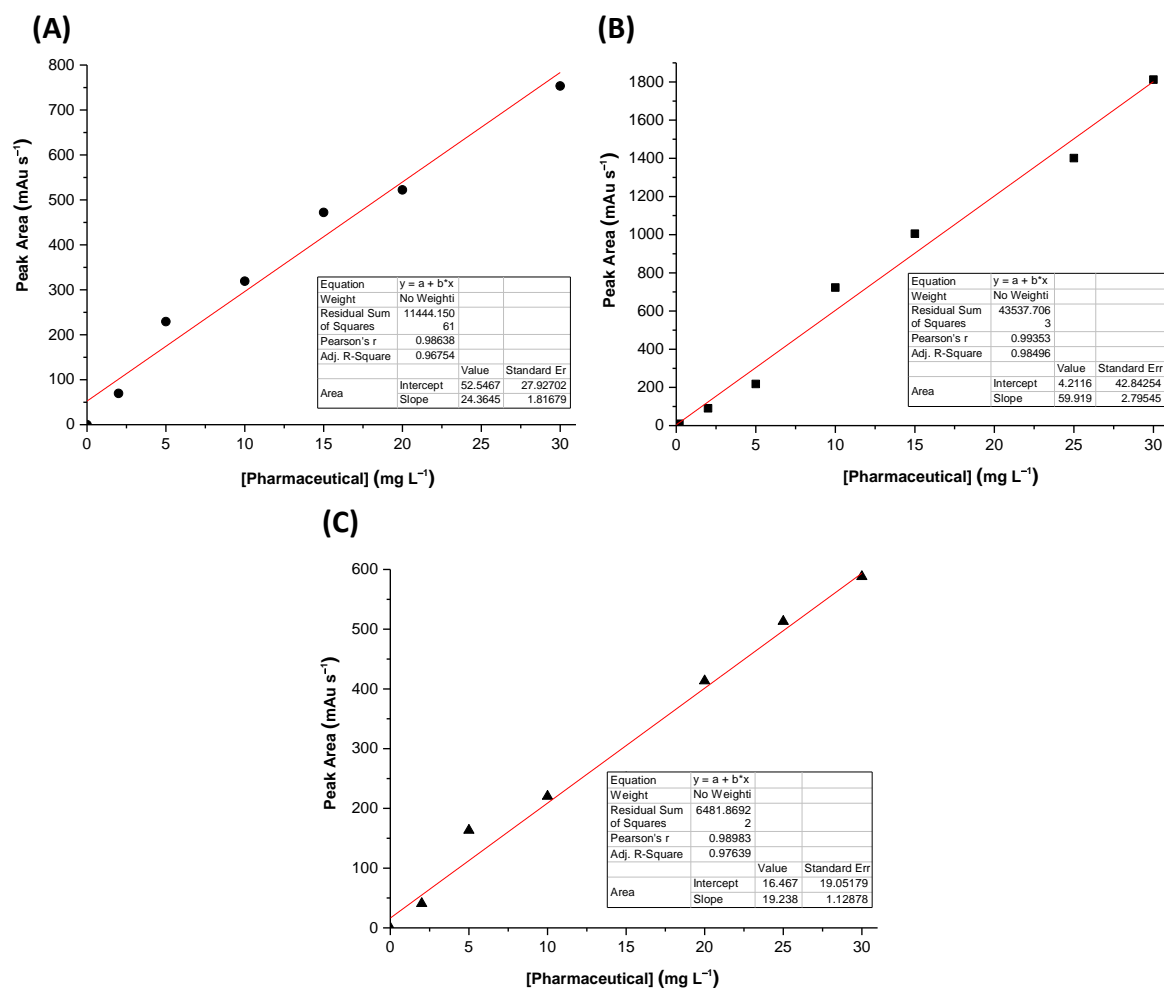


**Figure 65.** Calibration curve of (A) ibuprofen in ultrapure water measured at  $\lambda = 220$  nm (B) acetaminophen in ultrapure water measured at  $\lambda = 243$  nm, and (C) phenobarbital in ultrapure water measured at  $\lambda = 210$  nm by HPLC-DAD spectrophotometer.

#### 5.3.4.6. HPLC-DAD chromatograms

The chromatograms of the natural water samples of lake, river, and estuary were obtained without spiking of pharmaceuticals, running at the wavelengths of analysis for ibuprofen ( $\lambda = 220$  nm, retention time  $t_r = 9.5$  min), acetaminophen ( $\lambda = 243$  nm,  $t_r = 2.8$  min), and phenobarbital ( $\lambda = 210$  nm,  $t_r = 6.1$  min).

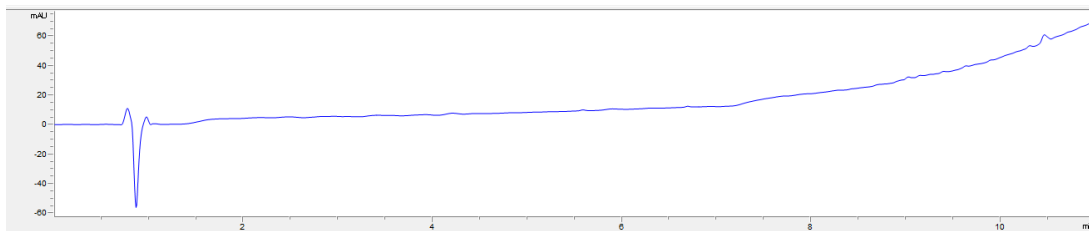


**Figure 66.** HPLC-DAD chromatogram for lake natural water sample ( $\lambda = 220$  nm).

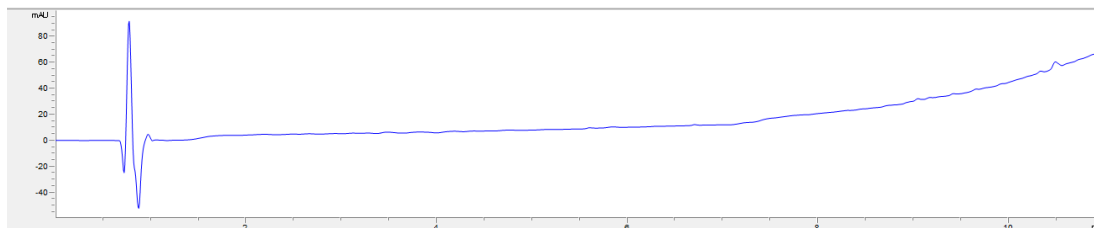


**Figure 67.** HPLC-DAD chromatogram for river natural water sample ( $\lambda = 220$  nm).

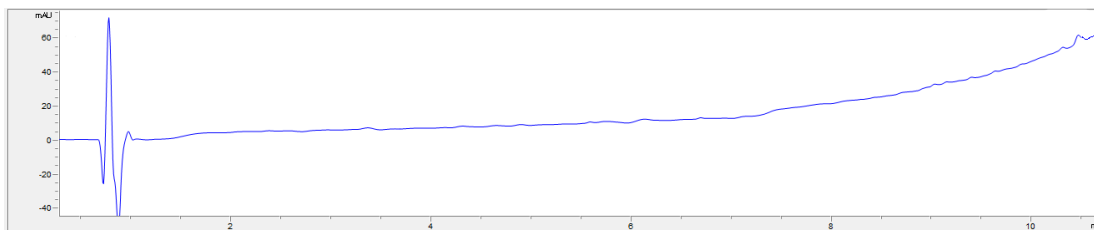


**Figure 68.** HPLC-DAD chromatogram for estuary natural water sample ( $\lambda = 220$  nm).

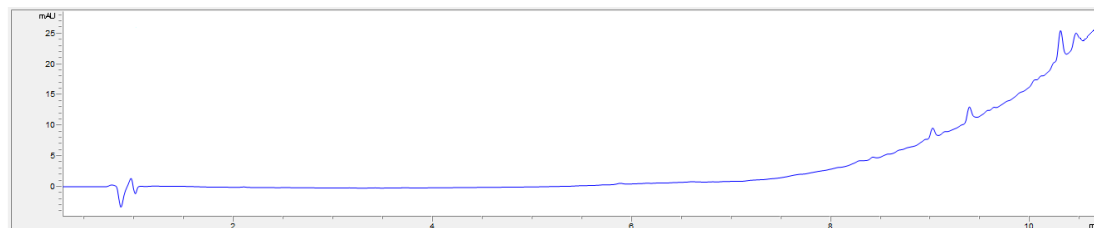


**Figure 69.** HPLC-DAD chromatogram for lake natural water sample ( $\lambda = 243$  nm).

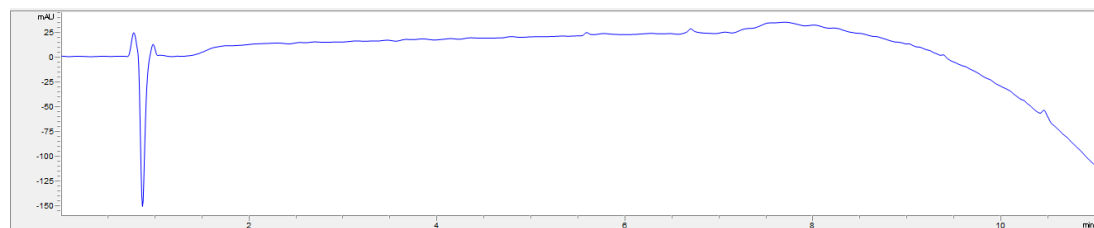


**Figure 70.** HPLC-DAD chromatogram for lake natural water sample ( $\lambda = 210$  nm).

The chromatograms of the natural water samples of lake, river, and estuary were obtained after spiking of pharmaceuticals running at the wavelengths of analysis for ibuprofen ( $\lambda = 220$  nm,  $t_r = 9.5$  min), acetaminophen ( $\lambda = 243$  nm,  $t_r = 2.8$  min), and phenobarbital ( $\lambda = 210$  nm,  $t_r = 6.1$  min).  $C_0$  corresponds to the concentration of pharmaceutical spiked in natural water samples;  $C_f$  corresponds to the concentration of pharmaceutical observed in natural water samples after spiking, calculated using the calibration curve of each pharmaceutical.

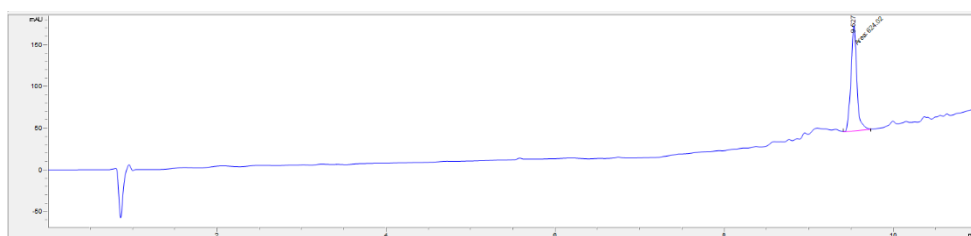


**Figure 71.** HPLC-DAD chromatogram for lake natural water sample ( $\lambda = 220$  nm,  $C_0$  (ibuprofen) = 20.63 mg L<sup>-1</sup>,  $C_f$  (ibuprofen) = 23.5 mg L<sup>-1</sup>).

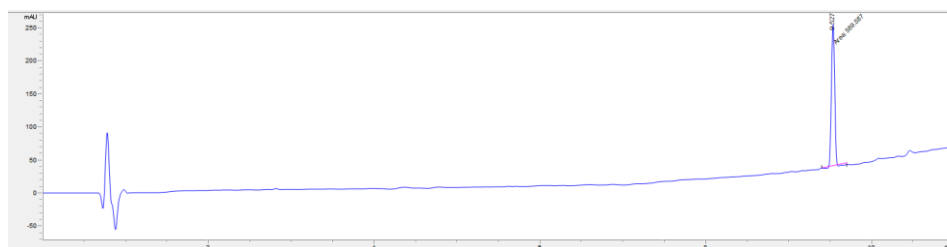


**Figure 72.** HPLC-DAD chromatogram for river natural water sample ( $\lambda = 220$  nm,  $C_0$  (ibuprofen) = 20.63 mg L<sup>-1</sup>,  $C_f$  (ibuprofen) = 22.1 mg L<sup>-1</sup>).

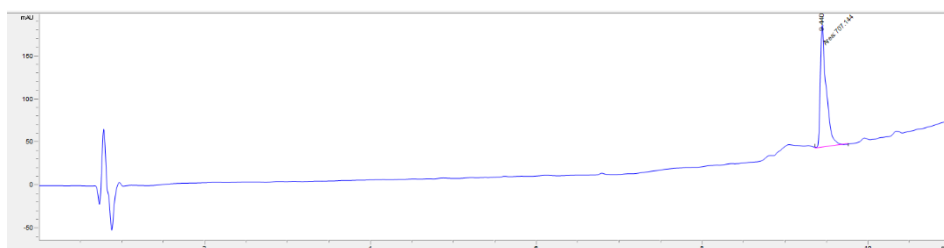


**Figure 73.** HPLC-DAD chromatogram for estuary natural water sample ( $\lambda = 220$  nm,  $C_0$  (ibuprofen) = 20.63 mg L<sup>-1</sup>,  $C_f$  (ibuprofen) = 26.9 mg L<sup>-1</sup>).

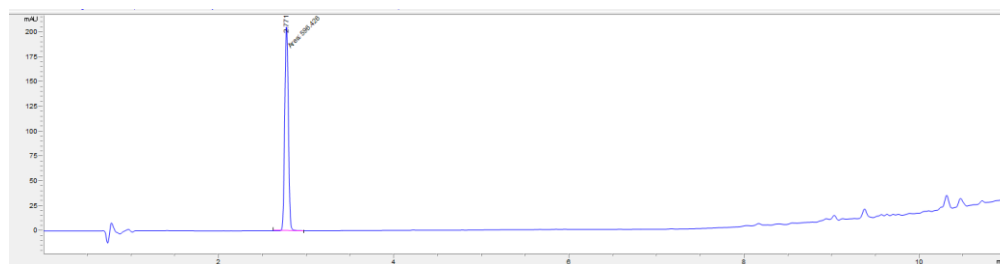


**Figure 74.** HPLC-DAD chromatogram for lake natural water sample ( $\lambda = 243$  nm,  $C_0$  (acetaminophen) =  $15.12$  mg L<sup>-1</sup>,  $C_f$  (acetaminophen) =  $10.5$  mg L<sup>-1</sup>).

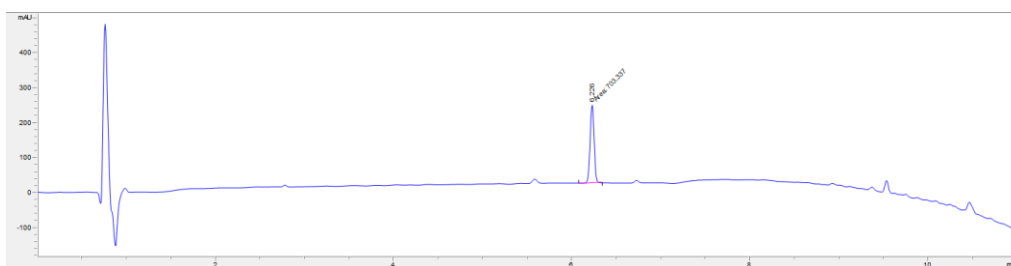


**Figure 75.** HPLC-DAD chromatogram for lake natural water sample ( $\lambda = 210$  nm,  $C_0$  (phenobarbital) =  $34.84$  mg L<sup>-1</sup>,  $C_f$  (phenobarbital) =  $35.7$  mg L<sup>-1</sup>).

The chromatograms of natural water samples of lake, river, and estuary after adsorption experiments with COF were obtained running at the wavelengths of analysis for ibuprofen ( $\lambda = 220$  nm,  $t_r = 9.5$  min), acetaminophen ( $\lambda = 243$  nm,  $t_r = 2.8$  min), and phenobarbital ( $\lambda = 210$  nm,  $t_r = 6.1$  min).  $C_0$  corresponds to the concentration of the pharmaceutical spiked in natural water samples.

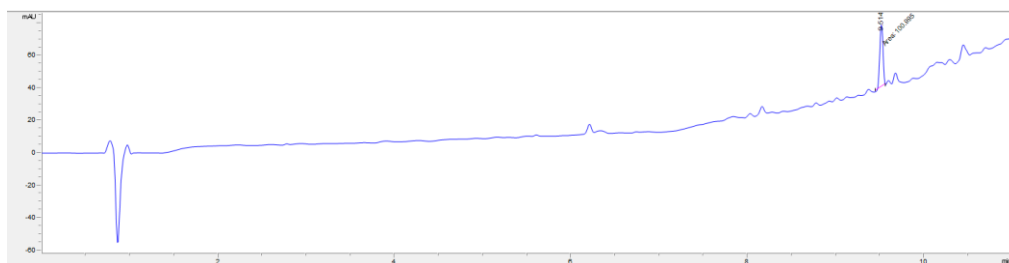


**Figure 76.** HPLC-DAD chromatogram for lake natural water sample ( $\lambda = 220$  nm,  $C_0$  (ibuprofen) =  $0.10$  mmol L<sup>-1</sup>).

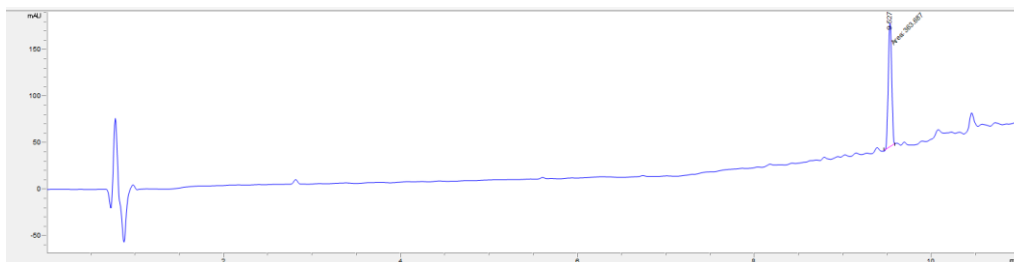


**Figure 77.** HPLC-DAD chromatogram for river natural water sample ( $\lambda = 220$  nm,  $C_0$  (ibuprofen) = 0.10 mmol L<sup>-1</sup>).

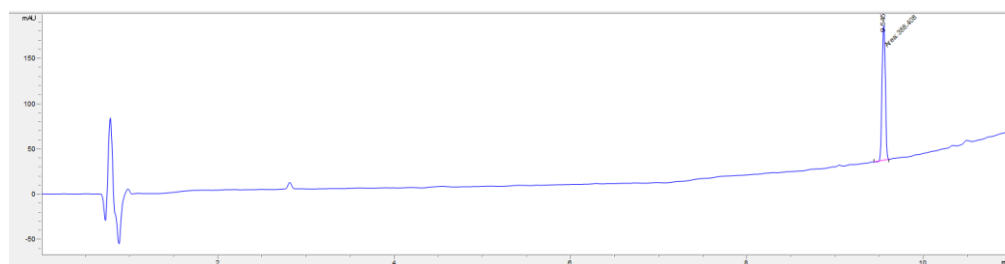


**Figure 78.** HPLC-DAD chromatogram for estuary natural water sample ( $\lambda = 220$  nm,  $C_0$  (ibuprofen) = 0.10 mmol L<sup>-1</sup>).

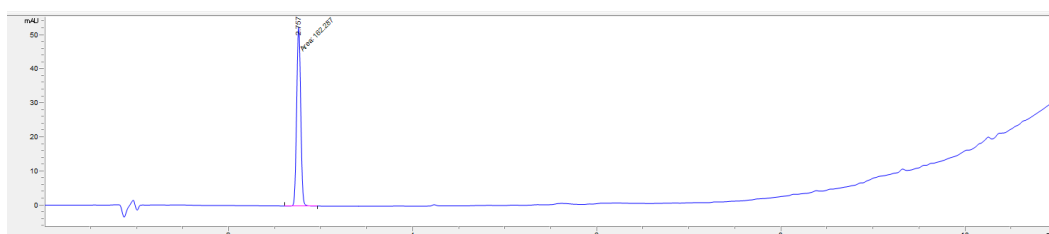


**Figure 79.** HPLC-DAD chromatogram for lake natural water sample ( $\lambda = 243$  nm,  $C_0$  (acetaminophen) = 0.15 mmol L<sup>-1</sup>).

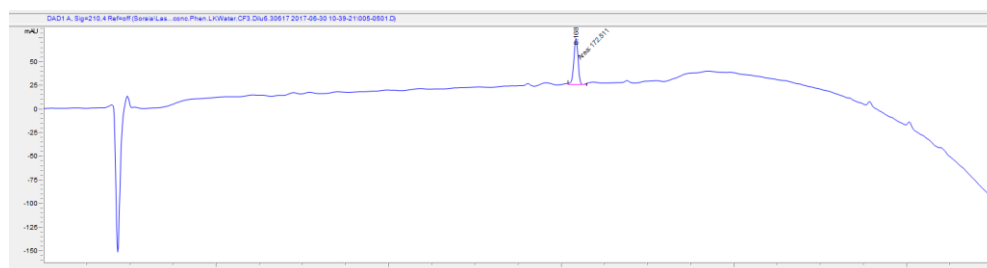


**Figure 80.** HPLC-DAD chromatogram for lake natural water sample ( $\lambda = 210$  nm,  $C_0$  (phenobarbital) = 0.15 mmol L<sup>-1</sup>).



### 5.3.5. Pharmaceutical pollutants adsorption in Tagus estuary

#### 5.3.5.1. Pharmaceutical pollutants extraction method

Standard SPE procedure was carried out as described by Dr. Vanessa Fonseca and Dr. Patrick Reis-Santos in MARE<sup>[195]</sup> with some modifications. Five water samples were collected in quintuplicate in low density polyethylene (LDPE) plastic bottles, previously rinsed with 10% nitric acid and ultrapure water. Samples were transported to the laboratory on ice and in the dark and were kept at 4 °C until processed. The non-acidified samples were processed within 24 h following collection.

Briefly, 500 mL of each water sample, previously acidified to pH 2 with formic acid, were consecutively filtered through a glass microfiber filter (GF/C<sup>TM</sup>), and polyamide membrane filters (0.45 and 0.2 µm). Then, samples were run through OASIS HLB cartridges, washed with 5 mL of methanol/water (10:90) and dried for 15 min at low vacuum pressure. Elution was performed with 6 mL of methanol and the extract dried under N<sub>2</sub> atmosphere at 40 °C. Three methods were employed to evaluate the efficiency of the COF and SPE in pharmaceutical surveillance (Figure 29 for a simplified representation):

##### *Method 1*

500 mL of each water sample, previously acidified to pH 2 with formic acid, were filtered through a nylon filter (80 µm). Then, 50 mg of TpBD-(CF<sub>3</sub>)<sub>2</sub> COF (100 mg L<sup>-1</sup>) were dispersed in the sample and the mixture was magnetically stirred for 4 h at r.t. The COF was collected by filtration (cellulose filter of 10–20 µm) and the water sample was run through OASIS HLB cartridges as described above for quantification by ultra-high-performance liquid chromatography and time-of-flight mass spectrometry (UHPLC-TOF-MS). For desorption, the COF was soaked in propan-2-ol (6 mL) for 2 h at r.t., under magnetic stirring. The COF was collected by filtration (cellulose filter of 10–20 µm) and the supernatant dried under N<sub>2</sub> flow at 40 °C. The dry residue was re-suspended in 500 µL of methanol/water (3:97), filtered through a PVDF Mini-UniPrep<sup>TM</sup> filter (0.45 µm), injected, and quantified by UHPLC-TOF-MS.

##### *Method 2*

Same as Method 1, but water samples were not acidified.

*Method 3*

500 mL of each water sample were filtered through a nylon filter (80  $\mu\text{m}$ ) and concentrated with OASIS HLB cartridges as described above for quantification by UHPLC-TOF-MS.

**5.3.5.2. UHPLC-TOF-MS analysis method**

An UHPLC Nexera X2 Shimadzu coupled with a Triple TOF<sup>TM</sup> 5600+ from AB Sciex (UHPLC-TOF-MS) was used for the chromatographic separation and mass spectrometry detection, following an adaptation of protocols previously described.<sup>[195,365]</sup> The UHPLC system comprised a vacuum degasser, an autosampler, a binary pump, and an oven for the chromatographic column (an analytical reverse-phase column Zorbax Eclipse Plus C18, 2.1 x 50 mm, 1.8  $\mu\text{m}$ , Agilent), maintained at 40 °C. Formic acid 0.1% (v/v) in water and acetonitrile were used as mobile phases A and B, respectively, all of high-performance liquid chromatography grade. At a 0.5 mL min<sup>-1</sup> flow rate, the gradient program used was: 0–5 min from 97% to 40% [A]; 5–9 min from 40% to 0% [A]; 9–10 min from 0% back to 97% [A]; 11–12 min 97% [A]. 10  $\mu\text{L}$  of each sample were injected by the autosampler, at 10 °C. The electrospray ion source was used in positive mode (ESI<sup>+</sup>) with full-scan data acquisition from 100 to 920 Da. The identification and quantification of pharmaceutical compounds was performed with PeakView<sup>TM</sup> and MultiQuant<sup>TM</sup> software, and it was based on the exact mass with an error below 10 ppm, a maximum variation of retention time set to 2.5% and an isotope ratio difference lower than 10%. A calibration of the TOF-MS detector was performed every 10 injections to ensure accurate mass resolution. Standards were weighted and dissolved in methanol (or water in the case  $\beta$ -lactams) to obtain stock solutions of 1 mg mL<sup>-1</sup>, that were kept at -20 °C and away from light. Dilutions of these stock solutions were then prepared to obtain convenient concentrations for the quantification of target compounds. The MultiQuant<sup>TM</sup> software was used to calculate the concentrations of the compounds detected in the samples, by resorting to a calibration curve, built with the chromatographic peak areas, with a concentration range between 0.8 ng L<sup>-1</sup> and 10 ng L<sup>-1</sup>. Selectivity, specificity, precision, linearity, and limit of detection (LOD) and quantification (LOQ) of each pharmaceutical were evaluated in order to validate the

optimized quantitative method. Limits of detection and quantification of each pharmaceutical and the percentages of recovery are presented in following Table 20. In terms of precision, all target compounds showed a coefficient of variation below 20%. Selectivity and specificity are daily evaluated by analyzing blank samples to verify the existence of any interference that might compromise the accurate and unequivocal identification of the target analytes. Linearity of the calibration curves, used in each batch of samples, is evaluated being the acceptance criteria a coefficient of correlation higher than 0.99 ( $R > 0.99$ ). LOD and LOQ were calculated during the validation procedure by adopting the criteria of a signal-to-noise ratio ( $S/N \geq 3$  and 10, respectively).

**Table 20.** The values for limit of detection (LOD) and limit of quantification (LOQ) as well as recovery for the pharmaceuticals detected in this study and precision as standard deviation.

Therapeutic group	Pharmaceutical	LOD (ng L <sup>-1</sup> )	LOQ (ng L <sup>-1</sup> )	Recovery (%)	Precision (SD %)
<b>β-Blockers</b>	Atenolol	0.01	0.03	104.4	4.2
	Bisoprolol	0.14	0.46	94.7	9.1
	Propranolol	0.06	0.21	100.9	6.5
<b>Antihypertensives</b>	Irbesartan	0.03	0.17	96.0	15.7
	Losartan	0.05	0.09	107.1	18.4
	Indapamide	0.03	0.09	100.4	4.0
<b>Lipid regulators</b>	Bezafibrate	0.07	0.24	85.7	8.6
<b>Anticonvulsants</b>	α-Hydroxyalprazolam	0.02	0.08	84.9	8.3
	Carbamazepine	0.01	0.05	102.9	18.7
	Gabapentin	0.81	2.69	80.6	6.1
	Topiramate	0.03	0.11	104.7	3.7
<b>Antibiotics</b>	Ciprofloxacin	3.47	11.56	110.5	4.7
	Flumequine	0.01	0.04	80.6	10.1
	Ofloxacin	0.99	3.31	91.5	2.6

	Sulfamethazine	0.14	0.47	100.9	8.2
	Sulfamethoxazole	0.03	0.09	99.5	3.7
	Sulfapyridine	0.46	1.52	104.4	3.3
	Tetracycline	0.48	1.61	112.6	8.2
	Trimethoprim	0.80	2.68	109.5	6.4
	Valnemulin	0.01	0.05	89.6	15.2
<b>Antidepressants</b>	Fluoxetine	0.01	0.03	109.3	7.8
	Sertraline	0.03	0.09	109.6	4.0
	Venlafaxine	0.02	0.08	99.6	7.3
<b>NSAID</b>	Diclofenac	0.02	0.05	106.0	8.8

#### 5.3.5.3. *Data analysis method*

Pharmaceutical quantification results are based on an average concentration detected in 5 samples collected in the Tagus estuary  $\pm$  standard deviation, in which the concentration found using the SPE standard method is used as the reference value. The results of pharmaceuticals detected and adsorption efficiency are expressed in %. Adsorption efficiency (%) corresponds to the concentration of pharmaceuticals remaining in the water supernatant after COF adsorption process with respect to the concentration found in the sample by SPE standard method (100%). Detection efficiency (%) expresses the concentration of pharmaceuticals found in the propan-2-ol supernatant after COF desorption with respect to the SPE standard method (100%).

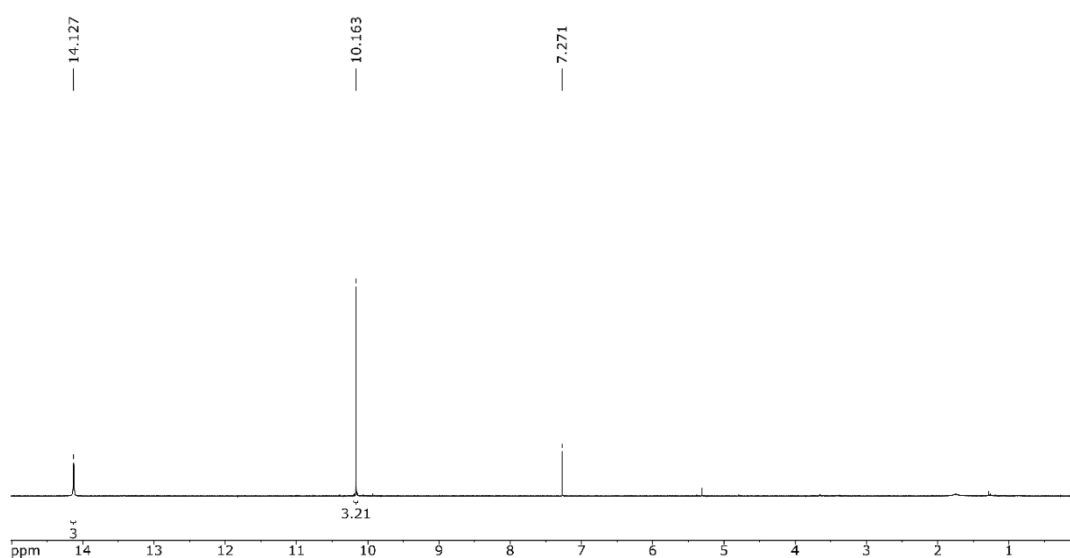
#### 5.3.5.4. *DI-MS-MS analysis method of diclofenac*

The analysis of diclofenac recoveries after sequential desorptions were performed in CACTI of Universidade de Vigo. Supernatants from the second, third, and fourth desorption with acetonitrile, acetone, and dichloromethane, respectively, were analysed using a 3500 AB Sciex triple quadrupole (Framingham, MA, USA) with an electrospray Turbo V Ion Source. ESI mode: negative. All data were acquired and processed using Analyst software (version 1.6.1). Ion source temperature was 550 °C, ion spray voltage was 4500 V, curtain

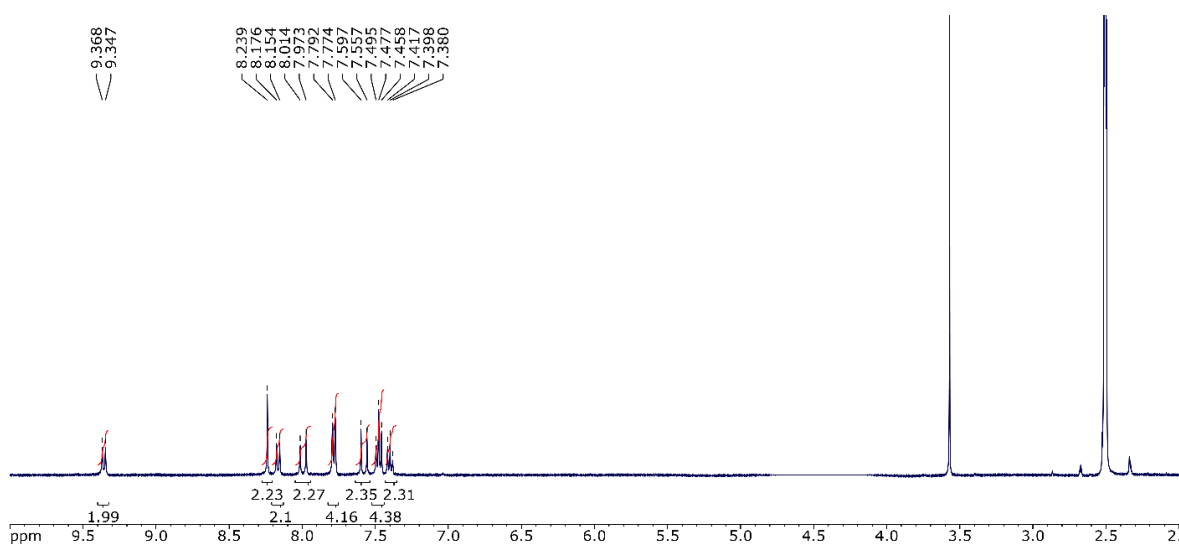
gas was 40 psi, ion source gases GS1 and GS2 were set at 60 and 75 psi, respectively, and the entrance potential was set at 10 V. MS parameters, such as declustering potential, collision energy, and collision cell exit potential, were adjusted by direct injection. All transitions were recorded using MRM (Multiple Reaction Monitoring). The LOD is 1.5 and LOQ 3.2 with a dynamic range between 3–200  $\mu\text{g L}^{-1}$ .

## 5.4. Characterization Data

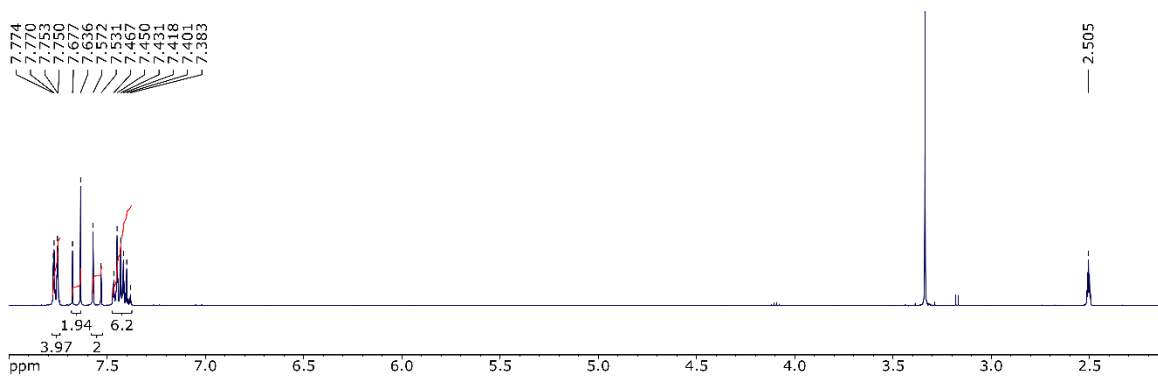
### 5.4.1. NMR spectra



**Figure 81.**  $^1\text{H}$  NMR spectrum of Tp measured at 400 MHz, in  $\text{CDCl}_3$ .



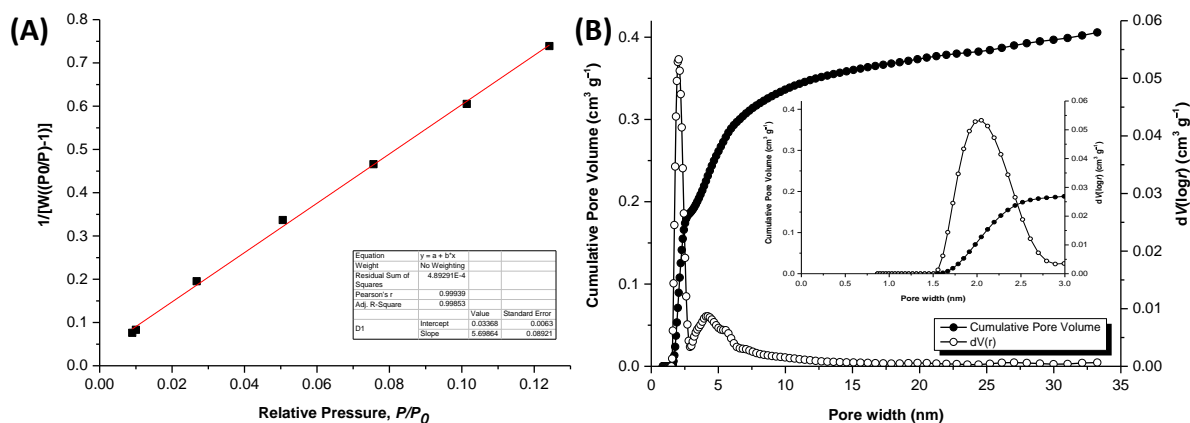
**Figure 82.**  $^1\text{H}$  NMR spectrum of model compound **2** at 400 MHz, in  $\text{DMSO-d}_6$ .



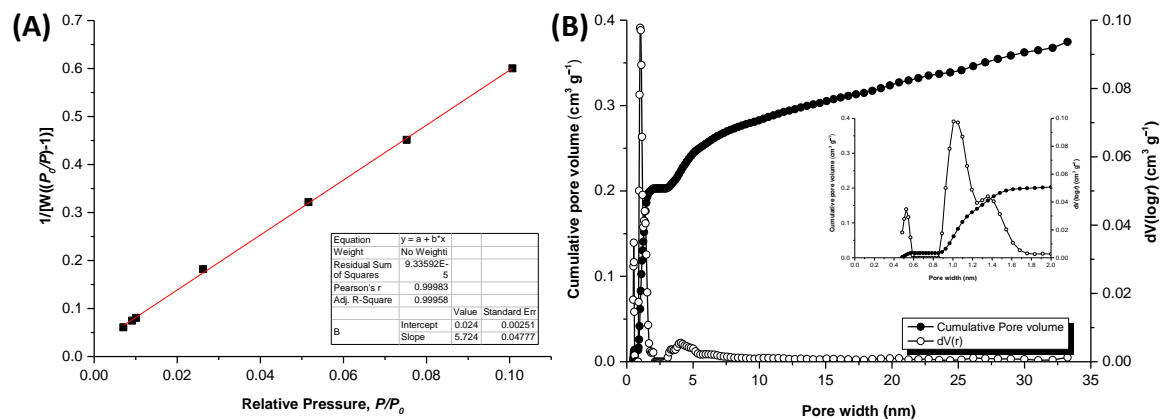
**Figure 83.**  $^1\text{H}$  NMR spectrum of model compound **3** at 400 MHz, in  $\text{DMSO-d}_6$ .

### 5.4.2. $\text{N}_2$ Physisorption

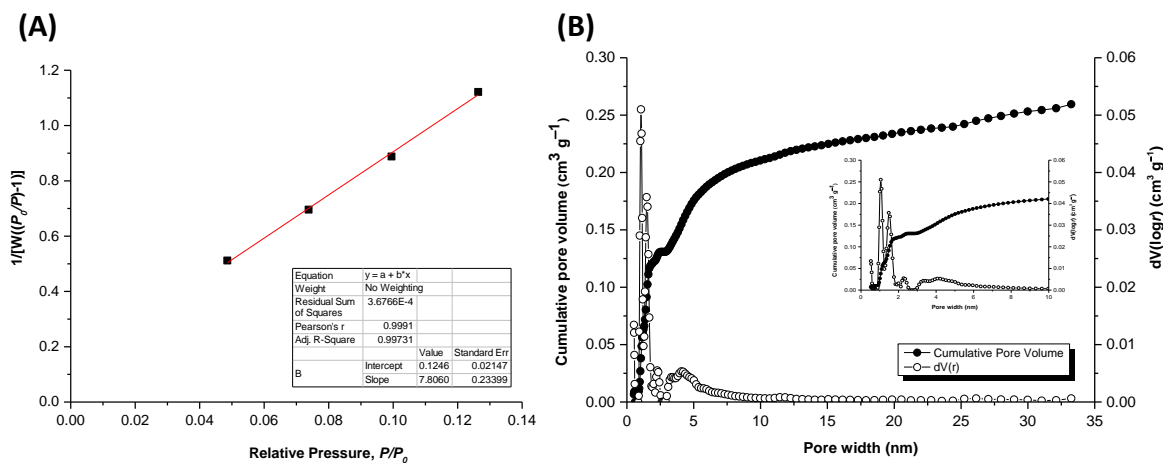
TpBD- $(\text{CH}_3)_2$  in mg scale



**Figure 84.** Multi-point BET plot and linear fit (A), and pore size distribution (hollow spheres) and cumulative pore volume (filled spheres) profile (B).

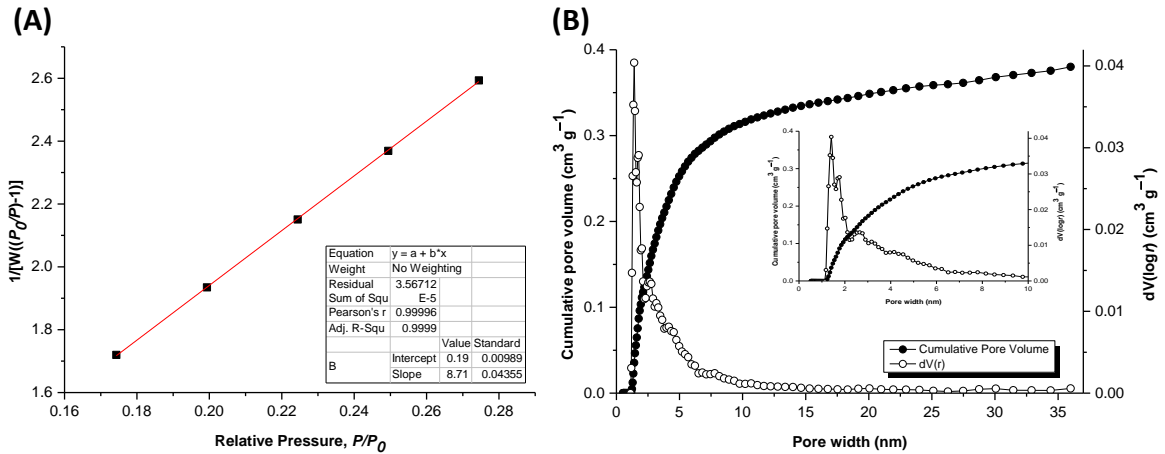
TpBD-(CH<sub>3</sub>)<sub>2</sub> in gram scale

**Figure 85.** Multi-point BET plot and linear fit (A), and pore size distribution (hollow spheres) and cumulative pore volume (filled spheres) profile (B).

TpBD-(NO<sub>2</sub>)<sub>2</sub>

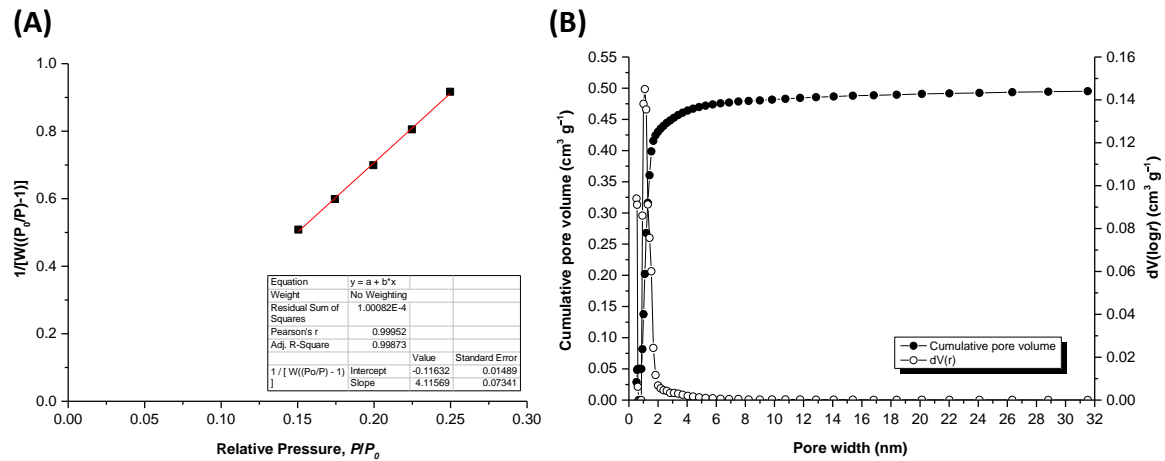
**Figure 86.** Multi-point BET plot and linear fit (A), and pore size distribution (hollow spheres) and cumulative pore volume (filled spheres) profile (B).

**TpBD-(NH<sub>2</sub>)<sub>2</sub>**



**Figure 87.** Multi-point BET plot and linear fit (A), and pore size distribution (hollow spheres) and cumulative pore volume (filled spheres) profile (B).

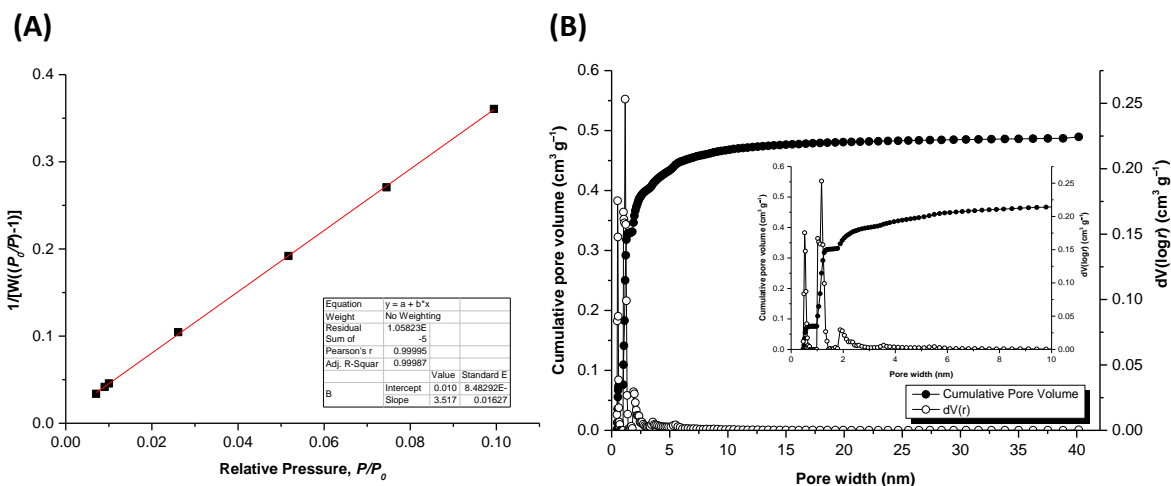
**TpBD-(CF<sub>3</sub>)<sub>2</sub> in mg scale**



**Figure 88.** Multi-point BET plot and linear fit (A), and pore size distribution (hollow spheres) and cumulative pore volume (filled spheres) profile (B).

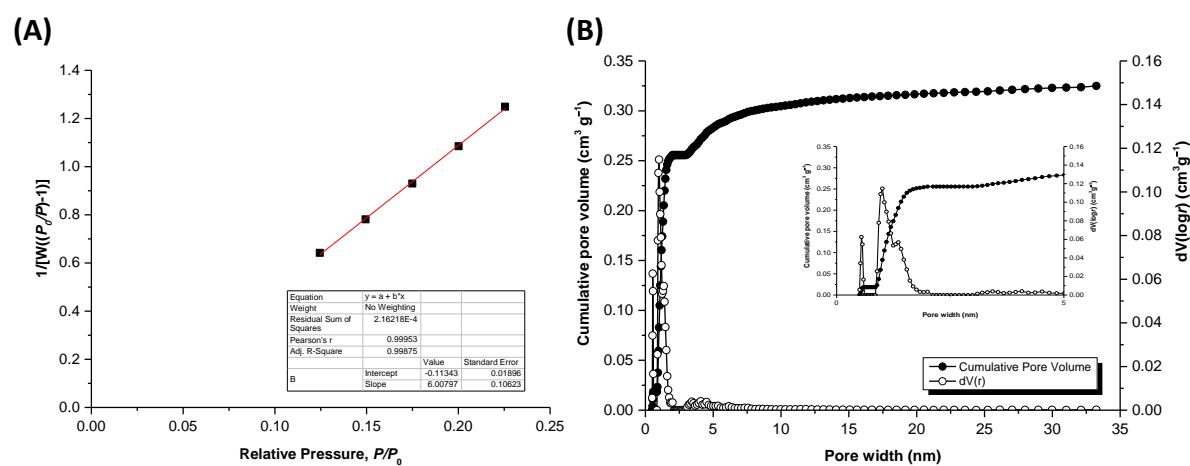


TpBD-(CF<sub>3</sub>)<sub>2</sub> in gram scale

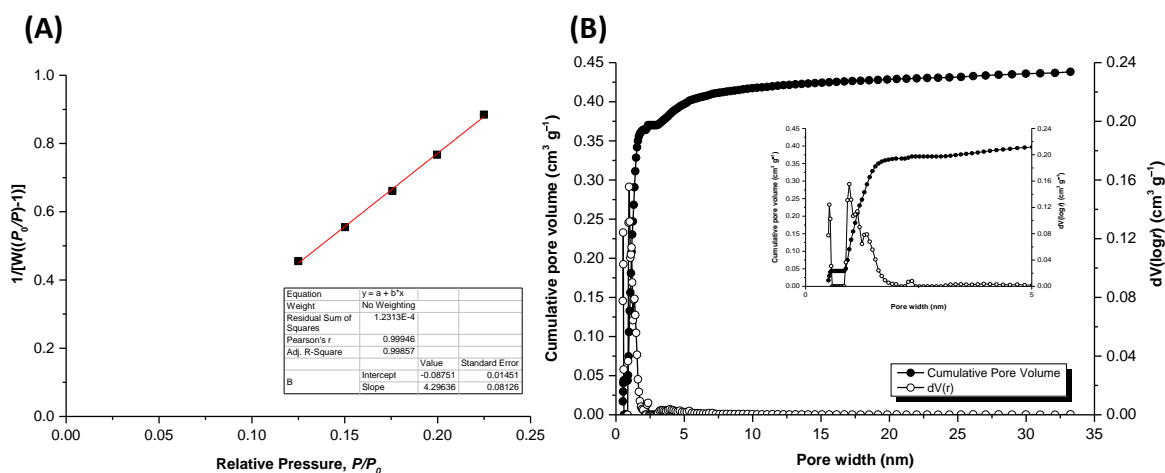


**Figure 89.** Multi-point BET plot and linear fit (A), and pore size distribution (hollow spheres) and cumulative pore volume (filled spheres) profile (B).

TpBD-(CF<sub>3</sub>)<sub>2</sub> after adsorption of ibuprofen



**Figure 90.** Multi-point BET plot and linear fit (A) and pore size distribution (hollow spheres) and cumulative pore volume (filled spheres) profile (B) of TpBD-(CF<sub>3</sub>)<sub>2</sub> after adsorption of ibuprofen.

TpBD-(CF<sub>3</sub>)<sub>2</sub> after desorption of ibuprofen

**Figure 91.** Multi-point BET plot and linear fit (A) and pore size distribution (hollow spheres) and cumulative pore volume (filled spheres) profile (B) of TpBD-(CF<sub>3</sub>)<sub>2</sub> after desorption of ibuprofen.

## 5.4.3. FT-IR data

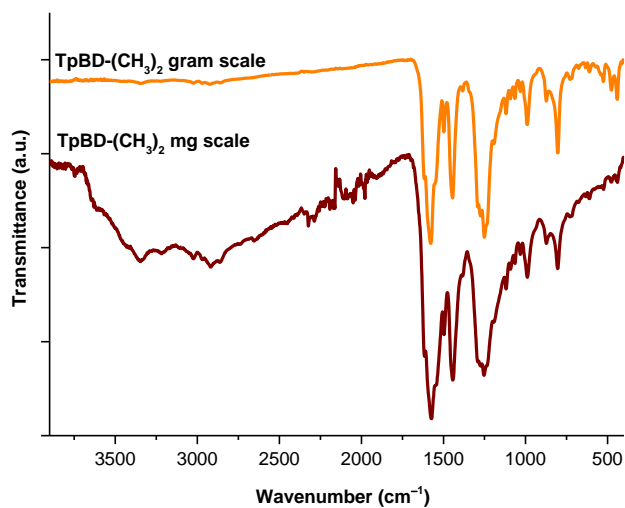


**Figure 92.** FT-IR spectrum of TpBD-(CH<sub>3</sub>)<sub>2</sub> prepared in mg scale (red) and in gram scale (orange).

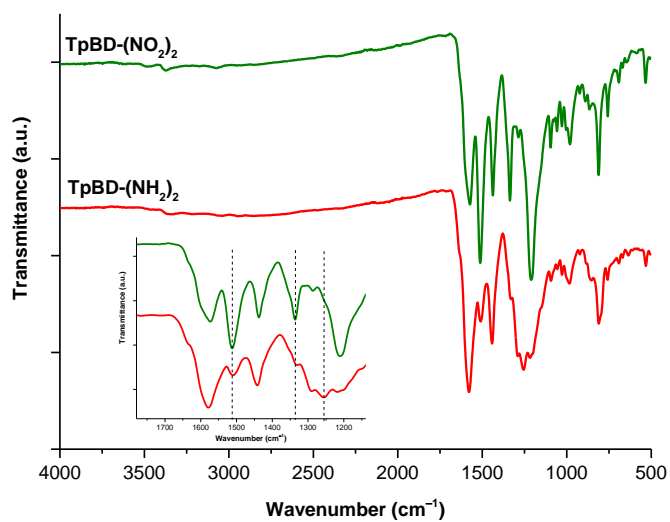


**Figure 93.** FT-IR spectrum of TpBD-(NO<sub>2</sub>)<sub>2</sub> and TpBD-(NH<sub>2</sub>)<sub>2</sub>.

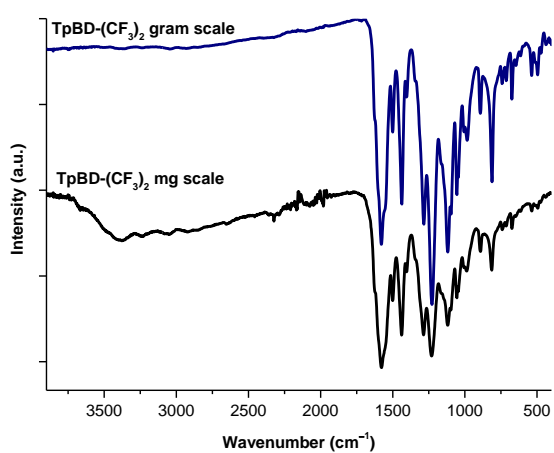


**Figure 94.** FT-IR spectrum of TpBD-(CF<sub>3</sub>)<sub>2</sub> prepared in mg scale (black) and in gram scale (blue).

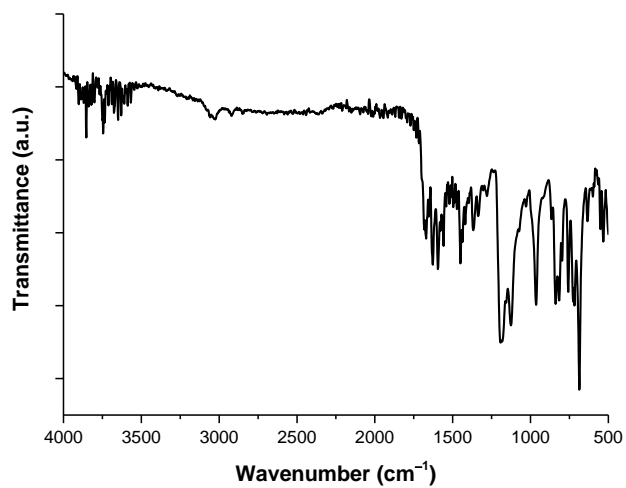


**Figure 95.** FT-IR spectrum of model compound 2.

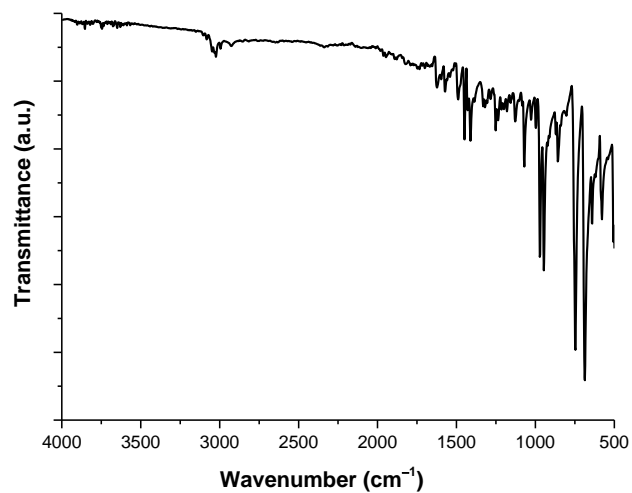


**Figure 96.** FT-IR spectrum of model compound 3.

## 5.4.4. TGA data

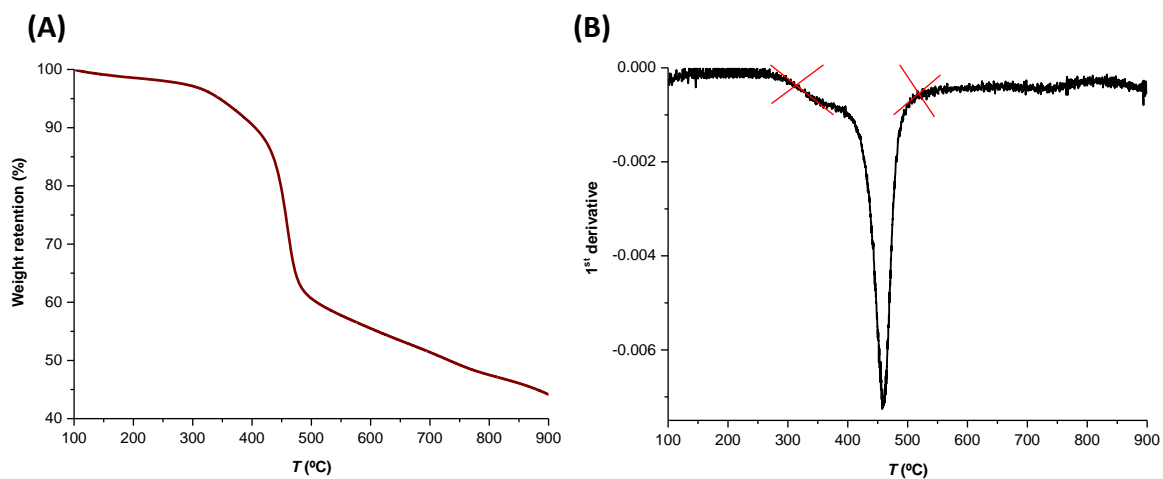


**Figure 97.** TGA data of TpBD-(CH<sub>3</sub>)<sub>2</sub> prepared in mg scale (A), and 1<sup>st</sup> derivative of the TGA data (B).

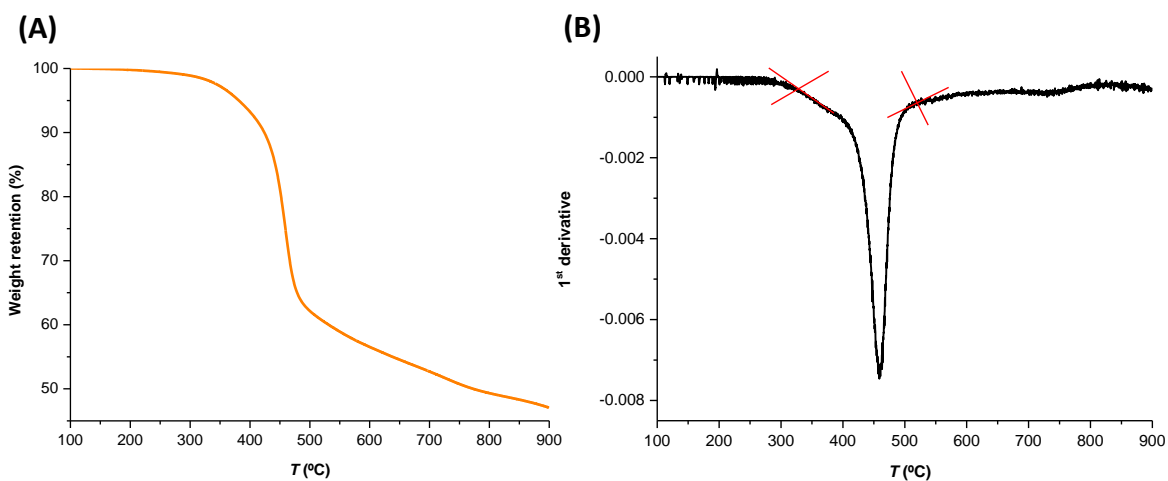


**Figure 98.** TGA data of TpBD-(CH<sub>3</sub>)<sub>2</sub> prepared in gram scale (A), and 1<sup>st</sup> derivative of the TGA data (B).

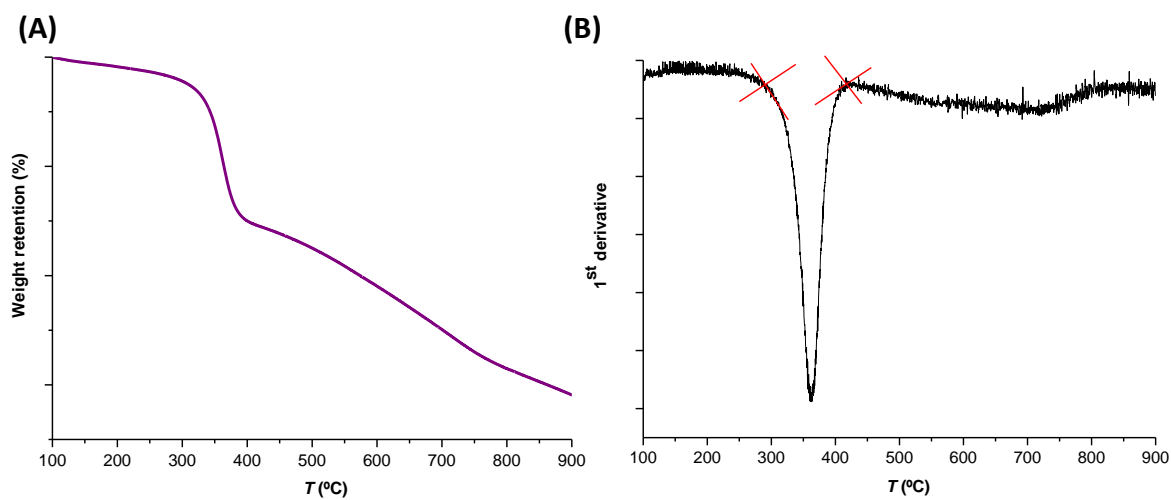


**Figure 99.** TGA data of TpBD-(NO<sub>2</sub>)<sub>2</sub> (A), and 1<sup>st</sup> derivative of the TGA data (B).

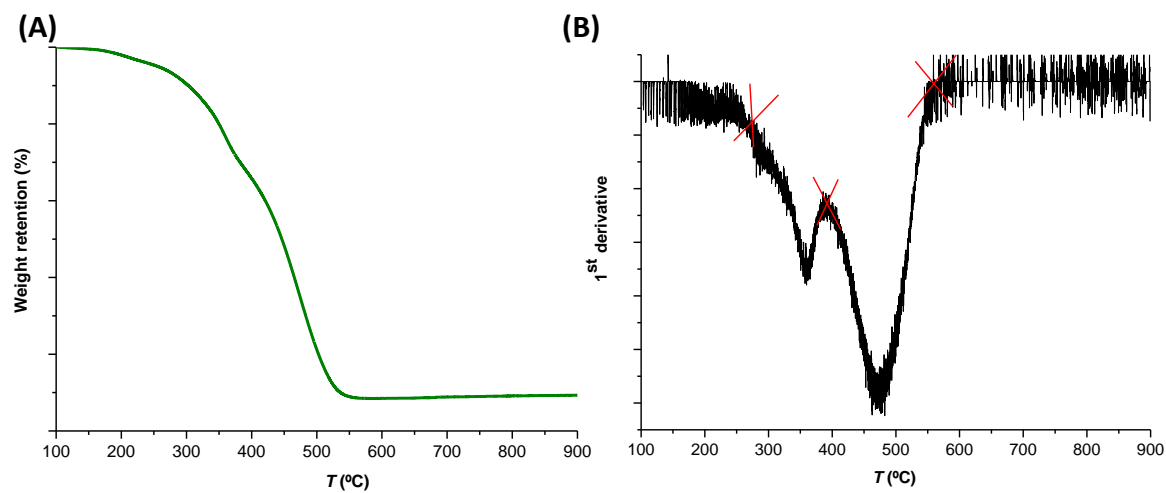


**Figure 100.** TGA data of TpBD-(NH<sub>2</sub>)<sub>2</sub> (A), and 1<sup>st</sup> derivative of the TGA data (B).

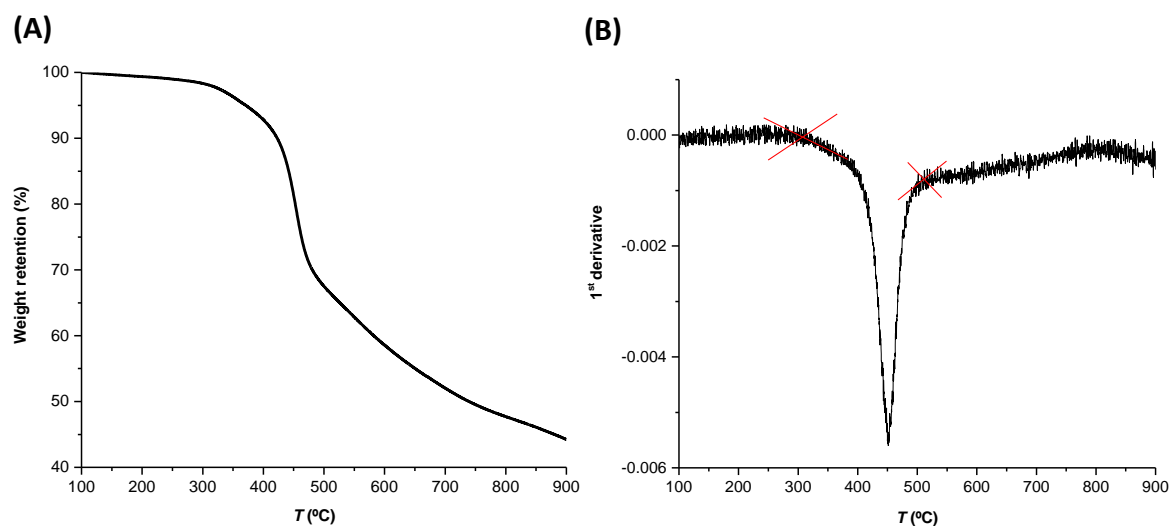


**Figure 101.** TGA data of TpBD-(CF<sub>3</sub>)<sub>2</sub> prepared in mg scale (A), and 1<sup>st</sup> derivative of the TGA data (B).

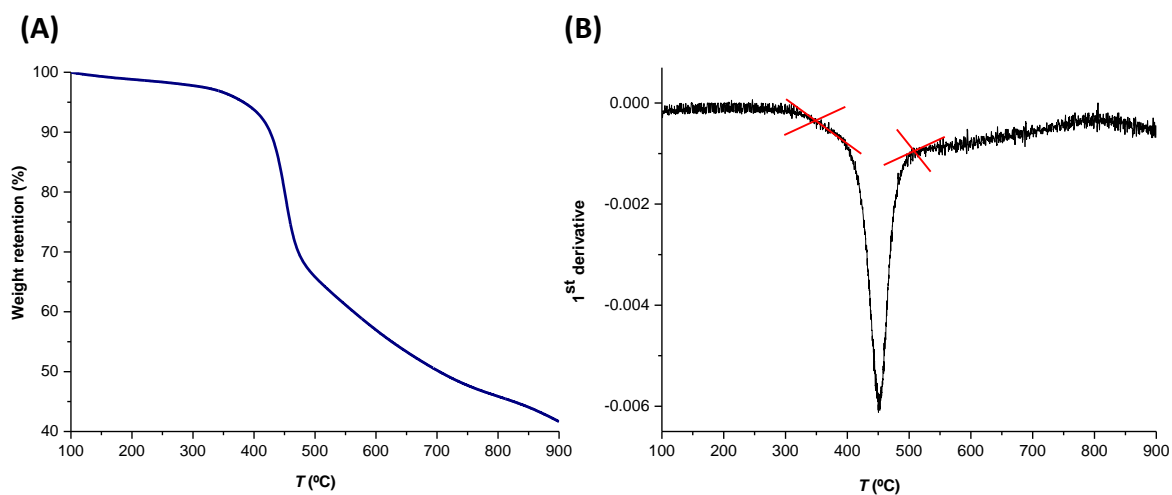


**Figure 102.** TGA data of TpBD-(CF<sub>3</sub>)<sub>2</sub> prepared in gram scale (A), and 1<sup>st</sup> derivative of the TGA data (B).

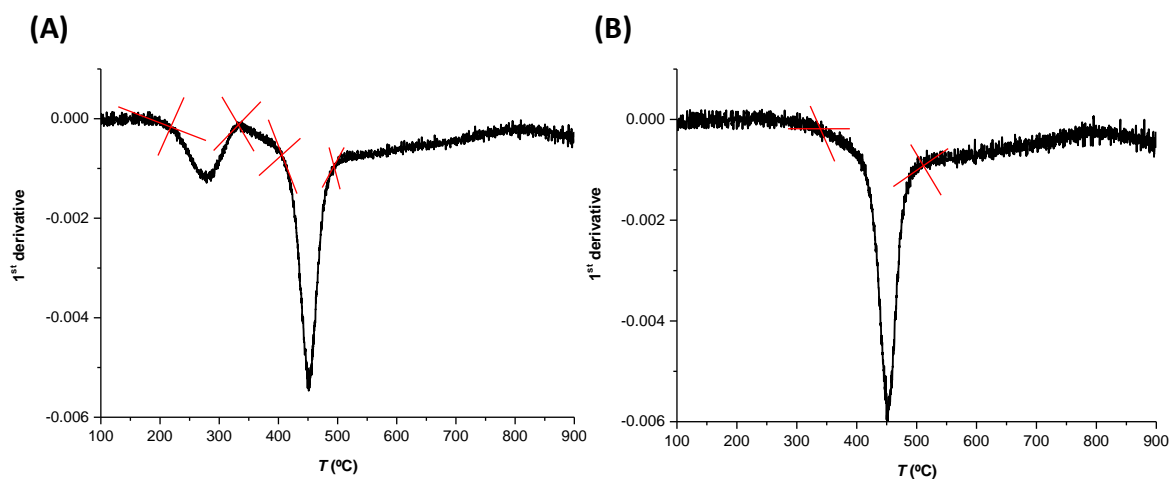


**Figure 103.** 1<sup>st</sup> derivative of the TGA data of TpBD-(CF<sub>3</sub>)<sub>2</sub> after adsorption of ibuprofen (A) and after desorption of ibuprofen (B).

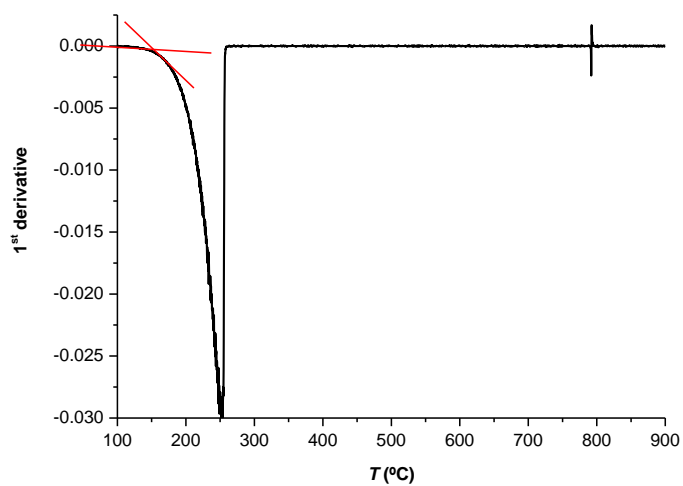


**Figure 104.** 1<sup>st</sup> derivative of the TGA data of ibuprofen.



### 5.4.5. Water contact angle measurements



**Figure 105.** Contact angles of 18° for TpBD-(CH<sub>3</sub>)<sub>2</sub>.

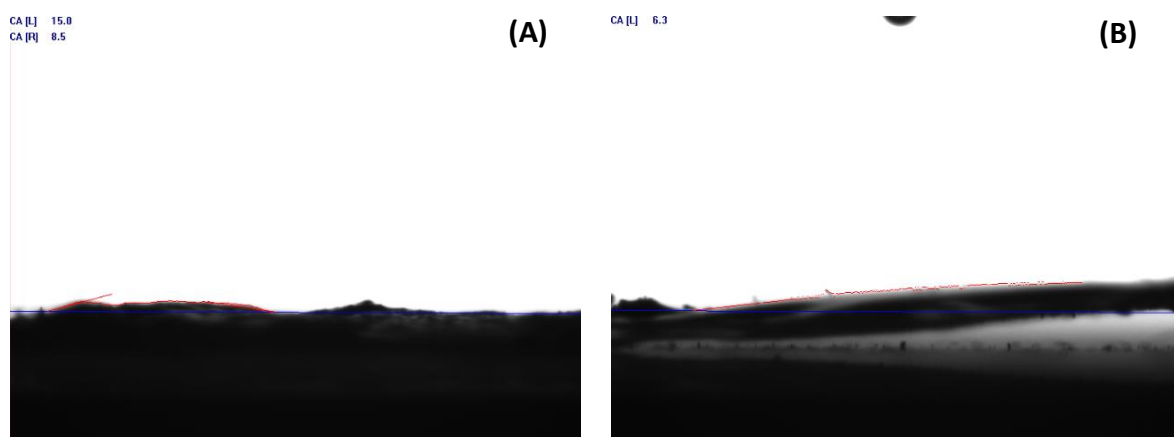


**Figure 106.** Contact angles of 15° for TpBD-(NO<sub>2</sub>)<sub>2</sub> (A) and 6.3° for TpBD-(NH<sub>2</sub>)<sub>2</sub> (B).

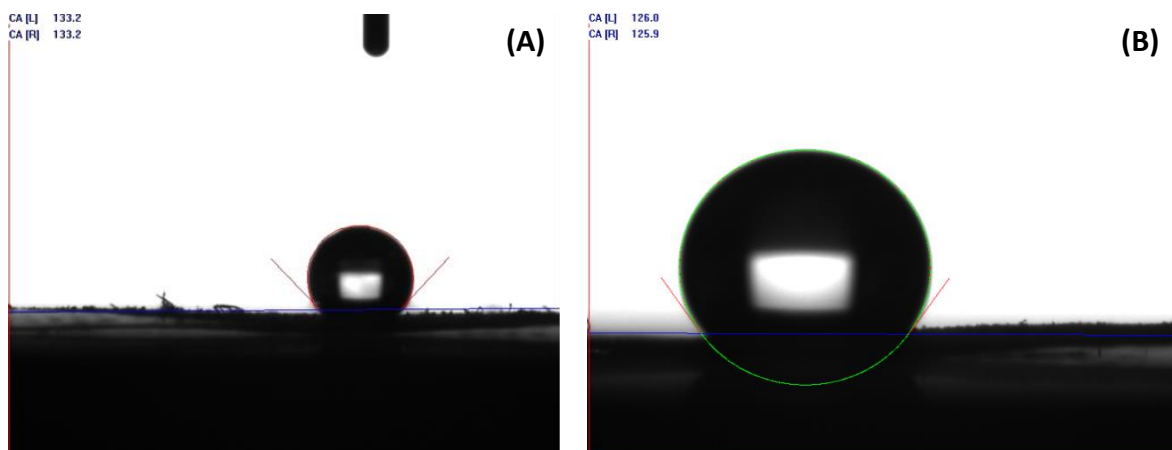


**Figure 107.** Contact angles of 133° for TpBD-(CF<sub>3</sub>)<sub>2</sub> prepared in mg scale (A), and 126° for TpBD-(CF<sub>3</sub>)<sub>2</sub> prepared in gram scale (B).

#### 5.4.6. SEM data

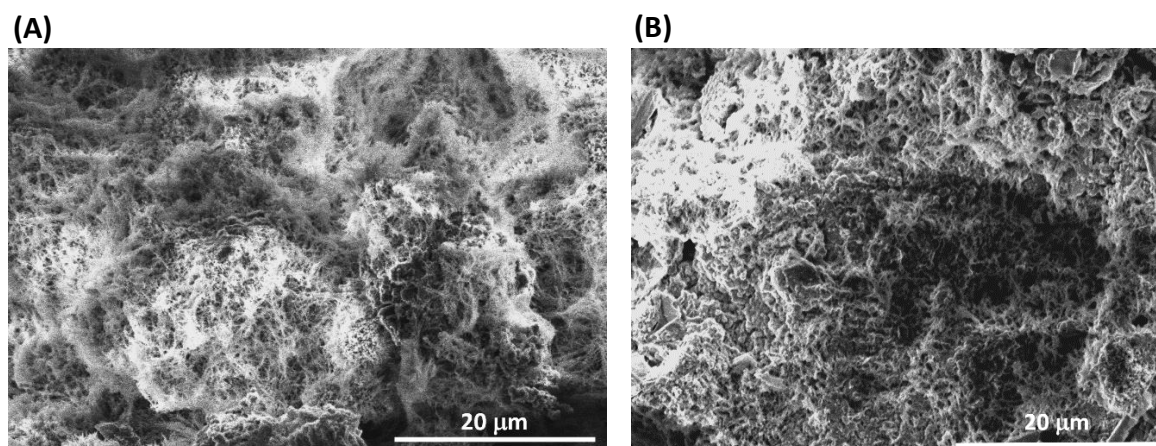


**Figure 108.** SEM images of TpBD-(NO<sub>2</sub>)<sub>2</sub> (A) and TpBD-(NH<sub>2</sub>)<sub>2</sub> (B).

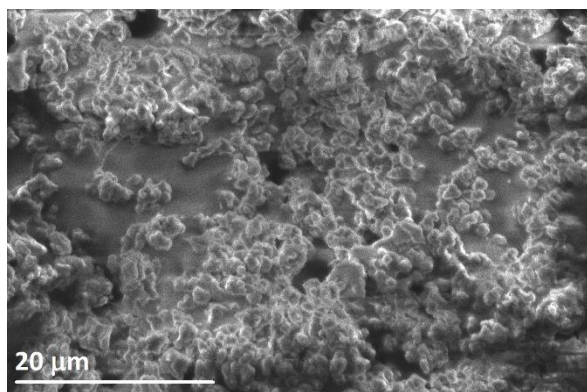


**Figure 109.** SEM image of TpBD-(CF<sub>3</sub>)<sub>2</sub> after desorption of ibuprofen.

#### 5.4.7. Computational models

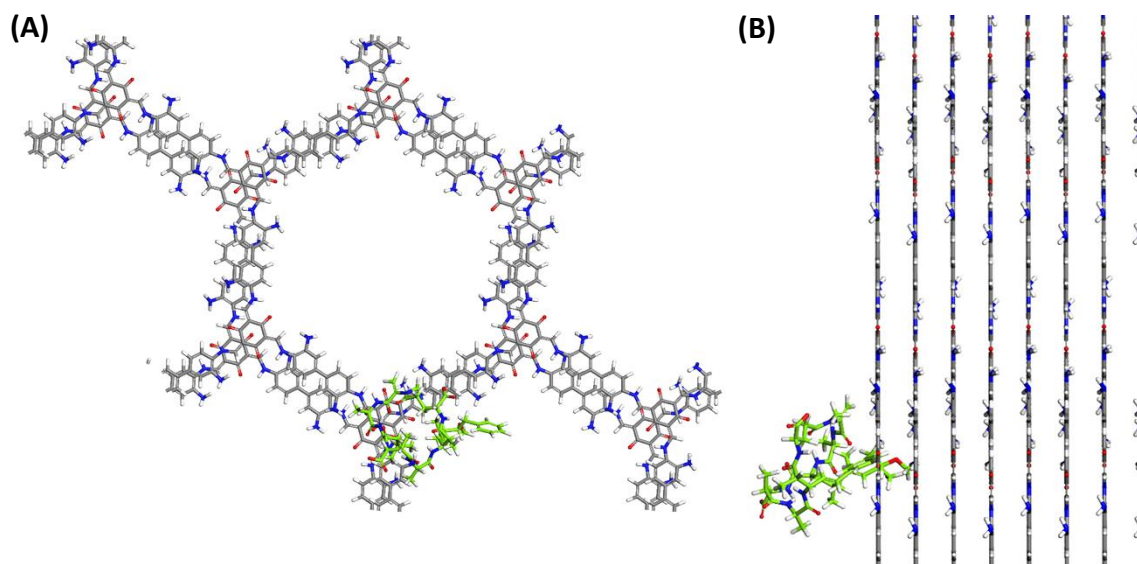


**Figure 110.** A top view along z axis (A) and side view along x axis (B) of the atomistic model of MC-LA in TpBD-(NH<sub>2</sub>)<sub>2</sub>, located on the surface of COF. Reprinted with permission from Ref. [249]. Copyright 2021, American Chemical Society.

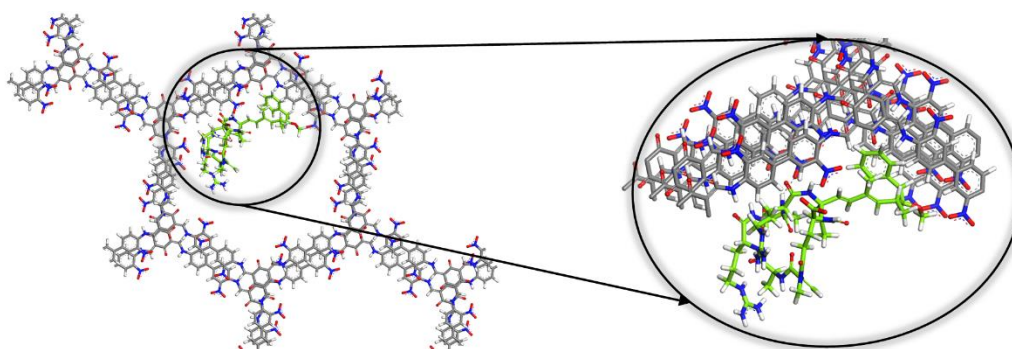


**Figure 111.** A top view along z axis of the atomistic model of MC-RR in TpBD-(NO<sub>2</sub>)<sub>2</sub>. Reprinted with permission from Ref. [249]. Copyright 2021, American Chemical Society.

#### 5.4.8. Point of zero charge (pzc) of TpBD-(CF<sub>3</sub>)<sub>2</sub>

In this titration method, two similar solutions (*blank* and *sample*) were prepared in 100 mL beakers, adding 25 mL of 0.01 M NaCl solution to each. Then, the pH values were adjusted to values of 1, 1.5, 2, 2.5, 3, 4, 6, 7, 8, and 9, with solutions of 0.1 M HCl and 0.1 M NaOH as needed. After, 75 mg of TpBD-(CF<sub>3</sub>)<sub>2</sub> was added to the *sample* solution. Both

solutions (*blank* and *sample*) were then shaken at r.t. for 72 h to reach the equilibrium. After this time, *sample* solutions were filtered, and the pH of both solutions (*blank* and *sample*) was measured. Obtained results were plotted (Figure 112) as the pH of *blank* solution after equilibrium time ( $\text{pH}_{\text{initial}}$ ) versus pH of *sample* solution after equilibrium time ( $\text{pH}_{\text{final}}$ ). In addition, a linear regression was also plotted. The  $\text{pzc}$  value was taken as the point where non-linear fitting of the points cross the linear regression (Figure 112).

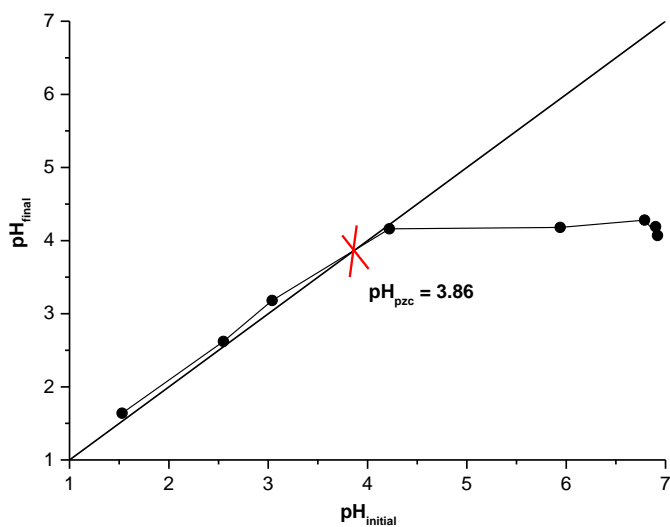


**Figure 112.**  $\text{pH}_{\text{pzc}}$  value of  $\text{TpBD}-(\text{CF}_3)_2$ .

## References

- [1] T. Liu, G. Liu, *Nat. Commun.* **2020**, *11*, 10–12.
- [2] M. A. Little, A. I. Cooper, *Adv. Funct. Mater.* **2020**, *30*, 1–30.
- [3] S. Zhang, Q. Yang, C. Wang, X. Luo, J. Kim, Z. Wang, Y. Yamauchi, *Adv. Sci.* **2018**, *5*, 1801116.
- [4] A. G. Slater, A. I. Cooper, *Science* **2015**, *348*, aaa8075.
- [5] A. C. Lokhande, I. A. Qattan, C. D. Lokhande, S. P. Patole, *J. Mater. Chem. A* **2020**, *8*, 918–977.
- [6] A. P. Cote, A. I. Benin, N. W. Ockwig, M. O’Keeffe, A. J. Matzger, O. M. Yaghi, *Science* **2005**, *310*, 1166–1170.
- [7] Z. Xia, Y. Zhao, S. B. Darling, *Adv. Mater. Interfaces* **2021**, *8*, 1–17.
- [8] S. P. S. Fernandes, V. Romero, B. Espiña, L. M. Salonen, *Chem. Eur. J.* **2019**, *25*, 6461–6473.
- [9] J. Liu, N. Wang, L. Ma, *Chem. Asian J.* **2020**, *15*, 338–351.
- [10] Y. Zhi, Z. Wang, H. L. Zhang, Q. Zhang, *Small* **2020**, 2001070.
- [11] L. P. L. Gonçalves, D. B. Christensen, M. Meledina, L. M. Salonen, D. Y. Petrovykh, E. Carbó-Argibay, J. P. S. Sousa, O. S. G. P. Soares, M. F. R. Pereira, S. Kegnæs, et al., *Catal. Sci. Technol.* **2020**, *10*, 1991–1995.
- [12] S. Mukherjee, Z. Zeng, M. M. Shirolkar, P. Samanta, A. K. Chaudhari, J. C. Tan, S. K. Ghosh, *Chem. Eur. J.* **2018**, *24*, 11771–11778.
- [13] C. S. Diercks, O. M. Yaghi, *Science* **2017**, *355*, eaal1585.
- [14] Y. Song, Q. Sun, B. Aguila, S. Ma, *Adv. Sci.* **2019**, *6*, 1801410.
- [15] S. Kandambeth, K. Dey, R. Banerjee, *J. Am. Chem. Soc.* **2019**, *141*, 1807–1822.
- [16] Z. Li, T. He, Y. Gong, D. Jiang, *Acc. Chem. Res.* **2020**, *53*, 1672–1685.
- [17] K. Geng, T. He, R. Liu, K. T. Tan, Z. Li, S. Tao, Y. Gong, Q. Jiang, D. Jiang, *Chem. Rev.* **2020**, *120*, 8814–8933.
- [18] B. Lukose, A. Kuc, J. Frenzel, T. Heine, *Beilstein J. Nanotechnol.* **2010**, *1*, 60–70.
- [19] C. Gropp, S. Canossa, S. Wuttke, F. Gándara, Q. Li, L. Gagliardi, O. M. Yaghi, *ACS Cent. Sci.* **2020**, *6*, 1255–1273.
- [20] X. Feng, X. Ding, D. Jiang, *Chem Soc Rev* **2012**, *41*, 6010–22.

- [21] S. J. Lyle, P. J. Waller, O. M. Yaghi, *Trends Chem.* **2019**, *1*, 172–184.
- [22] K. Geng, V. Arumugam, H. Xu, Y. Gao, D. Jiang, *Prog. Polym. Sci.* **2020**, *108*, 101288.
- [23] X. Li, P. Yadav, K. P. Loh, *Chem. Soc. Rev.* **2020**, *49*, 4835–4866.
- [24] M. S. Lohse, T. Bein, *Adv. Funct. Mater.* **2018**, *28*, 1–71.
- [25] S. Dalapati, S. Jin, J. Gao, Y. Xu, A. Nagai, D. Jiang, *J. Am. Chem. Soc.* **2013**, *135*, 17310–17313.
- [26] G. Lin, H. Ding, D. Yuan, B. Wang, C. Wang, *J. Am. Chem. Soc.* **2016**, *138*, 3302–3305.
- [27] J. T. Yu, Z. Chen, J. Sun, Z. T. Huang, Q. Y. Zheng, *J. Mater. Chem.* **2012**, *22*, 5369–5373.
- [28] M. G. Rabbani, A. K. Sekizkardes, Z. Kahveci, T. E. Reich, R. Ding, H. M. El-Kaderi, *Chem. Eur. J.* **2013**, *19*, 3324–3328.
- [29] Z. Li, X. Feng, Y. Zou, Y. Zhang, H. Xia, X. Liu, Y. Mu, *Chem. Commun.* **2014**, *50*, 13825–13828.
- [30] H. Fan, A. Mundstock, A. Feldho, A. Knebel, J. Gu, H. Meng, J. Caro, *J. Am. Chem. Soc.* **2018**, *140*, 10094–10098.
- [31] T. Yan, Y. Lan, M. Tong, C. Zhong, *ACS Sustain. Chem. Eng.* **2019**, *7*, 1220–1227.
- [32] M. Dogru, T. Bein, *Chem. Commun.* **2014**, *50*, 5531–5546.
- [33] A. K. Mandal, J. Mahmood, J. B. Baek, *ChemNanoMat* **2017**, *3*, 373–391.
- [34] Z. Meng, R. M. Stolz, K. A. Mirica, *J. Am. Chem. Soc.* **2019**, *141*, 11929–11937.
- [35] S.-Y. Ding, M. Dong, Y.-W. Wang, Y.-T. Chen, H.-Z. Wang, C. Y. Su, W. Wang, *J. Am. Chem. Soc.* **2016**, *138*, 3031–3037.
- [36] Z. Li, N. Huang, K. H. Lee, Y. Feng, S. Tao, Q. Jiang, Y. Nagao, S. Irle, D. Jiang, *J. Am. Chem. Soc.* **2018**, *140*, 12374–12377.
- [37] X. Wu, X. Han, Q. Xu, Y. Liu, C. Yuan, S. Yang, Y. Liu, J. Jiang, Y. Cui, *J. Am. Chem. Soc.* **2019**, *141*, 7081–7089.
- [38] P. Albacete, A. López-Moreno, S. Mena-Hernando, A. E. Platero-Prats, E. M. Pérez, F. Zamora, *Chem. Commun.* **2019**, *55*, 1382–1385.
- [39] S.-B. Yu, H. Lyu, J. Tian, H. Wang, D.-W. Zhang, Y. Liu, Z.-T. Li, *Polym. Chem.* **2016**, *7*, 3392–3397.
- [40] S. Kandambeth, B. P. Biswal, H. D. Chaudhari, K. C. Rout, S. Kunjattu H., S. Mitra, S.

- Karak, A. Das, R. Mukherjee, U. K. Kharul, et al., *Adv. Mater.* **2017**, *29*, 1603945.
- [41] X. Zhu, S. An, Y. Liu, J. Hu, H. Liu, C. Tian, S. Dai, X. Yang, H. Wang, C. W. Abney, S. Dai, *AIChE* **2017**, *63*, 3470–3478.
- [42] Y. Li, W. Chen, W. Hao, Y. Li, L. Chen, *ACS Appl. Nano Mater.* **2018**, *1*, 4756–4761.
- [43] Q. Sun, B. Aguila, J. Perman, L. D. Earl, C. W. Abney, Y. Cheng, H. Wei, N. Nguyen, L. Wojtas, S. Ma, *J. Am. Chem. Soc.* **2017**, *139*, 2786–2793.
- [44] N. Huang, L. Zhai, H. Xu, D. Jiang, *J. Am. Chem. Soc.* **2017**, *139*, 2428–2434.
- [45] W. Li, Y. Li, H. L. Qian, X. Zhao, C. X. Yang, X. P. Yan, *Talanta* **2019**, *204*, 224–228.
- [46] Y. Tao, X. H. Xiong, J. B. Xiong, L. X. Yang, Y. L. Fan, H. Feng, F. Luo, *J. Solid State Chem.* **2020**, *282*, 121126.
- [47] Y. Jiang, C. Liu, A. Huang, *ACS Appl. Mater. Interfaces* **2019**, *11*, 32186–32191.
- [48] G. Li, J. Ye, Q. Fang, F. Liu, *Chem. Eng. J.* **2019**, *370*, 822–830.
- [49] Y. Li, C. Wang, S. Ma, H. Zhang, J. Ou, Y. Wei, M. Ye, *ACS Appl. Mater. Interfaces* **2019**, *11*, 11706–11714.
- [50] Z. Li, Y. Zhang, H. Xia, Y. Mu, X. Liu, *Chem. Commun.* **2016**, *52*, 6613–6616.
- [51] Q. Sun, B. Aguila, L. D. Earl, C. W. Abney, L. Wojtas, P. K. Thallapally, S. Ma, *Adv. Mater.* **2018**, *30*, 1705479.
- [52] W. R. Cui, C. R. Zhang, W. Jiang, F. F. Li, R. P. Liang, J. Liu, J. D. Qiu, *Nat. Commun.* **2020**, *11*, 436.
- [53] X. H. Xiong, Y. Tao, Z. W. Yu, L. X. Yang, L. J. Sun, Y. L. Fan, F. Luo, *Chem. Eng. J.* **2020**, *384*, 123240.
- [54] F. F. Li, W. R. Cui, W. Jiang, C. R. Zhang, R. P. Liang, J. D. Qiu, *J. Hazard. Mater.* **2020**, *392*, 122333.
- [55] Q. Fang, J. Wang, S. Gu, R. B. Kaspar, Z. Zhuang, J. Zheng, H. Guo, S. Qiu, Y. Yan, *J. Am. Chem. Soc.* **2015**, *137*, 8352–8355.
- [56] L. Bai, S. Z. F. Phua, W. Q. Lim, A. Jana, Z. Luo, H. P. Tham, L. Zhao, Q. Gao, Y. Zhao, *Chem. Commun.* **2016**, *52*, 4128–4131.
- [57] V. S. Vyas, M. Vishwakarma, I. Moudrakovski, F. Haase, G. Savasci, C. Ochsenfeld, J. P. Spatz, B. V. Lotsch, *Adv. Mater.* **2016**, *28*, 8749–8754.
- [58] M. S. Lohse, T. Stassin, G. Naudin, S. Wuttke, R. Ameloot, D. De Vos, D. D. Medina, T.

- Bein, *Chem. Mater.* **2016**, *28*, 626–631.
- [59] S. He, T. Zeng, S. Wang, H. Niu, Y. Cai, *ACS Appl. Mater. Interfaces* **2017**, *9*, 2959–2965.
- [60] W. Ji, L. Xiao, Y. Ling, C. Ching, M. Matsumoto, R. P. Bisbey, D. E. Helbling, W. R. Dichtel, *J. Am. Chem. Soc.* **2018**, *140*, 12677–12681.
- [61] A. Mellah, S. P. S. Fernandes, R. Rodríguez, J. Otero, J. Paz, J. Cruces, D. D. Medina, H. Djamila, B. Espiña, L. M. Salonen, *Chem. Eur. J.* **2018**, *24*, 10601–10605.
- [62] R. Q. Wang, X. B. Wei, Y. Q. Feng, *Chem. Eur. J.* **2018**, *24*, 10979–10983.
- [63] W. Gao, Y. Tian, H. Liu, Y. Cai, A. Liu, Y.-L. Yu, Z. Zhao, G. Jiang, *Anal. Chem.* **2019**, *91*, 772–775.
- [64] V. Romero, S. P. S. Fernandes, P. Kovář, M. Pšenička, Y. V. Kolen'ko, L. M. Salonen, B. Espiña, *Microporous Mesoporous Mater.* **2020**, *307*, 110523.
- [65] S. Chandra, S. Kandambeth, B. P. Biswal, B. Lukose, S. M. Kunjir, M. Chaudhary, R. Babarao, T. Heine, R. Banerjee, *J. Am. Chem. Soc.* **2013**, *135*, 17853–17861.
- [66] I. Berlanga, M. L. Ruiz-González, J. M. González-Calbet, J. L. G. Fierro, R. Mas-Ballesté, F. Zamora, *Small* **2011**, *7*, 1207–1211.
- [67] D. N. Bunck, W. R. Dichtel, *J. Am. Chem. Soc.* **2013**, *135*, 14952–14955.
- [68] M. A. Khayum, S. Kandambeth, S. Mitra, S. B. Nair, A. Das, S. S. Nagane, R. Mukherjee, R. Banerjee, *Angew. Chemie Int. Ed.* **2016**, *55*, 15604–15608.
- [69] X. Guan, Y. Ma, H. Li, Y. Yusran, M. Xue, Q. Fang, Y. Yan, V. Valtchev, S. Qiu, *J. Am. Chem. Soc.* **2018**, *140*, 4494–4498.
- [70] Y. Gao, C. Wang, H. Hu, R. Ge, M. Lu, J. Zhang, Z. Li, P. Shao, D. Jiang, *Chem. Eur. J.* **2019**, *25*, 15488–15492.
- [71] J. Qiu, P. Guan, Y. Zhao, Z. Li, H. Wang, J. Wang, *Green Chem.* **2020**, *22*, 7537–7542.
- [72] B. Dong, W.-J. Wang, S.-C. Xi, D.-Y. Wang, R. Wang, *Chem. Eur. J.* **2021**, *27*, 2692–2698.
- [73] S. T. Yang, J. Kim, H. Y. Cho, S. Kim, W. S. Ahn, *RSC Adv.* **2012**, *2*, 10179–10181.
- [74] S. Dalapati, E. Jin, M. Addicoat, T. Heine, D. Jiang, *J. Am. Chem. Soc.* **2016**, *138*, 5797–5800.
- [75] L. M. Salonen, D. D. Medina, E. Carbó-Argibay, M. G. Goesten, L. Mafra, N. Guldris, J.



- M. Rotter, D. G. Stroppa, C. Rodríguez-Abreu, *Chem. Commun.* **2016**, *52*, 7986–7989.
- [76] F. J. Uribe-Romo, J. R. Hunt, H. Furukawa, C. Klöck, M. O’Keeffe, O. M. Yaghi, *J. Am. Chem. Soc.* **2009**, *131*, 4570–4571.
- [77] S. Y. Ding, J. Gao, Q. Wang, Y. Zhang, W. G. Song, C. Y. Su, W. Wang, *J. Am. Chem. Soc.* **2011**, *133*, 19816–19822.
- [78] S. B. Alahakoon, C. M. Thompson, A. X. Nguyen, G. Occhialini, G. T. McCandless, R. A. Smaldone, *Chem. Commun.* **2016**, *52*, 2843–2845.
- [79] H. li, *Green Chem.* **2019**, *21*, 649–657.
- [80] F. J. Uribe-Romo, C. J. Doonan, H. Furukawa, K. Oisaki, O. M. Yaghi, *J. Am. Chem. Soc.* **2011**, *133*, 11478–11481.
- [81] L. Stegbauer, K. Schwinghammer, B. V. Lotsch, *Chem. Sci.* **2014**, *5*, 2789–2793.
- [82] S. Kandambeth, A. Mallick, B. Lukose, M. V. Mane, T. Heine, R. Banerjee, *J. Am. Chem. Soc.* **2012**, *134*, 19524–19527.
- [83] B. P. Biswal, S. Chandra, S. Kandambeth, B. Lukose, T. Heine, R. Banerjee, *J. Am. Chem. Soc.* **2013**, *135*, 5328–5331.
- [84] J. Guo, Y. Xu, S. Jin, L. Chen, T. Kaji, Y. Honsho, M. A. Addicoat, J. Kim, A. Saeki, H. Ihee, S. Seki, S. Irle, M. Hiramoto, J. Gao, D. Jiang, *Nat. Commun.* **2013**, *4*, 2736.
- [85] E. Vitaku, C. N. Gannett, K. L. Carpenter, L. Shen, H. D. Abruña, W. R. Dichtel, *J. Am. Chem. Soc.* **2020**, *142*, 16–20.
- [86] B. Zhang, M. Wei, H. Mao, X. Pei, S. A. Alshimri, J. A. Reimer, O. M. Yaghi, *J. Am. Chem. Soc.* **2018**, *140*, 12715–12719.
- [87] X. Guan, H. Li, Y. Ma, M. Xue, Q. Fang, Y. Yan, V. Valtchev, S. Qiu, *Nat. Chem.* **2019**, *11*, 587–594.
- [88] X. Zhuang, W. Zhao, F. Zhang, Y. Cao, F. Liu, S. Bi, X. Feng, *Polym. Chem.* **2016**, *7*, 4176–4181.
- [89] X. Li, *Mater. Chem. Front.* **2021**, *5*, 2931–2949.
- [90] C. R. Deblase, W. R. Dichtel, *Macromolecules* **2016**, *49*, 5297–5305.
- [91] S. Kandambeth, D. B. Shinde, M. K. Panda, B. Lukose, T. Heine, R. Banerjee, *Angew. Chemie Int. Ed.* **2013**, *52*, 13052–13056.
- [92] X. Chen, M. Addicoat, E. Jin, L. Zhai, H. Xu, N. Huang, Z. Guo, L. Liu, S. Irle, D. Jiang, *J.*

- Am. Chem. Soc.* **2015**, *137*, 3241–3247.
- [93] A. Halder, S. Karak, M. Addicoat, S. Bera, A. Chakraborty, S. H. Kunjattu, P. Pachfule, T. Heine, R. Banerjee, *Angew. Chemie Int. Ed.* **2018**, *57*, 5797–5802.
- [94] A. Halder, M. Ghosh, A. Khayum M, S. Bera, M. Addicoat, H. S. Sasmal, S. Karak, S. Kurungot, R. Banerjee, *J. Am. Chem. Soc.* **2018**, *140*, 10941–10945.
- [95] L. Li, F. Lu, R. Xue, B. Ma, Q. Li, N. Wu, H. Liu, W. Yao, H. Guo, W. Yang, *ACS Appl. Mater. Interfaces* **2019**, *11*, 26355–26363.
- [96] X. Wu, X. Han, Y. Liu, Y. Liu, Y. Cui, *J. Am. Chem. Soc.* **2018**, *140*, 16124–16133.
- [97] P. J. Waller, S. J. Lyle, T. M. Osborn Popp, C. S. Diercks, J. A. Reimer, O. M. Yaghi, *J. Am. Chem. Soc.* **2016**, *138*, 15519–15522.
- [98] F. Haase, E. Troschke, G. Savasci, T. Banerjee, V. Duppel, S. Dörfler, M. M. J. Grundei, A. M. Burow, C. Ochsenfeld, S. Kaskel, B. V. Lotsch, *Nat. Commun.* **2018**, *9*, 2600.
- [99] X. Li, C. Zhang, S. Cai, X. Lei, V. Altoe, F. Hong, J. J. Urban, J. Ciston, E. M. Chan, Y. Liu, *Nat. Commun.* **2018**, *9*, 2998.
- [100] P. J. Waller, Y. S. Alfaraj, C. S. Diercks, N. N. Jarenwattananon, O. M. Yaghi, *J. Am. Chem. Soc.* **2018**, *140*, 9099–9103.
- [101] P.-F. Wei, M.-Z. Qi, Z.-P. Wang, S.-Y. Ding, W. Yu, Q. Liu, L.-K. Wang, H.-Z. Wang, W.-K. An, W. Wang, *J. Am. Chem. Soc.* **2018**, *140*, 4623–4631.
- [102] P. Das, S. K. Mandal, *Chem. Mater.* **2019**, *31*, 1584–1596.
- [103] J. H. Chong, M. Sauer, B. O. Patrick, M. J. MacLachlan, *Org. Lett.* **2003**, *5*, 3823–3826.
- [104] C. Zhao, C. S. Diercks, C. Zhu, N. Hanikel, X. Pei, O. M. Yaghi, *J. Am. Chem. Soc.* **2018**, *140*, 16438–16441.
- [105] J.-M. Lehn, J.-M. Lehn, *Chem. Soc. Rev.* **2007**, *36*, 151–60.
- [106] S. B. Alahakoon, S. D. Diwakara, C. M. Thompson, R. A. Smaldone, *Chem. Soc. Rev.* **2020**, *49*, 1344–1356.
- [107] F. Podjaski, C. Ochsenfeld, V. S. Vyas, F. Haase, L. Stegbauer, B. V. Lotsch, *Nat. Commun.* **2015**, *6*, 8508.
- [108] A. Halder, S. Kandambeth, B. P. Biswal, G. Kaur, N. C. Roy, M. Addicoat, J. K. Salunke, S. Banerjee, K. Vanka, T. Heine, S. Verma, R. Banerjee, *Angew. Chemie Int. Ed.* **2016**, *55*, 7806–7810.

- [109] J. Y. Yue, X. H. Liu, B. Sun, D. Wang, *Chem. Commun.* **2015**, *51*, 14318–14321.
- [110] S. Dalapati, M. Addicoat, S. Jin, T. Sakurai, J. Gao, H. Xu, S. Irle, S. Seki, D. Jiang, *Nat. Commun.* **2015**, *6*, 7786.
- [111] L. Ascherl, T. Sick, J. T. Margraf, S. H. Lapidus, M. Calik, C. Hettstedt, K. Karaghiosoff, M. Döblinger, T. Clark, K. W. Chapman, F. Auras, T. Bein, *Nat. Chem.* **2016**, *8*, 310–316.
- [112] F. Auras, L. Ascherl, A. H. Hakimioun, J. T. Margraf, F. C. Hanusch, S. Reuter, D. Bessinger, M. Döblinger, C. Hettstedt, K. Karaghiosoff, S. Herbert, P. Knochel, T. Clark, T. Bein, *J. Am. Chem. Soc.* **2016**, *138*, 16703–16710.
- [113] M. Martínez-Abadía, C. T. Stoppiello, K. Strutynski, B. Lerma-Berlanga, C. Martí-Gastaldo, A. Saeki, M. Melle-Franco, A. N. Khlobystov, A. Mateo-Alonso, *J. Am. Chem. Soc.* **2019**, *141*, 14403–14410.
- [114] S. B. Alahakoon, K. Tan, H. Pandey, G. T. Mccandless, D. Grinffiel, T. Thonhauser, R. Smaldone, *J. Am. Chem. Soc.* **2020**, *142*, 12987–12994.
- [115] X. Chen, M. Addicoat, S. Irle, A. Nagai, D. Jiang, *J. Am. Chem. Soc.* **2013**, *135*, 546–549.
- [116] S. B. Alahakoon, G. T. Mccandless, A. A. K. Karunathilake, C. M. Thompson, R. A. Smaldone, *Chem. Eur. J.* **2017**, *23*, 4255–4259.
- [117] S. B. Alahakoon, G. Occhialini, G. T. Mccandless, A. A. K. Karunathilake, S. O. Nielsen, R. A. Smaldone, *CrsytEngComm* **2017**, *19*, 4882–4885.
- [118] W. A. Braunecker, K. E. Hurst, K. G. Ray, Z. R. Owczarczyk, M. B. Martinez, N. Leick, A. Keuhlen, A. Sellinger, J. C. Johnson, *Cryst. Growth Des.* **2018**, *18*, 4160–4166.
- [119] Y. Yusran, Q. Fang, S. Qiu, *Isr. J. Chem.* **2018**, *58*, 971–984.
- [120] Y. Yusran, X. Guan, H. Li, Q. Fang, S. Qiu, *Natl. Sci. Rev.* **2020**, *7*, 170–190.
- [121] A. Nagai, Z. Guo, X. Feng, S. Jin, X. Chen, X. Ding, D. Jiang, *Nat. Commun.* **2011**, *2*, 536–538.
- [122] H. Xu, X. Chen, J. Gao, J. Lin, M. Addicoat, S. Irle, D. Jiang, *Chem. Commun.* **2014**, *50*, 1292–1294.
- [123] H. Xu, J. Gao, D. Jiang, *Nat. Chem.* **2015**, *7*, 905–912.
- [124] L. Merí-Bofí, S. Royuela, F. Zamora, M. L. Ruiz-González, J. L. Segura, R. Muñoz-Olivas,

- M. J. Mancheño, *J. Mater. Chem. A* **2017**, *5*, 17973–17981.
- [125] S. Royuela, E. García-Garrido, M. Martín Arroyo, M. J. Mancheño, M. M. Ramos, D. González-Rodríguez, Á. Somoza, F. Zamora, J. L. Segura, *Chem. Commun.* **2018**, *54*, 8729–8732.
- [126] L. Chen, K. Furukawa, J. Gao, A. Nagai, T. Nakamura, Y. Dong, D. Jiang, *J. Am. Chem. Soc.* **2014**, *136*, 9806–9809.
- [127] K. Li, N. K. Wong, M. J. Strauss, A. M. Evans, M. Matsumoto, W. R. Dichtel, A. Adronov, *J. Am. Chem. Soc.* **2021**, *143*, 649–656.
- [128] N. Huang, X. Chen, R. Krishna, D. Jiang, *Angew. Chemie Int. Ed.* **2015**, *54*, 2986–2990.
- [129] Q. Lu, Y. Ma, H. Li, X. Guan, Y. Yusran, M. Xue, Q. Fang, Y. Yan, S. Qiu, V. Valtchev, *Angew. Chem. Int. Ed.* **2018**, *57*, 6042–6048.
- [130] S. Rager, M. Dogru, V. Werner, A. Gavryushin, M. Götz, H. Engelke, D. D. Medina, P. Knochel, T. Bein, *CrystEngComm* **2017**, *19*, 4886–4891.
- [131] M. P. Sárria, A. Vieira, Â. Lima, S. P. S. Fernandes, I. Lopes, A. Gonçalves, A. C. Gomes, L. M. Salonen, B. Espiña, *Environ. Sci. Nano* **2021**, *8*, 1680–1689.
- [132] Y. Gao, *Chem. Commun.* **2016**, *52*, 7082.
- [133] C. Liu, Y. Jiang, A. Nalaparaju, J. Jiang, A. Huang, *J. Mater. Chem. A* **2019**, *7*, 24205–24210.
- [134] B. Y. Shin, G. E. Fryxell, W. Um, K. Parker, S. V Mattigod, R. Skaggs, *Adv. Funct. Mater.* **2007**, *17*, 2897–2901.
- [135] K.-K. Yee, N. Reimer, J. Liu, S.-Y. Cheng, S.-M. Yiu, J. Weber, N. Stock, Z. Xu, *J. Am. Chem. Soc.* **2013**, *135*, 7795–7798.
- [136] B. Aguila, Q. Sun, J. A. Perman, L. D. Earl, C. W. Abney, R. Elzein, R. Schlaf, S. Ma, *Adv. Mater.* **2017**, *29*, 1700665.
- [137] Q. Sun, B. Aguila, J. A. Perman, T. Butts, F. Xiao, S. Ma, *Chem* **2018**, *4*, 1–14.
- [138] S. F. Nakayama, M. Yoshikane, Y. Onoda, Y. Nishihama, M. Iwai-Shimada, M. Takagi, Y. Kobayashi, T. Isobe, *Trends Anal. Chem.* **2019**, *121*, 115410.
- [139] X. C. Hu, D. Q. Andrews, A. B. Lindstrom, T. A. Bruton, L. A. Schaidler, P. Grandjean, R. Lohmann, C. C. Carignan, A. Blum, S. A. Balan, C. P. Higgins, E. M. Sunderland, *Environ. Sci. Technol. Lett.* **2016**, *3*, 344–350.

- [140] K. Steenland, T. Fletcher, D. A. Savitz, *Environ. Health Perspect.* **2010**, *118*, 1100–1108.
- [141] A. M. Temkin, B. A. Hocevar, D. Q. Andrews, O. V. Naidenko, L. M. Kamendulis, *Int. J. Environ. Res. Public Health* **2020**, *17*, 1668.
- [142] Q. Liao, C. Ke, X. Huang, D. Wang, Q. Han, Y. Zhang, Y. Zhang, K. Xi, *Angew. Chemie Int. Ed.* **2021**, *60*, 1411–1416.
- [143] L. Cusin, H. Peng, A. Ciesielski, P. Samor, *Angew. Chem. Int. Ed.* **2021**, *60*, 14236–14250.
- [144] X. Han, J. Huang, C. Yuan, Y. Liu, Y. Cui, *J. Am. Chem. Soc.* **2018**, *140*, 892–895.
- [145] H. Qian, F. Meng, C. Yang, X. Yan, *Angew. Chem. Int. Ed.* **2020**, *59*, 17607–17613.
- [146] H. Liu, J. Chu, H. Liu, J. Chu, Z. Yin, X. Cai, L. Zhuang, H. Deng, *Chem* **2018**, *4*, 1696–1709.
- [147] X. T. Li, J. Zou, T. H. Wang, H. C. Ma, G. J. Chen, Y. Bin Dong, *J. Am. Chem. Soc.* **2020**, *142*, 6521–6526.
- [148] S. Subudhi, S. P. Tripathy, K. Parida, *Catal. Sci. Technol.* **2021**, *11*, 392–415.
- [149] M. Thommes, K. Kaneko, A. V. Neimark, J. P. Olivier, F. Rodriguez-reinoso, J. Rouquerol, K. S. W. Sing, *Pure Appl. Chem.* **2015**, *87*, 1051–1069.
- [150] M. R. Rao, Y. Fang, S. De Feyter, D. F. Perepichka, *J. Am. Chem. Soc.* **2017**, *139*, 2421–2427.
- [151] F. Ambroz, T. J. Macdonald, V. Martis, I. P. Parkin, *Small Methods* **2018**, *2*, 1800173.
- [152] World Health Organization, *Drinking-water*, <https://www.who.int/news-room/fact-sheets/detail/drinking-water> (accessed August 1, 2021)
- [153] EU 2000/60/EC. Establishing a Framework for Community Action in the Field of Water Policy. *Off. J. Eur. Communities* **2000**, *327*, 1–73.
- [154] European Commission. Commission staff working document on the implementation of the "Community Strategy for Endocrine Disrupters" - a range of substances suspected of interfering with the hormone systems of humans and wildlife (COM (1999) 706), (COM (2001) 262) and (SEC (2004) 1372). *SEC* **2007**, 1635.
- [155] EU 2008/105/EC. Environmental quality standards in the field of water policy, amending and subsequently repealing Council Directives 82/176/EEC, 83/513/EEC,

- 84/156/EEC, 84/491/EEC, 86/280/EEC and amending Directive 2000/60/EC of the European Parliament and of the Council. *Off. J. Eur. Communities* **2008**, 348, 84–97.
- [156] EU 2013/39/EU. Amending Directives 2000/60/EC and 2008/105/EC as regards priority substances in the field of water policy. *Off. J. Eur. Communities* **2013**, 226, 1–17.
- [157] EU 2015/495/EU. Establishing a watch list of substances for Union-wide monitoring in the field of water policy pursuant to Directive 2008/105/EC of the European Parliament and of the Council. *Off. J. Eur. Union* **2015**, L260, 6–17.
- [158] European Commission. Commission staff working document impact assessment. Proposal for a Directive of the European Parliament and of the Council on the quality of water intended for human consumption. *SWD* **2017**.
- [159] European Commission, Directive of the European Parliament and of the Council on the quality of water intended for human consumption. *Off. J. Eur. Union* **2020**, L435, 1–62.
- [160] S. Sharma, A. Bhattacharya, *Appl. Water Sci.* **2017**, 7, 1043–1067.
- [161] M. Díaz-González, M. Gutiérrez-Capitán, P. Niu, A. Baldi, C. Jiménez-Jorquera, C. Fernández-Sánchez, *Trends Anal. Chem.* **2016**, 77, 186–202.
- [162] S. N. Zulkifli, H. A. Rahim, W.-J. Lau, *Sensors Actuators B* **2018**, 255, 2657–2689.
- [163] F. P. Carvalho, A. Fajgelj, *Water. Air. Soil Pollut.* **2013**, 224, 1597.
- [164] S. D. Richardson, T. A. Ternes, *Anal. Chem.* **2014**, 86, 2813–2848.
- [165] NORMAN network, <https://www.norman-network.net> (accessed September 16, 2020).
- [166] C. S. A., E. C. Lima, *Ecotoxicol. Environ. Saf.* **2018**, 150, 1–17.
- [167] World Health Organization, *Guidelines for Drinking Water Quality*, [https://www.who.int/water\\_sanitation\\_health/publications/573-drinking-water-quality-guidelines-4-including-1st-addendum/en/](https://www.who.int/water_sanitation_health/publications/573-drinking-water-quality-guidelines-4-including-1st-addendum/en/) (accessed April 1, 2020).
- [168] R. Letterman D., Ed., *Water Quality and Treatment A Handbook of Community Water Supplies*, McGraw-Hill, INC, **1999**.
- [169] V. Valdiglesias, E. Pásaro, V. M. Prego-Faraldo, J. Méndez, B. Laffon, *Mar. Drugs* **2013**, 11, 4328–4349.

- [170] J. T. Maynes, K. S. Bateman, M. M. Cherney, A. K. Das, H. A. Luu, C. F. B. Holmes, M. N. G. James, *J. Biol. Chem.* **2001**, *276*, 44078–44082.
- [171] European Commission, *Off. J. Eur. Union* **2004**, *L139*, 55–255.
- [172] A. P. Louppis, A. V. Badeka, P. Katikou, E. K. Paleologos, M. G. Kontominas, *Toxicon* **2010**, *55*, 724–733.
- [173] C. Bosch-Orea, J. Sanchís, M. Farré, D. Barceló, *Anal. Bioanal. Chem.* **2017**, *409*, 5451–5462.
- [174] E. Takahashi, Q. Yu, G. Eaglesham, D. W. Connell, J. Mcbroom, S. Costanzo, G. R. Shaw, *Mar. Environ. Res.* **2007**, *64*, 429–442.
- [175] X. Li, Z. Li, J. Chen, Q. Shi, R. Zhang, S. Wang, X. Wang, *Chemosphere* **2014**, *111*, 560–567.
- [176] M. B. Peacock, C. M. Gibble, D. B. Senn, J. E. Cloern, R. M. Kudela, *Harmful Algae* **2018**, *73*, 138–147.
- [177] L. L. Mafra, P. K. W. Nolli, L. E. Mota, C. Domit, M. Soeth, L. F. G. Luz, B. F. Sobrinho, J. G. Leal, M. Di Domenico, *Harmful Algae* **2019**, *89*, 101662.
- [178] P. Vale, M. A. D. M. Sampayo, *Toxicon* **2003**, *41*, 187–197.
- [179] D. Manita, R. N. Alves, A. C. Braga, F. H. S. Fogaça, A. Marques, P. R. Costa, *Food Chem. Toxicol.* **2017**, *101*, 121–127.
- [180] A. Silva, L. Pinto, S. M. Rodrigues, H. de Pablo, M. Santos, T. Moita, M. Mateus, *Harmful Algae* **2016**, *53*, 33–39.
- [181] D. van der Merwe, Cyanobacterial (Blue-Green Algae) Toxins, in *Toxicol. Chem. Warf. Agents*, Elsevier Inc., **2015**, pp. 421–429.
- [182] T. L. Pham, T. N. Dang, Microcystins in Freshwater Ecosystems: Occurrence, Distribution, and Current Treatment Approaches, in *Water Wastewater Treatment Technologies*, Energy, Environment, and Sustainability, Springer, Singapore, **2019**, pp. 15–36.
- [183] E. P. Preece, F. J. Hardy, B. C. Moore, M. Bryan, *Harmful Algae* **2017**, *61*, 31–45.
- [184] Z. Svirčev, V. Baltić, M. Gantar, M. Juković, D. Stojanović, M. Baltić, *J. Environ. Sci. Heal. Part C* **2010**, *28*, 39–59.
- [185] B. A. Neilan, L. A. Pearson, J. Muenchhoff, M. C. Moffitt, E. Dittmann, *Environ.*

- Microbiol.* **2013**, *15*, 1239–1253.
- [186] World Health Organization, *Cyanobacterial toxins : Microcystin-LR in Drinking-water Background document for development of WHO Guidelines for Drinking-water Quality*, WHO/SDE/WSH/03.04/57, **2003**
- [187] V. Gupta, A. K. Ogawa, X. Du, K. N. Houk, R. W. Armstrong, *J. Med. Chem.* **1997**, *40*, 3199–3206.
- [188] M. J. Harke, M. M. Steffen, C. J. Gobler, T. G. Otten, S. W. Wilhelm, S. A. Wood, H. W. Paerl, *Harmful Algae* **2016**, *54*, 4–20.
- [189] C. Sobrino, A. Matthiensen, S. Vidal, H. Galvao, *Limnetica* **2004**, *23*, 133–144.
- [190] A. Gogoi, P. Mazumder, V. K. Tyagi, G. G. Tushara Chaminda, A. K. An, M. Kumar, *Groundw. Sustain. Dev.* **2018**, *6*, 169–180.
- [191] M. Patel, R. Kumar, K. Kishor, T. Mlsna, C. U. Pittman, D. Mohan, *Chem. Rev.* **2019**, *119*, 3510–3673.
- [192] World Health Organization, *Pharmaceuticals in drinking water*, WHO/HSE/WSH/11.05, **2011**.
- [193] European Commission, *Communication from the commission to the european parliament, the council and the european economic and social committee European Union Strategic Approach to Pharmaceuticals in the Environment*, COM **2019**.
- [194] I. Bragança, A. Plácido, P. Paíga, V. F. Domingues, C. Delerue-Matos, *Sci. Total Environ.* **2012**, *433*, 281–289.
- [195] P. Reis-Santos, M. Pais, B. Duarte, I. Caçador, A. Freitas, A. S. Vila Pouca, J. Barbosa, S. Leston, J. Rosa, F. Ramos, et al., *Mar. Pollut. Bull.* **2018**, *135*, 1079–1084.
- [196] European Medicines Agency, *Guideline on the Environmental Risk Assessment of Medicinal Products for Human Use*, EMEA/CHMP/SWP/4447/00 Rev.1, **2018**.
- [197] M.-K. Kim, K.-D. Zoh, *Environ. Eng. Res* **2016**, *21*, 319–332.
- [198] A. Andrade-Eiroa, M. Canle, V. Leroy-Cancellieri, V. Cerdà, *Trends Anal. Chem.* **2016**, *80*, 641–654.
- [199] M. Grassi, G. Kaykioglu, V. Belgiorno, Removal of Emerging Contaminants from Water and Wastewater by Adsorption Process, in *Emerging Compounds Removal from Wastewater*, Springer, Dordrecht, **2012**, pp. 15–37.



- [200] M. N. Rashed, Adsorption Technique for the Removal of Organic Pollutants from Water and Wastewater, in *Organic Pollutants Monitoring, Risk and Treatment*, IntechOpen, **2013**, pp. 167–194.
- [201] G. M. Marion, F. J. Millero, M. F. Camões, P. Spitzer, R. Feistel, C.-T. A. Chen, *Mar. Chem.* **2011**, *126*, 89–96.
- [202] B. S. Rathi, P. S. Kumar, *Environ. Pollut.* **2021**, *280*, 116995.
- [203] E. Worch, *Adsorption Technology in Water Treatment, Fundamentals, Processes, and Modeling*, De Gruyter, Boston, **2012**.
- [204] D. A. Alvarez, J. D. Petty, J. N. Huckins, T. L. Jones-Lepp, D. T. Getting, J. P. Goddard, S. E. Manahan, *Environ. Toxicol. Chem.* **2004**, *23*, 1640–1648.
- [205] M. J. Martínez Bueno, M. D. Hernando, A. Agüera, A. R. Fernández-Alba, *Talanta* **2009**, *77*, 1518–1527.
- [206] I. Carpinteiro, A. Schopfer, N. Estoppey, C. Fong, D. Grandjean, L. F. De Alencastro, *Anal. Bioanal. Chem.* **2016**, *408*, 1067–1078.
- [207] J. Xiong, Z. Wang, X. Ma, H. Li, J. You, *Sci. Total Environ.* **2019**, *648*, 1305–1312.
- [208] R. M. Schwartz, *Mar. Pollut. Bull.* **2006**, *52*, 121.
- [209] S. McKay, B. Tschärke, D. Hawker, K. Thompson, J. O. Brien, J. F. Mueller, S. Kaserzon, *Sci. Total Environ.* **2020**, *704*, 135891.
- [210] F. Mansour, M. Al-Hindi, R. Yahfoufi, G. M. Ayoub, M. N. Ahmad, *Rev. Environ. Sci. Bio/Technology* **2018**, *17*, 109–145.
- [211] J. Akhtar, N. A. S. Amin, K. Shahzad, *Desalin. Water Treat.* **2016**, *57*, 12842–12860.
- [212] L. Kovalova, D. R. U. Knappe, K. Lehnberg, C. Kazner, J. Hollender, *Environ. Sci. Pollut. Res.* **2013**, *20*, 3607–3615.
- [213] A. Tchinsa, M. F. Hossain, T. Wang, Y. Zhou, *Chemosphere* **2021**, *284*, 131393.
- [214] V. Pichon, F. Chapuis-Hugon, *Anal. Chim. Acta* **2008**, *622*, 48–61.
- [215] N. Rosman, W. N. W. Salleh, M. A. Mohamed, J. Jaafar, A. F. Ismail, Z. Harun, *J. Colloid Interface Sci.* **2018**, *532*, 236–260.
- [216] A. R. Bagheri, N. Aramesh, F. Sher, M. Bilal, *Chemosphere* **2021**, *270*, 129523.
- [217] J. S. Gan, X. B. Li, K. Rizwan, M. Adeel, M. Bilal, T. Rasheed, H. M. N. Iqbal, *Chemosphere* **2022**, *286*, 131710.

- [218] A. Sarafraz-Yazdi, N. Razavi, *Trends Anal. Chem.* **2015**, *73*, 81–90.
- [219] Q. Wang, Q. Gao, A. M. Al-Enizi, A. Nafady, S. Ma, *Inorg. Chem. Front.* **2020**, *7*, 300–339.
- [220] L. Jiao, J. Y. R. Seow, W. S. Skinner, Z. U. Wang, H.-L. Jiang, *Mater. Today* **2019**, *27*, 43–68.
- [221] J. Byun, H. A. Patel, D. Thirion, C. T. Yavuz, *Nat. Commun.* **2016**, *7*, 13377.
- [222] U. Díaz, A. Corma, *Coord. Chem. Rev.* **2016**, *311*, 85–124.
- [223] G. P. Mashile, P. N. Nomngongo, *Crit. Rev. Anal. Chem.* **2016**, *8347*, 1–8.
- [224] R. M. Kudela, *Compr. Anal. Chem.* **2017**, *78*, 379–409.
- [225] L. A. MacKenzie, *Curr. Opin. Biotechnol.* **2010**, *21*, 326–331.
- [226] L. MacKenzie, V. Beuzenberg, P. Holland, P. McNabb, A. Selwood, *Toxicol.* **2004**, *44*, 901–918.
- [227] M. Roué, H. T. Darius, M. Chinain, *Toxins* **2018**, *10*, 167.
- [228] G. Pizarro, Á. Moroño, B. Paz, J. M. Franco, Y. Pazos, B. Reguera, *Mar. Drugs* **2013**, *11*, 3823–3845.
- [229] S. W. Lv, J. M. Liu, Z. H. Wang, H. Ma, C. Y. Li, N. Zhao, S. Wang, *J. Environ. Sci.* **2019**, *80*, 169–185.
- [230] J. Wang, S. Zhuang, *Coord. Chem. Rev.* **2019**, *400*, 213046.
- [231] W. Zhang, L. Zhang, H. Zhao, B. Li, H. Ma, *J. Mater. Chem. A* **2018**, *6*, 13331–13339.
- [232] G.-H. Ning, Z. Chen, Q. Gao, W. Tang, Z. Chen, C. Liu, B. Tian, X. Li, K. P. Loh, *J. Am. Chem. Soc.* **2017**, *139*, 8897–8904.
- [233] H. Fan, J. Gu, H. Meng, A. Knebel, J. Caro, *Angew. Chemie Int. Ed.* **2018**, *57*, 4083–4087.
- [234] L. Huang, R. Shen, R. Liu, Q. Shuai, *J. Hazard. Mater.* **2020**, *392*, 122320.
- [235] C. H. Yang, J. S. Chang, D. J. Lee, *Chemosphere* **2020**, *253*, 126736.
- [236] Z. A. Ghazi, A. M. Khattak, R. Iqbal, R. Ahmad, A. A. Khan, M. Usman, F. Nawaz, W. Ali, Z. Felegari, S. U. Jan, A. Iqbal, A. Ahmad, *New J. Chem.* **2018**, *42*, 10234–10242.
- [237] S. Zhang, X. Zhao, B. Li, C. Bai, Y. Li, L. Wang, R. Wen, M. Zhang, L. Ma, S. Li, *J. Hazard. Mater.* **2016**, *314*, 95–104.
- [238] X. H. Xiong, Z. W. Yu, L. Le Gong, Y. Tao, Z. Gao, L. Wang, W. H. Yin, L. X. Yang, F. Luo,

- Adv. Sci.* **2019**, *6*, 1–8.
- [239] M. J. Klemes, Y. Ling, C. Ching, C. Wu, L. Xiao, D. E. Helbling, W. R. Dichtel, *Angew. Chemie Int. Ed.* **2019**, *58*, 12049–12053.
- [240] S. Wang, H. Niu, D. Cao, Y. Cai, *Talanta* **2019**, *194*, 522–527.
- [241] L. Xiao, C. Ching, Y. Ling, M. Nasiri, M. J. Klemes, T. M. Reineke, D. E. Helbling, W. R. Dichtel, *Macromolecules* **2019**, *52*, 3747–3752.
- [242] W. Ji, Y. Guo, H. Xie, X. Wang, X. Jiang, D. Guo, *J. Hazard. Mater.* **2020**, *397*, 122793.
- [243] W. Wang, S. Deng, L. Ren, D. Li, W. Wang, M. Vakili, B. Wang, J. Huang, Y. Wang, G. Yu, *ACS Appl. Mater. Interfaces* **2018**, *10*, 30265–30272.
- [244] W. Wang, S. Deng, L. Ren, D. Li, W. Wang, M. Vakili, B. Wang, J. Huang, Y. Wang, G. Yu, *ACS Appl. Mater. Interfaces* **2018**, *10*, 30265–30272.
- [245] W. H. Ji, Y. S. Guo, X. Wang, X. F. Lu, D. S. Guo, *J. Chromatogr. A* **2019**, *1595*, 11–18.
- [246] L. M. Salonen, S. R. Pinela, S. P. S. Fernandes, J. Louçano, E. Carbó-Argibay, M. P. Sarriá, C. Rodríguez-Abreu, J. Peixoto, B. Espiña, *J. Chromatogr. A* **2017**, *1525*, 17–22.
- [247] J. Hao, P. Chen, Q. Zhang, P. Chen, X. Zheng, Y. Wu, D. Ma, D. Wei, H. Liu, G. Liu, W. Lv, *Environ. Sci. Nano* **2019**, *6*, 3374–3387.
- [248] S. P. S. Fernandes, A. Mellah, P. Kovář, M. P. Sárria, M. Pšenička, H. Djamila, L. M. Salonen, B. Espiña, *Molecules* **2020**, *25*, 3132.
- [249] S. P. S. Fernandes, P. Kovář, M. Pšenička, A. M. S. Silva, L. M. Salonen, B. Espiña, *ACS Appl. Mater. Interfaces* **2021**, *13*, 15053–15063.
- [250] S. P. S. Fernandes, V. F. Fonseca, V. Romero, I. A. Duarte, A. Freitas, J. Barbosa, P. Reis-Santos, L. M. Salonen, B. Espiña, *Chemosphere* **2021**, *278*, 130364.
- [251] Y. Song, R. Ma, L. Hao, X. Yang, C. Wang, Q. Wu, Z. Wang, *J. Chromatogr. A* **2018**, *1572*, 20–26.
- [252] J.-M. Liu, X.-Z. Wang, C.-Y. Zhao, J.-L. Hao, G.-Z. Fang, S. Wang, *J. Hazard. Mater.* **2018**, *344*, 220–229.
- [253] D. A. Vazquez-Molina, G. S. Mohammad-Pour, C. Lee, M. W. Logan, X. Duan, J. K. Harper, F. J. Uribe-Romo, *J. Am. Chem. Soc.* **2016**, *138*, 9767–9770.
- [254] L. Chen, M. Zhang, F. Fu, J. Li, Z. Lin, *J. Chromatogr. A* **2018**, *1567*, 136–146.

- [255] S. Karak, S. Kandambeth, B. P. Biswal, H. S. Sasmal, S. Kumar, P. Pachfule, R. Banerjee, *J. Am. Chem. Soc.* **2017**, *139*, 1856–1862.
- [256] D. Wei, J. Li, Z. Chen, L. Liang, J. Ma, M. Wei, Y. Ai, X. Wang, *J. Mol. Liq.* **2020**, *301*, 112431.
- [257] V. Romero, S. P. S. Fernandes, L. Rodriguez-Lorenzo, Y. V. Kolen'ko, B. Espiña, L. M. Salonen, *Nanoscale* **2019**, *11*, 6072–6079.
- [258] Y. Liao, J. Li, A. Thomas, *ACS Macro Lett.* **2017**, *6*, 1444–1450.
- [259] Y. Li, C. X. Yang, X.-P. Yan, *Chem. Commun.* **2017**, *53*, 2511–2514.
- [260] W. Zhao, K. Hu, C. Hu, X. Wang, A. Yu, S. Zhang, *J. Chromatogr. A* **2017**, *1487*, 83–88.
- [261] Y. C. Yuan, B. Sun, A. M. Cao, D. Wang, L. J. Wan, *Chem. Commun.* **2018**, *54*, 5976–5979.
- [262] L. L. Wang, C. X. Yang, X. P. Yan, *Chempluschem* **2017**, *82*, 933–938.
- [263] K. Zhang, S. L. Cai, Y. L. Yan, Z. H. He, H. M. Lin, X. L. Huang, S.-R. Zheng, J. Fan, W. G. Zhang, *J. Chromatogr. A* **2017**, *1519*, 100–109.
- [264] H. L. Qian, C. Yang, X. P. Yan, *Chem. Commun.* **2018**, *54*, 11765–11768.
- [265] W. Li, L. Huang, D. Guo, Y. Zhao, Y. Zhu, *J. Chromatogr. A* **2018**, *1571*, 76–83.
- [266] S. Yuan, X. Li, J. Zhu, G. Zhang, P. Van Puyvelde, B. Van Der Bruggen, *Chem. Soc. Rev.* **2019**, *48*, 2665–2681.
- [267] L. Xu, J. Xu, B. Shan, X. Wang, C. Gao, *J. Memb. Sci.* **2017**, *526*, 355–366.
- [268] F. Pan, W. Guo, Y. Su, N. A. Khan, H. Yang, Z. Jiang, *Sep. Purif. Technol.* **2019**, *215*, 582–589.
- [269] R. Wang, M. Wei, Y. Wang, *J. Memb. Sci.* **2020**, *604*, 118090.
- [270] K. Dey, M. Pal, K. C. Rout, S. K. H., A. Das, R. Mukherjee, U. K. Kharul, R. Banerjee, *J. Am. Chem. Soc.* **2017**, *139*, 13083–13091.
- [271] S. Wuttke, D. D. Medina, J. M. Rotter, S. Begum, T. Stassin, R. Ameloot, M. Oschatz, M. Tsotsalas, *Adv. Funct. Mater.* **2018**, *28*, 1801545.
- [272] H. Wang, Z. Zeng, P. Xu, L. Li, G. Zeng, R. Xiao, Z. Tang, D. Huang, L. Tang, C. Lai, D. Jiang, Y. Li, H. Yi, L. Qin, S. Ye, X. Ren, W. Tang, *Chem. Soc. Rev.* **2019**, *48*, 488–516.
- [273] H. L. Qian, C. X. Yang, W. L. Wang, C. Yang, X. P. Yan, *J. Chromatogr. A* **2018**, *1542*, 1–18.

- [274] L. Valentino, M. Matsumoto, W. R. Dichtel, B. J. Mariñas, *Environ. Sci. Technol.* **2017**, *51*, 14352–14359.
- [275] R. Wang, X. Shi, A. Xiao, W. Zhou, Y. Wang, *J. Memb. Sci.* **2018**, *566*, 197–204.
- [276] E. Fux, Development And Evaluation of Passive Sampling and LC-MS Based Techniques for the Detection and Monitoring of Lipophilic Marine Toxins in Mesocosm and Field Studies, Dublin Institute of Technology, **2008**.
- [277] T. Suzuki, H. Uchida, R. Watanabe, *Compr. Anal. Chem.* **2017**, *78*, 137–192.
- [278] FAO/WHO, *Toxicity Equivalency Factors for Marine Biotoxins Associated with Bivalve Molluscs*, **2016**.
- [279] A. Li, F. Ma, X. Song, R. Yu, *J. Chromatogr. A* **2011**, *1218*, 1437–1442.
- [280] D. Seader, E. J. Henley, *Separation Process Principles*, John Wiley & Sons, Inc. **2006**.
- [281] L. Fan, G. Sun, J. Qiu, Q. Ma, P. Hess, A. Li, *J. Chromatogr. A* **2014**, *1373*, 1–8.
- [282] R. Apak, Adsorption of heavy metal ions on soil surfaces and similar substances, in: A.T. Hubbard (Ed.), *Encycl. Surf. Colloid Sci.*, Vol. 1, Marcel Dekker, Inc, New York, **2002**, pp. 385–417.
- [283] Z. Chen, B. Xing, W. B. McGill, *J. Environ. Qual.* **1999**, *28*, 1422–1428.
- [284] P. Rodríguez, A. Alfonso, E. Turrell, J. P. Lacaze, L. M. Botana, *Harmful Algae* **2011**, *10*, 447–455.
- [285] G. P. Mashile, P. N. Nomngongo, *Crit. Rev. Anal. Chem.* **2017**, *47*, 119–126.
- [286] R. Berger, G. Resnati, P. Metrangolo, E. Weber, J. Hulliger, *Chem. Soc. Rev.* **2011**, *40*, 3496–3508.
- [287] R. J. Glyn, G. Pattison, *J. Med. Chem.* **2021**, *64*, 10246–10259.
- [288] F. Dixit, B. Barbeau, M. Mohseni, *Sci. Total Environ.* **2019**, *655*, 571–580.
- [289] H. Zhao, J. Qiu, H. Fan, A. Li, *J. Chromatogr. A* **2013**, *1300*, 159–164.
- [290] W. Zhang, M. Lin, M. Wang, P. Tong, Q. Lu, L. Zhang, *J. Chromatogr. A* **2017**, *1503*, 1–11.
- [291] C. Huang, Y. Wang, Q. Huang, Y. He, L. Zhang, *Anal. Chim. Acta* **2019**, *1054*, 38–46.
- [292] J. M. González-Jartin, L. C. Alves, A. Alfonso, Y. Piñeiro, S. Y. Vilar, I. Rodriguez, M. G. Gomez, Z. V. Osorio, M. J. Sainz, M. R. Vieytes, J. Rivas, L. M. Botana, *Chemosphere* **2020**, *256*, 127019.

- [293] J. Liu, Y. Cai, Y. Deng, Z. Sun, D. Gu, B. Tu, D. Zhao, *Microporous Mesoporous Mater.* **2010**, *130*, 26–31.
- [294] Y. He, P. Wu, G. Li, L. Li, J. Yi, S. Wang, S. Lu, P. Ding, C. Chen, H. Pan, *Int. J. Biol. Macromol.* **2020**, *156*, 1574–1583.
- [295] S. Pavagadhi, A. L. L. Tang, M. Sathishkumar, K. P. Loh, R. Balasubramanian, *Water Res.* **2013**, *47*, 4621–4629.
- [296] W. Xia, X. Zhang, L. Xu, Y. Wang, J. Lin, R. Zou, *RSC Adv.* **2013**, *3*, 11007.
- [297] G. Dai, C. Quan, X. Zhang, J. Liu, L. Song, N. Gan, *Water Res.* **2012**, *46*, 1482–1489.
- [298] G. Dai, N. Gan, L. Song, S. Fang, N. Peng, *J. Oceanol. Limnol.* **2018**, *36*, 1103–1111.
- [299] W. Teng, Z. Wu, J. Fan, H. Chen, D. Feng, Y. Lv, J. Wang, A. M. Asiri, D. Zhao, *Energy Environ. Sci.* **2013**, *6*, 2765–2776.
- [300] J. A. Park, J. K. Kang, S. M. Jung, J. W. Choi, S. H. Lee, V. Yargeau, S. B. Kim, *Chemosphere* **2020**, *247*, 125811.
- [301] M. Klavarioti, D. Mantzavinos, D. Kassinos, *Environ. Int.* **2009**, *35*, 402–417.
- [302] “The DrugBank Database,” can be found under <https://www.drugbank.ca>, **2018**.
- [303] M. I. La Rotonda, G. Amato, F. Barbato, C. Silipo, A. Vittoria, *Quant. Struct. Act. Relationships* **1983**, *2*, 168–173.
- [304] L. F. Prescott, *Br. J. clin. Pharmac.* **1980**, *10*, 291–298.
- [305] J. Sangster, *Octanol-Water Partition Coefficients: Fundamentals and Physical Chemistry*, John Wiley & Sons, Ltd., **1997**.
- [306] D. D. Glover, D. Lalka, G. R. G. Monif, G. E. T. Al, *Infect. Dis. Obstet. Gynecol.* **1996**, *46*, 43–46.
- [307] P. W. Seo, B. N. Bhadra, I. Ahmed, N. A. Khan, S. H. Jhung, *Sci. Rep.* **2016**, *6*, 34462.
- [308] B. N. Bhadra, I. Ahmed, S. Kim, S. H. Jhung, *Chem. Eng. J.* **2017**, *314*, 50–58.
- [309] A. S. Mestre, J. Pires, J. M. F. Nogueira, A. P. Carvalho, *Carbon N. Y.* **2007**, *45*, 1979–1988.
- [310] N. Cai, P. Larese-Casanova, *J. Colloid Interface Sci.* **2014**, *426*, 152–161.
- [311] M. Engel, B. Chefetz, *Adv. Colloid Interface Sci.* **2019**, *271*, 101993.
- [312] C. Valls-Cantenys, M. Scheurer, M. Iglesias, F. Sacher, H. J. Brauch, V. Salvadó, *Anal. Bioanal. Chem.* **2016**, *408*, 6189–6200.

- [313] S. K. Behera, S. Y. Oh, H. S. Park, *Int. J. Environ. Sci. Technol.* **2012**, *9*, 85–94.
- [314] L. Huang, N. Mao, Q. Yan, D. Zhang, Q. Shuai, *ACS Appl. Nano Mater.* **2020**, *3*, 319–326.
- [315] IPMA, Climate Report from May 2017; ISSN 2183-107, *Lisbon, Portugal*.
- [316] P. Kwan, M. J. Brodie, *Epilepsia* **2004**, *45*, 1141–1149.
- [317] U. Hass, U. Duennbier, G. Massmann, *Water Res.* **2012**, *46*, 6013–6022.
- [318] P. Palma, A. Lima, M. Helena, M. João, N. Montemurro, S. Pérez, M. Lopez, D. Alda, *Sci. Total Environ.* **2020**, *709*, 136205.
- [319] R. Shawahna, N. U. Rahman, *DARU* **2011**, *19*, 83–99.
- [320] M. Bialer, *Epilepsia* **2012**, *53*, 3–11.
- [321] L. Yang, Y. Zhang, X. Liu, X. Jiang, Z. Zhang, T. Zhang, L. Zhang, *Chem. Eng. J.* **2014**, *246*, 88–96.
- [322] J. K. Challis, J. C. Carlson, K. J. Friesen, M. L. Hanson, C. S. Wong, *J. Photochem. Photobiol. A Chem.* **2013**, *262*, 14–21.
- [323] C. Stamm, K. Räsänen, F. J. Burdon, F. Altermatt, J. Jokela, A. Joss, M. Ackermann, R. I. L. Eggen, *Adv. Ecol. Res.* **2016**, *55*, 183–223.
- [324] A. A. Adegoke, A. C. Faleye, G. Singh, T. A. Stenström, *Molecules* **2017**, *22*, 29.
- [325] L. F. Angeles, S. Islam, J. Aldstadt, K. N. Saqeeb, M. Alam, M. A. Khan, F. T. Johura, S. I. Ahmed, D. S. Aga, *Sci. Total Environ.* **2020**, *712*, 136285.
- [326] S. R. Hughes, P. Kay, L. E. Brown, *Environ. Sci. Technol.* **2013**, *47*, 661–677.
- [327] P. A. Segura, M. François, C. Gagnon, S. Sauvé, *Environ. Health Perspect.* **2009**, *117*, 675–684.
- [328] J. Wang, R. Zhuan, L. Chu, *Sci. Total Environ.* **2019**, *646*, 1385–1397.
- [329] T. He, K. Geng, D. Jiang, *Trends Chem.* **2021**, 1–14.
- [330] E. Jin, M. Asada, Q. Xu, S. Dalapati, M. A. Addicoat, M. A. Brady, H. Xu, T. Nakamura, T. Heine, Q. Chen, et al., *Science* **2017**, *357*, 673–676.
- [331] E. Jin, J. Li, K. Geng, Q. Jiang, H. Xu, Q. Xu, D. Jiang, *Nat. Commun.* **2018**, *9*, 4143.
- [332] D. Becker, B. P. Biswal, P. Kaleńczuk, N. Chandrasekhar, L. Giebeler, M. Addicoat, S. Paasch, E. Brunner, K. Leo, A. Dianat, G. Cuniberti, R. Berger, X. Feng, *Chem. Eur. J.* **2019**, *25*, 6562–6568.

- [333] T. Jadhav, Y. Fang, W. Patterson, C. H. Liu, E. Hamzehpoor, D. F. Perepichka, *Angew. Chemie Int. Ed.* **2019**, *58*, 13753–13757.
- [334] H. Lyu, C. S. Diercks, C. Zhu, O. M. Yaghi, *J. Am. Chem. Soc.* **2019**, *141*, 6848–6852.
- [335] C. Yang, W. Zhang, J. Xu, L. Liu, *Nat. Commun.* **2019**, *10*, 2467.
- [336] D. L. Pastoetter, S. Xu, M. Borrelli, M. Addicoat, B. P. Biswal, S. Paasch, A. Dianat, H. Thomas, R. Berger, S. Reineke, E. Brunner, G. Cuniberti, M. Richter, X. Feng, *Angew. Chemie Int. Ed.* **2020**, *59*, 23620–23625.
- [337] S. Xu, G. Wang, B. P. Biswal, M. Addicoat, S. Paasch, W. Sheng, X. Zhuang, E. Brunner, T. Heine, R. Berger, X. Feng, *Angew. Chemie Int. Ed.* **2019**, *58*, 849–853.
- [338] E. Jin, Z. Lan, Q. Jiang, K. Geng, G. Li, X. Wang, D. Jiang, *Chem* **2019**, *5*, 1632–1647.
- [339] R. Chen, J. L. Shi, Y. Ma, G. Lin, X. Lang, C. Wang, *Angew. Chemie Int. Ed.* **2019**, *58*, 6430–6434.
- [340] J. Xu, Y. He, S. Bi, M. Wang, P. Yang, D. Wu, J. Wang, F. Zhang, *Angew. Chemie Int. Ed.* **2019**, *58*, 12065–12069.
- [341] Y. Yang, H. Niu, L. Xu, H. Zhang, Y. Cai, *Appl. Catal. B Environ.* **2020**, *269*, 118799.
- [342] S. Xu, H. Sun, M. Addicoat, B. P. Biswal, F. He, S. W. Park, S. Paasch, T. Zhang, W. Sheng, E. Brunner, Y. Hou, M. Richter, X. Feng, *Adv. Mater.* **2021**, *33*, 2006274.
- [343] C. Mo, M. Yang, F. Sun, J. Jian, L. Zhong, Z. Fang, J. Feng, D. Yu, *Adv. Sci.* **2020**, *7*, 1–8.
- [344] E. Article, Z. Fu, X. Wang, A. M. Gardner, X. Wang, S. Y. Chong, G. Neri, A. J. Cowan, L. Liu, X. Li, A. Vogel, R. Clowes, M. Bilton, L. Chen, R. S. Sprick, A. I. Cooper, *Chem. Sci.* **2020**, *11*, 543–550.
- [345] S. Li, L. Li, Y. Li, L. Dai, C. Liu, Y. Liu, J. Li, J. Lv, P. Li, B. Wang, *ACS Catal.* **2020**, *10*, 8717–8726.
- [346] S. Bi, P. Thiruvengadam, S. Wei, W. Zhang, F. Zhang, L. Gao, J. Xu, D. Wu, J. S. Chen, F. Zhang, *J. Am. Chem. Soc.* **2020**, *142*, 11893–11900.
- [347] W.-R. Cui, F.-F. Li, R.-H. Xu, C.-R. Zhang, X.-R. Chen, R.-H. Yan, R.-P. Liang, J.-D. Qiu, *Angew. Chemie Int. Ed.* **2020**, *59*, 17684–17690.
- [348] C. R. Zhang, W. R. Cui, W. Jiang, F. F. Li, Y. Di Wu, R. P. Liang, J. D. Qiu, *Environ. Sci. Nano* **2020**, *7*, 842–850.



- [349] W.-R. Cui, C.-R. Zhang, R.-H. Xu, X.-R. Chen, R.-H. Yan, W. Jiang, R.-P. Liang, J.-D. Qiu, *ACS ES&T Water* **2021**, *1*, 440–448.
- [350] C. Zhang, W. Cui, R. Xu, X. Chen, Y. Wu, R. Yan, R. Liang, J. Qiu, *CCS Chem.* **2021**, *3*, 168–179.
- [351] Z. Bin Cai, L. F. Liu, Y. Q. Hong, M. Zhou, *J. Coord. Chem.* **2013**, *66*, 2388–2397.
- [352] S. A. Barnett, A. J. Blake, N. R. Champness, C. Wilson, *Dalt. Trans.* **2003**, 2387–2394.
- [353] Y. Hu, C. Y. Li, X. M. Wang, Y. H. Yang, H. L. Zhu, *Chem. Rev.* **2014**, *114*, 5572–5610.
- [354] M. Lafrance, C. N. Rowley, T. K. Woo, K. Fagnou, *J. Am. Chem. Soc.* **2006**, *128*, 8754–8756.
- [355] J. Xu, C. Yang, S. Bi, W. Wang, Y. He, D. Wu, Q. Liang, X. Wang, F. Zhang, *Angew. Chemie Int. Ed.* **2020**, *59*, 2–11.
- [356] S. He, Q. Rong, H. Niu, Y. Cai, *Chem. Commun.* **2017**, *53*, 9636–9639.
- [357] Q. Liao, C. Ke, D. Wang, Y. Zhang, Q. Han, Y. Zhang, K. Xi, *ChemRxiv* **2021**, DOI 10.26434/chemrxiv.14214479.v1.
- [358] F. Liu, Z. Ma, Y. Deng, M. Wang, P. Zhou, W. Liu, S. Guo, M. Tong, D. Ma, *Environ. Sci. Technol.* **2021**, *55*, 5371–5381.
- [359] Dassault Systèmes BIOVIA Materials Studio 8.0, Dassault Systèmes, San Diego **2017**.
- [360] S. Plimpton, *J. Comput. Phys.* **1995**, *117*, 1–19.
- [361] H. Sun, S. J. Mumby, J. R. Maple, A. T. Hagler, *J. Am. Chem. Soc.* **1994**, *116*, 2978–2987.
- [362] H. Sun, *J. Phys. Chem. B* **1998**, *102*, 7338–7364.
- [363] H. Heinz, *J. Comput. Chem.* **2010**, *31*, 1564–1568.
- [364] H. Heinz, T. J. Lin, R. Kishore Mishra, F. S. Emami, *Langmuir* **2013**, *29*, 1754–1765.
- [365] A. Freitas, S. Leston, J. Rosa, M. Castilho, J. Barbosa, P. Rema, M. Â. Pardal, F. Ramos, *Food Addit. Contam. Part A* **2014**, *31*, 817–826.